Investigating the Dynamics of Aggregation in Chromophores used in Organic Photovoltaics with the Help of Simulations

Von der Universität Bayreuth
zur Erlangung des Grades eines
Doktors der Naturwissenschaften (Dr. rer. nat.)
genehmigte Abhandlung

von

Axel Bourdick
geboren in Frankfurt am Main

1. Gutachter: Prof. Dr. Stephan Gekle
2. Gutachter: Prof. Dr. Stephan Kümmel

When one experiences truth, the madness of finding fault with others disappears.

Contents

1 Summary

Through the burning of fossil fuels and a steadily and rapidly rising global energy demand, mankind faces serious challenges today, like the anthropogenic climate change. It is necessary to develop a sustainable, renewable energy supply because fossil fuel resources are finite. An obvious eco-friendly energy source is the sun. With the help of solar cells light can be harvested directly. The development of organic solar cells is one of the recent developments in this field. They are easy and cheap to manufacture in comparison with classical inorganic devices. They can be applied to flexible materials, which enables a broad spectrum of new applications. Although a lot of progress has been made in recent years, there is still a large need for research because they achieve relatively low efficiency and lifetime.

To develop a better understanding of these new materials it is of vital importance to better understand the aggregation mechanisms of π-conjugated chromophores. The molecular arrangement determines the formation of ordered and unordered domains in a material, which defines the electrooptical properties of the final device. Insights about the aggregation process can be used to design molecules optimized for specific properties and applications.

This thesis investigates the molecular aggregation process of chromophores under different aspects. Combined molecular dynamics and density functional theory computer simulations are employed to investigate the systems on molecular length- and timescales. These methods are suitable to complement experimental results and to develop a deeper understanding of the underlying processes. Different structures often interact uniquely with light and can be therefore spectrally separated. Hence, optical spectroscopy is a valuable tool to investigate the formation of aggregates and morphologic properties of a material. The results of this thesis are combined mainly with absorption- and photoluminescence spectroscopy.

Over the last years good results have been achieved with small π-conjugated molecules. A promising system is the molecule named T1, achieving high efficiencies and good aggregation properties. It is not fully understood why this is the case. It is unclear why structurally similar systems exhibits significantly different traits. The publication in chapter 5.1 investigates the aggregation of T1 and the structurally similar molecule H1 in dependence of temperature and concentration. H1 has a different central donor unit resulting in a point-symmetric molecular structure, while T1 is axis-symmetric. H1 does not show aggregation in solution, but still manages to form crystalline domains in processed films, especially if processed with a high boiling point additive.

Molecular dynamics simulations are used to characterise the possible structures in solution. For T1, two different aggregation pathways can be identified. The experimental results can be reproduced with the simulations, which shows that aggregation in H1 is possible but rare. The molecules must be aligned in a specific fashion and need to be very close to one another. Therefore, significant molecular overlap has to be achieved before an aggregate is formed. A lot of solvent must be displaced first, which is why aggregation is kinetically hindered. This publication results in an increased understanding of the aggregation process of these molecules.

Aggregation is often induced by cooling down a solution. By lowering the temperature, rotational degrees of freedom freeze-out, resulting in planarization. There are reports indicating that planarization is beneficial for aggregation, while other investigations observe planarization because of the formation of aggregates. The underlying processes are poorly understood. This thesis investigates this question in the publication in section 5.2. The planar molecule CT and the twisted TT are investigated. Surprisingly, experimental results show strong aggregation in TT and weak aggregation in CT, while computer simulations predict a similar aggregation strength in these systems. This discrepancy is solved with additional molecular dynamics and time-dependent density functional theory calculations. The results indicate that TT planarizes because of aggregation, resulting in a lower energy. For CT, non-emissive, excimer-like configurations are identified. With the help of these insights, the experimental data can be interpreted and a deeper understanding of the role of planarity is developed.

The publication in section 5.3 investigates the polymer polythiophene, which can be used in organic solar cells. Manufacturing methods are discussed, with which specific crystal structures can be obtained. Crystalline polythiophene can be in a lamellar and in a herringbone-like arrangement. These structures can also be observed in the simulations with lattice constants that are in good agreement with the experimental values. Therefore, simulations can be used to support the interpretation of the experimental results.

Zusammenfassung

Durch die Nutzung von fossilen Brennstoffen und einem rasant steigenden globalen Energiebedarf steht die Menschheit heute vor großen Herausforderungen, wie zum Beispiel dem anthropogenen Klimawandel. Durch die Endlichkeit der fossilen Ressourcen ist es notwendig, eine nachhaltige, regenerative Energieversorgung zu entwickeln. Eine naheliegende, umweltfreundliche Energiequelle ist dabei die Sonne. Mit Hilfe von Solarzellen lässt sich die Sonneneinstrahlung direkt nutzbar machen. Zu den jüngsten Entwicklungen in diesem Bereich gehören organische Solarzellen. Organische Solarzellen lassen sich potenziell einfacher und kostengünstiger herstellen als klassische, anorganischen Solarzellen und können auf flexible Materialien aufgebracht werden, wodurch eine Reihe neuer Anwendungsfälle erschlossen werden kann. Zwar konnten in den letzten Jahren große Fortschritte erzielt werden, trotzdem gibt es in diesem Bereich immensen Forschungsbedarf, da sie bisher relativ geringe Wirkungsgrade und Lebensdauer erreichen.

Um ein besseres Verständnis dieser neuen Materialien zu entwickeln, ist es von essenzieller Bedeutung, den molekularen Aggregationsmechanismus von π-konjugierten Chromophoren zu untersuchen. Wie sich die Moleküle anordnen bestimmt die Formation von geordneten und ungeordneten Domänen in dem Material, wodurch wiederum die optoelektronischen Eigenschaften der fertigen Solarzelle bestimmt werden. Erkenntnisse, über die der Aggregation zugrunde liegenden Prozesse können genutzt werden, um Moleküle zu designen, die für spezielle Eigenschaften und Anforderungen optimiert sind.

Diese Dissertation untersucht den molekularen Aggregationsprozess von Chromophoren unter verschiedenen Aspekten. Hierfür werden kombinierte Molekulardynamik und Dichtefunktionaltheorie Computersimulationen eingesetzt, um die Systeme auf molekularen Längen- und Zeitskalen zu untersuchen. Diese Methoden eignen sich hervorragend, um experimentelle Ergebnisse komplementär zu ergänzen und helfen somit ein tieferes Verständnis der zugrunde liegenden Prozesse zu entwickeln. Verschiedene Strukturen wechselwirken häufig in unterschiedlicher Weise mit Licht und können daher spektral getrennt werden, wodurch optische Spektroskopie Methoden ein wertvolles Werkzeug sind, um die Entstehung von Aggregaten und die morphologischen Eigenschaften eines Materials zu untersuchen. Die Ergebnisse dieser Arbeit werden hautsächlich mit Absorptions- und Photolumineszenz Spektroskopie kombiniert.

In den letzten Jahren hat sich herausgestellt, dass mit dem Einsatz von kleinen π-konjugierten Molekülen gute Ergebnisse erzielt werden können. Ein vielver-

sprechendes System ist das Molekül T1, welches eine hohe Effizienz und gute Aggregation erzielt. Warum gerade dieses Molekül so gute Eigenschaften besitzt ist nicht vollständig verstanden. Es ist auch unklar, warum strukturell sehr ähnliche Systeme ein signifikant anderes Verhalten aufweisen. Die Publikation in Kapitel 5.1 untersucht die Aggregation von T1 und einem strukturell ähnlichen Molekül H1 in Abhängigkeit von Temperatur und Konzentration. H1 besitzt eine andere zentrale Donoreinheit und damit auch eine andere Symmetrie. Die Struktur von T1 ist achsensymmetrisch, die von H1 punktsymmetrisch. In Lösung kann keine Aggregation von H1 beobachtet werden, wohingegen sich im fertigen Film durchaus kristalline Domänen befinden können, wenn dieser mit Hilfe eines hochsiedenen Lösungsmitteladditivs hergestellt wird.

Mit Hilfe von Molekulardynamiksimulationen können wir die in der Lösung auftretenden Strukturen charakterisieren. Hierbei zeigen sich zwei unterschiedliche Aggregationspfade für T1. Die experimentellen Ergebnisse können mit den Simulationen reproduziert werden. Hierbei zeigt sich, dass ein Aggregat in H1 zwar möglich, aber unwahrscheinlich ist, da die Moleküle in ganz bestimmter Weise orientiert sein müssen und die Reichweite der attraktiven Wechselwirkung sehr kurz ist. Demnach muss eine deutliche Überlappung erzielt werden, um aggregieren zu können. Hierfür muss Lösungsmittel verdrängt werden, wodurch die Aggregation kinetisch blockiert ist. Mit der vorliegenden Untersuchung ist es uns gelungen, den Aggregationsprozess dieser Systeme besser zu verstehen.

Häufig wird Aggregation induziert indem die Temperatur einer Lösung erniedrigt wird. Mit abnehmender Temperatur frieren molekulare Rotationsfreiheitsgrade aus, was eine Planarisierung zur Folge hat. Es gibt sowohl Untersuchungen, die darauf hinweisen, dass Planarisierung vorteilhaft für das Aggregationsverhalten ist, als auch Studien, die nahelegen, dass Planarisierung durch Aggregation erzeugt wird. Die zugrunde liegenden Prozesse sind hierbei nicht ausreichend verstanden. Die vorliegende Dissertation beschäftigt sich mit dieser Frage in der Publikation in Kapitel 5.2. Untersucht wird das Molekül CT, welches sehr planar ist und das Molekül TT, das eine gewundene Struktur aufweist. Überraschenderweise zeigt sich experimentell ein starkes Aggregationsverhalten in TT und ein schwaches in CT, wohingegen Simulationen ein ähnliches Aggregationsverhalten der beiden Systeme postulieren. Mit Hilfe von weiteren Molekulardynamik und zeitabhängigen Dichtefunktionaltheorie Simulationen lässt sich diese Diskrepanz auflösen. Die Ergebnisse legen nahe, dass TT durch die Aggregation planarisiert, wodurch es zu einem Energiegewinn kommt. Für CT konnte gezeigt werden, dass es nicht-strahlende, Exzimer artige Zustände gibt. Mit diesen Erkenntnissen können die experimentellen Daten erklärt und ein

tieferes Verständnis für die Rolle der Planarität entwickelt werden.

Die Publikation in Kapitel 5.3 beschäftigt sich mit dem Polymer Polythiophen, welches in organischen Solarzellen verwendet werden kann. Hier werden Herstellungsverfahren diskutiert, mit deren Hilfe man gezielt verschiedene Kristallstrukturen in dem Material erzielen kann. Kristallines Polythiophen kann in einer lamellaren oder einer fischgrätenartigen Struktur vorliegen. Diese Strukturen können in den Simulationen beobachtet werden mit guter Übereinstimmung mit den experimentell ermittelten Gitterkonstanten. Hiermit gelingt es uns, die Interpretation der Daten mit Hilfe von Simulationen zu unterstützen.

2 Introduction

2.1 Motivation of this dissertation

The industrial revolution changed how humans use energy.[1] Innovations and technical progress provided easy and widespread access to energy stored in fossil fuels like coal, oil and natural gas. While these energy sources paved the way to modern society, the information age and a closely intertwined global economy, the underlying dynamics has led to a steadily and largescale increase of global energy demands. As a consequence, mankind faces serious challenges today.[2–5] The burning of fossil fuels damages and influences the environment in a variety of ways. Because humans do not live independently of their environment but rather in symbiosis with it, the endangerment of complex ecosystems directly threatens our basis of existence. The amount of fossil fuels is finite[6] and can therefore not satisfy rising energy demands on arbitrarily long time-scales. In order for this system to be sustainable, regenerative energy sources like solar, wind and geothermal need to be established on a large scale. The burning of fossil fuels releases greenhouse gases, like CO_2, into the atmosphere, which causes global warming and climate change.[7–12] In 2016, the international community of states set the ambitious goal to limit global warming to well under 2°C above pre-industrial levels, known as the *Paris Agreement*.[13] Achieving this target is a challenging global task and will take a considerable amount of effort.[14–16] While the large scale use of fossil fuels provided a rapid head start for innovation, technology, population growth and society, this is not sustainable in the long run.

Solar cells are devices which convert sunlight into electricity and are needed in a diversified, decentralized, well-integrated, sustainable energy grid of the future.[17] Classical solar cells are made from inorganic compounds, like silicon- or gallium-based materials. Today, this technology is well established on the market. Conversion efficiencies over 26% have been reported for real world silicon solar cells.[18] Long lifetimes[19] and high efficiencies[20] give them economic viability. However, they are rigid and heavy in their design, difficult to install and the manufacturing is relatively energy intensive which leads to a long payback time.[21–23] These limitations restrict their field of application. To compensate for these disadvantages, the development of organic solar cells has become a focus of interest during the last decade. Organic solar cells are made from hydrocarbon-based molecules. Often small organic molecules or polymers with π-conjugated delocalized electron systems are used. With this approach the molecules interact via π-π stacking with one another, resulting in self-organization and useful electrooptical properties due to the formation of electronic donors and acceptors which enables charge separation. Efficiencies of up to 17.3% have been reported for hybrid organic solar cells of a tandem-like structure.[24]

Organic photovoltaics is a branch of organic electronics, which incorporates other devices like organic transistors (OFET)[25;26] and light emitting diodes (OLED)[27–29]. Organic displays are for example economically viable and are used in modern smart phones. The purpose of OLEDs is to produce light from electricity. In an organic solar cell, the opposite is true. Here, energy from light is captured and converted to power some electronic device. In these devices, the molecular structuring process is crucial for the electronic interactions and therefore also determines the properties of the final device. A lot about the aggregation process is poorly understood at the moment. For example, molecules often planarize during the aggregation process, and it is not clear if planarization is a prerequisite for or a consequence of the formation of aggregates. The aggregation process is difficult to observe directly experimentally, because the time and length scales of molecular structuring processes is inaccessible. Therefore, indirect methods are needed to help gain valuable insights into the underlying mechanisms at work. One method to do this, which is used in this thesis, is molecular dynamics (MD) simulation. The modeling of molecular interactions with powerful computers provides an important tool to develop a better understanding of the system in question and can therefore complement and interpret experimental data.

Organic solar cells are a promising field due to the availability of cheap and easily scalable solution-deposition methods like blade coating[30–32] or ink-jet printing.[33–37] With this, organic photovoltaics technology can be tuned to a wide range of applications.[38] It becomes possible to manufacture partially transparent thin films, which can be integrated into facades, like windows, to make use of energy-harvesting surfaces in urban environments. Compared to classical photovoltaics, organic materials are better to meet functional and aesthetic demands required in modern smart buildings.[39] By tuning their optical properties, organic solar cells can also be used in the design of indoor internet of things (IoT).[40] They can be incorporated into fabrics resulting in wearable power generating clothing because they can be integrated into flexible materials.[41] With their lightweight, easy to manufacture nature, organic photovoltaics can help to bring power generating capabilities to poor and remote regions all around the world, where classical photovoltaic devices are difficult to deploy.[42] With the advance of technological possibilities and the more wide-spread use of these exciting materials, new innovative fields of applications are expected to arise in the future. The main challenges when designing organic photovoltaic devices are the low efficiency and stability which is why research is needed to manufacture devices better suited for applications.[43;44]

The main goal of this thesis is to deploy a better understanding of the molecular structuring and aggregation process of π-conjugated chromophores used in organic

photovoltaics in solution and during film formation. The chromophores investigated are small molecules and one polymer. The systems are made of subunits, which are often used in a wide spectrum of possible materials. Insights gained might be therefore useful for other materials as well. They are designed with key differences in mind to be able to investigate specific features like symmetry, bending angle or planarity. Computer simulations are used to investigate those questions. A combination of semi-classical MD and quantum mechanical density functional theory (DFT) simulations are employed to model structural and electronic properties and dynamics. Simulations are used to support and help interpret experimental results. How molecular structures form influences the electronic properties of the system and therefore how they interact with electromagnetic waves. Optical absorption and emission spectroscopy are therefore valuable methods to investigate morphology and structure formation experimentally. The investigations are done in dependence of key parameters like temperature, solvent, concentration or processing conditions. With this approach key insights and a better understanding about the formation of aggregates and the resulting electronic and morphologic properties are obtained. This fundamental research is important to obtain a better understanding of the materials in question and can therefore help to design molecules with specific properties resulting in better devices.

2.2 Morphology

The molecular structuring process is very important for the device properties. How the molecules align determines the electrooptical properties of the material, like charge transfer or quantumefficiency.[45;46] At the nanoscopic scale, the molecules self-assemble in a certain way. These structures arrange into crystal-like or ordered and unordered domains on the mesoscopic scale which in turn determine the properties and performance of the final device.[47;48] Absorption and photoluminescence spectroscopy are valuable tools to gain experimental insights about structural information under varying conditions. However, the short time and length scales of molecular structuring makes it difficult to observe this process directly. Hereby, molecular dynamics simulation can support the experimental results. The simulations of individual atoms provide insights into how the molecules order in dependence of controllable parameters, like solvent or temperature and can thereby help and give complementary insights, to paint a bigger picture about the processes involved. With MD, it becomes possible to investigate the dynamics on nanometer length scales directly. Of course, one does not investigate reality itself, but just a simulation of it. However, by keeping the possibilities and limitations of this powerful tool in mind, additional insights can be gained trough the combination with experimental data. Therefore, a huge emphasis is laid in this thesis to make good models of the molecules in question.

Optically active chromophores frequently have large delocalized conjugated orbitals. Due to attractive π-π interactions, they can self-assemble into locally ordered domains.[49;50] This often introduces polycrystalline structures and therefore defects like grain boundaries or spatially separated domains. These defects might in turn hinder charge transport, acting as traps, therefore counteracting positive effects gained by local ordering. These effects might be wanted, for example when the goal is to obtain a large mono-crystalline domain, or they might be unwanted, for example if the goal is to achieve a blend of different domains with a certain size distribution. However, getting more control over the structuring processes is beneficial in either case. The aggregation process and the resulting morphology can be influenced through varying molecular parameters like solvent, concentration, the presence of molecular side-chains or the addition of a high boiling point solvent additive.[51] The latter is believed to prolong solvent evaporation time, giving the molecules more time to reorient and rearrange themselves into self-assembled larger structures.[52–54]

One method to manufacture thin organic solar cell films is spin-coating.[55;56] At constant temperature, a sample containing the optically active material, solvents and additional substances are applied to a substrate, which is rotated at high angular speeds to spread the coating solution uniformly. Excess material is cast away from the substrate while the solvent evaporates quickly, which in turn increases the concentration of the chromophore. The aggregation and restructuring process occurs under non-equilibrium conditions during this fast dry off process. With this procedure, thin films in the order of 10 nm to 500 nm can be achieved.[57] The structuring process and therefore the device morphology can be influenced by the processing conditions. For example, during spin-coating, temperature, processing speed and the solvent used are parameters influencing the device properties. The structure can also be influenced in post-processing after film formation with techniques like *thermal annealing* or *solvent annealing*.[58–63] To understand the complex film formation process, the interactions between chromophores in solution have to be understood first.

In figure 1 an example is shown, illustrating how the molecular structure influences device properties.[64] Figure 1a)-c) shows transmission electron microscope (TEM) images of the polymer PCDTBT:PC$_{70}$BM films cast from chloroform (CF), chlorobenzene (CB) and dichlorobenzene (DCB) solvents respectively. The insets show surface images measured by atomic force microscopy (AFM). The morphology of the films varies drastically due to the different solvents used during processing, which also directly influences the device performance. Figure 1d) displays the incident photon-to-current efficiency (IPCE). The current-voltage characteristics of the

devices can be seen in figure 1e). Both quantities depend heavily on the morphology and therefore on the processing conditions.
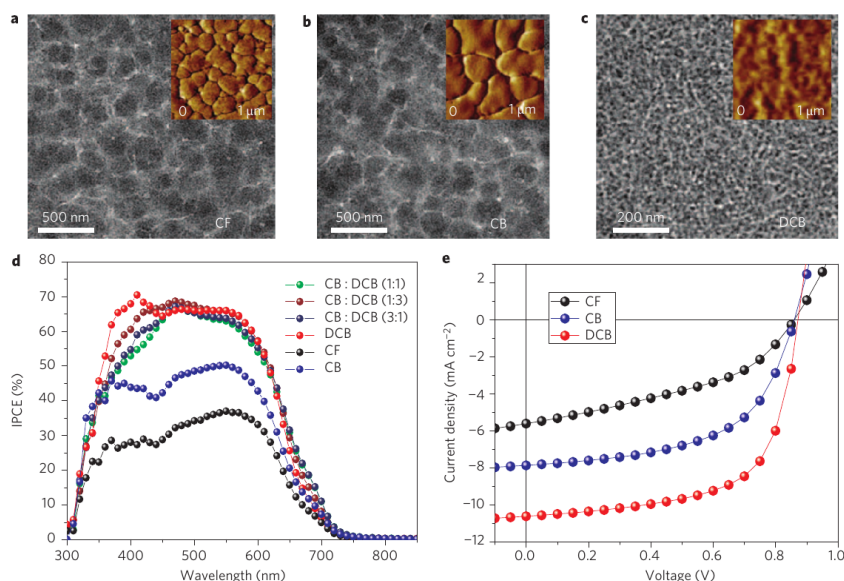

Figure 1: a)-c) TEM images of PCDTBT:PC$_{70}$BM films cased from CF, CB and DCB solvents. The insets show AFM images. c) displays the IPCE spectra and d) the J-V graphs of the devices. Reprinted with permission from *Springer Nature Customer Service Centre GmbH*: Nature Photonics; Bulk heterojunction solar cells with internal quantum efficiency approaching 100%; Park, S.H. et al; Copyright$^{©}$ (2009).

Aggregation of a π-conjugated molecule in solution can often be induced by cooling of the sample.[65] On the one hand, solvent quality is often a function of temperature. On the other hand, a reduction in temperature leads to a *freezing out* of rotational degrees of freedom and therefore to a planarization effect.[66–68] The details of this process are at the moment poorly understood. For example, it is not clear if planarization is a necessary condition for aggregation, or if in turn aggregation promotes planarization. This is one of the important questions this thesis tries to shed light on. Due to technical reasons, chromophores are often designed with large, bulky side-chains attached to them in order to increase solubility. This is necessary to make processing of the material possible. Therefore, a trade-off has to be made. Too many, or too large side-chains can be in the way during the aggregation process, counteracting the formation of locally ordered domains. On the other hand, chromophores can also exhibit too much aggregation behavior.[69]

Organic solar cells come in a variety of ways. The simplest form is a single layer solar cell, which is made of an organic electronic material between two metallic conductors.[70;71] Other designs are bilayer solar cells[72], consisting of an electron

donor and an electron acceptor layer, or bulk heterojunction solar cells, in which electron rich donor materials and electron deficient acceptor molecules (i.e. fullerene) are blended into disordered domains of the order of nanometres.[64;73;74] All of these devices require individual morphologic properties. An example for the morphology of a bilayer and a bulk heterojunction organic solar cell is shown in figure 2. Unordered domains often exist in a kinetically frozen, thermodynamic nonequilibrium state. Exposure to light or temperature therefore can cause a restructuring process, leading to the degradation of the device.[75] A better understanding of the molecular structuring process during device formation can help to gain insights about type, structure, distribution and stability of these domains, which can be used to improve device performance and counteract degradation effects, increasing lifetime.
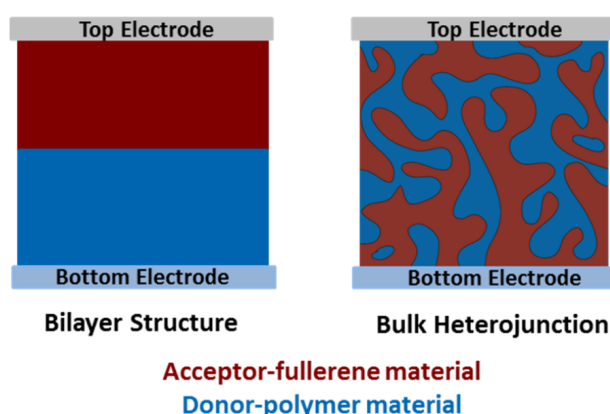
Figure 2: Architecture of bilayer and bulk heterojunction solar cells. Reprinted from[76] under the *Creative Commons Attribution License*.

The conversion of solar energy to electrical power happens through several steps.[69] Firstly, a photon is absorbed in the active material, creating a bound electron-hole pair. The absorption properties of the material are important for this step to access a large portion of the solar spectrum. The excited state then needs to diffuse to a donor acceptor interface before it relaxes to the ground state. The excitation only has a finite lifetime, which limits the diffusion length. At the interface, the excitation might induce a charge-transfer state. The charges now need to be separated before they recombine. Finally, the charges are transported through the layers and extracted at the cathode or anode.[77] Each of these steps is subject to loss channels and is influenced by the morphological properties of the device on multiple length scales. This highlights the importance of understanding the molecular structuring process in these materials. Given the outlined energy harvesting mechanism, the advantage of a bulk heterojunction solar cell becomes evident. Due to the blending of different domains, the interface area increases and the mean diffusion length of excitations to boundaries decreases, resulting in potentially increased efficiency.

Sterically demanding side-chains or additional groups can be introduced to suppress

excessive aggregation to tune the distribution of the domains.[78;79] The relationship between side-chains and aggregation is another important topic investigated in this thesis.

2.3 Methological details

The key concepts, which are used as the main methods of investigation in this thesis, are briefly described in the following.

2.3.1 Molecular dynamics simulations

Molecular Dynamics (MD) is a computational method to study the time dependent behavior of particles, often atoms and molecules.[80;81] Physical interactions are described by classical force fields, which can be divided into bonded, intramolecular interactions like bonds, angles, dihedrals and non-bonded interactions, for example Lennard-Jones or Coulomb interactions. In the simplest case, a bond between two atoms is modeled via a harmonic spring potential but different functions can be used to model each interaction. Bonds are stabilized by the LINCS method.[82] At every time step, the force fields are evaluated to calculate a resulting force acting on each particle in the simulation box. The forces are used to solve the classical Newtonian equation of motion for each particle, the resulting positions are the coordinates for the next time step. A popular integrator used in this thesis is the leap-frog algorithm.[83] Particles (usually atoms) are simulated individually and the calculation is classical. Of course, at molecular length scales, quantum mechanics cannot be neglected, which is why the classical force fields are designed to reproduce the quantum nature of the system. A full quantum mechanical description of a system of many particles is computationally not possible with current technology, which is why this trade-off is made. With this approach fast simulation speed can be achieved, while maintaining a reasonable amount of accuracy. Typical system sizes are in the range of 10^3 - 10^6 particles, characteristic simulation times are in the order of ps to µs, the resulting size of a typical simulation box is in the order of 1nm to 100nm. Usually, periodic boundary conditions (pbc) are implemented to avoid finite size effects. MD Simulations were carried out with the popular, well-established GROMACS simulation package.[84–90]
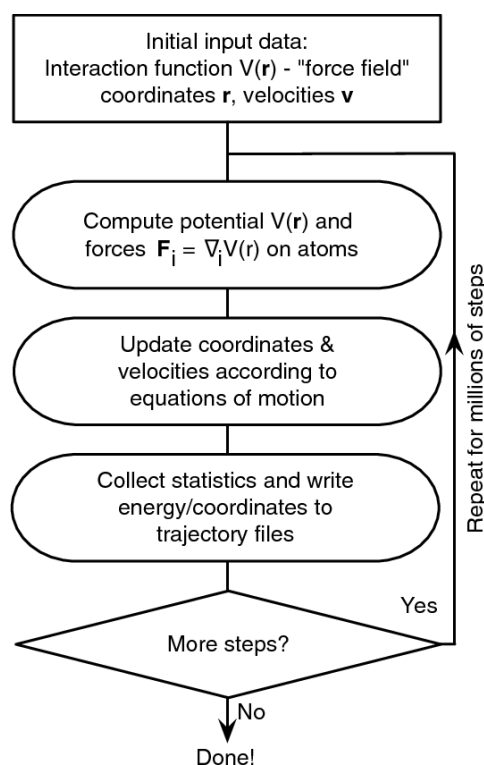
Figure 3: Simplified flowchart of a typical MD simulation.[91] Reprinted with
permission from *Springer Nature Customer Service Centre GmbH*: Methods
in molecular biology; Molecular dynamics simulations; Lindahl, E.;
Copyright[©] (2015).

A typical procedure of a MD simulation is displayed in figure 3. After the interacting
force fields have been defined, a system of particles is prepared by the selection of
the starting and boundary conditions. The relevant parameters for the simulation
are set (i.e. ensemble, target temperature, target pressure or volume). Algorithms
are selected for the integrator, the thermostat and barostat. Possible restraints to the
system can also be applied. After that, the simulation is performed. Typically, one
starts with different minimization and equilibration simulations to prepare the system
in a physically meaningful, equilibrated state for the production run. The positions,
velocities and forces on each particle can be saved periodically. The trajectory of
a simulation can be inspected visually with a suitable program like VMD.[92] The
data is used in post-processing in order to calculate meaningful physical quantities
describing the system.

2.3.2 Free energy and umbrella sampling

An important quantity, which is used to describe molecular aggregation processes in
this thesis, is the free energy difference between states of interest, which is a concept
describing the maximum amount of work that a system can perform at constant

temperature. The free energy is defined in equation 1, where Q denotes the canonical partition function of the system in question and β being the Boltzmann's constant.

$$F = -\frac{1}{\beta} \ln Q \tag{1}$$

A thermodynamic system of many particles can be defined by its microstate. For example, a classical ideal gas is completely described by the position and momentum of every particle. In contrast, the system can also be described in terms of statistically averaged macroscopic properties like temperature, pressure or energy, which define the macrostate. A given macrostate can correspond to various possible microstates, all of which have a certain probability of occurring. A system coupled to a heat bath will tend to minimize its internal energy while also maximizing its disorder to reach an equilibrium state. Both conditions have to be considered when evaluating if some process is able to happen spontaneously. What about a process which decreases the internal energy but also decreases disorder? Clearly, it is not enough to maximize the entropy or minimize the energy because they could be interconnected. The free energy is the Legendre transformation of the internal energy with respect to the entropy. Depending on the ensemble, the free Helmholtz energy involves a constant volume, temperature and number of particles (eq. 2). If the pressure is kept constant and the volume can change, the Gibbs free energy is obtained.

$$F = U - TS \tag{2}$$

The following derivations and relations are equivalent for the Helmholtz and the Gibbs free energy, apart from the ensemble used.[93] According to this relation, the free energy becomes minimal if the internal energy gets smaller or the entropy S increases. The free energy therefore minimizes the energy while maximizing the entropy, which is why the free energy difference between two states of interest is a meaningful physical quantity determining if a process can take place spontaneously in a system. The transition between one state to another is described by a reaction parameter χ, which has to be chosen in a way to suitably reflect the physical change of the system one is interested in. To characterize the system, χ can be chosen in many ways, for example distance, angle, gyration radius or energy. The partition function Q can then be expressed in dependence of the reaction parameter as seen in equation 3.

$$Q(\chi) = \frac{\int \delta[\chi(r) - \chi] \exp[-\beta E)] d^N r}{\int \exp[-(\beta E)] d^N r} \tag{3}$$

The quantity $Q(\chi) d\chi$ can be interpreted as a probability density of states. In an ergodic system the ensemble average $Q(\chi)$ and the time average $P(\chi)$ becomes equal for time tending to infinity (eq. 4).

$$Q(\chi) = P(\chi) = \lim_{t \to \infty} \frac{1}{t} \int_0^t \rho[\chi(t')]dt' \tag{4}$$

A system is ergodic, if the whole phase space is sampled. So in principle, one can simulate a system to sample $P(\chi)$, and then directly calculate the free energy with equation 1. However, in practice simulation time is finite.

Regions of the phase space around an energetic minimum are sampled excessively while regions with high energy are only visited rarely because the system is much more likely to be in a state of low energy. If the states of interest are separated by one or multiple energetic barriers, significantly larger than the typical energy of thermal fluctuations, transition events become very rare, which makes direct sampling in a realistic time frame impractical. Different approaches have been developed to deal with this problem, one of which is umbrella sampling. The reaction pathway is divided into smaller segments, each of which is sampled individually and then recombined to the global free energy profile $F(\chi)$ with the *weighted histogram analysis method* (WHAM).[94] In each *simulation window* the system is restraint by the introduction of a biased potential, which in the simplest case is a harmonic potential. The bias potential is an additive energy term, which depends on the reaction coordinate (eq. 5).

$$E^b(r) = E^u(r) + w_i(\chi) \tag{5}$$

The biased potentials for each window ($P_i^b(\chi)$) are obtained by MD simulations and relate to the free energy via equation 6,

$$F_i(\chi) = -\frac{1}{\beta} \ln(P_i^b(\chi)) - w_i(\chi) + F_i \tag{6}$$

whereas the window dependent term F_i is defined in equation 7.

$$F_i = -\frac{1}{\beta} \ln\langle \exp[-\beta w_i(\chi)] \rangle \tag{7}$$

To combine the different windows into one global free energy surface, the F_i have to be estimated. With the WHAM method, as the name suggests, the global distribution is assumed to be a weighted sum of the individual simulated windows (eq. 8).

$$P^u(\chi) = \sum_i g_i(\chi) P_i^u(\chi) \tag{8}$$

A rule to derive a good estimate of the weighting factors (g_i) can be derived by demanding that the statistical error of the free energy minimizes (eq. 9).

$$\frac{\partial \sigma^2(P^u)}{\partial g_i} = 0 \tag{9}$$

With this condition the weights can be expressed via equation 10. They are normalized $\sum_i g_i = 1$.

$$g_i = \frac{N_i \exp[-\beta w_i(\chi) + \beta F_i]}{\sum_j (N_j \exp[-\beta w_j(\chi) + \beta F_j])} \tag{10}$$

The F_i can then be calculated with equation 11.

$$\exp(-\beta F_i) = \int P^u(\chi) \exp[-\beta w_i(\chi)]d\chi \tag{11}$$

Because P^u depends on the weights via equation 8, which in turn depends on the F_i via equation 10, equation 11 provides a rule which has to be iterated until convergence.

2.3.3 Metadynamics

A different approach to construct a biased potential and ensure a good sampling of the phase space is metadynamics (metaD).[95–97] A biased potential $V(\vec{s}, t)$ is added which is composed of successively added Gaussians. The phase space is spanned by so called collective variables (CVs). The added functions are placed in regions of the phase space, which the system occupies the most, i.e. regions of low free energy. One can think of the bias as *filling up* the free energy landscape. The added potential is shown in equation 12.

$$V(\vec{s}, t) = \sum_{k\tau < t} W(k\tau) \exp(-\sum_{i=1}^{d} \frac{(s_i - s_i(q(k\tau)))^2}{2\sigma_i^2}) \tag{12}$$

The parameters of the additional potentials are the Gaussian deposition stride τ, which determines the rate, with which potentials are added, the width σ_i in the space of the CVs and the height $W(k\tau)$. Constructing the bias this way results in the long time limit in an effective flat energy landscape because the bias resembles the negative of the energy (equation 13).

$$V(\vec{s}, t \to \infty) = -F(\vec{s}) + C \tag{13}$$

In *well-tempered metadynamics* the Gaussian height scales with simulation time according to equation 14.

$$W(k\tau) = W_0 \exp(-\frac{V(\vec{s}(q(k\tau)), k\tau)}{k_B \Delta T}) \tag{14}$$

With this the biased potential converges according to equation 15.

$$V(\vec{s}, t \to \infty) = -\lambda F(\vec{s}) + C \tag{15}$$

This introduces the bias factor $\lambda = \frac{T + \Delta T}{T}$ as an additional input parameter. Metadynamics simulations have been performed with plumed[98], which is available as a

plugin for the GROMACS MD simulation software. Due to its nature, metadynamics simulation is performed in one long simulation and can therefore not be calculated in parallel in contrast to umbrella sampling, in which each window can be simulated individually.

2.3.4 Density functional theory

Solving a many body quantum mechanical problem directly is infeasible, due to the fact, that every particle is interacting with every other one. Therefore, suitable approximations and simplifications are necessary to compute a system in a reasonable amount of time while still being able to sufficiently model reality. One popular and versatile method to model the quantum mechanical behavior of a many particle system is density functional theory (DFT).[99;100] One key quantity of interest is the electron density $n(\vec{r})$, which describes the electronic structure of a system. Important concepts in DFT are the Hohenberg-Kohn theorems.[101] According to the postulates of quantum mechanics, a given external potential $v_{ext}(\vec{r})$, with a given number of electrons N determines the ground state wavefunction and the ground state electron density $n_0(\vec{r})$ (except for degeneracies). The first Hohenberg-Kohn theorem shows, that the reverse is also true, i.e. the external potential $v_{ext}(\vec{r})$ is uniquely determined (except for an additive constant) by the ground-state density $n_0(\vec{r})$ and therefore $n_0(\vec{r})$ also specifies the Hamiltonian and the wavefunction. The second Hohenberg-Kohn theorem states, that the exact ground-state density can be obtained by minimizing the energy functional in equation 16.

$$E_0 = min_n \langle \Psi[n]|H|\Psi[n] \rangle \tag{16}$$

To construct the energy E[n], the Kohn-Sham scheme is used.[102] A given system of interacting particles is reduced to a fictitious system of non-interacting particles, which generate the same density as the system of interest. Hence, the non-interacting particles move in an effective Kohn-Sham potential v_s (eq. 17).

$$v_s = v_{ext}(\vec{r}) + \underbrace{\frac{\delta E_H[n]}{\delta n(\vec{r})}}_{v_H(\vec{r})} + \underbrace{\frac{\delta E_{xc}[n]}{\delta n(\vec{r})}}_{v_{xc}(\vec{r})} \tag{17}$$

Hereby $v_{ext}(\vec{r})$ denotes the external potential of the system of interacting particles and $E_H[n]$ is the analytically known Hartree energy. All unknown terms and interaction are packed in the exchange-correlation potential $v_{xc}(\vec{r})$. With this approach only the exchange correlation term has to be approximated instead of the whole energy. The effective potential v_s can then be used to solve the non-interacting Schroedinger Equation, yielding the ground state density of the interacting system. Various methods have been developed to approximate the exchange-correlation term like the

local density approximation (LDA) or the *generalized gradient approximation* (GGA) methods.[103] The computational accuracy can be increased by combining different approximations for different interactions, because some are better at describing short range interactions and others long range interactions. This approach leads to so called *range separated hybrid functionals*. Often a range-separated exchange part is combined with a range independent correlation term (eq. 18).

$$v_{xc} = v_x^{lr,\omega} + v_x^{sr,\omega} + v_c^{sr,lr} \tag{18}$$

The range separation parameter ω determines the transition between the different interactions. A simple approach to separate the interaction is to divide the two-electron operator $\frac{1}{r_{12}}$ according to equation 19[104].

$$\frac{1}{r_{12}} = \underbrace{\frac{1 - \mathrm{erf}(\omega r_{12})}{r_{12}}}_{short\ range} + \underbrace{\frac{\mathrm{erf}(\omega r_{12})}{r_{12}}}_{long\ range} \tag{19}$$

The range-separation parameter ω can be determined by demanding that the vertical ionization potential[105], which is the energy difference of a system of N and $N-1$ electrons, must be the negative energy of the *highest occupied molecular orbital* (HOMO) (eq 20).

$$IP = E[n_{N-1}] - E[n_N] = -\epsilon_{HOMO} \tag{20}$$

This provides a self-consistent, ab-initio tuning method for the range-separation parameter, because all quantities of equation 20 can be calculated by DFT itself. DFT calculations are employed to refine the models used in MD simulations. Because we are interested in the aggregation behavior of conjugated molecules, the dihedral angle between aromatic rings is of significant importance. To model them accurately, the dihedral angles between aromatic rings for all systems have been calculated by DFT in dependence of the angle. The resulting potential energy surfaces were incorporated into the MD models. We also calculated the charge distribution with DFT and added them to our MD models. Furthermore, we employed TD-DFT to characterize the dynamic electrooptical properties of some systems to help interpret the results. DFT calculations within the scope of this thesis were performed with the help of the Gaussian09 RevE.01.[106]

2.3.5 Model building

To simulate molecules with MD simulations, a model of the system in question has to be built first. In this section, a brief description about this process, and the combination of DFT and MD simulation methods, is outlined.

Structure files of molecules can be generated conveniently with JME.[107] The *automated topology builder and repository* provides a useful tool to automatically generate a force field for a given molecular structure.[108–110] based on the Gromos54a7 force field.[111] Depending on the system size, different levels of theory are applied. For systems smaller than 50 atoms, a full quantum chemical calculation is performed by the algorithm, which we used to generate starting force fields for the systems investigated. We chose to refine these models with our own DFT calculations in order to model the relevant physical properties in a most realistic manner. Because the charge distribution is crucial for the molecular aggregation process, we incorporated our own charge distribution calculated with the DFT software Gaussian 09. The investigated chromophores have a lot of aromatic rings, whose relative orientation is crucial for the aggregation process and the conjugation length of the delocalized electron orbitals. Therefore, the dihedral angles between the individual aromatic rings are of vital importance to replicate meaningful physical behavior. We calculated the potential energy surfaces (PES) of these dihedral angles with DFT and incorporated the results in our MD models. With these refinements, the model is a appropriate way to investigate the physical interactions on molecular length and time scales. More details can be found in the corresponding sections of the publications printed in section 5 or in their supporting information.

In the publication presented in section 5.2 we even go further. The models used in MD simulations, which are refined by our own quantum chemical DFT calculations, are used to generate average structures of stable aggregates, which are fed back into time dependent density functional theory (TD-DFT) calculations, in order to obtain insights about the electronic structure of the aggregates. Together with the experimental results, we are therefore able to integrate a broad range of methods, which leads to a deeper understanding about the properties of the systems.

3 Overview of the publications

In this section an overview of the research performed within the scope of this thesis is given. First, the systems investigated are introduced, followed by a brief description of the scientific context and the core results for each thesis. Hereby emphasis is laid on the overall context and the connection between the individual publications.

3.1 Investigated systems
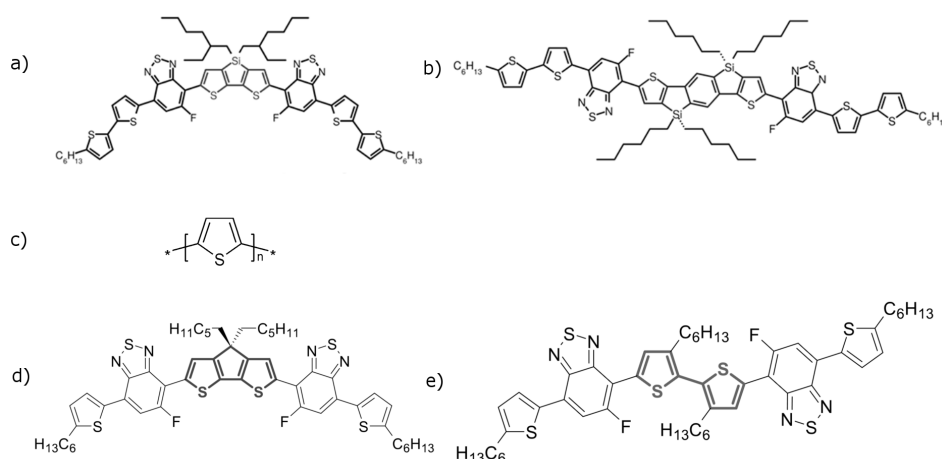
Figure 4: The molecules investigated are displayed in this figure: a) p-DTS(FBTTh$_2$)$_2$
(T1). b) SIDT(FBTTh$_2$)$_2$ (H1). c) Polythiophene. d) connected thiophenes
(CT). e) twisted thiophenes (TT).

The molecules, which are the main interest of this investigation are shown in figure 4 and are introduced in the following. Recent research has shown promising results by using small, soluble molecules as the donor material in organic solar cells.[112–117] They are often designed with electron-rich donor (D) and electron-deficient acceptor (A) subunits placed on the same molecule, resulting in a D-A-D-A-D arrangement.[118;119] All molecules presented in figure 4, except for polythiophene (figure 4c)), which is a polymer, are of this design. The outer donor units of T1[i] (figure 4a) are made out of two thiophene compounds. The acceptor units are benzothiadiazole rings. The fluorine atom locks the torsion angles between the aromatic rings in a planar position, resulting in an increase of the conjugation length.[120] This design is reflected in the other D-A-D-A-D systems as well. The central donor unit is made of three aromatic rings and can be thought of as two thiophene units connected via a silicon atom. The molecular arrangement is mirror symmetric to a central axis. The outer donor and acceptor units in H1[ii] (Figure 4b) are the same as in T1. In this system the

---

[i]chemical name: p-DTS(FBTTh$_2$)$_2$

[ii]chemical name: SIDT(FBTTh$_2$)$_2$

central donor unit consists of five aromatic rings, which results in a point symmetric arrangement of the whole molecule. The only difference between T1 and H1 is the central donor unit, which determines the molecular symmetry. Both systems exhibit a very different aggregation behavior. One of the questions investigated is, why they differ so much. The molecules T1 (figure 4a) and H1 (figure 4b) are addressed in section 3.3.1. Hence, by investigating their aggregation properties, valuable insights can be gained into how the symmetry relates to structuring processes.

The system CT[iii] (Figure 4c) is very similar to T1, but differs in a few important aspects. It is shorter, the outer donor unit is only made of one thiophene module. The acceptor units are the same as in the previous two systems. The central donor unit can be pictured like in T1, but the two rings are connected via a carbon rather than a silicon atom. TT[iv] (Figure 4d) has the same outer donor and acceptor units as CT. As opposed to the rest of the molecules introduced so far, the central donor unit consists of two separate thiophene like rings, twisted against each other with an angle of $67°$. This rotation is achieved by attaching two bulky side-chains, who repel each other. The molecular structure of CT is very planar and rigid, while TT is twisted on purpose. One question of this thesis is to gain insights about the role of planarity during the aggregation process, which is investigated by comparing these two model systems. This topic is investigated in section 3.3.2.

The molecules introduced so far are very similar. They are from building blocks, which are often used in short conjugated molecules or in polymers. The discussion of the molecular structural properties shows, that key aspects like symmetry or rotational degrees of freedom can be used as parameters to influence molecular arrangement. Furthermore, the molecule CT has a different central atom, carbon, versus silicon in T1. This influences the shape of the molecule. The heavier silicon atom in T1 bents the whole molecule to a more banana like shape, while the lighter carbon atom results in a straighter arrangement.[121] The twisted nature of TT results in a decrease of the conjugation length, i.e. the section over which electronic excitations can be delocalized. The coupled π-orbital system is interrupted by the twisting of the central donor unit.

Lastly, the publication presented in section 3.3.3 evaluates the possible crystal packing structures of a polythiophene (PT) (Figure 4e) chain in dependence of different manufacturing pathways. PT is closely related to P3HT, which has been extensively studied in the last decade.[67;122–126]

[iii]acronym for connected thiophene.

[iv]acronym for twisted thiophenes.

3.2 Summary and scientific context

The goal of this thesis is to investigate the aggregation behavior of chromophors with simulations to support experimental results. The molecules investigated within the scope of this work have been chosen to answer specific questions about the aggregation process.

During the last few years, small conjugated molecules have gotten a lot of attention as an optically active ingredient in organic solar cells. In comparison to conjugated polymers, they are relatively straightforward to manufacture, their chemical structure can be changed easily, they often have a high degree of crystallinity and a well-defined molecular weight.[127–134]

One promising systems, for which high efficiencies over 11%[135;136] have been reported is the small molecule T1.[137–142] Previous investigations[142] could show that aggregation can be induced in T1 solutions by cooling. A freezing out of torsional motion is observed in the spectra before aggregation. This is interpreted as the same three-step aggregation mechanism as in conjugated polymers: 1) A cooling induced planarization of the backbone increases the conjugation length, after which 2) aggregates form. 3) Afterwards further planarization takes place. Another observation is that the unorder-order phase transition is induced in a very narrow temperature window. This well-defined phase transition implies a high degree of order and crystallizability, which is indeed reflected in the thin films. They can be manufactured with nearly 100% aggregates. The excellent performance in comparison with similar systems, like H1, is at the moment not fully understood. H1[143–145] is structurally closely related, but exhibits significantly different aggregation behavior. No aggregation can be observed in solution, even at high concentration and low temperature even though aggregates are present in spin coated films. Crystallization can be drastically improved with high boiling point additives, like diiodooctane.[146] H1 exhibits an even wider band gap than T1 and can be used in bulk heterojunction solar cells with a higher open circuit voltage in comparison with T1.[141] Both molecules cover a broad spectral absorption range, which leads to high efficiency.

The aggregation behavior of H1 and T1 in MTHF solution is investigated in the publication printed in section 5.1. Interestingly, the aggregation of H1 in solution has not been studied before. We use optical spectroscopy to investigate the absorption and photoluminescence spectra in dependence of concentration and temperature. The results are interpreted with the help of complementary MD simulations. The force fields for the models used in the simulations are refined with DFT calculations in order to make realistic models of the systems. The possible aggregate conformations are characterized. T1 can undergo two distinct aggregation pathways in dependence

of intermolecular orientation. The molecules can be aligned in the opposite direction, which we identify as a type A aggregate, because the energetic minimum is lower, and in a type B aggregate, in which the molecules are aligned in the same direction. For H1, only one aggregate structure is observed. Free energy calculations help to gain deeper insights about the dynamics of the aggregation process. The experimental data suggests that T1 aggregates very easily while H1 does not. This can be reproduced by the simulations. Due to the fact that H1 possesses bulkier side-chains, it is straightforward to assume that they hinder aggregation. Remarkably, our MD simulations suggest that aggregation does not change qualitatively by removing them. By investigating the interaction of the conjugated small molecules with the solvent, we are able to postulate a mechanism explaining this discrepancy. Solvent aggregation in H1 is possible, but rare. An attractive force between two H1 molecules is only observed if the molecules are aligned in a very specific way and even then, the range of this attraction is very small. This means that the molecules have to be aligned exactly the right way and need to be very close to one another to snap into an aggregate. Therefore, a considerable molecular overlap has to be achieved randomly before the molecules experience an attractive force. This requires a lot of solvent molecules to be displaced, which is why aggregation in H1 is kinetically hindered. This is partly due to the molecular symmetry of H1, which makes this large overlap necessary. During spin-coating, the average distance between molecules is decreased steadily due to the evaporation of solvent. This increases the likelihood of two H1 molecules coming close together in the right way to aggregate. This explains why aggregates can be observed in films. Given that the addition of a high boiling point additive is theorized to increase the time the system has to aggregate, the molecules are more likely to reorientate to the right position, which also explains why crystallinity can be enhanced with diiodooctane.

In summary, the publication presented in section 5.1 can paint a coherent picture of the aggregation process and the underlying dynamics at work. We are able to explain the difference in aggregation behavior of T1 and H1. The results show, that not every small molecule with large delocalized conjugated orbitals is able to easily form molecular structures despite structural similarity. Parameters like the molecular symmetry, the interactions with the solvent and the pathway into an aggregate have to be kept in mind when designing new materials. Nevertheless, we can also show that possible aggregates exist, which explains the formation of structures during film formation. Our analysis is also consistent with the fact that diiodooctane improves the crystallinity of H1 films. The results of this study can therefore help, by comparison with investigations of similar π-conjugated chromophores, to elucidate the molecular structuring process of small molecules used in organic photovoltaics. With

this, design strategies can be derived to help improve solar cell device performance.

When cooling down a solution with T1 molecules, a planarization of the backbone is observed prior to the formation of aggregates.[142;147] The publication printed in section 5.2 investigates the role of planarization during the aggregation process. The molecules investigated are CT, which is very planar and TT, in which the central donor unit is twisted.[148] It is known that planarization plays an important role in the aggregation of conjugated polymers but the exact details of the causality are poorly understood. It is not clear if planarization is the driving factor of aggregation or aggregation induces planarization. One way to induce planarization is to cool down a solution. There are studies on π-conjugated polymers and small molecules, indicating a cooling-induced backbone planarization effect precedes the formation of aggregates.[67;126;142;147;149] It has been also shown that aggregation can be increased by the introduction of conformational locks like the fluorine atoms in the small molecules investigated in this thesis, which reduces torsional motion and therefore increases planarity.[150–153] On the other hand, there are also studies highlighting the planarization as a consequence of aggregation.[154;155] For a better understanding of the complex aggregation process it is useful to understand the role of planarity. We investigate, if a planar backbone is of advantage for the self-assembly process, or if planarity may also be induced by the assembly process.

We employ optical spectroscopy in dependence of concentration and temperature in hexane to gain insights about the aggregation dynamics. To help interpret these results, we also conduct MD, DFT and TD-DFT calculations. With our analysis we can show that the behavior of these systems is not straight forward. TT exhibits strong aggregation even though its twisted nature, while CT only shows very weak signs of aggregation despite its similarity to the well-ordered system T1. Free energy MD simulations show a similar energy gain of these two systems which is in contrast with the experimental results. Molecular dynamics simulation enables us to artificially force-planarize TT and compare the aggregation behavior with the twisted model. With these simulations we are able to show that the aggregation of planarized TT is significantly stronger than the twisted module. It is therefore reasonable to assume that the molecule planarizes as a consequence of the molecular structuring process, because energy can be gained from that. By analyzing the building blocks of CT and TT individually, it becomes clear that planarization in TT leads to a larger number of attractive interactions between individual subunits of the molecule, which explains the increased energy gain. Energy also has to be invested into the planarization process, which is why the molecules will reach equilibrium in a more planar configuration than in single molecules.

Similarly to T1, CT also shows type A and type B structures, but in this system, the energetic difference between the two pathways is much smaller. For TT, we only find one possible configuration. We also investigate the influence of the side-chains by simulating models without them. These calculations suggest that they only have a minor role in structure formation. Furthermore, we use MD simulations to calculate average molecular arrangements of the minimum structures, which we then use to perform TD-DFT calculations in order to investigate their electronic properties. With this approach we are able to identify non-emissive excimer structures in CT, explaining the spectroscopic results. Upon cooling, CT first forms non-emissve excimer-type structures, which act as a precursor until aggregation sets in at lower temperatures.

In summary, this publication manages to explain counter-intuitive results and an apparent mismatch between experiment and simulation by employing a broad variety of techniques which leads to a coherent picture of the underlying dynamics at play. The investigation indicates that twisted molecular configurations do not necessarily prevent aggregation. In fact, a planarizing effect due to the formation of aggregates might be able to induce strong aggregation in heavily twisted molecules. It therefore becomes clear that the connection between planarization and structure formation is complicated and cannot be understood from a single viewpoint. The interactions within chromophores have to be evaluated individually on a case to case basis. However, our results support the hypothesis that non-planar molecular structures are not necessarily preventing aggregation. The structuring process can also be the cause for planarizing effects. Furthermore, we are able to show that molecular self-assembly can also lead to non-emissive excimers.

Remarkably CT, shows a significant different behavior than T1, despite their molecular structure being very similar. T1 exhibits very strong aggregation behavior, whereas CT exhibits only weak aggregation, which we attributed to the formation of non-emissive excimer-like precursor aggregates. There could be several reasons for this. T1 has a heavy silicon atom in the middle of the central donor units, one more thiophene ring at the outer donor unit, and a different bending angle. These factors could lead to a different electronic interactions during the formation of aggregates. Also, one has to keep in mind that the systems were investigated in different solvents. The side-chains are also different which may influence solubility. However, this raises new questions, which are worth pursuing in future investigation to explain this difference in detail.

With the publication presented in section 5.3 another aspect of the aggregation process is explored. We investigate a Polythiophene polymer, which is structurally closely related to the *work horse* in organic photovoltaics, P3HT. We employ different processing conditions during film formation, which can be used to influence the crystalline structure of the film and therefore its optical properties. By adding a dopant, that can be rinsed out after processing, different structures emerge. With the help of MD simulations, we are able to confirm the stability of different arrangements in dependence of intermolecular distances. The polymer can crystallize in a lamellar π-π stacking configuration or in a so-called herringbone fashion, in which adjacent rows of molecules are orientated differently. Here, we simulate crystalline structures in contrast to the other two publications. By employing MD simulations, we are able to investigate the crystal structures on molecular length scales, which helps interpret the experimental results. The results of this investigation can therefore be used to better influence the morphologic properties of films made from π-conjugated polymers.

3.3 Summary of individual publications

The following sections will give a more detailed summary of the individual publications.

### 3.3.1 Elucidating Aggregation Pathways in the Donor-Acceptor Type Molecules p-DTS(FBTTh$_2$)$_2$ and p-SIDT(FBTTh$_2$)$_2$

In this publication the aggregation behavior of the molecules p-DTS(FBBTTh$_2$)$_2$ (T1) and p-SIDT(FBTTh$_2$)$_2$ (H1) is investigated in MTHF solution, during spin-coating and in a thin film. These molecules are used for organic photovoltaics and are of a D-A-D-A-D like design structure, in which electron-rich donor (D) and electron-deficient acceptor (A) subunits are placed on the same molecule. Hereby, we investigate different aggregation pathways for T1 and a hindered aggregation pathway for H1 and discuss why H1 can still be processed to a thin film despite a kinetically hindered aggregation. The molecular structure of T1 is axis symmetric while H1 has a point symmetric configuration. This symmetry difference influences the structuring process. To gain insights about these systems, a combination of experimental and simulation methods is employed. Temperature dependent absorption and emission spectroscopy methods are complemented by molecular dynamics simulations based on force fields derived by time dependent quantum mechanical calculations. Experimentally, samples of different concentration were prepared for T1 and H1 in the solvent MTHF. Temperature dependent spectroscopic measurements were performed to test if aggregation can be induced. In figure 5 the absorption and

photoluminescence spectra of T1 and H1 are shown in dependence of temperature. Above a critical temperature of about 205K the spectra of T1 are very similar in low and high concentration. The spectral shape of very dilute samples is largely independent of temperature at low concentrations the probability of aggregate formation is very low, due to the large mean distance of the molecules, which is why we always measure a single molecule spectrum. At high concentrations, additional low energy features emerge below the critical temperature (fig. 5a). This behavior is characteristic for aggregate formation due to the electronic interaction of multiple monomers, an aggregate interacts differently with light.

In H1, the spectral shape stays always the same, even at high concentrations and low temperatures. The formation of aggregates cannot be observed experimentally in an MTHF solution. However, H1 is still able to align in ordered domains in the final thin film. In figure 5b and 5d we show the spectra for a film cased from a chlorbenzol solution for T1 and H1. The low energy aggregation feature in the spectra of T1 is more pronounced in the film, as in the low temperature high concentration T1 MTHF solution. In H1 thin film, there is also a low energy feature emerging, which hints at the formation of ordered structures. One important question, which arises from this, is how the film formation happens in H1. Because in solution there seem to be no prominent aggregation formation visible, yet in the film ordered structures clearly emerge, so how does this ordering process takes place? H1 can form aggregates in the thin film but not in solution which is a very different behavior than T1. This raises the question how the film formation and aggregation behavior looks like in the different materials. Due to the spectral form, the H1 aggregate seems to be more of a J-type than a H-type aggregate.

To investigate why T1 aggregates in solution, while H1 does not, we supplement the experimental results with molecular dynamics calculations. With the help of DFT simulations, we calculated the ground state and first excited state geometry of T1 and H1. We used quantum chemical methods, to calculate the charge distribution of the ground state structures and implemented them in our MD models. The charge distribution is crucial for the electrochemical and aggregation properties of the systems. The donor and acceptor parts of the molecules consist of different units with one or more conjugated rings, which are connected via single C-C bonds. The relative angles and dynamic rotational degrees of freedom between these units is very important for the aggregation behavior. It is important to know, for example, if the molecule is flat or twisted, because in dependence of this fact different structures can form. To make our models more accurate, we calculate the potential energy surface (PES) of the dihedral angles between these units with DFT. We adjusted the parameters of our MD models to reproduce the behavior calculated by quantum

mechanical calculations to improve the viability of our simulations. Both molecules possess a very flat geometry, the equilibrium dihedral angles between donor and acceptor units are very close to a planar configuration. However, due to thermal noise, the angles fluctuate around the equilibrium value. The magnitude of the fluctuations is determined by the energy of the noise and therefore given by the temperature. At lower temperature, the amplitude of these fluctuation decreases. We described this behavior in the main text of the publication as a freezing out of the rotational degrees of freedom.
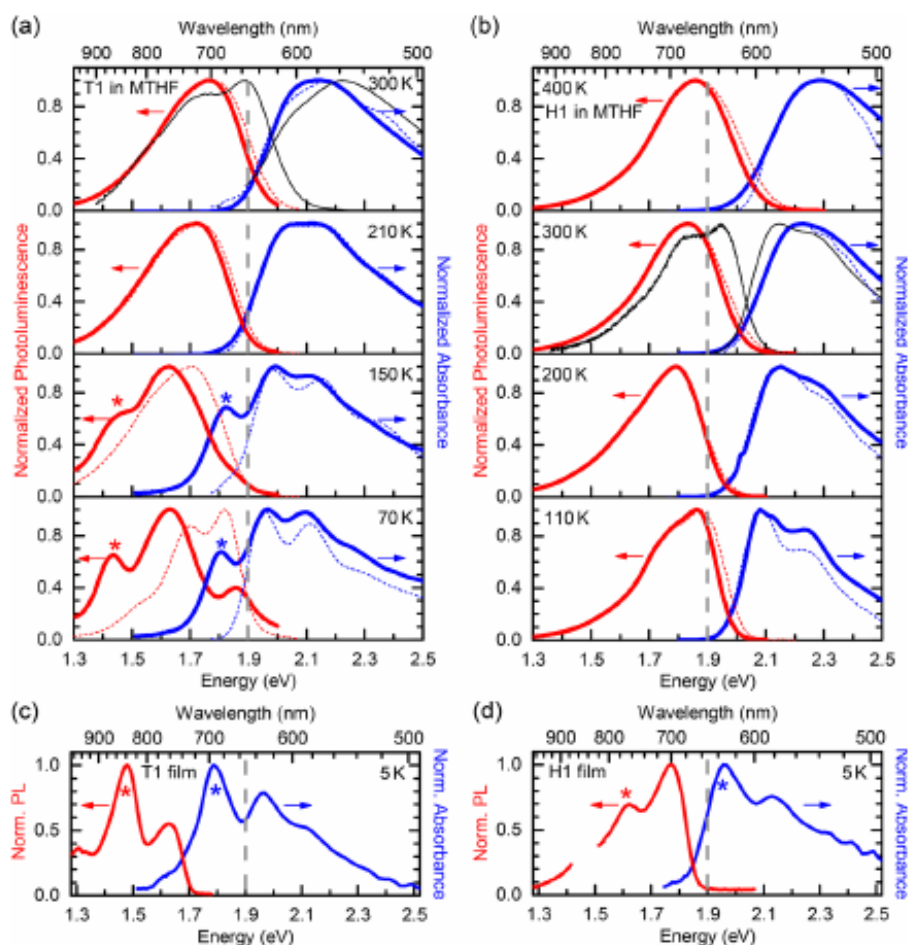
Figure 5: In a) the normalized photoluminescence (red) and absorption (blue) of T1 can be seen in dependence of temperature. The corresponding data for H1 is shown in b). In c) the spectra for a thin film cast from a CB solution is shown for T1 and in d) for H1.

We employed umbrella sampling calculations to determine the free energy of the aggregation process for both systems. We average over multiple independent starting configurations to sample the whole configurational phase space. For T1, we identify two different aggregation pathways, one in which the molecules are aligned in the opposing direction (type A) and one, in which the molecules are aligned in the
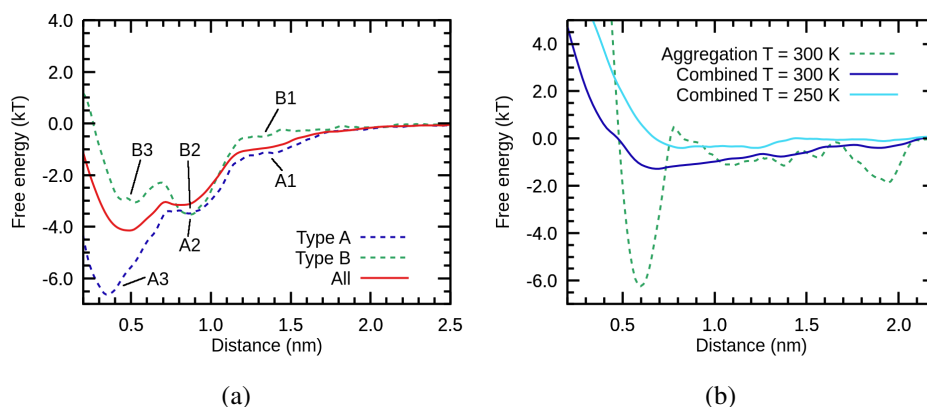
Figure 6: a) Free energy of T1 for type A and type B aggregation and the whole configurational phase space. b) Combined free energy of H1 for T = 300 K and 250 K. The dashed line is single free energy graph, in which the rare aggregation occurs.

same direction (type B) (fig. 6(a)). We also calculated the energy of the individual subunits. In a type A aggregate, the benzothiadiazole acceptor units can stack nicely on one another, while they are slightly displaced against each other. Most of the energy gain stems from the acceptor units stacking. Type A aggregation exhibits a larger energy gain in this system, which is why we investigate this pathway further by calculating the free energy temperature dependent between 400 K and 250 K. The energy gain from stacking increases with decreasing temperature, while the attraction range between two individual T1 molecules increases. The aggregation of T1 and the behavior at lower temperatures agrees with the experimental results.

We also calculated the free energy of H1. To sample the whole configurational phase space we averaged over many different starting configurations. In most of the simulations, the system is not able to form aggregates most of the time. However, there is a rare event, in which aggregation actually happens. In figure 6(b) we display the averaged free energy of H1 at T=300 K and T=250 K and one single free energy calculation, in which we observed this rare stacking event. The energy gain of this minimum is quit pronounced at -6.0 k_bT. The minimum is also very slim. The global minimum appears at a distance of about 0.6 nm, above 0.8 nm the energy landscape remains flat. This means that the molecules have to be aligned in a very specific fashion and have to be very near to each other to experience an attractive force and the formation of an aggregate. If you displace the two molecules only slightly against each other, the aggregate becomes unstable. There is a possible H1 aggregate with a large energetic minimum but the pathway into this minimum seems to be difficult to access. We also calculated the free energy of H1 at lower temperatures (T=250 K), which did not improve aggregation. This is in agreement with the experiment. During spin-coating and film formation, more and more solvent is evaporated until

there are only chromophore molecules left. This means, that the concentration increases rapidly and significantly, which decreases the average distance between H1 molecules. The molecules can aggregate due to the high concentration and short distances. It is much more likely for the H1 molecules to align in the right fashion with a neighboring molecule and snap into an aggregate.

One possible reason for the difference in aggregation behavior might be presence of side-chains. H1 possesses bulkier side-chains which might get in the way during aggregate formation and therefore hinder this process. To investigate this, we made additional models in which we removed the side-chains. The aggregation behavior of T1 increases slightly without side-chains but does not change for H1. We therefore conclude that the presence of bulky side-chains is not the main reason for the difference in aggregation behavior. To further investigate the difference, we calculate the free energy of each unit separately and find that the bulk of the energy is gained from the stacking of the acceptor units. We now look at the interaction of the chromophores with the solvent. Due to the point-symmetric nature of H1, there are no different type A and type B pathways like in T1. During aggregation both molecules must slide completely on top of each other. H1 also has a larger central donor unit, consisting of five conjugated rings, while T1 has only three. This led us to suspect that during H1 aggregation a lot of solvent has to be displaced in comparison with T1. The formation of a H1 aggregate is therefore kinetically hindered due to the necessary displacement of a lot of solvent molecules. To test this hypothesis, we calculated the solvent distribution in a box-like volume, the base of which encloses the central donor units. The analysis of the solvent distribution functions show, that during a type A aggregation, the solvent shell in front of the T1 central donor unit is mostly unaffected, while it has to be displaced during a type B aggregation. This explains the larger energy gain in a T1 type A aggregate compared to a type B aggregate, because much less solvent has to be displaced. If we compare the solvent distribution of a H1 aggregate in front of the central donor unit, we find that the solvent distribution changes drastically compared to a H1 monomer. The shape of the solvent distribution remains the same but is shifted to higher distances because now there is a second H1 molecule in the way. Our calculations therefore suggest that a lot more solvent has to be displaced during H1 aggregate formation than during T1 aggregate formation, which is why the aggregation of H1 is kinetically hindered.

3.3.2 What is the role of planarity and torsional freedom for aggregation in a π-conjugated donor-acceptor model oligomer?

This publication investigates the role of rigidity and planarity during the aggregation process. The systems of interest are the very planar CT, which is similar to

the previously investigated molecule T1, and TT, in which the central donor unit consists of two thiophene rings with side-chains attached to them. The interaction between the side-chains results in a twisted central donor unit with an angle of about 68°, calculated with DFT. The molecules were designed in order to investigate the difference in aggregation in dependence of planarity. It is known that planarization plays an important role during the aggregation process. On the one hand, there are reports highlighting that aggregation induces planarization, and on the other, molecules are often designed with planarity in mind in order to increase order and crystallinity. In contrast, there are also reports that torsional and rotational freedom can be beneficial for aggregation. Because of that, it is not clear if planarization is the driving factor of aggregation, or aggregation induces planarization. We study this question by employing temperature dependent absorption and emission spectroscopy for different concentrations in hexane complemented by MD, DFT and TD-DFT calculations.

For low concentration of TT ($5 \cdot 10^{-6} M$) the spectra change very little upon cooling. For medium concentration ($5 \cdot 10^{-5} M$) additional spectral features at lower energies emerge at 220 K and below. At even higher concentrations ($2.5 \cdot 10^{-4} M$) the additional features are even more pronounced and show light scattering features from small particles. This means, that at high concentration precipitation takes place due to strong aggregation at low temperature. From the spectral analysis we conclude that TT forms weakly interacting H-type aggregates upon cooling. Independent of concentration an additional low energy shoulder emerges upon cooling. The central dihedral potential for TT was calculated for the ground and the first excited state. This reveals two minima of the central dihedral angle for an excited TT single molecule. One at 50°, close to the cis-planar configuration, and one at 140°, which is closer to a trans-planar configuration. Consequently, there are two possible ways an excited TT molecule can emit a photon to relax to the ground state corresponding to different energies. We attribute the high energy shoulder in emission to the excited cis-planar configuration.

The situation is different in CT. For high concentrations ($5 \cdot 10^{-6} M$) the spectra change very little upon cooling. At medium concentration ($5 \cdot 10^{-5} M$) a very weak low energy feature emerges, which gets more pronounced at high concentration ($2.5 \cdot 10^{-4} M$). In comparison to TT, the low energy spectral features are much less pronounced, implying worse aggregation behavior. Upon cooling we also observe a reduction in absorption and a change in peak ratio which gets more pronounced by cooling and by increased concentration.

To better compare the spectral features of CT and TT we look at the relative, normal-

ized photoluminescence intensities in dependence of concentration and temperature. In both systems, the relative emission intensity as a function of temperature is constant for low concentrations, due to which only single molecules are present in the samples. At higher concentration the intensity declines steeply with the emerging of additional low energy features in TT. This decline is also present at the medium and high concentrations of CT, starting at 250 K and below. However, the reduction in intensity does not correlate in an obvious way to additional spectral features, implying that somehow intensity is lost through a non-radiative channel. The experimental analysis shows a strong aggregation behavior in the twisted system TT, but only very weak aggregation in the planar molecule CT. This is counterintuitive, because CT is very similar to T1, which aggregates easily, while the twisted nature of TT is expected to hinder aggregation.

To help interpret these results we employ free energy MD simulations. We used DFT calculations to make accurate models of the systems in question. We are able to characterize the possible aggregate structures. Similarly to T1, CT can undergo a type A aggregation, in which the molecules are aligned in the opposite direction, or a type B aggregation, in which they are orientated the same way. The free energy suggests a similar energy gain upon aggregation for CT and TT, which is in contrast with the experimental results. To investigate the role of the side-chains we also have done simulations for models without them. Without side-chains, the energy gain upon aggregation in CT only increases slightly, implying that they play a minor role. For TT, the increase is more drastic. This is to be expected, because the interactions of the side-chains is the reason for the twisted nature of the molecules. Although we kept the twisted potential intact, the missing interaction between the side-chains increases the energy gain. The side-chains can therefore not explain the difference in aggregation behavior. Because our central question is about planarity, we built artificial models of TT forced into a trans- and a cis-planar configuration. Calculations reveal that the trans-planar model is the energetically most favored one. Aggregation of the twisted TT molecules yields an energy gain of about 5.5 kT, while the global minimum of the trans-planar model is at about 9.5 kT. This large increase in energy gain implies a planarization effect of TT in solution, because it is energetically favored. The trans-planar configuration is consistent with crystalline TT structures found in the cast film. We also calculated the free energy of the stacking process of individual subunits of CT and TT. These calculations show, that a planarization of TT results in a larger amount of attractive interactions between individual units in comparison with CT, explaining the energy gain.

When discussing planarity in TT, one has to distinguish two different effects. Upon cooling, the thermal energy decreases, therefore the rotational motion of the dihedral angles around their equilibrium value is subject to lower fluctuations. However,

planarization can also mean a change of the mean twisted central dihedral angle to a more planar overall configuration, which is what we have done by building a trans-planar model. Upon cooling, the solvent quality and the rotational fluctuations decrease. This is necessary for aggregation because it can only be observed at low temperatures. After aggregation it becomes energetically favored for the central dihedral to change its mean value, therefore planarizing the whole aggregate.

We use the results from the MD simulations to further explore the electronic properties of the aggregates with the help of TD-DFT simulations. We calculated the oscillator strength and the charge transfer character for the optimized aggregate structures. These calculations reveal that the CT type A configuration is a non-emissive aggregate. This explains why we see only weak spectral aggregation features in CT and the decline in the normalized relative emission intensity.

In summary, with the help of MD, DFT and TD-DFT simulations, we are able to explain the experimental results. CT is able to aggregate in a type A and a type B aggregate, but only type B can be seen in the spectrum because type A is a non-emissive excimer. The strong aggregation behavior of TT can be explained by the already significant attraction between the molecules in their twisted state followed by further planarization of the central dihedral angle after aggregation due to a gain in energy.

3.3.3 Directing the Aggregation of Native Polythiophene during in Situ Polymerization

One widely investigated material is poly-3-hexylthiophene (P3HT), a workhorse polymer for organic photovoltaics. One common way to influence structural properties is the introduction of side-chains. In this publication we explore the aggregation process of Polythiophene (PT), which is structurally closely related to P3HT but without the side-chains on each monomer. The removal of the side-chains influences solubility and therefore the aggregation behavior and the planarity of single molecule polymer backbone in solution.[156] PT often aggregates in a herringbone like structure with only short range order interactions. Here, we demonstrate how the aggregation process and the crystalline structure of the final thin film can be tailored by the manufacturing process. We use grazing incidence wide-angle X-ray scattering (GI-WAXS) measurements, molecular dynamic simulations and spectroscopic analysis to investigate the structural properties of PT.

During the polymerization process, we use iron(III) p-toluenesulfonate hexahydrate (FeTos) as an oxidation agent and a chemical dopant. The monomer used is bithiophene (BT). Iron(III) ions oxidize the monomer molecules, which enables polymerization. If a lot of oxidizing agent is present, the polymer chains further oxidize in a second step, which is effectively a chemical doping of the chains, re-

sulting in a free charge carrier on the conjugated polymer chains. Simulations show that the excess positive charge electrostatically attracts a FeTos anion, which align perpendicular to the polymer backbone.[157] Our goal is to exploit this doping process during fabrication resulting in improved performance. Therefore, after the spin coating process, we rinse out all leftover monomers and oxidant molecules. The choice of the solvent used for washing out influences the electronic properties. When using acetonitrile, the polymer molecules remain in their doped state, while using ethanol removes the doping and the FeTos anions. We are therefore able to obtain doped and undoped PT in the final thin film. We investigate the doping process by varying the molar fraction of FeTos present in the reaction mixture from 0.25 to 0.75.

herringbone π-stacking
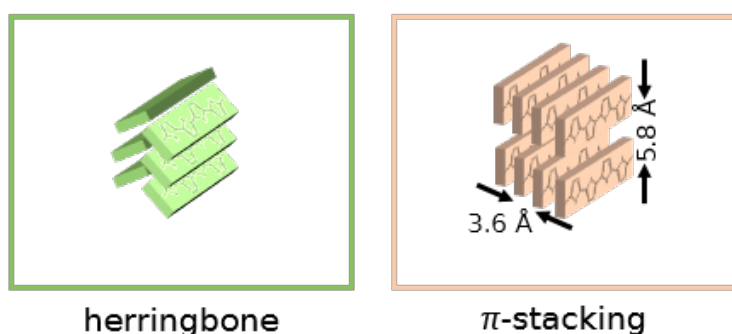
Figure 7: In this figure we show the possible crystal packings of a PT polymer. The chains can be arranged in a herringbone or in a lamellar arrangement.

With four-point probe measurements we are able to show that the conductivity of the doped PT film is several orders of magnitude above the conductivity of undoped PT and hence conclude, that rinsing with acetonitrile leaves the doped, conducting state intact. The conductivity increases drastically with the level of doping. We therefore discriminate PT films synthesized under iron deficiency (FeTos fraction below 0.5) and iron excess (FeTos fraction more than 0.5). At high doping levels an additional Bragg peak arises in the GIWAXS measurements (at $d = 8.2$Å) implying the formation of a new crystal plane. According to earlier findings, a critical level of doping results in a structural rearrangement of the molecules.[158] The PT polymer backbones arrange in a parallel, π-stacked fashion and form a lamellar structure with dopant molecules in between the stacks. The possible arrangements a lattice of PT chains can be in, is shown in figure 7.

In the following we will discuss the structural properties of the semiconducting PT films, rinsed with ethanol. Native PT is known to aggregate in a herringbone (HB) fashion. The herringbone structure results in a poor overlap of π-orbitals and is therefore dominated by short range order interactions. We investigate semiconducting PT films processed under iron deficiency and iron excess by radially integrating the

GIWAXS measurement in the radial and horizontal direction. Both samples show three distinct peaks in the radial direction, which match the HB structure, while only the sample fabricated under iron excess shows an additional peak at $d = 5.8$Å. In the vertical direction, the PT film synthesized with high FeTos concentration exhibits an additional peak at $d = 3.6$Å. The PT manufactured under iron deficiency only arrange in the HB structure, while another crystalline packing is present in the film made with iron excess. By comparison with the conducting films, we conclude that the sample with iron excess additionally form a lamellar π-stacked film.

We therefore manage to show, that undoped, semiconducting PT can aggregate in a π-stacked crystal, which has not been reported before. We confirm the feasibility of our proposed structuring mechanism with MD simulations. We simulate a crystal of 100 PT 10-mers. We used DFT calculations to calculate the dihedral angle PES between the individual thiophene rings and the charge distribution. The results are incorporated into our molecular models. We constrain the intermolecular distances of the crystal to values observed in the experiment (5.8Å and 3.6Å). The PT chains all align in the same orientation, resulting in a lamellar structure. When the constraints are removed, the distances and orientations change to a HB structure. The distances from the simulation ($a = 7.10$Å and $b = 5.71$Å) agree with the experimental values ($a = 7.81$Å and $b = 5.56$Å). The simulation results indicate that the HB structure exhibits a global energetic minimum for the system, while a lamellar structure is possible when the distances are restraint. The introduction of excess doping during the manufacturing process leads to the attraction of FeTos anions to the polymer backbones. The presence of these anions restraints the distances between the polymer chains resulting in a lamellar orientation. After the doping molecules are washed out, the crystal is unable to rearrange itself into a HB structure and remains in a lamellar configuration. This crystal structure persists through thermal annealing at 200°C, indicating a certain stability.

We also perform absorbance and emission spectroscopy measurements of the semi-conducting PT thin films. We interpret the spectra as a superposition of an amorphous contribution from disordered PT chains and vibronic transitions of aggregated polymer chains. Analysis of the different spectra shows an increased fraction of ordered PT backbones with increased iron excess during the polymerization process. Furthermore, a redshift indicates increased intermolecular interaction when using high amounts of FeTos. The synthesis under iron excess therefore seems to increase order within the films and results in a lamellar crystal structure. In summary, we are able to show, that the type of crystal structure can be tuned by variation of the amount of oxidizing agent. A high level of doping leads to an increase in conductivity and

results in a new crystal packing structure. The π-stacking of the PT molecules is preserved even after dedoping.

4 References

[1] E. A Wrigley. Energy and the english industrial revolution. *Philosophical Transactions of the Royal Society A: Mathematical, Physical and Engineering Sciences*, 371(1986):20110568, 2013.

[2] Nicola Armaroli and Vincenzo Balzani. The future of energy supply: Challenges and opportunities. *Angewandte Chemie International Edition*, 46(1-2):52–66, 2007.

[3] Joel G. Kingsolver, H. Arthur Woods, Lauren B. Buckley, Kristen A. Potter, Heidi J. MacLean, and Jessica K. Higgins. Complex Life Cycles and the Responses of Insects to Climate Change. *Integrative and Comparative Biology*, 51(5):719–732, 06 2011.

[4] Florinda Martins, Carlos Felgueiras, Miroslava Smitkova, and Nídia Caetano. Analysis of fossil fuel energy consumption and environmental impacts in european countries. *Energies*, 12:964, 03 2019.

[5] Jonathan L. Bamber, Michael Oppenheimer, Robert E. Kopp, Willy P. Aspinall, and Roger M. Cooke. Ice sheet contributions to future sea-level rise from structured expert judgment. *Proceedings of the National Academy of Sciences*, 116(23):11195–11200, 2019.

[6] Shahriar Shafiee and Erkan Topal. When will fossil fuel reserves be diminished? *Energy Policy*, 37(1):181 – 189, 2009.

[7] John Tyndall. I. the bakerian lecture.- on the absorption and radiation of heat by gases and vapours, and on the physical connexion of radiation, absorption, and conduction. *Philosophical Transactions of the Royal Society of London*, 151:1–36, 1861.

[8] Svante Arrhenius. Xxxi. on the influence of carbonic acid in the air upon the temperature of the ground. *The London, Edinburgh, and Dublin Philosophical Magazine and Journal of Science*, 41(251):237–276, 1896.

[9] E. O. Hulburt. The temperature of the lower atmosphere of the earth. *Phys. Rev.*, 38:1876–1890, Nov 1931.

[10] Roger Revelle and Hans E. Suess. Carbon dioxide exchange between atmosphere and ocean and the question of an increase of atmospheric co2 during the past decades. *Tellus*, 9(1):18–27, 1957.

[11] Michael E. Mann, Raymond S. Bradley, and Malcolm K. Hughes. Northern hemisphere temperatures during the past millennium: Inferences, uncertainties, and limitations. *Geophysical Research Letters*, 26(6):759–762, 1999.

[12] Aradhna K. Tripati, Christopher D. Roberts, and Robert A. Eagle. Coupling of co2 and ice sheet stability over major climate transitions of the last 20 million years. *Science*, 326(5958):1394–1397, 2009.

[13] United Nations. Paris agreement. Treaty No. XXVII-7-d, Dez 2015.

[14] Andrei Sokolov, Sergey Paltsev, Henry Chen, and Erwan Monier. Climate Impacts of the Paris Agreement. In *EGU General Assembly Conference Abstracts*, EGU General Assembly Conference Abstracts, pages EPSC2016–8016, Apr 2016.

[15] David G Victor, Keigo Akimoto, Yoichi Kaya, Mitsutsune Yamaguchi, Danny Cullenward, and Cameron Hepburn. Prove paris was more than paper promises. *Nature News*, 548(7665):25, 2017.

[16] Joeri Rogelj, Michel Den Elzen, Niklas Höhne, Taryn Fransen, Hanna Fekete, Harald Winkler, Roberto Schaeffer, Fu Sha, Keywan Riahi, and Malte Meinshausen. Paris agreement climate proposals need a boost to keep warming well below 2 c. *Nature*, 534(7609):631–639, 2016.

[17] M. Liserre, T. Sauter, and J. Y. Hung. Future energy systems: Integrating renewable energy sources into the smart power grid through industrial electronics. *IEEE Industrial Electronics Magazine*, 4(1):18–37, March 2010.

[18] Kunta Yoshikawa, Hayato Kawasaki, Wataru Yoshida, Toru Irie, Katsunori Konishi, Kunihiro Nakano, Toshihiko Uto, Daisuke Adachi, Masanori Kanematsu, Hisashi Uzu, and Kenji Yamamoto. Silicon heterojunction solar cell with interdigitated back contacts for a photoconversion efficiency over 26%. *Nature Energy*, 2(5):17032, Mar 2017.

[19] D. C. Jordan and S. R. Kurtz. Photovoltaic degradation rates—an analytical review. *Progress in Photovoltaics: Research and Applications*, 21(1):12–29, 2013.

[20] Martin A. Green, Yoshihiro Hishikawa, Ewan D. Dunlop, Dean H. Levi, Jochen Hohl-Ebinger, and Anita W.Y. Ho-Baillie. Solar cell efficiency tables (version 51). *Progress in Photovoltaics: Research and Applications*, 26(1):3–12, 2018.

[21] M.J. (Mariska) de Wild-Scholten. Energy payback time and carbon footprint of commercial photovoltaic systems. *Solar Energy Materials and Solar Cells*, 119:296 – 305, 2013. Thin-film Photovoltaic Solar Cells.

[22] A. Louwen, W.G.J.H.M. van Sark, R.E.I. Schropp, W.C. Turkenburg, and A.P.C. Faaij. Life-cycle greenhouse gas emissions and energy payback time of current and prospective silicon heterojunction solar cell designs. *Progress in Photovoltaics: Research and Applications*, 23(10):1406–1428, 2015.

[23] Erik Alsema. Chapter iv-2 - energy payback time and co2 emissions of pv systems. In Augustin McEvoy, Tom Markvart, and Luis Castañer, editors, *Practical Handbook of Photovoltaics (Second Edition)*, pages 1097 – 1117. Academic Press, Boston, second edition edition, 2012.

[24] Lingxian Meng, Yamin Zhang, Xiangjian Wan, Chenxi Li, Xin Zhang, Yanbo Wang, Xin Ke, Zuo Xiao, Liming Ding, Ruoxi Xia, Hin-Lap Yip, Yong Cao, and Yongsheng Chen. Organic and solution-processed tandem solar cells with 17.3% efficiency. *Science*, 361(6407):1094–1098, 2018.

[25] Gilles Horowitz. Organic field-effect transistors. *Advanced Materials*, 10(5):365–377, 1998.

[26] Adrien Pierre, Mahsa Sadeghi, Marcia M. Payne, Antonio Facchetti, John E. Anthony, and Ana Claudia Arias. All-printed flexible organic transistors enabled by surface tension-guided blade coating. *Advanced Materials*, 26(32):5722–5727, 2014.

[27] Jeremy H Burroughes, Donal DC Bradley, AR Brown, RN Marks, K Mackay, Richard H Friend, PL Burns, and AB Holmes. Light-emitting diodes based on conjugated polymers. *nature*, 347(6293):539, 1990.

[28] Sebastian Reineke, Frank Lindner, Gregor Schwartz, Nico Seidler, Karsten Walzer, Björn Lüssem, and Karl Leo. White organic light-emitting diodes with fluorescent tube efficiency. *Nature*, 459(7244):234, 2009.

[29] C David Müller, Aurelie Falcou, Nina Reckefuss, Markus Rojahn, Valèrie Wiederhirn, Paula Rudati, Holger Frohne, Oskar Nuyken, Heinrich Becker, and Klaus Meerholz. Multi-colour organic light-emitting displays by solution processing. *Nature*, 421(6925):829, 2003.

[30] Wenchao Zhao, Shaoqing Zhang, Yun Zhang, Sunsun Li, Xiaoyu Liu, Chang He, Zhong Zheng, and Jianhui Hou. Environmentally friendly solvent-processed organic solar cells that are highly efficient and adaptable for the blade-coating method. *Advanced Materials*, 30(4):1704837, 2018.

[31] Chun-Yu Chen, Hao-Wen Chang, Yu-Fan Chang, Bo-Jie Chang, Yuan-Sheng Lin, Pei-Siou Jian, Han-Cheng Yeh, Hung-Ta Chien, En-Chen Chen, Yu-Chiang Chao, Hsin-Fei Meng, Hsiao-Wen Zan, Hao-Wu Lin, Sheng-Fu Horng, Yen-Ju Cheng, Feng-Wen Yen, I-Feng Lin, Hsiu-Yuan Yang, Kuo-Jui Huang, and Mei-Rurng Tseng. Continuous blade coating for multi-layer large-area organic light-emitting diode and solar cell. *Journal of Applied Physics*, 110(9):094501, 2011.

[32] Yung-Ming Liao, Hung-Min Shih, Kuang-Hui Hsu, Chain-Shu Hsu, Yu-Chiang Chao, Sheng-Chia Lin, Chun-Yao Chen, and Hsin-Fei Meng. High-performance poly(2,3-diphenyl-1,4-phenylene vinylene)-based polymer light-emitting diodes by blade coating method. *Polymer*, 52(17):3717 – 3724, 2011.

[33] Claudia N. Hoth, Pavel Schilinsky, Stelios A. Choulis, and Christoph J. Brabec. Printing highly efficient organic solar cells. *Nano Letters*, 8(9):2806–2813, 2008. PMID: 18683989.

[34] Guodong Wang, Muhammad Abdullah Adil, Jianqi Zhang, and Zhixiang Wei. Large-area organic solar cells: Material requirements, modular designs, and printing methods. *Advanced Materials*, 31(45):1805089, 2019.

[35] T. R. Hebner, C. C. Wu, D. Marcy, M. H. Lu, and J. C. Sturm. Ink-jet printing of doped polymers for organic light emitting devices. *Applied Physics Letters*, 72(5):519–521, 1998.

[36] Stephen Forrest. The path to ubiquitous and low-cost organic electronic appliances on plastic. *Nature*, 428:911–8, 05 2004.

[37] T. Aernouts, T. Aleksandrov, C. Girotto, J. Genoe, and J. Poortmans. Polymer based organic solar cells using ink-jet printed active layers. *Applied Physics Letters*, 92(3):033306, 2008.

[38] Graham Morse, Richard Harding, Nicolas Blouin, Hannah Buerckstrummer, Agnieszka Pron, Stephan Wieder, David Mueller, , and Stephane Berny. Organic photovoltaic applications for iot, architecture, and wearables. *Material Matters*, 12(3):101 – 109, 2017.

[39] Marco Casini. *Smart buildings: Advanced materials and nanotechnology to improve energy-efficiency and environmental performance*. Woodhead Publishing, 2016.

[40] Yiqiang Zhan, Yongfeng Mei, and Lirong Zheng. Materials capability and device performance in flexible electronics for the internet of things. *J. Mater. Chem. C*, 2:1220–1232, 2014.

[41] S. Arumugam, Y. Li, S. Senthilarasu, R. Torah, A. L. Kanibolotsky, A. R. Inigo, P. J. Skabara, and S. P. Beeby. Fully spray-coated organic solar cells on woven polyester cotton fabrics for wearable energy harvesting applications. *J. Mater. Chem. A*, 4:5561–5568, 2016.

[42] Olle Inganäs and Shimelis Admassie. 25th anniversary article: organic photovoltaic modules and biopolymer supercapacitors for supply of renewable electricity: a perspective from africa. *Advanced Materials*, 26(6):830–848, 2014.

[43] Suren A. Gevorgyan, Morten V. Madsen, Bérenger Roth, Michael Corazza, Markus Hösel, Roar R. Søndergaard, Mikkel Jørgensen, and Frederik C. Krebs. Lifetime of organic photovoltaics: Status and predictions. *Advanced Energy Materials*, 6(2):1501208, 2016.

[44] Omar A. Abdulrazzaq, Viney Saini, Shawn Bourdo, Enkeleda Dervishi, and Alexandru S. Biris. Organic solar cells: A review of materials, limitations, and possibilities for improvement. *Particulate Science and Technology*, 31(5):427–442, 2013.

[45] V. K. Thorsmølle, R. D. Averitt, J. Demsar, D. L. Smith, S. Tretiak, R. L. Martin, X. Chi, B. K. Crone, A. P. Ramirez, and A. J. Taylor. Morphology effectively controls singlet-triplet exciton relaxation and charge transport in organic semiconductors. *Phys. Rev. Lett.*, 102:017401, Jan 2009.

[46] Peter K. Watkins, Alison B. Walker, and Geraldine L. B. Verschoor. Dynamical monte carlo modelling of organic solar cells: The dependence of internal quantum efficiency on morphology. *Nano Letters*, 5(9):1814–1818, 2005. PMID: 16159229.

[47] Theodoros A. Papadopoulos, Luca Muccioli, Stavros Athanasopoulos, Alison B. Walker, Claudio Zannoni, and David Beljonne. Does supramolecular ordering influence exciton transport in conjugated systems? insight from atomistic simulations. *Chem. Sci.*, 2:1025–1032, 2011.

[48] Ashish Sharma, Stavros Athanasopoulos, Patrick C. Tapping, Randy P. Sabatini, Olivia F. McRae, Markus Müllner, Tak W. Kee, and Girish Lakhwani. Emission decay pathways sensitive to circular polarization of excitation. *The Journal of Physical Chemistry C*, 122(42):23910–23916, 2018.

[49] Scott A. Mauger, Lilian Chang, Stephan Friedrich, Christopher W. Rochester, David M. Huang, Peng Wang, and Adam J. Moulé. Self-assembly of selective interfaces in organic photovoltaics. *Advanced Functional Materials*, 23(15):1935–1946, 2013.

[50] Timothy S. Gehan, Monojit Bag, Lawrence A. Renna, Xiaobo Shen, Dana D. Algaier, Paul M. Lahti, Thomas P. Russell, and Dhandapani Venkataraman. Multiscale active layer morphologies for organic photovoltaics through self-assembly of nanospheres. *Nano Letters*, 14(9):5238–5243, 2014. PMID: 25102376.

[51] Sooncheol Kwon, Hongkyu Kang, Jong-Hoon Lee, Jinho Lee, Soonil Hong, Heejoo Kim, and Kwanghee Lee. Effect of processing additives on organic photovoltaics: Recent progress and future prospects. *Advanced Energy Materials*, 7(10):1601496, 2017.

[52] Yonghee Kim, Geunjin Kim, Jongjin Lee, and Kwanghee Lee. Morphology controlled bulk-heterojunction layers of fully electro-spray coated organic solar cells. *Solar Energy Materials and Solar Cells*, 105:272 – 279, 2012.

[53] Jeffrey Peet, Erin Brocker, Yunhua Xu, and Guillermo C. Bazan. Controlled β-phase formation in poly(9,9-di-n-octylfluorene) by processing with alkyl additives. *Advanced Materials*, 20(10):1882–1885, 2008.

[54] Jui-Fen Chang, Baoquan Sun, Dag W. Breiby, Martin M. Nielsen, Theis I. Sölling, Mark Giles, Iain McCulloch, and Henning Sirringhaus. Enhanced mobility of poly(3-hexylthiophene) transistors by spin-coating from high-boiling-point solvents. *Chemistry of Materials*, 16(23):4772–4776, 2004.

[55] David B. Mitzi, Laura L. Kosbar, Conal E. Murray, Matthew Copel, and Ali Afzali. High-mobility ultrathin semiconducting films prepared by spin coating. *Nature*, 428:299–303, 2004.

[56] Fengjiao Zhang, Chong-an Di, Nikolai Berdunov, Yuanyuan Hu, Yunbin Hu, Xike Gao, Qing Meng, Henning Sirringhaus, and Daoben Zhu. Ultrathin film organic transistors: Precise control of semiconductor thickness via spin-coating. *Advanced Materials*, 25(10):1401–1407, 2013.

[57] David B. Hall, Patrick Underhill, and John M. Torkelson. Spin coating of thin and ultrathin polymer films. *Polymer Engineering & Science*, 38(12):2039–2045, 1998.

[58] Edward J. W. Crossland, Khosrow Rahimi, Günter Reiter, Ullrich Steiner, and Sabine Ludwigs. Systematic control of nucleation density in poly(3-hexylthiophene) thin films. *Advanced Functional Materials*, 21(3):518–524, 2011.

[59] Khosrow Rahimi, Ioan Botiz, Natalie Stingelin, Navaphun Kayunkid, Michael Sommer, Felix Peter Vinzenz Koch, Ha Nguyen, Olivier Coulembier, Philippe Dubois, Martin Brinkmann, and Günter Reiter. Controllable processes for generating large single crystals of poly(3-hexylthiophene). *Angewandte Chemie International Edition*, 51(44):11131–11135, 2012.

[60] Gang Li, Vishal Shrotriya, Yan Yao, and Yang Yang. Investigation of annealing effects and film thickness dependence of polymer solar cells based on poly(3-hexylthiophene). *Journal of Applied Physics*, 98(4):043704, 2005.

[61] G. Li, Y. Yao, H. Yang, V. Shrotriya, G. Yang, and Y. Yang. "solvent annealing" effect in polymer solar cells based on poly(3-hexylthiophene) and methanofullerenes. *Advanced Functional Materials*, 17(10):1636–1644, 2007.

[62] Mariano Campoy-Quiles, Toby A. M. Ferenczi, Tiziano Agostinelli, Pablo G. Etchegoin, Youngkyoo Kim, Thomas D. Anthopoulos, Paul N. Stavrinou, Donal D. C. Bradley, and Jenny Nelson. Morphology evolution via self-organization and lateral and vertical diffusion in polymer:fullerene solar cell blends. *Nature materials*, 7 2:158–64, 2008.

[63] Xiaoniu Yang, Joachim Loos, Sjoerd C. Veenstra, Wiljan J. H. Verhees, Martijn M. Wienk, Jan M. Kroon, Matthias A. J. Michels, and René A. J. Janssen. Nanoscale morphology of high-performance polymer solar cells. *Nano Letters*, 5(4):579–583, 2005. PMID: 15826090.

[64] Sung Heum Park, Anshuman Roy, Serge Beaupré, Shinuk Cho, Nelson Coates, Ji Sun Moon, Daniel Moses, Mario Leclerc, Kwanghee Lee, and Alan J. Heeger. Bulk heterojunction solar cells with internal quantum efficiency approaching 100%. *Nature Photonics*, 3(5):297–302, May 2009.

[65] Fabian Panzer, Heinz Bässler, and Anna Köhler. Temperature induced order–disorder transition in solutions of conjugated polymers probed by optical spectroscopy. *The Journal of Physical Chemistry Letters*, 8(1):114–125, 2017. PMID: 27966973.

[66] Byeong-Kwan An, Johannes Gierschner, and Soo Young Park. π-conjugated cyanostilbene derivatives: A unique self-assembly motif for molecular nanostructures with enhanced emission and transport. *Accounts of Chemical Research*, 45(4):544–554, 2012. PMID: 22085759.

[67] Dominic Raithel, Sebastian Baderschneider, Thiago B. de Queiroz, Ruth Lohwasser, Jürgen Köhler, Mukundan Thelakkat, Stephan Kümmel, and Richard Hildner. Emitting species of poly(3-hexylthiophene): From single, isolated chains to bulk. *Macromolecules*, 49(24):9553–9560, 2016.

[68] Marcia Levitus, Kelli Schmieder, Holly Ricks, Ken D. Shimizu, Uwe H. F. Bunz, and Miguel A. Garcia-Garibay. Steps to demarcate the effects of chromophore aggregation and planarization in poly(phenyleneethynylene)s. 1. rotationally interrupted conjugation in the excited states of 1,4-bis(phenylethynyl)benzene. *Journal of the American Chemical Society*, 123(18):4259–4265, 2001. PMID: 11457192.

[69] Anna Köhler and Heinz Bässler. *Electronic processes in organic semiconductors: An introduction*. John Wiley & Sons, 2015.

[70] Lijun Huo, Tao Liu, Xiaobo Sun, Yunhao Cai, Alan J Heeger, and Yanming Sun. Single-junction organic solar cells based on a novel wide-bandgap polymer with efficiency of 9.7%. *Advanced Materials*, 27(18):2938–2944, 2015.

[71] Zhicai He, Biao Xiao, Feng Liu, Hongbin Wu, Yali Yang, Steven Xiao, Cheng Wang, Thomas P Russell, and Yong Cao. Single-junction polymer solar cells with high efficiency and photovoltage. *Nature Photonics*, 9(3):174, 2015.

[72] Kwan H. Lee, Paul E. Schwenn, Arthur R. G. Smith, Hamish Cavaye, Paul E. Shaw, Michael James, Karsten B. Krueger, Ian R. Gentle, Paul Meredith, and Paul L. Burn. Morphology of all-solution-processed "bilayer" organic solar cells. *Advanced Materials*, 23(6):766–770, 2011.

[73] Gilles Dennler, Markus C. Scharber, and Christoph J. Brabec. Polymer-fullerene bulk-heterojunction solar cells. *Advanced Materials*, 21(13):1323–1338, 2009.

[74] M. C. Scharber, D. Mühlbacher, M. Koppe, P. Denk, C. Waldauf, A. J. Heeger, and C. J. Brabec. Design rules for donors in bulk-heterojunction solar cells-towards 10% energy-conversion efficiency. *Advanced Materials*, 18(6):789–794, 2006.

[75] Antonio Guerrero and Germà Garcia-Belmonte. Recent advances to understand morphology stability of organic photovoltaics. *Nano-Micro Letters*, 9(1):10, Oct 2016.

[76] Hsing-Ju Wang, Chih-Ping Chen, and Ru-Jong Jeng. Polythiophenes comprising conjugated pendants for polymer solar cells: a review. *Materials*, 7(4):2411–2439, 2014.

[77] Weiran Cao and Jiangeng Xue. Recent progress in organic photovoltaics: device architecture and optical design. *Energy Environ. Sci.*, 7:2123–2144, 2014.

[78] Wangqiao Chen and Qichun Zhang. Recent progress in non-fullerene small molecule acceptors in organic solar cells (oscs). *J. Mater. Chem. C*, 5:1275–1302, 2017.

[79] Jing Liu, Lik-Kuen Ma, Zhengke Li, Huawei Hu, Tingxuan Ma, Chenhui Zhu, Harald Ade, and He Yan. A random donor polymer based on an asymmetric building block to tune the morphology of non-fullerene organic solar cells. *J. Mater. Chem. A*, 5:22480–22488, 2017.

[80] Daan Frenkel and Berend Smit. *Understanding molecular simulation: from algorithms to applications*, volume 1. Elsevier, 2001.

[81] M. P. Allen and D. J. Tildesley. *Computer Simulation of Liquids*. Clarendon Press, New York, NY, USA, 1989.

[82] Berk Hess, Henk Bekker, Herman JC Berendsen, and Johannes GEM Fraaije. Lincs: a linear constraint solver for molecular simulations. *Journal of computational chemistry*, 18(12):1463–1472, 1997.

[83] R.W. Hockney. Potential calculation and some applications. *Methods Comput. Phys. 9: 135-211(1970).*, 1 1970.

[84] H.J.C. Berendsen, D. van der Spoel, and R. van Drunen. Gromacs: A message-passing parallel molecular dynamics implementation. *Computer Physics Communications*, 91(1):43 – 56, 1995.

[85] Erik Lindahl, Berk Hess, and David van der Spoel. Gromacs 3.0: a package for molecular simulation and trajectory analysis. *Molecular modeling annual*, 7(8):306–317, Aug 2001.

[86] David van der Spoel, Erik Lindahl, Berk Hess, Gerrit Groenhof, Alan Mark, and Herman Berendsen. Gromacs: fast, flexible, and free. *Journal of computational chemistry*, 26:1701–18, 12 2005.

[87] Berk Hess, Carsten Kutzner, David van der Spoel, and Erik Lindahl. Gromacs 4: Algorithms for highly efficient, load-balanced, and scalable molecular simulation. *Journal of Chemical Theory and Computation*, 4(3):435–447, 2008. PMID: 26620784.

[88] Sander Pronk, Szilárd Páll, Roland Schulz, Per Larsson, Pär Bjelkmar, Rossen Apostolov, Michael R. Shirts, Jeremy C. Smith, Peter M. Kasson, David van der Spoel, Berk Hess, and Erik Lindahl. GROMACS 4.5: a high-throughput and highly parallel open source molecular simulation toolkit. *Bioinformatics*, 29(7):845–854, 02 2013.

[89] Szilárd Páll, Mark James Abraham, Carsten Kutzner, Berk Hess, and Erik Lindahl. Tackling exascale software challenges in molecular dynamics simulations with gromacs. In Stefano Markidis and Erwin Laure, editors, *Solving Software Challenges for Exascale*, pages 3–27, Cham, 2015. Springer International Publishing.

[90] Mark James Abraham, Teemu Murtola, Roland Schulz, Szilárd Páll, Jeremy C. Smith, Berk Hess, and Erik Lindahl. Gromacs: High performance molecular simulations through multi-level parallelism from laptops to supercomputers. *SoftwareX*, 1-2:19 – 25, 2015.

[91] Erik Lindahl. Molecular dynamics simulations. *Methods in molecular biology*, 1215:3–26, 2008.

[92] William Humphrey, Andrew Dalke, and Klaus Schulten. VMD – Visual Molecular Dynamics. *Journal of Molecular Graphics*, 14:33–38, 1996.

[93] Johannes Kästner. Umbrella sampling. *Wiley Interdisciplinary Reviews: Computational Molecular Science*, 1(6):932–942, 2011.

[94] Shankar Kumar, Djamal Bouzida, Robert H. Swendsen, Peter A. Kollman, and John M. Rosenberg. The weighted histogram analysis method for free-energy calculations on biomolecules. i: The method. 1992.

[95] Alessandro Barducci, Giovanni Bussi, and Michele Parrinello. Well-tempered metadynamics: A smoothly converging and tunable free-energy method. *Phys. Rev. Lett.*, 100:020603, Jan 2008.

[96] Bradley M. Dickson. Approaching a parameter-free metadynamics. *Phys. Rev. E*, 84:037701, Sep 2011.

[97] Alessandro Barducci, Massimiliano Bonomi, and Michele Parrinello. Metadynamics. *WIREs Computational Molecular Science*, 1(5):826–843, 2011.

[98] Gareth A. Tribello, Massimiliano Bonomi, Davide Branduardi, Carlo Camilloni, and Giovanni Bussi. Plumed 2: New feathers for an old bird. *Computer Physics Communications*, 185(2):604 – 613, 2014.

[99] Reiner M Dreizler and Eberhard KU Gross. *Density functional theory: an approach to the quantum many-body problem*. Springer Science & Business Media, 2012.

[100] Klaus Capelle. A bird's-eye view of density-functional theory. *Brazilian Journal of Physics*, 36(4A):1318–1343, 2006.

[101] P. Hohenberg and W. Kohn. Inhomogeneous electron gas. *Phys. Rev.*, 136:B864–B871, Nov 1964.

[102] W. Kohn and L. J. Sham. Self-consistent equations including exchange and correlation effects. *Phys. Rev.*, 140:A1133–A1138, Nov 1965.

[103] W. Kohn. Nobel lecture: Electronic structure of matter—wave functions and density functionals. *Rev. Mod. Phys.*, 71:1253–1266, Oct 1999.

[104] Thierry Leininger, Hermann Stoll, Hans-Joachim Werner, and Andreas Savin. Combining long-range configuration interaction with short-range density functionals. *Chemical Physics Letters*, 275(3):151 – 160, 1997.

[105] T Koopmans. Über die zuordnung von wellenfunktionen und eigenwerten zu den einzelnen elektronen eines atoms. *Physica*, 1(1):104 – 113, 1934.

[106] M. J. Frisch, G. W. Trucks, H. B. Schlegel, G. E. Scuseria, M. A. Robb, J. R. Cheeseman, G. Scalmani, V. Barone, G. A. Petersson, H. Nakatsuji, X. Li, M. Caricato, A. V. Marenich, J. Bloino, B. G. Janesko, R. Gomperts, B. Mennucci, H. P. Hratchian, J. V. Ortiz, A. F. Izmaylov, J. L. Sonnenberg, D. Williams-Young, F. Ding, F. Lipparini, F. Egidi, J. Goings, B. Peng, A. Petrone, T. Henderson, D. Ranasinghe, V. G. Zakrzewski, J. Gao, N. Rega, G. Zheng, W. Liang, M. Hada, M. Ehara, K. Toyota, R. Fukuda, J. Hasegawa, M. Ishida, T. Nakajima,

Y. Honda, O. Kitao, H. Nakai, T. Vreven, K. Throssell, J. A. Montgomery, Jr., J. E. Peralta, F. Ogliaro, M. J. Bearpark, J. J. Heyd, E. N. Brothers, K. N. Kudin, V. N. Staroverov, T. A. Keith, R. Kobayashi, J. Normand, K. Raghavachari, A. P. Rendell, J. C. Burant, S. S. Iyengar, J. Tomasi, M. Cossi, J. M. Millam, M. Klene, C. Adamo, R. Cammi, J. W. Ochterski, R. L. Martin, K. Morokuma, O. Farkas, J. B. Foresman, and D. J. Fox. Gaussian~09 Revision E.01, 2016. Gaussian Inc. Wallingford CT.

[107] Peter Ertl. Molecular structure input on the web. *Journal of Cheminformatics*, 2(1):1, Feb 2010.

[108] Alpeshkumar K. Malde, Le Zuo, Matthew Breeze, Martin Stroet, David Poger, Pramod C. Nair, Chris Oostenbrink, and Alan E. Mark. An automated force field topology builder (atb) and repository: Version 1.0. *Journal of Chemical Theory and Computation*, 7(12):4026–4037, 2011. PMID: 26598349.

[109] Stefan Canzar, Mohammed El-Kebir, René Pool, Khaled Elbassioni, Alpeshkumar K Malde, Alan E Mark, Daan P Geerke, Leen Stougie, and Gunnar W Klau. Charge group partitioning in biomolecular simulation. *Journal of Computational Biology*, 20(3):188–198, 2013.

[110] Katarzyna B. Koziara, Martin Stroet, Alpeshkumar K. Malde, and Alan E. Mark. Testing and validation of the automated topology builder (atb) version 2.0: prediction of hydration free enthalpies. *Journal of Computer-Aided Molecular Design*, 28(3):221–233, Mar 2014.

[111] Nathan Schmid, Andreas P. Eichenberger, Alexandra Choutko, Sereina Riniker, Moritz Winger, Alan E. Mark, and Wilfred F. van Gunsteren. Definition and testing of the gromos force-field versions 54a7 and 54b7. *European Biophysics Journal*, 40(7):843, Apr 2011.

[112] Bright Walker, Chunki Kim, and Thuc-Quyen Nguyen. Small molecule solution-processed bulk heterojunction solar cells. *Chemistry of Materials*, 23(3):470–482, 2011.

[113] Yuze Lin, Yongfang Li, and Xiaowei Zhan. Small molecule semiconductors for high-efficiency organic photovoltaics. *Chem. Soc. Rev.*, 41:4245–4272, 2012.

[114] Amaresh Mishra and Peter Bäuerle. Small molecule organic semiconductors on the move: Promises for future solar energy technology. *Angewandte Chemie International Edition*, 51(9):2020–2067, 2012.

[115] Ye Huang, Edward J. Kramer, Alan J. Heeger, and Guillermo C. Bazan. Bulk heterojunction solar cells: Morphology and performance relationships. *Chemical Reviews*, 114(14):7006–7043, 2014. PMID: 24869423.

[116] Christopher J. Takacs, Yanming Sun, Gregory C. Welch, Louis A. Perez, Xiaofeng Liu, Wen Wen, Guillermo C. Bazan, and Alan J. Heeger. Solar cell efficiency, self-assembly, and dipole–dipole interactions of isomorphic narrow-band-gap molecules. *Journal of the American Chemical Society*, 134(40):16597–16606, 2012. PMID: 22950622.

[117] John A. Love, Ikuhiro Nagao, Ye Huang, Martijn Kuik, Vinay Gupta, Christopher J. Takacs, Jessica E. Coughlin, Li Qi, Thomas S. van der Poll, Edward J. Kramer, Alan J. Heeger, Thuc-Quyen Nguyen, and Guillermo C. Bazan. Silaindacenodithiophene-based molecular donor: Morphological features and use in the fabrication of compositionally tolerant, high-efficiency bulk heterojunction solar cells. *Journal of the American Chemical Society*, 136(9):3597–3606, 2014. PMID: 24559286.

[118] Jessica E. Coughlin, Andriy Zhugayevych, Ronald C. Bakus, Thomas S. van der Poll, Gregory C. Welch, Simon J. Teat, Guillermo C. Bazan, and Sergei Tretiak. A combined experimental and theoretical study of conformational preferences of molecular semiconductors. *The Journal of Physical Chemistry C*, 118(29):15610–15623, 2014.

[119] Gregory C. Welch, Louis A. Perez, Corey V. Hoven, Yuan Zhang, Xuan-Dung Dang, Alexander Sharenko, Michael F. Toney, Edward J. Kramer, Thuc-Quyen Nguyen, and Guillermo C. Bazan. A modular molecular framework for utility in small-molecule solution-processed organic photovoltaic devices. *J. Mater. Chem.*, 21:12700–12709, 2011.

[120] Ting Lei, Xin Xia, Jie-Yu Wang, Chen-Jiang Liu, and Jian Pei. "conformation locked" strong electron-deficient poly(p-phenylene vinylene) derivatives for ambient-stable n-type field-effect transistors: Synthesis, properties, and effects of fluorine substitution position. *Journal of the American Chemical Society*, 136(5):2135–2141, 2014. PMID: 24422749.

[121] Gregory C. Welch, Ronald C. Bakus, Simon J. Teat, and Guillermo C. Bazan. Impact of regiochemistry and isoelectronic bridgehead substitution on the molecular shape and bulk organization of narrow bandgap chromophores. *Journal of the American Chemical Society*, 135(6):2298–2305, 2013. PMID: 23298395.

[122] Peter Kohn, Zhuxia Rong, Kai H. Scherer, Alessandro Sepe, Michael Sommer, Peter Müller-Buschbaum, Richard H. Friend, Ullrich Steiner, and Sven Hüttner. Crystallization-induced 10-nm structure formation in p3ht/pcbm blends. *Macromolecules*, 46(10):4002–4013, 2013.

[123] Kim Tremel and Sabine Ludwigs. *Morphology of P3HT in Thin Films in Relation to Optical and Electrical Properties*, pages 39–82. Springer Berlin Heidelberg, Berlin, Heidelberg, 2014.

[124] Patrick Pingel, Achmad Zen, Ruben D. Abellón, Ferdinand C. Grozema, Laurens D.A. Siebbeles, and Dieter Neher. Temperature-resolved local and macroscopic charge carrier transport in thin p3ht layers. *Advanced Functional Materials*, 20(14):2286–2295, 2010.

[125] Markus Reichenberger, Sebastian Baderschneider, Daniel Kroh, Steffen Grauf, Jürgen Köhler, Richard Hildner, and Anna Köhler. Watching paint dry: the impact of diiodooctane on the kinetics of aggregate formation in thin films of poly (3-hexylthiophene). *Macromolecules*, 49(17):6420–6430, 2016.

[126] Fabian Panzer, Michael Sommer, Heinz Bässler, Mukundan Thelakkat, and Anna Köhler. Spectroscopic signature of two distinct h-aggregate species in poly(3-hexylthiophene). *Macromolecules*, 48(5):1543–1553, 2015.

[127] Huan Li, Yifan Zhao, Jin Fang, Xiangwei Zhu, Benzheng Xia, Kun Lu, Zhen Wang, Jianqi Zhang, Xuefeng Guo, and Zhixiang Wei. Improve the performance of the all-small-molecule nonfullerene organic solar cells through enhancing the crystallinity of acceptors. *Advanced Energy Materials*, 8(11):1702377, 2018.

[128] Haijun Bin, Jia Yao, Yankang Yang, Indunil Angunawela, Chenkai Sun, Liang Gao, Long Ye, Beibei Qiu, Lingwei Xue, Chenhui Zhu, Chunhe Yang, Zhi-Guo Zhang, Harald Ade, and Yongfang Li. High-efficiency all-small-molecule organic solar cells based on an organic molecule donor with alkylsilyl-thienyl conjugated side chains. *Advanced Materials*, 30(27):1706361, 2018.

[129] Bright Walker, Arnold B. Tamayo, Xuan-Dung Dang, Peter Zalar, Jung Hwa Seo, Andres Garcia, Mananya Tantiwiwat, and Thuc-Quyen Nguyen. Nanoscale phase separation and high photovoltaic efficiency in solution-processed, small-molecule bulk heterojunction solar cells. *Advanced Functional Materials*, 19(19):3063–3069, 2009.

[130] Hannah Bürckstümmer, Elena V. Tulyakova, Manuela Deppisch, Martin R. Lenze, Nils M. Kronenberg, Marcel Gsänger, Matthias Stolte, Klaus Meerholz, and Frank Würthner. Efficient solution-processed bulk heterojunction solar cells by antiparallel supramolecular arrangement of dipolar donor–acceptor dyes. *Angewandte Chemie International Edition*, 50(49):11628–11632, 2011.

[131] Olivia P. Lee, Alan T. Yiu, Pierre M. Beaujuge, Claire H. Woo, Thomas W. Holcombe, Jill E. Millstone, Jessica D. Douglas, Mark S. Chen, and Jean M. J. Fréchet. Efficient small molecule bulk heterojunction solar cells with high fill factors via pyrene-directed molecular self-assembly. *Advanced Materials*, 23(45):5359–5363, 2011.

[132] Huixia Shang, Haijun Fan, Yao Liu, Wenping Hu, Yongfang Li, and Xiaowei Zhan. A solution-processable star-shaped molecule for high-performance organic solar cells. *Advanced Materials*, 23(13):1554–1557, 2011.

[133] Guodan Wei, Siyi Wang, Kai Sun, Mark E. Thompson, and Stephen R. Forrest. Solvent-annealed crystalline squaraine: Pc70bm (1:6) solar cells. *Advanced Energy Materials*, 1(2):184–187, 2011.

[134] Jiaoyan Zhou, Xiangjian Wan, Yongsheng Liu, Yi Zuo, Zhi Li, Guangrui He, Guankui Long, Wang Ni, Chenxi Li, Xuncheng Su, and Yongsheng Chen. Small molecules based on benzo[1,2-b:4,5-b']dithiophene unit for high-performance solution-processed organic solar cells. *Journal of the American Chemical Society*, 134(39):16345–16351, 2012. PMID: 22989014.

[135] Li Nian, Ke Gao, Yufeng Jiang, Qikun Rong, Xiaowen Hu, Dong Yuan, Feng Liu, Xiaobin Peng, Thomas P. Russell, and Guofu Zhou. Small-molecule solar cells with simultaneously enhanced short-circuit current and fill factor to achieve 11% efficiency. *Advanced Materials*, 29(29):1700616, 2017.

[136] Jianqi Zhang, Yajie Zhang, Jin Fang, Kun Lu, Zaiyu Wang, Wei Ma, and Zhixiang Wei. Conjugated polymer–small molecule alloy leads to high efficient ternary organic solar cells. *Journal of the American Chemical Society*, 137(25):8176–8183, 2015. PMID: 26052738.

[137] John A. Love, Christopher M. Proctor, Jianhua Liu, Christopher J. Takacs, Alexander Sharenko, Thomas S. van der Poll, Alan J. Heeger, Guillermo C. Bazan, and Thuc-Quyen Nguyen. Film morphology of high efficiency solution-processed small-molecule solar cells. *Advanced Functional Materials*, 23(40):5019–5026, 2013.

[138] Aung Ko Ko Kyaw, Dong Hwan Wang, Chan Luo, Yong Cao, Thuc-Quyen Nguyen, Guillermo C. Bazan, and Alan J. Heeger. Effects of solvent additives on morphology, charge generation, transport, and recombination in solution-processed small-molecule solar cells. *Advanced Energy Materials*, 4(7):1301469, 2014.

[139] Qiuju Liang, Jie Han, Chunpeng Song, Zaiyu Wang, Jingming Xin, Xinhong Yu, Zhiyuan Xie, Wei Ma, Jiangang Liu, and Yanchun Han. Tuning molecule diffusion to control the phase separation of the p-dts(fbtth2)2/ep-pdi blend system via thermal annealing. *J. Mater. Chem. C*, 5:6842–6851, 2017.

[140] Yanming Sun, Gregory Welch, Wei Lin Leong, Christopher Takacs, Guillermo Bazan, and Alan Heeger. Solution-processed small-molecule solar cells with 6.7 *Nature materials*, 11:44–8, 11 2011.

[141] John A. Love, Ikuhiro Nagao, Ye Huang, Martijn Kuik, Vinay Gupta, Christopher J. Takacs, Jessica E. Coughlin, Li Qi, Thomas S. van der Poll, Edward J. Kramer, Alan J. Heeger, Thuc-Quyen Nguyen, and Guillermo C. Bazan. Silaindacenodithiophene-based molecular donor: Morphological features and use in the fabrication of compositionally tolerant, high-efficiency bulk heterojunction solar cells. *Journal of the American Chemical Society*, 136(9):3597–3606, 2014. PMID: 24559286.

[142] Markus Reichenberger, John A. Love, Alexander Rudnick, Sergey Bagnich, Fabian Panzer, Anna Stradomska, Guillermo C. Bazan, Thuc-Quyen Nguyen, and Anna Köhler. The effect of intermolecular interaction on excited states in p - dts(fbtth2)2. *The Journal of Chemical Physics*, 144(7):074904, 2016.

[143] John A. Love, Ikuhiro Nagao, Ye Huang, Martijn Kuik, Vinay Gupta, Christopher J. Takacs, Jessica E. Coughlin, Li Qi, Thomas S. van der Poll, Edward J. Kramer, Alan J. Heeger, Thuc-Quyen Nguyen, and Guillermo C. Bazan. Silaindacenodithiophene-based molecular donor: Morphological features and use in the fabrication of compositionally tolerant, high-efficiency bulk heterojunction solar cells. *Journal of the American Chemical Society*, 136(9):3597–3606, 2014. PMID: 24559286.

[144] Niva A Ran, Steffen Roland, John A Love, Victoria Savikhin, Christopher J Takacs, Yao-Tsung Fu, Hong Li, Veaceslav Coropceanu, Xiaofeng Liu, Jean-Luc Brédas, et al. Impact of interfacial molecular orientation on radiative recombination and charge generation efficiency. *Nature communications*, 8(1):79, 2017.

[145] Rui-Rong Bai, Cai-Rong Zhang, You-Zhi Wu, Li-Hua Yuan, Mei-Ling Zhang, Yu-Hong Chen, Zi-Jiang Liu, and Hong-Shan Chen. Interface configuration effects on excitation, exciton dissociation, and charge recombination in organic photovoltaic heterojunction. *International Journal of Quantum Chemistry*, n/a(n/a):e26103, 2019.

[146] Maged Abdelsamie, Neil D. Treat, Kui Zhao, Caitlin McDowell, Mark A. Burgers, Ruipeng Li, Detlef-M. Smilgies, Natalie Stingelin, Guillermo C. Bazan, and Aram Amassian. Toward additive-free small-molecule organic solar cells: Roles of the donor crystallization pathway and dynamics. *Advanced Materials*, 27(45):7285–7292, 2015.

[147] Markus Reichenberger, Daniel Kroh, Giovanni M. M. Matrone, Konstantin Schötz, Stephan Pröller, Oliver Filonik, Margret E. Thordardottir, Eva M. Herzig, Heinz Bässler, Natalie Stingelin, and Anna Köhler. Controlling aggregate formation in conjugated polymers by spin-coating below the critical temperature of the disorder–order transition. *Journal of Polymer Science Part B: Polymer Physics*, 56(6):532–542, 2018.

[148] Cheng Zhou, Qiuhong Cui, Caitlin McDowell, Martin Seifrid, Xiankai Chen, Jean-Luc Brédas, Ming Wang, Fei Huang, and Guillermo C. Bazan. Topological transformation of π-conjugated molecules reduces resistance to crystallization. *Angewandte Chemie International Edition*, 56(32):9318–9321, 2017.

[149] Christina Scharsich, Florian S. U. Fischer, Kevin Wilma, Richard Hildner, Sabine Ludwigs, and Anna Köhler. Revealing structure formation in pcpdtbt by optical spectroscopy. *Journal of Polymer Science Part B: Polymer Physics*, 53(20):1416–1430, 2015.

[150] Hui Huang, Lei Yang, Antonio Facchetti, and Tobin J. Marks. Organic and polymeric semiconductors enhanced by noncovalent conformational locks. *Chemical Reviews*, 117(15):10291–10318, 2017. PMID: 28671815.

[151] Nicholas E. Jackson, Brett M. Savoie, Kevin L. Kohlstedt, Monica Olvera de la Cruz, George C. Schatz, Lin X. Chen, and Mark A. Ratner. Controlling conformations of conjugated polymers and small molecules: The role of nonbonding interactions. *Journal of the American Chemical Society*, 135(28):10475–10483, 2013. PMID: 23800150.

[152] Karl J. Thorley and Iain McCulloch. Why are s–f and s–o non-covalent interactions stabilising? *J. Mater. Chem. C*, 6:12413–12421, 2018.

[153] Weifeng Zhang, Zupan Mao, Naihang Zheng, Jiabin Zou, Liping Wang, Congyuan Wei, Jianyao Huang, Dong Gao, and Gui Yu. Highly planar cross-conjugated alternating polymers with multiple conformational locks: synthesis, characterization and their field-effect properties. *J. Mater. Chem. C*, 4:9266–9275, 2016.

[154] Caroline De Leener, Emmanuelle Hennebicq, Juan-Carlos Sancho-Garcia, and David Beljonne. Modeling the dynamics of chromophores in conjugated polymers: The case of poly(2-methoxy-5-(2'-ethylhexyl)oxy 1,4-phenylene vinylene) (meh-ppv). *The Journal of Physical Chemistry B*, 113(5):1311–1322, 2009. PMID: 19143498.

[155] Joakim Kärnbratt, Mélina Gilbert, Johannes K. Sprafke, Harry L. Anderson, and Bo Albinsson. Self-assembly of linear porphyrin oligomers into well-defined aggregates. *The Journal of Physical Chemistry C*, 116(37):19630–19635, 2012.

[156] Carl Poelking, Kostas Daoulas, Alessandro Troisi, and Denis Andrienko. *Morphology and Charge Transport in P3HT: A Theorist's Perspective*, pages 139–180. Springer Berlin Heidelberg, Berlin, Heidelberg, 2014.

[157] Amar Chaalane, Djillali Mahi, and Ahmed Dkhissi. Structural and electronic properties of doped oligothiophenes in the presence of p-toluenesulfonate acids. *Theoretical Chemistry Accounts*, 134(5):66, Apr 2015.

[158] Takakazu Yamamoto, Atsushi Morita, Yuichi Miyazaki, Tsukasa Maruyama, Hiroshi Wakayama, Zhen Hua Zhou, Yoshiyuki Nakamura, Takaki Kanbara, Shintaro Sasaki, and Kenji Kubota. Preparation of π-conjugated poly(thiophene-2,5-diyl), poly(p-phenylene), and related polymers using zerovalent nickel complexes. linear structure and properties of the π-conjugated polymers. *Macromolecules*, 25(4):1214–1223, 1992.

5 Publications

The following publications are the basis for this thesis. Firstly, the authors contribution will be briefly described for each publication, after which they are reprinted in full text including their supporting information.

Authors contribution

Elucidating Aggregation Pathways in the Donor-Acceptor Type Molecules p-DTS(FBTTh$_2$)$_2$ and p-SIDT(FBTTh$_2$)$_2$

This publication is published in *the Journal of Physical Chemistry B* 2018, 122, 39, 9191-9201

The authors are: <u>Axel Bourdick</u>, Markus Reichenberger, Anna Stradomska, Guillermo C. Bazan, Thuc-Quyen Nguyen, Anna Köhler and Stephan Gekle

This publication is based on the experimental work of Markus Reichenberger, who was responsible for measuring and interpreting the experimental results. I built models of the molecules with the help of DFT calculations performed by Anna Stradomska. I performed all MD simulations and made the figures related to them. I investigated the systems under varying parameters, like temperature, different solvents or the presence of side-chains. I investigated the interaction of the molecules with the solvent and the individual building blocks separately. With the help of my simulation results we were able to interpret the experimental data and paint a coherent picture of the underlying mechanisms of the aggregation process and explain the difference between the two molecules T1 and H1. I wrote large parts of the text of this publication. I was involved in frequent discussions with the coauthors. Within the scope of this publication I visited Anna Stradomska in Glasgow on a two week research trip, during which we worked together on this system and were able to gain valuable insights into the aggregation behavior. Anna Köhler and Stephan Gekle supervised this project.

What is the role of planarity and torsional freedom for aggregation in a π-conjugated donor-acceptor model oligomer?

The results of this work are in its final draft phase. We plan to submit this paper to the *Journal of Materials Chemistry*.

The authors are: Stefan Wedler, <u>Axel Bourdick</u>, Stavros Athanasopoulos, Stephan Gekle, Fabian Panzer, Guillermo C. Bazan, Thuc-Quyen Nguyen, Anna Köhler

This publication is based on the experimental work of Stefan Wedler who is the lead author. The experiments were performed by Stefan Wedler who also interpreted the results. I performed DFT simulations in order to build models used in the MD simulations. I performed all MD simulations. I performed free energy calculations with umbrella sampling and metadynamics, for different temperatures and solvents. I investigated models of the molecules as they are, without side-chains, and forced planarized. I had the idea to force TT into a planar configuration and look at the change in aggregation behavior. The DFT and TD-DFT calculations used for the interpretation of the results were conceptualized and performed by me and Stavros Athanasopoulos in close collaboration. In frequent discussions with Anna Köhler and Stefan Wedler we together worked on solutions to upcoming problems. I wrote the for the MD simulation relevant parts of the manuscript and the SI. Anna Köhler and Stephan Gekle supervised this project.

Directing the Aggregation of Native Polythiophene during in Situ Polymerization

This publication is published in *ACS Omega* 2018, 3, 6, 6388-6394

The authors are: Jenny Lebert, Eva M. Kratzer, <u>Axel Bourdick</u>, Mihael Coric, Stephan Gekle and Eva M. Herzig

This publication is based on the experimental work of Jenny Lebert and Eva Herzig. It was suspected that polythiophene exists in two different crystal packings in dependence of the processing route. Eva Herzig asked me to participate in this project in order to support the interpretation of a lamellar and a herringbone structure with simulations. It was my task to find out how I can do that with MD simulations. I built models of polythiophene chains with different length with the help of DFT simulations. I tried various simulation approaches. It turned out, that the suspected structures can be reproduced by the simulations of crystal structures with different lattice parameters between them, which agrees with the experimental results. I wrote the parts of the manuscript and the SI, which deal with the simulations.

5.1 Elucidating Aggregation Pathways in the Donor-Acceptor Type Molecules p-DTS(FBTTh$_2$)$_2$ and p-SIDT(FBTTh$_2$)$_2$

Axel Bourdick, Markus Reichenberger, Anna Stradomska, Guillermo C. Bazan,
Thuc-Quyen Nguyen, Anna Köhler and Stephan Gekle

Elucidating Aggregation Pathways in the Donor−Acceptor Type Molecules p-DTS(FBTTh₂)₂ and p-SIDT(FBTTh₂)₂

Axel Bourdick,[†] Markus Reichenberger,[‡] Anna Stradomska,[§] Guillermo C. Bazan,[∥] Thuc-Quyen Nguyen,[∥] Anna Köhler,[‡,⊥] and Stephan Gekle[*,†]

[†]Biofluid Simulation and Modeling, Theoretische Physik VI, Universität Bayreuth, 95440 Bayreuth, Germany
[‡]Soft Matter Optoelectronics, Department of Physics, Universität Bayreuth, 95440 Bayreuth, Germany
[§]School of Chemistry, University of Glasgow, Glasgow G12 8QQ, United Kingdom
[∥]Center for Polymers and Organic Solids, Departments of Chemistry and Biochemistry and Materials, University of California in Santa Barbara, California 93106, United States
[⊥]Bayreuth Institute of Macromolecular Research (BIMF), Universität Bayreuth, 95440 Bayreuth, Germany

Ⓢ Supporting Information

ABSTRACT: We investigated the aggregation behavior of the donor−acceptor molecules p-DTS(FBTTh₂)₂ (T1) and p-SIDT(FBTTh₂)₂ (H1) in MTHF solutions. Using optical spectroscopy, we found that T1 forms aggregates in solution while H1 aggregates only when processed as a thin film, but not in solution. Free energy molecular dynamics (MD) simulations based on force fields derived from quantum-mechanical density functional theory fully reproduce this difference. Our simulations reveal that this difference is not due to the lengthy carbon side chains. Rather, the molecular symmetry of T1 allows for an aggregated state in which the central donor units are spatially well-separated while a similar configuration is sterically impossible for H1. As a consequence, any aggregation of H1 necessarily involves aggregation of the central donors which requires, as a first step, stripping the central donor of its protective MTHF solvation shell. This unfavorable process leads to a significant kinetic hindrance for aggregation and explains the strongly differing aggregation behavior of T1/H1 in MTHF despite their otherwise similar structures.
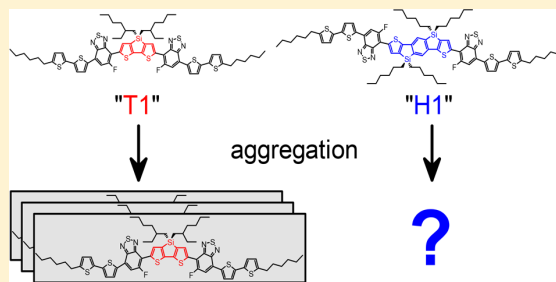
INTRODUCTION

Organic photovoltaics have become an important field of research in past decades. In the past, organic bulk heterojunction solar cells have been made mostly with a conjugated polymer as the donor and a fullerene derivative as the acceptor.[1] Recent research, however, could show promising results in the operation of organic solar cells in which soluble small molecules are used as the donor component.[2−9] High efficiencies of more than 14% are reported in ternary blends involving such molecules.[10,11] In comparison to the properties of conjugated polymers, the well-defined molecular weight, ease of purification and processing, and high degree of crystallinity in small molecules make them excellent candidates for potential industrial applications.[3,12−17]

One widely studied system which has proven to be particularly suitable for the design of organic solar cells is the soluble small molecule 7,7′-[4,4-bis(2-ethylhexyl)-4H-silolo[3,2-b:4,5-b′]dithiophene-2,6-diy-l]bis[6-fluoro-4-(5′-hexyl-[2,2′-bithiophene]-5-yl)benzo[c][1,2,5]thiadiazole] with the short name p-DTS(FBTTh₂)₂ and the colloquial denomination T1.[3] T1 is made of alternating donor (D) and acceptor (A) units, resulting in a D−A−D−A−D structure.

Such molecular designs have been shown to cover a broad spectral range and lead to high power conversion efficiencies in organic solar cells.[18−23] In addition to the spectral absorption range of the material, the properties of an organic device depend crucially on the processing conditions and the resulting film morphology.[8,24] Recently, it has been shown that T1 strongly aggregates in solution and can form a crystalline film by spin-coating.[8,25−28] Besides T1, the soluble donor−acceptor type small molecule benzo[1,2-b:4,5-b]bis(4,4′-dihexyl-4H-silolo[3,2-b]-thiophene-2,2′-diyl)bis(6-fluoro-4-(5′-hexyl-[2,2′-bithio-phene]-5-yl)benzo[c][1,2,5]thiadiazole with the short name p-SIDT(FBTTh₂)₂, or H1, was designed.[9,29] H1 exhibits an even wider band gap and can be used to manufacture bulk heterojunction solar cells with a higher open circuit voltage (0.91 V) compared to that of T1.[9] In contrast to T1, a film of H1 is typically quenched into an amorphous state so that a solvent additive is needed to

promote the crystallization.[28] Interestingly, the aggregation behavior of H1 in solution has not been studied to date.

In this work, we use absorption and emission spectroscopy in combination with molecular dynamics (MD) simulations and time-dependent density functional theory (TD-DFT) calculations to investigate the aggregation processes of T1 and H1 in solution and during spin-coating of a thin film. We find that H1 exhibits a significantly different aggregation behavior than the previously studied T1. T1 builds aggregates in solution, whereas optical experiments demonstrate the absence of H1 aggregates in solution. However, aggregates of H1 can be observed in a spin-cast film, especially when promoted by using a solvent additive. We conduct MD simulations based on DFT-derived force fields which are able to reproduce the experimentally found (non)aggregation of T1 (H1) in solution. Free energy surfaces derived from the MD simulations show that T1 can aggregate in different geometrical conformations and that aggregation of H1 is in principle possible, but appears to be kinetically hindered in solution. Interestingly, this behavior persists even when completely removing the carbon side chains. By investigating the energetic properties of the individual building blocks during the stacking process, we present evidence that the different aggregation behavior can be traced back to a kinetic hindrance of aggregation by solvent molecules (as recently found also for a perylene-based system[30]) surrounding the central donor units: While for T1 there exists an aggregated configuration in which these solvent shells can remain largely intact, aggregation in H1 always requires removal of the shells, thus explaining its much lower tendency of aggregation.

■ EXPERIMENTAL METHODS

Sample Preparation. 7,7′-[4,4-Bis(2-ethylhexyl)-4*H*-silolo[3,2-*b*:4,5-*b*′]dithiophene-2,6-diyl]bis[6-fluoro-4-(5′-hexyl-[2,2′-bithiophene]-5-yl)benzo[*c*][1,2,5]thiadiazole], i.e., T1, was prepared as reported in ref 31, and benzo[1,2-b:4,5-b]bis(4,4′-dihexyl-4*H*-silolo[3,2-*b*]thiophene-2,2′-diyl)bis(6-fluoro-4-(5′-hexyl-[2,2′-bithiophene]-5-yl)-benzo[*c*][1,2,5]-thiadiazole, i.e., H1, as reported in ref 9, respectively. For measurements taken in solution, we prepared (i) 2-methyltetrahydrofuran (MTHF) solutions at a concentration of 1.6×10^{-4} M (0.2 g/L) for T1 and 3.5×10^{-4} M (0.5 g/L) for H1, (ii) MTHF solutions at a concentration of 4.1×10^{-5} M for T1 and 7.0×10^{-6} M for H1, and (iii) hexane solutions at 1.0×10^{-4} M for T1 and 8.4×10^{-5} M for H1. For spin-coating thin films, solutions were made out of chlorobenzene (CB) at a concentration of 6.6×10^{-3} M (8 g/L) for T1 and 5.6×10^{-3} M (8 g/L) for H1. In general, the solutions were prepared by stirring for several hours at around 50 °C, to completely dissolve the material, except for the hexane solutions, where we first dissolved the molecules in a very small amount of MTHF (1% of the total final solution) before adding hexane. We measured these solutions always immediately after preparation, where all the material seemed to be dissolved and the solution was clear. For spectroscopic measurements, solutions were filled into a 1 mm fused silica cuvette. Films were prepared on Spectrosil B quartz substrates by spin-coating out of a 80 °C hot solution at 800 rpm for 60 s or, for in situ time-resolved UV−vis absorption spectroscopy, by spin-coating a solution at about 300 rpm for 60 s at 275 K.

Absorption and Emission Measurements. Temperature-dependent absorption and photoluminescence (PL) measurements in MTHF solutions and films, in a temperature range between 400 and 5 K, were carried out with a home-built experimental setup consisting of a temperature controlled continuous flow helium cryostat from Oxford Instruments, a xenon lamp as light source for absorption measurements, two correlated monochromators (one before and one after the sample), a continuous-wave diode laser from Coherent at 405 nm (3.06 eV) for photoluminescence measurements, and a silicon diode connected to a lock-in-amplifier as detection unit. The emission spectra were corrected for the transmission of the setup. Absorption and emission spectra were recorded successively at the same temperature and sample spot. The sample cooling was done in steps with a waiting time of 20 min after each temperature was reached. The PL and absorption spectra are corrected for changes in absorption or scattering, respectively, upon lowering the temperature.[25] For absorption and emission measurements in hexane solution at room temperature, a Cary 5000 UV−vis spectrometer from Varian and a FP-8600 spectral photometer from Jasco were utilized. For emission measurements, the samples were excited at 3.06 eV (405 nm) photon energy. We obtained absorption spectra taken during spin-casting in air using a home-built setup, which consists of a white light LED as light source inside a spin-coater and an attached detection unit (a charge-coupled device camera from Andor-Solis in kinetic mode with a fiber-coupled MS125 spectrograph from Oriel Instruments in front) that takes one picture every 60 ms.

Quantum Chemical Calculations. Quantum chemical calculations were carried out analogous to ref 25. Ground state geometry optimization was performed using density functional theory (DFT), while the vertical excitations and the optimization of the geometry of the first excited state were performed using time-dependent density functional theory (TD-DFT). All calculations were performed with the Gaussian09 revision D.01 program.[32] The long-range corrected functional CAM-B3LYP[33] was used, together with the 6-31G** basis set, as the previous studies demonstrated that it accurately describes properties of similar molecules.[26,34] In all calculations the alkyl chains were replaced by methyl groups. No symmetry constraints were imposed on the ground state nor on the excited state geometry. Influence of the solvent (tetrahydrofuran) was modeled using a polarizable continuum media model, using the integral equation formalism (IEFPCM). For geometry optimizations, the equilibrium solvation was used, while for the vertical excitations from the ground state a state-specific nonequilibrium solvation was used, where the slow (rotational) component of the solvent response was calculated for the ground state, and only the fast (electronic) contribution was calculated for the excited state.[35,36] The exact details of how the models used in this study were obtained can be found in the Supporting Information.

Molecular Dynamics Simulations. Molecular dynamics simulations were performed with Gromacs[37] using the Gromos 53a6 force field.[38] The structure files of T1 and H1 were created with JME[39] and Avogadro.[40] On this basis, a first set of force field files was calculated using the *Automated Force Field Topology Builder and Repository* (ATB)[41] for T1[42] and H1[43] to get a template-based model of the nonbonded interactions. Charges and potential energy surfaces (PES) of the dihedrals were then taken from quantum chemical calculations (without side chains) and incorporated into the force field models as detailed in the Supporting Information. Force fields for the full molecules including side chains were built using data from the

The Journal of Physical Chemistry B Article
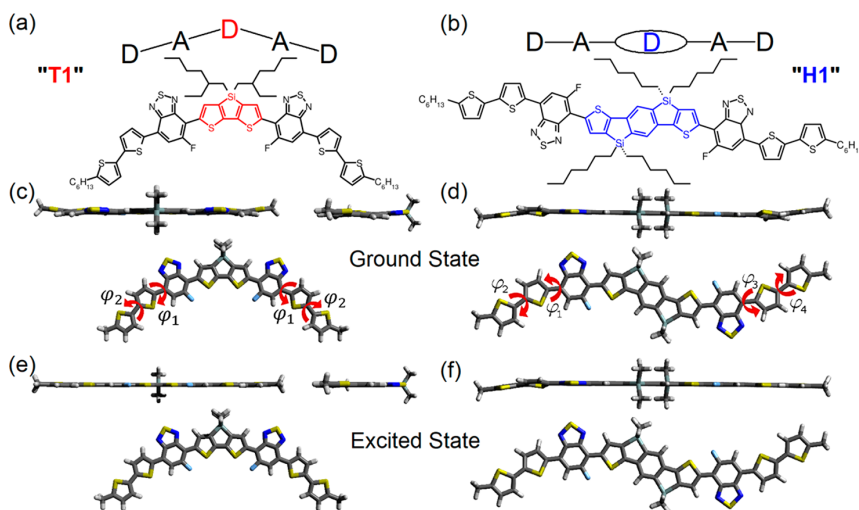
Figure 1. Structures of the molecules p-DTS(FBTTh$_2$)$_2$ (T1, on the left) and p-SIDT(FBTTh$_2$)$_2$ (H1, on the right): (a, b) schematic chemical monomer structures and the donor−acceptor tandem structure and (c−f) quantum chemical calculations for the molecules in THF solution. In detail, (c, d) ground state geometry, with $\varphi_1 = 11.9°$ and $\varphi_2 = 17.5°$ for T1 and $\varphi_1 = \varphi_3 = 11.6°$ and $\varphi_2 = \varphi_4 = 17.4°$ for H1, as well as (e, f) relaxed first excited state geometry, with $\varphi_1 = 0.4°$ and $\varphi_2 = 3.1°$ for T1, and $\varphi_1 = 10.7°$, $\varphi_2 = 17.3°$, $\varphi_3 = 0.1°$, and $\varphi_4 = 0.0°$ for H1, in side and top views. Parts of the graphics in parts c and e are reprinted with permission from ref 25. Copyright 2016 American Chemical Society.

ATB database for the side chains and stitching them together with the main part. The charges at the boundary were adjusted to ensure a vanishing net charge. The force field and structure files for the solvent MTHF were taken from the ATB Database.[44] For the simulations, all-atom force field topologies were used, and the visual analysis of the molecular structure and trajectories was carried out with VMD.[45]

Umbrella sampling[46] was used for the free energy calculations. The systems contained two solute molecules in a rectangular box solvated in MTHF. Between 1000 and 1700 solvent molecules were used. The distance between the center of mass of the solute molecules was chosen as the reaction coordinate. Configurations along this pathway were obtained with the Gromacs pull code. In all cases, we started with a random configuration at high distances, nearly half of the box length, and then squeezed the molecules together while cutting out snapshots of the sampling at given distances to generate the starting configurations used for umbrella sampling. After equilibration of the umbrella windows, the simulations were conducted as NPT ensembles. The spring constants used can be found in the Supporting Information. The free energy was calculated with the *Weighted Histogram Analysis Method,*[47] which is implemented in Gromacs as *gmx wham*. We used a typical simulation time of 80 ns per umbrella window and between 30 and 60 windows with a spacing between 0.3 and 0.6 nm. For the model of T1 with side chains we sampled the reaction coordinate with 17 simulations, each time using a different starting configuration, which were then combined to a resulting free energy representing the whole phase space. For the other cases (T1 without side chains, H1 with and without side chains) we used 12 different simulations. Further details are given in the Supporting Information. Calculations were performed locally and on the JURECA supercomputer of the Jülich Supercomputing Centre.[48] For clarity of presentation and in order to have a constant reference point at infinity, in all free energy data the ideal contribution $2kT \ln(r)$, which is simply due to an increase in available volume[49] and is identical for all molecules, has been removed.

■ RESULTS AND DISCUSSION

Figure 1 shows the chemical structures and quantum chemical calculations in tetrahydrofuran (THF) solution for the donor−acceptor type molecules T1 and H1. H1 has a longer central donor unit and more side chains compared to T1 (see colored structures in Figure 1a,b). Quantum chemical calculations for the donor−acceptor type molecules in tetrahydrofuran (THF) solution show that the ground state geometry of T1 is quite planar, without torsion between the central dithienosilole (DTS) donor and the fluorobenzothiadiazole acceptor. A small torsion angle φ_1 of about 12° exists between the fluorobenzothiadiazole acceptor and the dithiophene donor, and a torsion angle φ_2 of about 18° is observed between the two thiophenes (Figure 1c).[25] The ground state geometry of H1 is also quite planar without torsion between the central silaindacenodithiophene (SIDT) donor and the fluorobenzothiadiazole acceptor. The torsion angles φ_1 and φ_3 between the fluorobenzothiadiazole acceptor and the dithiophene donor on each side are about 12°. The torsion angles φ_2 and φ_4 between the two thiophenes on each side are about 17° (Figure 1d). The relaxed excited state geometry of T1 in THF is calculated to be entirely flat (Figure 1e)[25] and so is the relaxed excited state geometry of H1 in THF, except on one side. There, the torsion angles φ_1 between the fluorobenzothiadiazole acceptor and the dithiophene donor and φ_2 between the two thiophenes remain about the same as in the ground state geometry (Figure 1f). Here we note that it is surprising that the relaxed excited state geometry of H1 is asymmetric. As the DFT calculations show, the geometry of the excited molecules does not change significantly as compared to their ground state. On the basis of these observations, the force fields for the MD simulations were built to model the ground state (see Experimental Methods section).

The evolution of the absorption and emission spectra upon cooling a MTHF solution of T1 (Figure 2a) at two different concentrations, 1.6×10^{-4} and 4.1×10^{-5} M, is discussed in detail in ref 25. We briefly summarize the main findings in

55
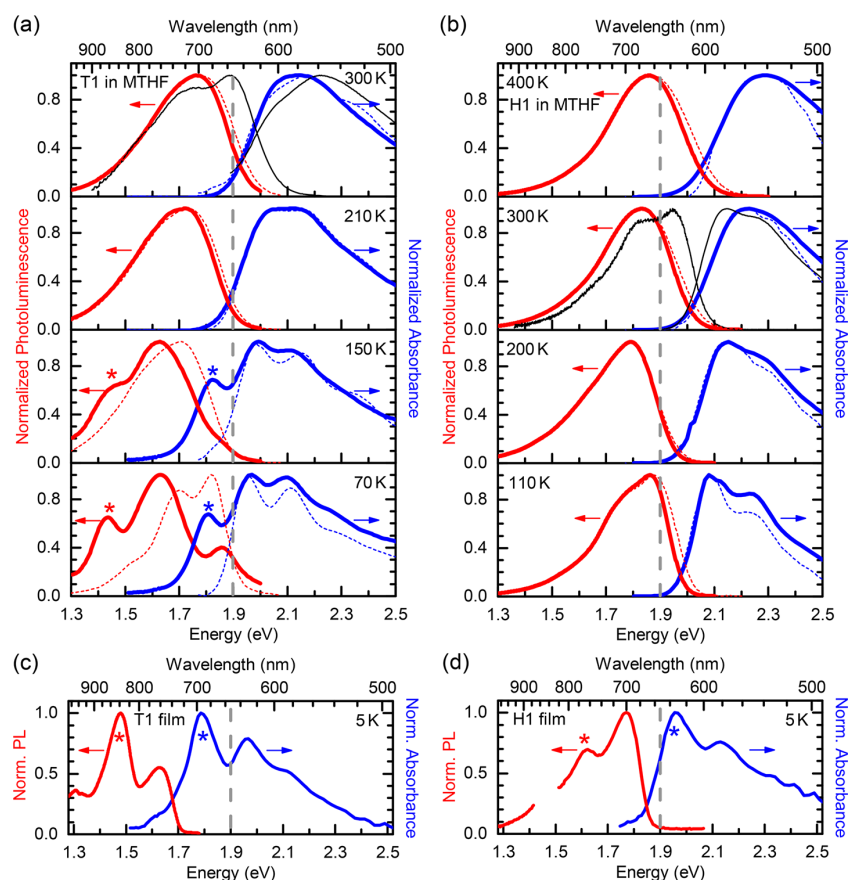
Figure 2. Normalized photoluminescence (red lines) and absorption (blue lines) spectra of (a, c) T1 and (b, d) H1, taken in (a, b) an MTHF solution and (c, d) in the thin film, spin-cast from a CB solution, at different temperatures. In parts a and b, the solid lines belong to a more concentrated solution ($c = 1.6 \times 10^{-4}$ M for T1 and $c = 3.5 \times 10^{-4}$ M for H1), and the dashed lines belong to a more dilute solution ($c = 4.1 \times 10^{-5}$ M for T1 and $c = 7.0 \times 10^{-6}$ M for H1). At 300 K, the spectra taken in hexane solution are also indicated (black lines). The vertical gray dashed lines at 1.9 eV are a guide to the eye. The red and blue stars highlight spectral features of aggregates. Part of the graphic in part a is reprinted with permission from ref 25. Copyright 2016 American Chemical Society.

order to allow a clear comparison with H1 below: (i) Upon cooling, the absorption spectra show a bathochromic shift and a more resolved vibronic structure. This is attributed to a gradual freezing out of the rotational dynamics of the molecules. (ii) The emission spectra lack vibrational structure. This is attributed to interactions between the excited T1 and the moderately polar solvent MTHF that stabilizes emission from a charge-transfer state. (iii) In a solution of the nonpolar solvent hexane at room temperature, the emission shows vibrational structure and is not shifted to the red spectral range, since the interactions between the solute and the solvent molecules do not occur (thin black lines in Figure 2a). (iv) Below the glass transition temperature of MTHF at 137 K, the matrix of solvent molecules is frozen. As a result, the emission spectrum shifts to an energetic position comparable to the hexane solution. Findings i−iv apply for both concentrations investigated. (v) In the more concentrated MTHF solution of T1 (thick solid lines in Figure 2a), a disorder−order transition sets in at temperatures lower than 205 K, so that aggregates of T1 form that coexist with the dissolved monomers. As a result, emission from aggregates superimposes on the emission from monomers in the more concentrated MTHF solution of T1. The spectral features due to the aggregates are indicated by

stars. Particularly evident are an additional absorption peak centered at about 1.8 eV and an additional shoulder in emission near 1.4 eV.

Figure 2b shows the temperature-dependent photoluminescence and absorption spectra of H1 in MTHF solution of two different concentrations, 3.5×10^{-4} and 7.0×10^{-6} M. Comparison of the more dilute solution of H1 to the more dilute solution of T1 shows the same spectral behavior which is solely due to monomers, as described in detail for T1 in ref 25. While for T1, the absorption and emission spectra at the two concentrations coincide above the critical temperature of 205 K, and additional features appear due to the formation of ordered, aggregated structures below 205 K, this is not the case for H1. H1 in MTHF solution shows virtually the same absorption and emission spectra at the higher concentration as at the lower concentration. From this we infer that H1, in contrast to T1, does not form ordered structures ("aggregates") in solution, even at high concentration and low temperature. The absence of aggregates is further confirmed by site-selective measurements of H1 in the more concentrated solution at different temperatures (see Figure S1 in the Supporting Information).
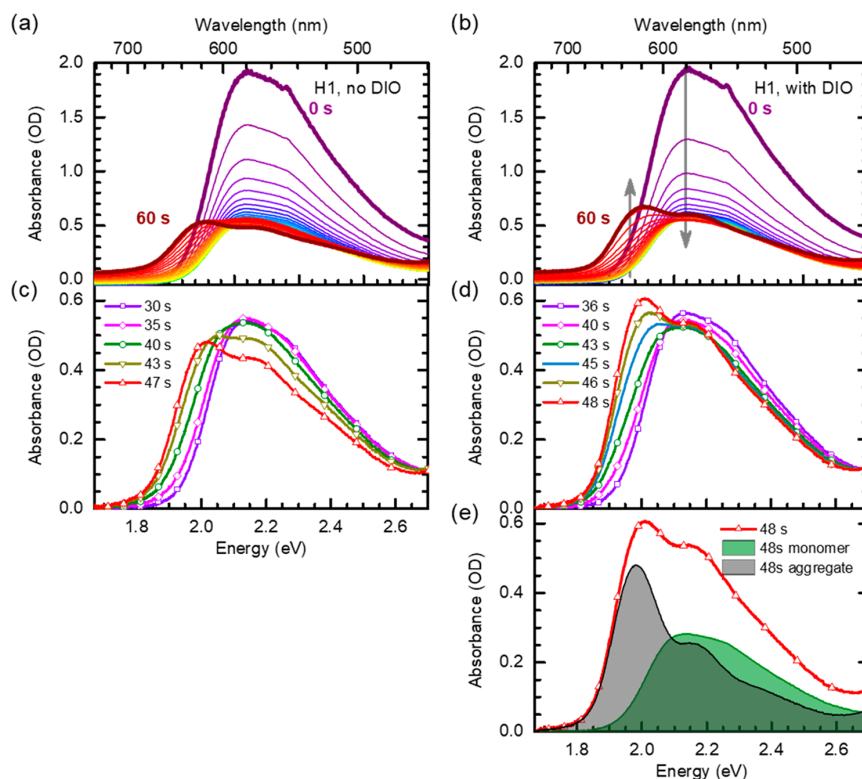
Figure 3. Absorption spectra of H1 taken every 1.16 s from 0 to 60 s during spin-coating a chlorobenzene solution (a) without and (b) with 0.4% of DIO at 275 K. A magnification of the data in part a in the time range between 30 and 47 s is shown in part c, and a magnification of the data in part b between 36 and 48 s is shown in part d, set to zero at 1.65 eV to account for scattering. The gray arrows indicate the evolution of the absorption spectra with time. (e) Absorption spectrum of an H1 film with DIO at 48 s, taken from part b, separated into contributions attributed to monomers and aggregates.

We next focus on studying aggregation of T1/H1 in thin films produced by spin-coating (Figure 2c,d). A thin film of T1 at 5 K shows absorption and emission spectra that are dominated by the transitions on the ordered, electronically interacting structures that we refer to as "aggregates".[25] This is evident by the bathochromic shift of the well-structured thin film spectra compared to the spectra in the more dilute MTHF solutions, as well as by the coincidence of the thin film spectral features with the aggregate spectral features in the more concentrated solution, as indicated by the stars. Similar to T1, some structure and a bathochromic shift compared to the solution spectra are also observed in the thin film spectra of H1 at 5 K (Figure 2d). This suggests that H1 may form aggregates in a thin film, yet not in a solution. In fact, ordered structures of H1 have previously been reported in films of H1, whereas attempts to obtain single crystals out of solution have been unsuccessful.[9,28]

To address the formation of aggregates in thin films, we investigate in Figure 3 the spectral changes during film formation by time-resolved in situ UV−vis absorption measurements. Figure 3a shows the absorption spectra of H1 taken at different times during spin-coating from an 8 g/L chlorobenzene solution at 275 K without an additive, and Figure 3b shows the absorption spectra with 0.4% diiodooctane (DIO). The spectral changes we observe in Figure 3a follow the pattern seen previously during in situ absorption measurements.[24,50] Initially, we observe a broad

spectrum centered at 2.15 eV that, by comparison with Figure 2b, can be assigned to the disordered, nonaggregated molecules. The optical density of this absorption reduces during the first ∼30 s while the shape remains unchanged. We attribute the reduction of absorption to material loss. The transformation from a "liquid" to a "solid" film takes place between 30 and 47 s from the start of spin-coating and is detailed in Figure 3c. The absorption spectra continuously acquire more structure and seem to shift to lower energies upon solidification. From this data it is not clear if the bathochromic shift is due to dispersion, because the surrounding of the H1 molecules changes upon the transfer from the liquid solution to a solid film, or due to aggregation, where we would have a superposition of dispersion and resonance interaction between the H1 molecules. In particular, it is not possible to distinguish whether the entire spectrum shifts to the red spectral range while acquiring more resolution, or whether the peak at 2.15 eV reduces while a peak at 2.0 eV emerges.

This becomes clearer when comparing the absorption spectra in Figure 3a,c with the ones in Figures 3b,d, where a small amount of the high boiling point solvent additive DIO was added to the solution before spin-coating. Here, it is evident that the peak at 2.0 eV increases while the peak at 2.15 eV changes only a little. Moreover, there is an isosbestic point at about 2.1 eV, indicating a direct transformation from a disordered to an ordered conformation. Evidently, dimers or

57
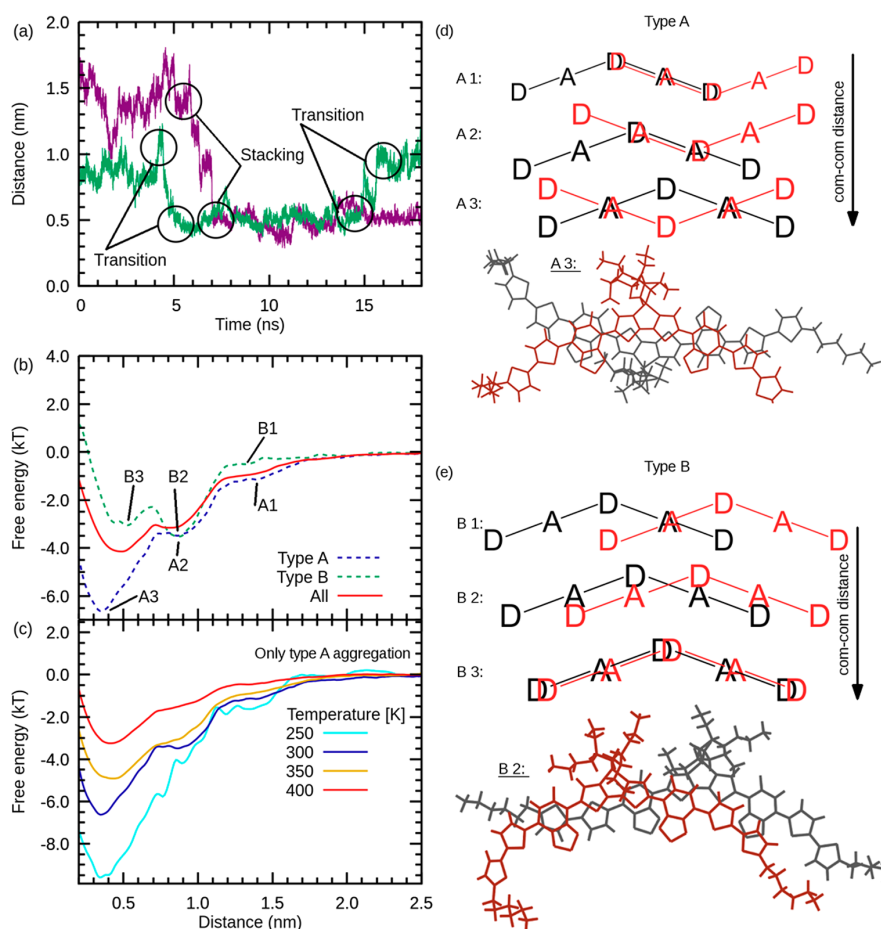
Figure 4. (a) Examples of aggregation simulations of two T1 molecules in an MTHF environment at room temperature, visualizing the aggregation process. (b) The free energy calculated by umbrella sampling as a function of the com−com distance. The solid line depicts the free energy of the whole configurational phase space. The dashed lines describe type A (blue) and type B (green) aggregation. (c) Free energy as a function of temperature for type A aggregation only. (d, e) Aggregated configurations corresponding to the local minima are shown schematically for type A (d) and type B (e) aggregation. For the ones with the lowest energy, a snapshot of the configuration is shown.

larger aggregates of H1 form. Evidently, the high-boiling-point additive DIO promotes the aggregation of H1, consistent with the observations of Love et al.[9] and Abdelsamie et al.[28] and with reports for polymers like poly(3-hexylthiophene-2,5-diyl) (P3HT).[24] The data of Figure 3d can be employed to differentiate between the absorption spectrum of the disordered H1 molecules and that of the ordered, interacting H1 molecules, as shown in Figure 3e. For this, the spectrum at 36 s is suitably normalized and subtracted from the spectrum at 48 s, and the resulting difference spectrum is assigned to the aggregate absorption. While there is a certain degree of freedom in how to normalize the monomer spectrum, so the ratio between the 0−0 and the 0−1 peak in the aggregate can vary (see Figure S2 in the Supporting Information), the resulting shape always indicates a more J-like than H-like character. Further details, in particular for different film preparation techniques, are given in the Supporting Information (Figure S3). These changes in experimental protocol do not significantly affect the resulting spectra.

Concluding the experimental part of this study, we have shown that in an MTHF solution of the molecule H1, in contrast to T1, a disorder−order phase transition cannot be induced and H1 does not aggregate even at high concentration and low temperature. In contrast, during film formation, when solvent molecules are removed and the concentration of H1 molecules is highly increased, aggregation is clearly observed.

In the following, we use molecular dynamics (MD) simulations based on DFT-derived force fields to investigate why the aggregation behavior of H1 differs so drastically from T1 in solution. In Figure 4a we show the center-of-mass distance between two T1 molecules in MTHF at room temperature as a function of time. Two representative simulations are shown; more data can be found in the Supporting Information. At first, the distance fluctuates randomly due to thermal noise until the two molecules start attracting each other and form an aggregate, which usually happens on the time scale of nanoseconds. At room temperature it is also possible for the formed stacks to break up again or change between different stacking distances.

To gain a better understanding of the stacking process we calculate the free energy as a function of the center-of-mass distance (averaging over 17 starting configurations as detailed in the Experimental Methods section). The result is shown in Figure 4b as the solid red line. Two clear minima at 0.5 and 0.8

Article

nm are observed which can also be seen in the time trajectories of Figure 4a. The two minima have a similar depth compared to the large distance value taken here as zero. A more detailed analysis of the aggregation process reveals that the system can undergo two distinct stacking pathways (see Figure S7a in the Supporting Information) which are shown in Figure 4b as dashed lines. We name both pathways in accordance with the nomenclature of the observed static crystal structures in ref 27. Type A reflects the case in which the molecules are oriented opposite to each other, whereas they are oriented in the same direction during a type B aggregation. Type A aggregation exhibits a global minimum at 0.50 nm with an energy difference of $6kT$. The pathway shows two additional minima, one at 0.70 nm and one at 1.40 nm. Type B aggregation shows minima at the same distances, but in contrast to type A aggregation the deepest minimum for this reaction pathway is the one at 0.70 nm. The overall energy gain from a type A aggregation is larger than from a type B aggregation.

We proceed to investigate the temperature dependence of the free energy for type A aggregation in T1, the result of which is displayed in Figure 4c. Here, we start sampling the reaction pathway with the system aggregated in a type A conformation and then pull the molecules apart to ensure a sampling of the type A pathway. We choose this pathway because it is energetically more favored at room temperature and a sampling of the whole phase space would be computationally very expensive, especially at lower temperatures. At higher temperatures, the minima become less pronounced with the global one showing an energy difference of $5kT$ at 350 K. At 400 K, the minima are shallower which means only limited aggregation is to be expected. At room temperature, a clear minimum is observed with an energy difference of about $6kT$. At the lowest investigated temperature of 250 K the energy gain hints at significant aggregation behavior. The increased tendency to form aggregates upon decreasing the temperature fully agrees with the experimental results. For all local minima, the corresponding structures of the aggregates are shown schematically in Figure 4d for type A and Figure 4e for type B aggregation together with a snapshot at the lowest energy for both pathways.

We also investigate the aggregation behavior of H1 with MD simulations. Three representative examples of aggregation simulations are depicted in Figure 5a. Two H1 molecules are placed in a box of MTHF, and the center-of-mass distance of the molecules is displayed as a function of time. No spontaneous aggregation is observed. Even when strongly increasing the simulation time, aggregation remains an extremely rare event as shown in Table S3 of the Supporting Information. The distance between the two H1 molecules does not drop below 1 nm. This behavior differs drastically from T1 (Figure 4a) which, in systems of similar size, typically aggregates within a few nanoseconds.

Figure 5b shows the free energy of H1 in MTHF at $T = 300$ K and $T = 250$ K as solid lines. In agreement with the experimental observations, the free energy for H1 does not exhibit a local minimum and thus reproduces the non-aggregation of H1 in solution. Similar to T1, the 300 K free energy curve of Figure 5b is obtained by combining 12 different starting configurations which are shown individually in Figure S7b of the Supporting Information. Interestingly, there is a rare pathway (observed for one out of the 12 starting configurations and shown as the dashed line in Figure 5b) exhibiting a pronounced minimum at 0.6 nm. This minimum
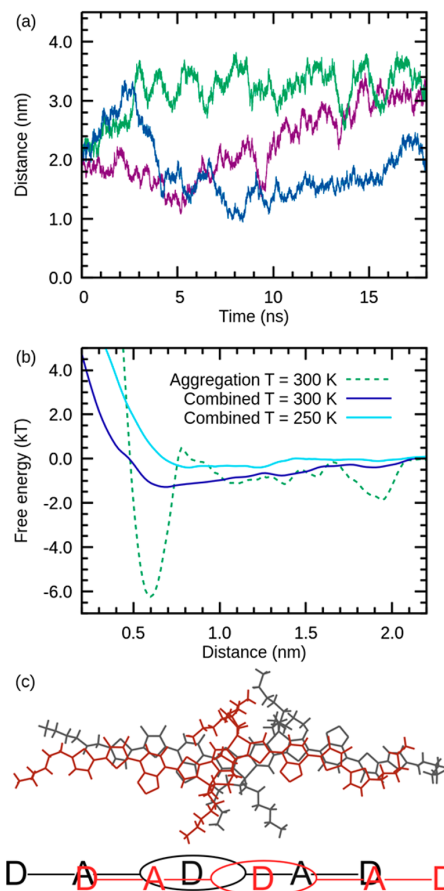

Figure 5. (a) Example of simulations of two H1 molecules in a MTHF environment at room temperature. (b) The free energy of the system as a function of the com−com distance. The solid lines represent averaged configurations at 300 K (blue) and 250 K (cyan). The dashed line is an example for the rare pathway in which aggregation can occur. (c) Snapshot and schematic illustration of the aggregated structure corresponding to the minimum in part b.

shows that aggregation of H1 is in principle possible and energetically favorable. The observed minimum, however, has a very small attraction range: beyond 0.8 nm the energy surface is rather flat (and may even exhibit a kinetic barrier), which means that the two molecules must be very close to one another to experience an attractive force. The observed aggregate of H1 in MTHF is shown schematically and by a snapshot in Figure 5c: The molecules have to be aligned in a very specific fashion where the central donor units are largely overlapping with one another. This structure is notably different than the minimum energy structure of T1 shown as A3 in Figure 4c. For T1, aggregation could be induced by lowering the temperature of the solution, both in experiment and in the simulation, while experimentally for H1 aggregation in solution is absent even at the lowest temperatures measured. To address this in our simulation, we calculate the free energy of H1 in solution at $T = 250$ K, which is also depicted in Figure 5b. For this, we combined 10 different starting configurations, all of which only showed a repulsive behavior. The resulting free energy curve for $T = 250$ K looks qualitatively similar to the one at $T = 300$ K, indicating that aggregation of H1 is
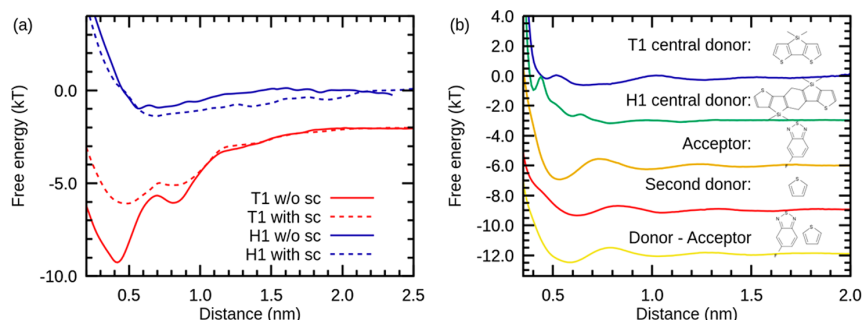
Figure 6. (a) Free energy of T1 and H1 with and without side chains at $T = 300$ K in MTHF. (b) The free energy of aggregation for the donor and acceptor units in MTHF at $T = 300$ K and the free energy of donor−acceptor aggregation. The dominating contribution to molecular aggregation does not stem from aggregation of the central donor units but from the aggregation of the lateral donor and acceptor units.
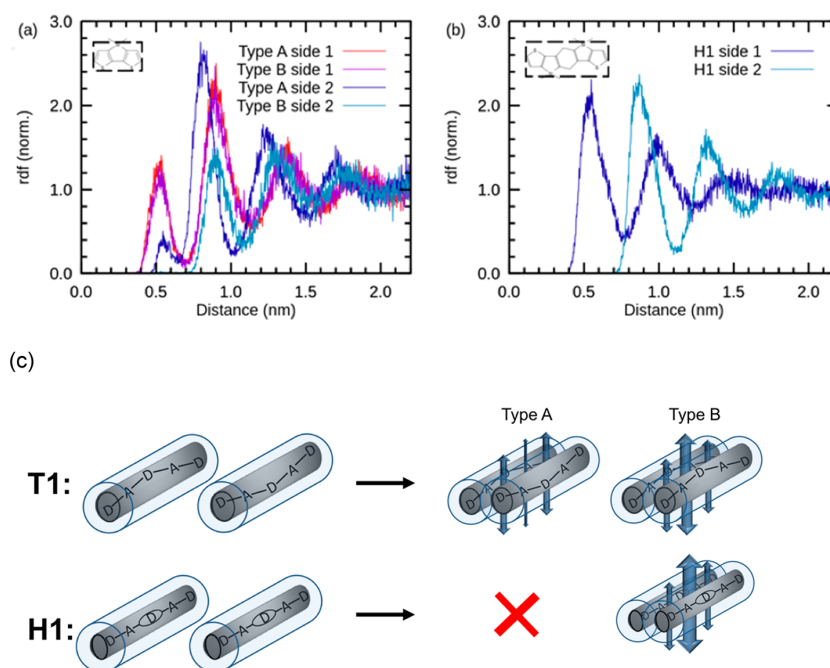
Figure 7. (a, b) Radial distribution functions of MTHF around the central donor units counting only MTHF molecules inside a tube perpendicular to the central donor units (insets, see main text). In part a, the rdfs for type A and type B aggregates of T1 are shown to be identical in the direction toward the bulk (side 1, red and violet curve), but strikingly different for the direction toward the aggregating partner (side 2, blue and cyan curve); for type B the first peak is completely absent and the second strongly reduced, thus confirming our notion that type B aggregation requires removal of the solvent shell. In part b, H1 aggregation is shown to be similar to type B aggregation of T1. Part c depicts a sketch of the aggregation process as summarized in the main text.

absent even at lower temperatures. Comparing the results for H1 in Figure 5b with the results for T1 in Figure 4b demonstrates that the computational models for H1 and T1 exhibit a different aggregation behavior between the two compounds in agreement with the experimental observations.

One reason for the different aggregation of T1 and H1 could be the hindrance of aggregation due to the presence of side chains. Both molecules have two hexyl groups attached to the outer donor units. However, T1 has only two 2-ethylhexyl groups attached to the central donor unit, whereas H1 possesses two pairs of hexyl groups located on opposing sides of the large central donor unit, resulting in a total of four carbon−hydrogen groups (Figure 1). The presence of the four side chains in H1 could hinder the aggregation because the

side chains can get in between the molecules and prevent an attraction. To investigate the influence of the side chains, we built models for T1 and H1 without side chains by replacing each of them with methyl groups. In Figure 6a, we calculate their aggregation free energy in MTHF at room temperature. For T1 without side chains, the global minimum becomes more pronounced which suggests that type A aggregation is stronger in this case. For H1, the free energy does not show a significant difference with or without side chains. More specifically, in contrast to what might be intuitively expected, removal of the side chains does not lead to improved aggregation behavior of H1. Thus, the side chains can be ruled out as the reason for the hindered aggregation of H1 in solution.

Article

We next consider the building blocks of the systems individually. Both molecules differ only in the central donor unit while the lateral acceptor and donor units on both sides are identical for T1 and H1. Figure 6b shows that for both molecules there is very little energy gained by stacking the central donor units themselves. This is due to the rather strong interaction between the central donor units and the structurally similar MTHF solvent molecules which serve as a protective shell. In vacuum, where solvent effects are absent, both T1 and H1 strongly aggregate as shown in Figure S8 in the Supporting Information which corroborates our finding. The lateral acceptor and donor units shown by the yellow and red curves in Figure 6b on the other hand do exhibit a certain aggregation behavior. We thus conclude that the dominant energy gain by aggregation of the whole molecule in solution must lie in the stacking of these lateral acceptor and donor units.

These observations suggest a possible explanation for the different aggregation of T1 and H1. The mirror symmetry of T1 allows two molecules to form a configuration in which mainly the acceptor and, to a lesser extent, the second donor units aggregate while the central donors remain spatially separated (A3 in Figure 4d). This configuration is both energetically favorable (due to the energy gain by stacking the lateral units) and relatively easy to reach as the protective solvent coating on the central donor remains largely intact. A configuration in which the central donor units overlap (type B aggregation in Figure 4e) is energetically still favorable, but is kinetically more difficult to reach due to the required removal of the solvent around the central donor. With this in mind, we proceed to consider the very rare aggregated state of H1 shown in Figure 5c. Here, the central donor units closely overlap representing a configuration qualitatively similar to the states B2 and B3 of T1. By arguments similar to those above, this configuration, while being energetically favorable in principle, is difficult to reach kinetically due to the required removal of solvent around the central donor. A configuration with aggregated lateral units and at the same time spatially separated central donor units corresponding to the easy-to-reach type A aggregation of T1 is not possible for H1. We speculate that this deficiency is the key element to explain the experimentally and computationally observed kinetic barrier in the aggregation of H1 molecules in solution.

To further corroborate this explanation, we proceed to study radial distribution functions (rdfs) of the MTHF solvent molecules surrounding the central donor units of T1 and H1. In order to get a clear picture of solvent stacking around the central donor, we consider rdfs only for those solvent molecules located in a rectangular tube with the planar central donor at its center and extending perpendicularly in both up and down directions. The insets in Figure 7a,b illustrate the cross section through such a tube containing the central donor unit of T1 and H1, respectively. For isolated monomers, both directions around the monomer possess an identical solvent shell, and thus, the rdfs for both sides are identical (not shown). Starting from a central donor in an aggregated state, however, one direction (here called side 1) points into the bulk while the second direction (side 2) points toward the aggregation partner. Thus, a difference in the two rdfs is expected.

We start by comparing type A and type B aggregation of T1 in Figure 7a. As is to be expected, the rdfs for side 1 extending into the bulk are structurally very similar for type A and type B aggregation (red and violet curves). For side 2 extending

toward the T1 aggregation partner, however, the picture changes drastically: in type A aggregation (blue curve) this rdf is structurally similar to the one in the bulk direction, except that the first peak is smaller. For type B aggregation (cyan curve) the first peak completely disappears, and even the second peak is strongly reduced. This difference confirms that type A aggregation happens with a largely preserved solvation shell while type B requires almost complete removal of the MTHF shell around the central donor of T1.

We next show the rdfs to side 1 and side 2 for aggregated H1 in Figure 7b. Indeed, as can be expected from the geometrical similarity between T1 type B and H1 aggregation (Figures 4e and 5c), we find that the rdfs are strongly asymmetric and that for side 2, pointing toward the aggregation partner, the first peak is completely absent. Accordingly, we conclude that H1 aggregation requires removal of the solvent shell.

Figure 7c summarizes the proposed mechanism behind the different aggregation of T1 and H1 in MTHF solvent. The molecular symmetry of T1 allows for two types of aggregates, one in which the central donors are spatially separated and thus retain their respective solvation shells (type A) and one in which the central donors stack and solvent needs to be squeezed out between them (type B). Due to the energetically favorable T1-MTHF interaction, formation of the latter is kinetically hindered. The molecular symmetry of H1 only allows for type B aggregation, and accordingly, aggregation of H1 suffers the same kinetic hindrance due to the requirement of squeezing out the solvent shell before aggregation.

■ CONCLUSION

We investigated the dynamical aggregation behavior of p-DTS(FBTTh₂)₂ (T1) and p-SIDT(FBTTh₂)₂ (H1) in solution and thin films using a combination of absorption and emission measurements and molecular dynamics simulations. The experimental results demonstrate a clear aggregation behavior of T1 in solution and film, whereas no aggregation can be observed for H1 in solution, even in highly concentrated solutions and at low temperature. Nevertheless, in a spin-cast thin film, aggregates of H1 appear and the aggregation behavior can further be promoted by the use of a high boiling point solvent additive.

To explain the experimental findings, we conducted MD simulations based on force fields derived from quantum chemical DFT simulations. The resulting free energy curves fully reproduce the experimentally observed contrast between aggregating T1 and nonaggregating H1 in solution. For T1, we identified two distinct aggregation pathways. Type A aggregation, in which molecules are aligned oppositely avoiding overlap of the central donor units, is energetically favored and easier to reach than type B aggregation, in which the central donors aggregate and are thus forced to remove their protective solvent coating. When lowering the temperature, the strength of the aggregation tendency increases, consistent with the experimental results. For H1, the free energy landscape does not exhibit local minima, thus reproducing the nonaggregating behavior of this molecule. Nevertheless, there is a rare pathway in which the free energy exhibits a minimum showing that aggregation is possible. The attraction range for this aggregate is, however, very small, and it can only occur if the molecules obey a rather special alignment. This is consistent with the experimental observation that H1 does not aggregate in solution but can do so when processed as a thin film.

By conducting simulations without side chains, we could rule out H1's bulky carbon side chains as a somewhat intuitive explanation for its nonaggregating behavior. Instead, we could identify molecular symmetry as the key difference between T1 and H1. Simulations revealed that the dominant favorable energetic contribution to molecular aggregation stems from stacking of the lateral acceptor and donor units, while stacking of the central donor units is kinetically hindered and much less favorable as it requires removing the solvent shell of strongly bound MTHF molecules. Accordingly, the mirror symmetric T1 preferably aggregates in a type A configuration where the acceptor units stack but the central donors remain spatially well-separated, each retaining its protective solvent shell. Such a configuration is impossible for the point symmetric geometry of H1 leaving as its only possibility a type B configuration in which the central donors show significant overlap. In solution, this configuration requires removal of solvent molecules and is thus difficult, though not impossible, to reach. In a spin-cast film where only few solvent molecules are present, however, the solvent-induced kinetic barrier disappears. Taken together, these observations explain our experimental findings that T1 aggregates easily in solution and film while H1 shows aggregation only in highly concentrated films, but not in solution.

■ ASSOCIATED CONTENT

Ⓢ Supporting Information

The Supporting Information is available free of charge on the ACS Publications website at DOI: 10.1021/acs.jpcb.8b06283.

> Additional characterization data including PL spectra; absorption spectra; simulation models, general parameters, aggregation simulations, and free energy simulations; aggregation free energies; and natural transition orbitals (PDF)

■ AUTHOR INFORMATION

Corresponding Author

*E-mail: stephan.gekle@uni-bayreuth.de.

ORCID Ⓞ

Guillermo C. Bazan: 0000-0002-2537-0310
Anna Köhler: 0000-0001-5029-4420
Stephan Gekle: 0000-0001-5597-1160

Notes

The authors declare no competing financial interest.

■ ACKNOWLEDGMENTS

■ REFERENCES

(1) Thompson, B. C.; Fréchet, J. M. Polymer-Fullerene Composite Solar Cells. *Angew. Chem., Int. Ed.* **2008**, *47*, 58−77.

(2) Walker, B.; Kim, C.; Nguyen, T.-Q. Small Molecule Solution-Processed Bulk Heterojunction Solar Cells. *Chem. Mater.* **2011**, *23*, 470−482.

(3) Sun, Y.; Welch, G. C.; Leong, W. L.; Takacs, C. J.; Bazan, G. C.; Heeger, A. J. Solution-Processed Small-Molecule Solar Cells with 6.7% Efficiency. *Nat. Mater.* **2012**, *11*, 44−48.

(4) Lin, Y.; Li, Y.; Zhan, X. Small Molecule Semiconductors for High-Efficiency Organic Photovoltaics. *Chem. Soc. Rev.* **2012**, *41*, 4245−4272.

(5) Mishra, A.; Bäuerle, P. Small Molecule Organic Semiconductors on the Move: Promises for Future Solar Energy Technology. *Angew. Chem., Int. Ed.* **2012**, *51*, 2020−2067.

(6) Huang, Y.; Kramer, E. J.; Heeger, A. J.; Bazan, G. C. Bulk Heterojunction Solar Cells: Morphology and Performance Relationships. *Chem. Rev.* **2014**, *114*, 7006−7043.

(7) Takacs, C. J.; Sun, Y. M.; Welch, G. C.; Perez, L. A.; Liu, X. F.; Wen, W.; Bazan, G. C.; Heeger, A. J. Solar Cell Efficiency, Self-Assembly, and Dipole-Dipole Interactions of Isomorphic Narrow-Band-Gap Molecules. *J. Am. Chem. Soc.* **2012**, *134*, 16597−16606.

(8) Love, J. A.; Proctor, C. M.; Liu, J.; Takacs, C. J.; Sharenko, A.; van der Poll, T. S.; Heeger, A. J.; Bazan, G. C.; Nguyen, T.-Q. Film Morphology of High Efficiency Solution-Processed Small-Molecule Solar Cells. *Adv. Funct. Mater.* **2013**, *23*, 5019−5026.

(9) Love, J. A.; Nagao, I.; Huang, Y.; Kuik, M.; Gupta, V.; Takacs, C. J.; Coughlin, J. E.; Qi, L.; van der Poll, T. S.; Kramer, E. J.; et al. Silaindacenodithiophene-Based Molecular Donor: Morphological Features and Use in the Fabrication of Compositionally Tolerant, High-Efficiency Bulk Heterojunction Solar Cells. *J. Am. Chem. Soc.* **2014**, *136*, 3597−3606.

(10) Zhang, J.; Zhang, Y.; Fang, J.; Lu, K.; Wang, Z.; Ma, W.; Wei, Z. Conjugated Polymer-Small Molecule Alloy Leads to High Efficient Ternary Organic Solar Cells. *J. Am. Chem. Soc.* **2015**, *137*, 8176−8183.

(11) Zhang, S.; Qin, Y.; Zhu, J.; Hou, J. Over 14% Efficiency in Polymer Solar Cells Enabled by a Chlorinated Polymer Donor. *Adv. Mater.* **2018**, *30*, 1800868.

(12) Walker, B.; Tamayo, A. B.; Dang, X. D.; Zalar, P.; Seo, J. H.; Garcia, A.; Tantiwiwat, M.; Nguyen, T.-Q. Nanoscale Phase Separation and High Photovoltaic Efficiency in Solution-Processed, Small-Molecule Bulk Heterojunction Solar Cells. *Adv. Funct. Mater.* **2009**, *19*, 3063−3069.

(13) Bürckstümmer, H.; Tulyakova, E. V.; Deppisch, M.; Lenze, M. R.; Kronenberg, N. M.; Gsanger, M.; Stolte, M.; Meerholz, K.; Würthner, F. Efficient Solution-Processed Bulk Heterojunction Solar Cells by Antiparallel Supramolecular Arrangement of Dipolar Donor-Acceptor Dyes. *Angew. Chem., Int. Ed.* **2011**, *50*, 11628−11632.

(14) Lee, O. P.; Yiu, A. T.; Beaujuge, P. M.; Woo, C. H.; Holcombe, T. W.; Millstone, J. E.; Douglas, J. D.; Chen, M. S.; Fréchet, J. M. J. Efficient Small Molecule Bulk Heterojunction Solar Cells with High Fill Factors via Pyrene-Directed Molecular Self-Assembly. *Adv. Mater.* **2011**, *23*, 5359−5363.

(15) Shang, H.; Fan, H.; Liu, Y.; Hu, W.; Li, Y.; Zhan, X. A Solution-Processable Star-Shaped Molecule for High-Performance Organic Solar Cells. *Adv. Mater.* **2011**, *23*, 1554−1557.

(16) Wei, G. D.; Wang, S. Y.; Sun, K.; Thompson, M. E.; Forrest, S. R. Solvent-Annealed Crystalline Squaraine: PC$_{70}$BM (1:6) Solar Cells. *Adv. Energy Mater.* **2011**, *1*, 184−187.

(17) Zhou, J. Y.; Wan, X. J.; Liu, Y. S.; Zuo, Y.; Li, Z.; He, G. R.; Long, G. K.; Ni, W.; Li, C. X.; Su, X. C.; et al. Small Molecules Based on Benzo[1,2-b:4,5-b′]dithiophene Unit for High-Performance Solution-Processed Organic Solar Cells. *J. Am. Chem. Soc.* **2012**, *134*, 16345−16351.

Article

(18) Kim, J. Y.; Lee, K.; Coates, N. E.; Moses, D.; Nguyen, T.-Q.; Dante, M.; Heeger, A. J. Efficient Tandem Polymer Solar Cells Fabricated by All-Solution Processing. *Science* **2007**, *317*, 222−225.

(19) You, J. B.; Dou, L. T.; Yoshimura, K.; Kato, T.; Ohya, K.; Moriarty, T.; Emery, K.; Chen, C. C.; Gao, J.; Li, G.; Yang, Y. A Polymer Tandem Solar Cell with 10.6% Power Conversion Efficiency. *Nat. Commun.* **2013**, *4*, 1446.

(20) Dennler, G.; Scharber, M. C.; Ameri, T.; Denk, P.; Forberich, K.; Waldauf, C.; Brabec, C. J. Design Rules for Donors in Bulk-Heterojunction Tandem Solar Cells - Towards 15% Energy-Conversion Efficiency. *Adv. Mater.* **2008**, *20*, 579−583.

(21) Dou, L. T.; You, J. B.; Yang, J.; Chen, C. C.; He, Y. J.; Murase, S.; Moriarty, T.; Emery, K.; Li, G.; Yang, Y. Tandem Polymer Solar Cells Featuring a Spectrally Matched Low-Bandgap Polymer. *Nat. Photonics* **2012**, *6*, 180−185.

(22) Li, W. W.; Furlan, A.; Hendriks, K. H.; Wienk, M. M.; Janssen, R. A. J. Efficient Tandem and Triple-Junction Polymer Solar Cells. *J. Am. Chem. Soc.* **2013**, *135*, 5529−5532.

(23) Hadipour, A.; de Boer, B.; Wildeman, J.; Kooistra, F. B.; Hummelen, J. C.; Turbiez, M. G. R.; Wienk, M. M.; Janssen, R. A. J.; Blom, P. W. M. Solution-Processed Organic Tandem Solar Cells. *Adv. Funct. Mater.* **2006**, *16*, 1897−1903.

(24) Reichenberger, M.; Baderschneider, S.; Kroh, D.; Grauf, S.; Köhler, J.; Hildner, R.; Köhler, A. Watching Paint Dry: The Impact of Diiodooctane on the Kinetics of Aggregate Formation in Thin Films of Poly(3-hexylthiophene). *Macromolecules* **2016**, *49*, 6420−6430.

(25) Reichenberger, M.; Love, J. A.; Rudnick, A.; Bagnich, S.; Panzer, F.; Stradomska, A.; Bazan, G. C.; Nguyen, T.-Q.; Köhler, A. The Effect of Intermolecular Interaction on Excited States in p-DTS(FBTTH₂)₂. *J. Chem. Phys.* **2016**, *144*, 074904.

(26) Coughlin, J. E.; Zhugayevych, A.; Bakus, R. C.; van der Poll, T. S.; Welch, G. C.; Teat, S. J.; Bazan, G. C.; Tretiak, S. A Combined Experimental and Theoretical Study of Conformational Preferences of Molecular Semiconductors. *J. Phys. Chem. C* **2014**, *118*, 15610−15623.

(27) van der Poll, T. S.; Zhugayevych, A.; Chertkov, E.; Bakus, R. C.; Coughlin, J. E.; Teat, S. J.; Bazan, G. C.; Tretiak, S. Polymorphism of Crystalline Molecular Donors for Solution-Processed Organic Photovoltaics. *J. Phys. Chem. Lett.* **2014**, *5*, 2700−2704.

(28) Abdelsamie, M.; Treat, N. D.; Zhao, K.; McDowell, C.; Burgers, M. A.; Li, R. P.; Smilgies, D. M.; Stingelin, N.; Bazan, G. C.; Amassian, A. Toward Additive-Free Small-Molecule Organic Solar Cells: Roles of the Donor Crystallization Pathway and Dynamics. *Adv. Mater.* **2015**, *27*, 7285−7292.

(29) Ran, N. A.; Roland, S.; Love, J. A.; Savikhin, V.; Takacs, C. J.; Fu, Y. T.; Li, H.; Coropceanu, V.; Liu, X. F.; Brédas, J. L.; et al. Impact of Interfacial Molecular Orientation on Radiative Recombination and Charge Generation Efficiency. *Nat. Commun.* **2017**, *8*, 79.

(30) Hollfelder, M.; Gekle, S. Dynamic Stacking Pathway of Perylene Dimers in Aromatic and Nonaromatic Solvents. *J. Phys. Chem. B* **2015**, *119*, 10216−10223.

(31) van der Poll, T. S.; Love, J. A.; Nguyen, T.-Q.; Bazan, G. C. Non-Basic High-Performance Molecules for Solution-Processed Organic Solar Cells. *Adv. Mater.* **2012**, *24*, 3646−3649.

(32) Frisch, M. J.; Trucks, G. W.; Schlegel, H. B.; Scuseria, G. E.; Robb, M. A.; Cheeseman, J. R.; Scalmani, G.; Barone, V.; Mennucci, B.; Petersson, G. A.; et al. *Gaussian 09*, Revision D.01; Gaussian, Inc.: Wallingford, CT, 2009.

(33) Yanai, T.; Tew, D. P.; Handy, N. C. A New Hybrid Exchange-Correlation Functional Using the Coulomb-Attenuating Method (CAM-B3LYP). *Chem. Phys. Lett.* **2004**, *393*, 51−57.

(34) Zhugayevych, A.; Postupna, O.; Bakus, R. C., II; Welch, G. C.; Bazan, G. C.; Tretiak, S. Ab Initio Study of a Molecular Crystal for Photovoltaics: Light Absorption, Exciton and Charge Carrier Transport. *J. Phys. Chem. C* **2013**, *117*, 4920−4930.

(35) Improta, R.; Barone, V.; Scalmani, G.; Frisch, M. J. A State-Specific Polarizable Continuum Model Time Dependent Density Functional Theory Method for Excited State Calculations in Solution. *J. Chem. Phys.* **2006**, *125*, 054103.

(36) Improta, R.; Scalmani, G.; Frisch, M. J.; Barone, V. Toward Effective and Reliable Fluorescence Energies in Solution by a New State Specific Polarizable Continuum Model Time Dependent Density Functional Theory Approach. *J. Chem. Phys.* **2007**, *127*, 074504.

(37) Hess, B.; Kutzner, C.; van der Spoel, D.; Lindahl, E. GROMACS 4: Algorithms for Highly Efficient, Load-Balanced, and Scalable Molecular Simulation. *J. Chem. Theory Comput.* **2008**, *4*, 435−447.

(38) Oostenbrink, C.; Villa, A.; Mark, A. E.; Van Gunsteren, W. F. A Biomolecular Force Field Based on the Free Enthalpy of Hydration and Solvation: The GROMOS Force-Field Parameter Sets 53A5 and 53A6. *J. Comput. Chem.* **2004**, *25*, 1656−1676.

(39) Ertl, P. Molecular Structure Input on the Web. *J. Cheminf.* **2010**, *2*, 1−9.

(40) Hanwell, M. D.; Curtis, D. E.; Lonie, D. C.; Vandermeersch, T.; Zurek, E.; Hutchison, G. R. Avogadro: An Advanced Semantic Chemical Editor, Visualization, and Analysis Platform. *J. Cheminf.* **2012**, *4*, 17−1.

(41) Malde, A. K.; Zuo, L.; Breeze, M.; Stroet, M.; Poger, D.; Nair, P. C.; Oostenbrink, C.; Mark, A. E. An Automated Force Field Topology Builder (ATB) and Repository: Version 1.0. *J. Chem. Theory Comput.* **2011**, *7*, 4026−4037.

(42) *ATB Database: p-DTS(FBTTh₂)₂ Structure and Toplogy Files.* https://atb.uq.edu.au/molecule.py?molid=30972 (accessed March 31, 2016).

(43) *ATB Database: p-SIDT(FBTTh₂)₂ Structure and Toplogy Files.* https://atb.uq.edu.au/molecule.py?molid=34613 (accessed October 25, 2016).

(44) *ATB Database: MTHF Structure and Topology Files.* https://atb.uq.edu.au/molecule.py?molid=879 (accessed September 12, 2015).

(45) Humphrey, W.; Dalke, A.; Schulten, K. VMD: Visual Molecular Dynamics. *J. Mol. Graphics* **1996**, *14*, 33−38.

(46) Kästner, J. Umbrella Sampling. *WIREs Comput. Mol. Sci.* **2011**, *1*, 932−942.

(47) Hub, J. S.; de Groot, B. L.; van der Spoel, D. g_wham - A Free Weighted Histogram Analysis Implementation Including Robust Error and Autocorrelation Estimates. *J. Chem. Theory Comput.* **2010**, *6*, 3713−3720.

(48) Krause, D. Jülich-Supercomputing-Centre JURECA: General-Purpose Supercomputer at Jülich Supercomputing Centre. *JLSRF* **2016**, *2*, A62.

(49) Sedlmeier, F.; von Hansen, Y.; Mengyu, L.; Horinek, D.; Netz, R. R. Water Dynamics at Interfaces and Solutes: Disentangling Free Energy and Diffusivity Contributions. *J. Stat. Phys.* **2011**, *145*, 240−252.

(50) Reichenberger, M.; Kroh, D.; Matrone, G. M. M.; Schötz, K.; Pröller, S.; Filonik, O.; Thordardottir, M. E.; Herzig, E.; Bässler, H.; Stingelin, N.; et al. Controlling Aggregate Formation in Conjugated Polymers by Spin-Coating Below the Critical Temperature of the Disorder-Order Transition. *J. Polym. Sci., Part B: Polym. Phys.* **2018**, *56*, 532−542.

Supporting Information to

Elucidating Aggregation Pathways in the Donor-Acceptor Type Molecules p-DTS(FBTTh$_2$)$_2$ and p-SIDT(FBTTh$_2$)$_2$

Axel Bourdick[1], Markus Reichenberger[2], Anna Stradomska[3], Guillermo C. Bazan[4], Thuc-Quyen Nguyen[4], Anna Köhler[2,5] and Stephan Gekle[1,*]

[1] Biofluid Simulation and Modeling, Theoretische Physik VI, Universität Bayreuth, 95440 Bayreuth (Germany)

[2] Soft Matter Optoelectronics, Department of Physics, Universität Bayreuth, 95440 Bayreuth (Germany)

[3] School of Chemistry, University of Glasgow, Glasgow G12 8QQ (United Kingdom)

[4] Departments of Chemistry and Biochemistry and Materials, Center for Polymers and Organic Solids, University of California in Santa Barbara, California 93106 (USA)

[5] Bayreuth Institute of Macromolecular Research (BIMF), Universität Bayreuth, 95440 Bayreuth (Germany)

[*] Corresponding Author: stephan.gekle@uni-bayreuth.de

Additional experimental results

Sample preparation

7,7-[4,4-bis(2-ethylhexyl)-4*H*-silolo[3,2-*b*:4,5-*b*′]dithiophene-2,6-diyl]bis[6-fluoro-4-(5′-hexyl-[2,2′-bithiophene]-5-yl)benzo[*c*][1,2,5]thiadiazole], p-DTS(FBTTh$_2$)$_2$ or "T1", was prepared as reported in ref.[1] and benzo[1,2-b:4,5-b]bis(4,4′-dihexyl-4H-silolo[3,2-b]thiophene-2,2′-diyl)bis(6-fluoro-4-(5′-hexyl-[2,2′-bithiophene]-5-yl)-benzo[c][1,2,5]thiadiazole, p-SIDT(FBTTh$_2$)$_2$ or "H1", as reported in ref.[2] respectively. For site-selective measurements, solutions of the two molecules were prepared in 2-methyl-tetrahydrofurane (MTHF) at concentrations of $1.6 \cdot 10^{-4}$ M (0.2 g/l) for T1 and $1.4 \cdot 10^{-4}$ M (0.2 g/l) for H1. Additionally we prepared chlorobenzene (CB) solutions at a concentration of $1.2 \cdot 10^{-4}$ M (0.15 g/l) for T1 and $1.1 \cdot 10^{-4}$ M (0.15 g/l) for H1. We stirred for several hours at around 50°C, to completely dissolve the material. For spin-coating thin films, solutions were made out of CB at a concentration of $6.6 \cdot 10^{-3}$ M (8 g/l) for T1 and $5.6 \cdot 10^{-3}$ M (8 g/l) for H1. Films were prepared as cast, with 0.4 percent by volume of 1,8-diiodooctan or annealed at 110°C for ten minutes. For spectroscopic measurements, solutions were filled into a 1 mm fused silica cuvette and films were prepared on Spectrosil B quartz substrates by spin-coating out of a 80°C hot solution at 800 rpm for 60 s.

Absorption and emission measurements

Steady-state absorption measurements of films and in CB solution at room temperature were carried out in a Cary 5000 UV/Vis spectrometer from Varian. Site-selective photoluminescence measurements with the sample in a temperature controlled continuous flow helium cryostat were carried out using the 355 nm pulsed emission from a Nd:YAG laser as input for a computer controlled UV/Vis optical parametric oscillator to obtain a tunable excitation pulse with a duration of 4-5 ns at 10 Hz. The detection system was a charge-coupled device camera from Andor coupled to a MS125 spectrograph.

S2

Results
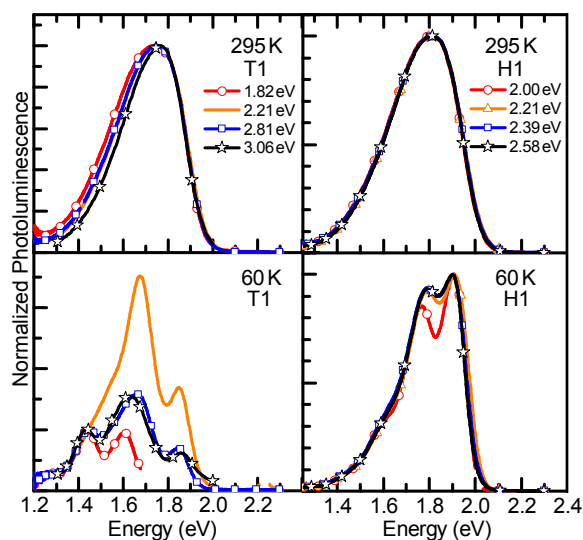
Figure S1: Normalized photoluminescence spectra of T1 (on the left, taken from ref. [3]) and H1 (on the right) for different excitation energies, taken in a 1.6·10^{-4} M MTHF solution of T1 and a 1.4·10^{-4} M MTHF solution of H1 at 295 K (top panels) and at 60 K (bottom panels).

Figure S1 shows normalized photoluminescence spectra of T1 and H1 in a MTHF solution obtained for excitation at different energies. At 295 K, for both T1 and H1, identical and broad emission spectra result, no matter at which energy between 1.82 eV and 3.06 eV we excite the solution. At 60 K, a T1 solution contains monomers and aggregates, so when exciting the T1 solution at different energies between 1.82 eV and 3.06 eV, we see emission from both monomers and aggregates. Exciting at 1.82 eV, where only aggregates of T1 absorb, we see emission only from aggregates of T1. The absorption spectrum of H1 at 60 K, compared to a H1 solution at 295 K, is shifted to lower energies and shows a vibrational structure. When we excite the solution at different energies between 2.00 eV and 2.58 eV, the emission spectra also show a vibronic structure and they are nearly identical. Only the emission spectrum at an excitation of 2.00 eV is more structured, which is due to the higher photoluminescence intensity because of the excitation near the absorption maximum. The site-selective photoluminescence spectra of H1 at 295 K and at 60 K are similar and no additional low energetic contribution rises, which would be characteristic for aggregates. This clearly

confirms the absence of any aggregate emission and thus of any aggregates of H1 in solution.
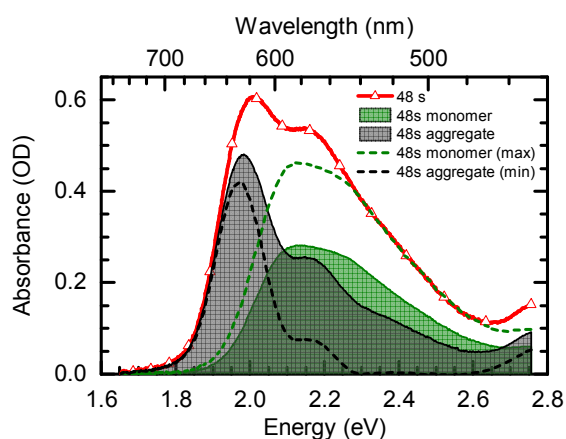
Figure S2: Absorption spectrum of an H1 film spun from CB solution with 0.4% of diiodooctane (DIO), taken at 48 s from the start of spin-coating (red line) and separated into contributions attributed to monomers (green solid line) and aggregates (black solid line) (like in Figure 3e in the main text). Here, we additionally normalized the monomer spectrum, which is the solution spectrum at 0 s, to the high energy tail of the 48 s spectrum, to obtain the maximum possible monomer contribution (dashed green line) and thus the minimum possible aggregate contribution (dashed black line). A comparison shows that there is a certain degree of freedom in how to normalize the monomer spectrum, so the ratio between the 0-0 and the 0-1 peak in the aggregate can vary.

In Figure S2, we show the absorption spectrum of an H1 film. There is a certain degree of freedom in how to normalize the monomer spectrum, due to which the ratio between the 0-0 and the 0-1 peak can vary.
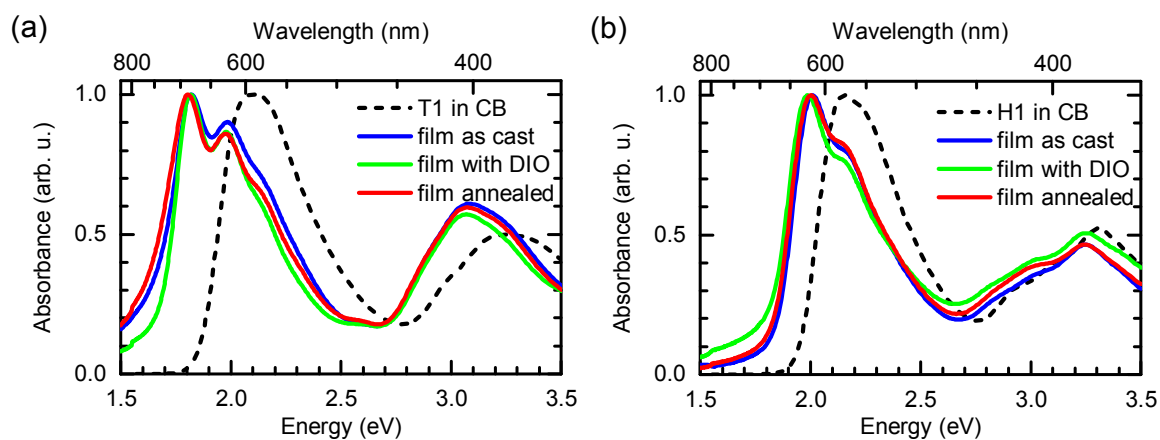
Figure S3: Absorption spectra (a) of T1 and (b) of H1 in CB solution (dashed black line), in a film as cast from CB solution (blue line), in a film spun from CB solution with 0.4% of DIO (green line) and in a film spun from CB which was thermally annealed at 110°C afterwards (red line). The spectra are normalized to one at their maximum.

In Figure S3 we compare the absorption spectra of T1 and of H1 in CB solution and in films of different preparation, i.e. as cast from CB solution, spun from CB solution with 0.4% of the high boiling point solvent additive diiodooctane (DIO) and spun from CB with thermal annealing afterwards. For both molecules the film spectra are shifted towards lower energies compared to the solution spectra. In the case of a CB solution, the absorption maxima of T1 shift from 1.81 eV to 2.10 eV by 300 meV and the absorption maxima of H1 shift from 2.00 eV to 2.15 eV by 150 meV. In the T1 films, the ratio between the first two absorption peaks at 1.81 eV and 1.98 eV increases with DIO and thermal annealing from 1.11 to 1.16, which is indicative for more ordering in the films. In the H1 films, the ratio between the first two absorption peaks at 2.00 eV and 2.15 eV increases with DIO from 1.24 to 1.31 and stays about the same after thermal annealing with 1.22, which is indicative for more ordering in the film at least upon adding DIO.

Methodical details for MD Simulations

Determination of partial charges

Tight convergence criteria were requested in geometry optimizations and an ultrafine integration grid was used. RESP charges were fitted using Antechamber (from Amber 14) based on Gaussian calculations. The charge distribution is shown in Figure S4, we used the ones calculated with the RESP method.

a) T1 charges

atom	MKL	RESP	atom	MKL	RESP
1 C	-0.019441	0.014304	41 C	-0.303759	-0.257341
2 S	-0.022428	-0.018558	42 F	-0.160978	-0.145482
3 C	0.085201	0.050550	43 C	0.247297	0.244779
4 C	0.013698	-0.051681	44 H	0.218137	0.209318
5 C	-0.432357	-0.355320	45 C	0.057935	0.086667
6 H	0.073810	0.081990	46 C	-0.149376	-0.166498
7 C	-0.205198	-0.156622	47 C	-0.225393	-0.168584
8 Si	1.032120	0.955472	48 C	0.166010	0.099334
9 C	0.085201	0.050550	49 S	-0.142237	-0.135516
10 C	-0.432357	-0.355320	50 C	-0.149376	-0.166498
11 S	-0.022428	-0.018558	51 C	-0.225393	-0.168584
12 C	-0.632719	-0.584144	52 C	0.166010	0.099334
13 C	-0.632719	-0.584144	53 S	-0.142237	-0.135516
14 C	0.013698	-0.051681	54 H	0.134887	0.127500
15 C	-0.019441	0.014304	55 H	0.189909	0.174720
16 H	0.073810	0.081990	56 H	0.134887	0.127500
17 H	0.142224	0.131184	57 H	0.189909	0.174720
18 H	0.142224	0.131184	58 C	-0.096848	-0.076570
19 H	0.142224	0.131184	59 C	-0.096848	-0.076570
20 H	0.142224	0.131184	60 C	-0.065407	-0.050480
21 H	0.142224	0.131184	61 C	-0.372844	-0.358828
22 H	0.142224	0.131184	62 C	0.216635	0.197224
23 C	0.241931	0.216259	63 S	-0.097474	-0.094921
24 C	0.247297	0.244779	64 S	-0.097474	-0.094921
25 C	-0.052125	-0.070225	65 C	-0.065407	-0.050480
26 C	-0.303759	-0.257341	66 C	-0.372844	-0.358828
27 C	0.344925	0.263775	67 C	0.216635	0.197224
28 F	-0.160978	-0.145482	68 H	0.168980	0.159871
29 H	0.218137	0.209318	69 C	-0.300633	-0.277674
30 C	0.057935	0.086667	70 H	0.204389	0.197201
31 C	-0.205198	-0.156622	71 H	0.168980	0.159871
32 C	0.241931	0.216259	72 C	-0.300633	-0.277674
33 C	-0.052125	-0.070225	73 H	0.204389	0.197201
34 C	0.344925	0.263775	74 H	0.111048	0.105522
35 N	-0.315726	-0.300923	75 H	0.111048	0.105522
36 N	-0.340281	-0.328955	76 H	0.111048	0.105522
37 N	-0.315726	-0.300923	77 H	0.111048	0.105522
38 N	-0.340281	-0.328955	78 H	0.111048	0.105522
39 S	0.295604	0.286976	79 H	0.111048	0.105522
40 S	0.295604	0.286976			

b) H1 charges

atom	RESP	atom	RESP	Atom	RESP
1 C	0.172480	33 C	0.059405	65 H	0.129911
2 C	-0.172679	34 C	-0.182198	66 H	0.129911
3 C	-0.257173	35 C	-0.134184	67 H	0.129911
4 C	-0.056194	36 C	0.053027	68 H	0.129911
5 S	-0.114701	37 S	-0.085002	69 H	0.129911
6 C	0.198525	38 C	-0.065284	70 H	0.129911
7 C	-0.255712	39 C	-0.055734	71 H	0.129911
8 C	0.296619	40 C	-0.335054	72 H	0.129911
9 C	-0.237696	41 C	0.165187	73 H	0.129911
10 C	-0.072441	42 S	-0.081217	74 H	0.129911
11 C	0.277014	43 C	-0.281676	75 H	0.129911
12 C	0.236575	44 C	-0.255712	76 H	0.129911
13 F	-0.135917	45 C	0.236575	77 H	0.107346
14 C	-0.365457	46 C	0.277014	78 H	0.107346
15 C	-0.134379	47 C	-0.072441	79 H	0.107346
16 C	0.198525	48 C	0.296619	80 H	0.107346
17 C	-0.134379	49 C	-0.237696	81 H	0.107346
18 C	-0.365457	50 N	-0.310026	82 H	0.107346
19 N	-0.347194	51 N	-0.347194	83 H	0.185287
20 N	-0.310026	52 S	0.302625	84 H	0.140521
21 S	0.302625	53 F	-0.135917	85 H	0.158556
22 Si	0.902924	54 C	0.059405	86 H	0.146917
23 C	-0.056194	55 C	-0.182198	87 H	0.193669
24 C	-0.257173	56 C	-0.134184	88 H	0.193669
25 C	-0.172679	57 C	0.053027	89 H	0.146917
26 C	0.172480	58 S	-0.085002	90 H	0.158556
27 S	-0.114701	59 C	-0.065284	91 H	0.140521
28 Si	0.902924	60 S	-0.081217	92 H	0.185287
29 C	-0.580848	61 C	0.165187	93 H	0.102777
30 C	-0.580848	62 C	-0.055734	94 H	0.148001
31 C	-0.580848	63 C	-0.335054	95 H	0.148001
32 C	-0.580848	64 C	-0.281676	96 H	0.102777

Figure S4: Calculated charges for (a) T1 and (b) H1. Pictures of the structures are given, to show how the atoms are numbered.

*Determination of dihedral energies*

Rotations around three bonds were investigated for both systems (T1 and H1): (i) between the central donor unit and the acceptor unit, (ii) between the acceptor and thiophene, (iii) between the two thiophenes. Relaxed potential energy scans were performed for the relevant fragments of the original T1 molecule. In relaxed scans, all other degrees of freedom (except for the scanned one) are fully optimized at each scan step. Scans were performed from 0° to 180°, in intervals of 5° as shown by the red lines in Figure S5 a) – c).

We incorporated the calculated PES of the dihedrals in our MD model by excluding all atoms at the edge of a ring at a donor-acceptor boundary from interacting with one another via non-bonded interactions. There are two reasons for this. First, atoms which are only six bonds apart nevertheless can approach very closely leading to numerical errors in the computation of the non-bonded forces.[4] Second, the interactions in question are already modeled by the DFT calculations and are incorporated in the resulting PES. An example is presented in Figure S5d, in which all blue marked atoms are excluded from interacting via non-bonded interactions with all orange marked atoms. We removed the dihedral parameters connecting the various parts of the molecule and added our own. The PES in the MD model were calculated by rotating the ring around the dihedral angle in question with enforced rotation. The potential energy of this process was determined with the Gromacs tool gmx energy. We implemented the new dihedrals with Ryckaert-Bellemans potentials[4] to replicate the DFT data. This new model matches closely with the DFT data in contrast to the original ATB proposed dihedrals as displayed in Figure S5.

The charges, bonds, and angles of the side-groups, 2-ethylhexyl[5] and hexyl[6], were adjusted to fit the corresponding values from the ATB Database, because for small molecules (less than 40 atoms) a more accurate calculation (B3LYP/6-31G* level of theory + Hessian) can be provided by the algorithm. The charges at the boundaries to the rest of the T1 molecule were adjusted slightly to ensure a vanishing net charge.

The Automated Topology Builder was not able to perform the same calculations for H1. The algorithm could not find an initial structure of the molecule, because the energy

minimization algorithm failed.[7] We therefore obtained a force field for the central donor unit[8] and added the rest of the molecule by reusing the corresponding parameters of the T1 calculation. The charges and dihedrals from quantum chemical calculations were incorporated in the same way as for T1 (Figures S4b and S6). For all molecules used in the MD Simulations, all-atoms forcefields were build.
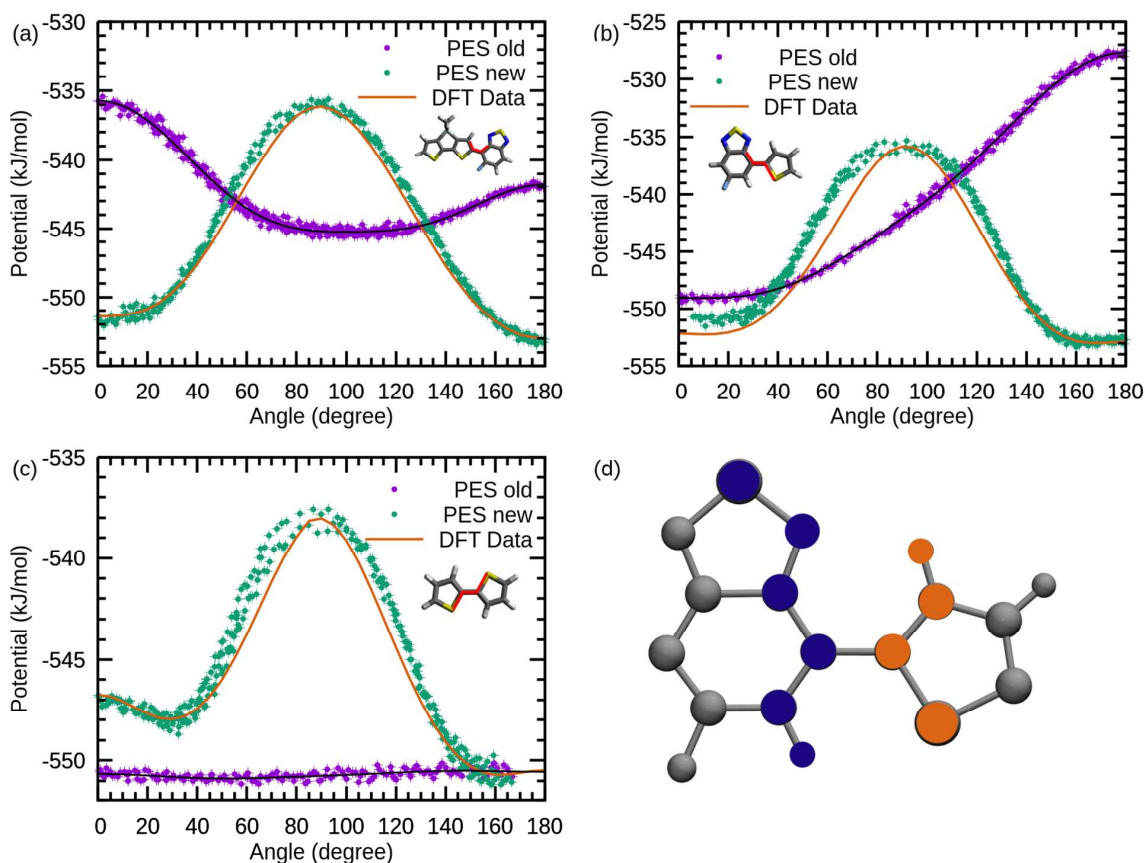
Figure S5: In this figure we present the implemented dihedral PES for (a) the one between the central donor unit and the acceptor unit, (b) between the acceptor and thiophene and (c) between the two thiophenes of T1. For all cases, the PES given by the ATB Algorithm is shown together with the calculated DFT data and the new PES of the MD model after implementing the data. In (d) an example is given for which atoms the non-bonded interaction is turned off. All blue marked atoms are excluded to interact with all orange marked atoms via non-bonded interactions.
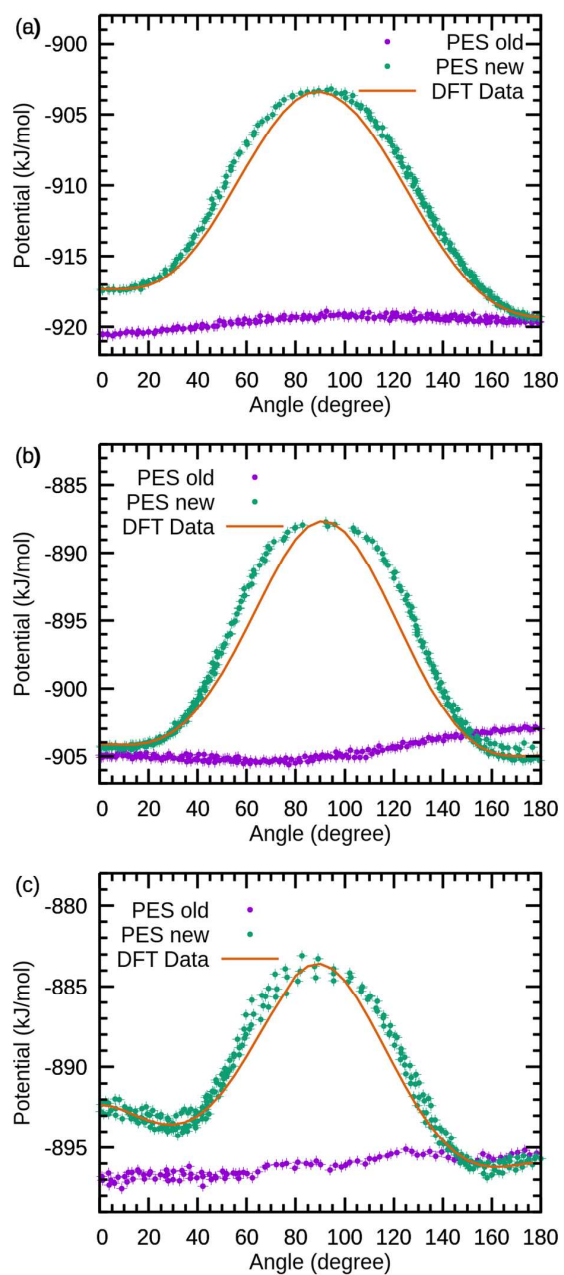
Figure S6: In this figure we present the implemented dihedral PES for (a) the one between the central donor unit and the acceptor unit, (b) between the acceptor and thiophene and (c) between the two thiophenes of H1.

S9

General parameters

The parameters given in Table S1 were used for all MD simulations. The distances were always determined by the distance between the center of masses of the molecules in question. The boxes were generated with the Gromacs tool gmx insert-molecules. The settings gen_temp and ref_t were set to the desired temperature.

Option	Value
Integrator	md
dt	0.002
Nstxout	200
constraint_algorithm	lincs
constraints	h-bonds
lincs_iter	1
lincs_order	4
ns_type	Grid
nstlist	15
rlist	1.0
rcoulomb	1.0
rvdw	1.0
coulombtype	PME
tcoupl	v-rescale
tau_t	0.1
pcoupl	Berendsen
pcoupltype	isotropic
tau_p	2.0
ref_p	1.0
compressibility	4.5e-5
pbc	xyz
DispCorr	EnerPres
gen_seed	-1

Table S1: The Gromacs parameters used for all simulations.

S10

Aggregation simulations

For all aggregation simulations, a short NPT simulation (400 ps) was performed to equilibrate the system to the right pressure (volume) and temperature. We then started in a random configuration with a box of two solvent molecules and 900 MTHF molecules. The simulation box was kept as small as possible, to increase the probability to observe aggregation. The box length was 4.98 nm on average. The system then evolves freely and the distance between the two solute molecules is calculated to see if they aggregate. In Table S2 an overview of the relevant simulations is given for T1. Aggregation can be observed in 15 out of 18 simulations (83%) of a total runtime of about 5.8 μs.

Number	Time [ns]	Aggregation
1	322.2	Yes
2	321.7	Yes
3	322.1	No
4	323.3	Yes
5	321.6	Yes
6	322.6	Yes
7	318.6	Yes
8	323.2	Yes
9	320.5	Yes
10	322.9	Yes
11	317.7	Yes
12	320.9	Yes
13	322.6	Yes
14	322.2	No
15	321.4	Yes
16	321.7	No
17	321.8	Yes
18	322.8	Yes

Table S2: Overview of all T1 aggregation simulations. The length of each simulation is given and a note if stacking behavior occurs or not. Aggregation behavior is counted as a yes, if any of the structures identified in the main text occurs and stays stable for at least 5 ns.

The aggregation simulations for H1 are listed in Table S3. It has to be noted, that sometimes the ends of the two molecules loosely bind to one another resulting in a metastable configuration. This is not counted as an aggregate because this behavior is not reflected in a noticeable energy decrease in the free energy calculations.

Aggregation can be observed in 5 out of 37 simulations (13.5%) of a total time of about 13.4 μs.

Number	Time [ns]	Aggregation
1	367.6	No
2	364.8	No
3	367.8	No
4	368.1	No
5	367.0	No
6	350.3	No
7	366.3	No
8	369.4	Yes
9	367.3	Yes
10	361.0	No
11	361.8	No
12	367.5	No
13	366.8	No
14	366.5	No
15	366.5	No
16	365.3	No
17	365.0	No
18	366.0	Yes
19	365.3	Yes
20	365.8	No
21	365.5	No
22	365.7	No
23	365.9	No
24	366.7	Yes
25	367.6	No
26	364.8	No
27	367.7	No
28	368.1	No
29	367.0	No
30	350.3	No
31	366.3	No
32	369.4	No
33	367.3	No
34	361.0	No
35	361.8	No
36	367.5	No
37	366.8	No

Table S3: Overview of all H1 aggregation simulations. The length of each simulation is given and a note if aggregation behavior occurs or not.

S12

Free energy simulations

For manipulating the distance between molecules a pull code was added to the Gromacs .mdp input file. The additional parameters are displayed in Table S4.

pull	yes
pull-coord1-type	umbrella
pull-coord1-geometry	distance
pull-coord1-dim	Y Y Y
pull-ngroups	2
pull-ncoords	1
pull-group1-name	System_&_r_1
pull-group2-name	System_&_r_2
pull-coord1-start	yes
pull-coord1-groups	1 2
pull-coord1-rate	<variable>
pull_coord1_k	<variable>

Table S4: Additional parameters used in the free energy simulations. The settings pull-coord1-rate and pull_coord1_k were variable between different simulations.

The windows for the free energy calculations were obtained in the following way if not stated differently: A brief NPT simulation of 400 ps was conducted to equilibrate the temperature and pressure of the system. The size of the resulting cubic simulation boxes is between 4.4 nm and 5.0 nm in box length. Starting from a random configuration we pulled the two solute molecules apart from one another until the simulation aborted due to the distance getting larger than half the box length.

A frame near the end of this simulation was extracted and used as a starting configuration for a simulation in which we squeezed the molecules slowly together. For this process, we calculated the distance in dependence of time and extracted configurations at evenly spaced distances, which were used as starting configurations for the umbrella windows. For each window, a brief NPT simulation of 400 ps was run before the actual free energy calculation started. This process was repeated for each free energy simulation. In Table S5 and Figure S7a, we give an overview of all free energy simulations used in Figure 4b in the main text.

S13

Number	Time [ns] per window	Number of windows
1	80	37
2	80	34
3	80	35
4	80	35
5	80	34
6	80	35
7	80	30
8	80	33
9	115	36
10	115	36
11	80	35
12	80	34
13	125	35
14	160	36
15	80	34
16	80	35
17	100	34

Table S5: Overview over all free energy calculations used in Figure 4b in the main text. To generate the whole free energy graph, all windows of all simulations in this table were combined to calculate the total free energy. Run 13 is shown as a representation of type B aggregation. To represent type A pathway, we show the same free energy curve used In Figure 4c.

For the temperature dependent calculations of aggregation Type A (Figure 4c in the main text), we took the starting windows from simulation 14 in Table S5 and added some windows from the same pathway sampling to increase the resolution. The details for each temperature are displayed in Table S6.

Temperature [K]	Time [ns] per window	Number of windows
400	160	44
350	140	39
300	160	36
250	240	65

Table S6: Overview over the temperature dependent free energy calculations of T1 presented in Figure 4c in the main text.

S14

77

In Table S7 and Figure S7b, the results of all free energy calculations for H1 at room temperature (Figure 5b in the main text) are presented.

Number	Time [ns] per window	Number of windows
1	150	42
2	200	32
3	100	35
4	100	35
5	140	34
6	100	34
7	100	36
8	100	35
9	100	35
10	100	33
11	40	36
12	40	34

Table S7: Overview over all free energy calculations used in Figure 5b in the main text at T = 300 K. To generate the whole free energy graph, all windows of all simulations in this table were combined to calculate the total free energy. Run 1 is shown in Figure 5b as a representative of no aggregation and run 10 as the only representative of aggregation behavior.

The free energy of H1 at lower temperature (T = 250 K) in Figure 5b in the main text is a composite of several independent calculations, which are displayed in Table S8.

Number	Time [ns] per window	Number of windows
1	80	32
2	80	33
3	80	32
4	80	32
5	80	32
6	80	18
7	80	32
8	80	31
9	80	30

Table S8: Overview over all free energy calculations used in Figure 5b in the main text for H1 at T = 250 K.
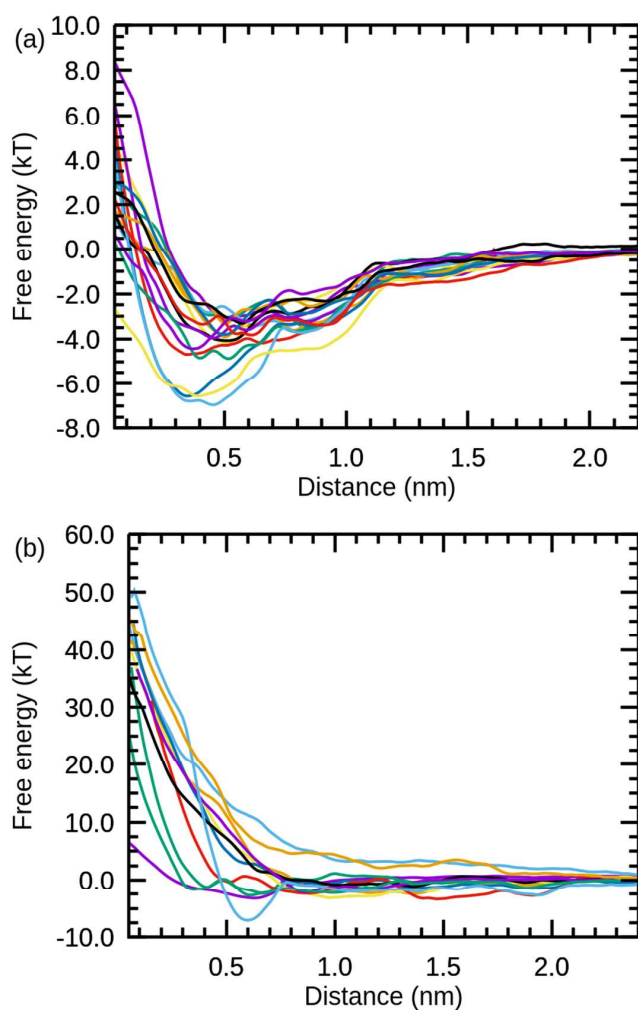
Figure S7: Overview over all free energy calculations (a) used in Figure 4b in the main text for T1 and (b) used in Figure 5b in the main text at T = 300 K for H1.

Parameters for the free energy without side-chains in Figure 6a in the main text are listed in Table S9 for T1 and in Table S10 for H1.

Number	Time [ns] per window	Number of windows
1	80	34
2	80	35
3	80	35
4	80	33
5	80	35
6	80	36
7	80	34
8	80	34
9	80	35
10	80	31

Table S9: Overview over all free energy calculations used in Figure 6a in the main text for T1 without side-groups.

Number	Time [ns] per window	Number of windows
1	120	31
2	120	34
3	120	35
4	120	33
5	80	33
6	80	33
7	80	33
8	80	32
9	80	34
10	80	34
11	80	34
12	50	31

Table S10: Overview over all free energy calculations used in Figure 6a in the main text for H1 without side-groups.

S17

Additional data from MD Simulations

Aggregation in vacuum

In Figure S8 we present the free energy of T1 and H1 in a vacuum obtained by umbrella sampling.
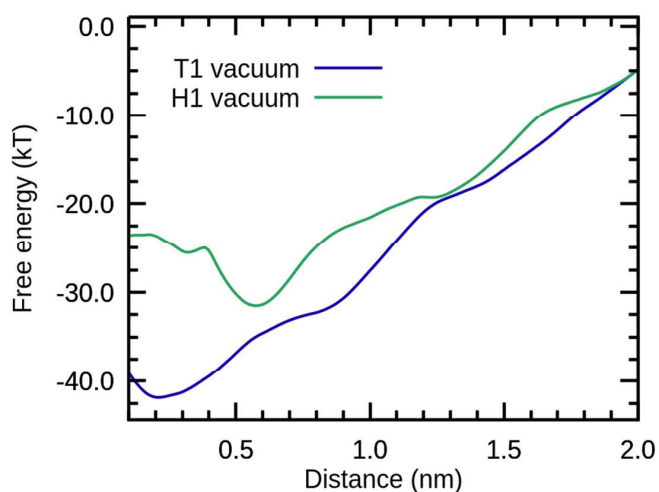
Figure S8: Free energy gained by aggregation in vacuum. The figure clearly demonstrates that the kinetic barrier observed for H1 aggregation is a solvent-induced effect.

Additional results from DFT simulations

The character of the excited states was investigated using natural transition orbitals (NTOs).[9]

(a) hole   electron   82.3%   14.8%

(b) hole   electron   70.7%   25.3%
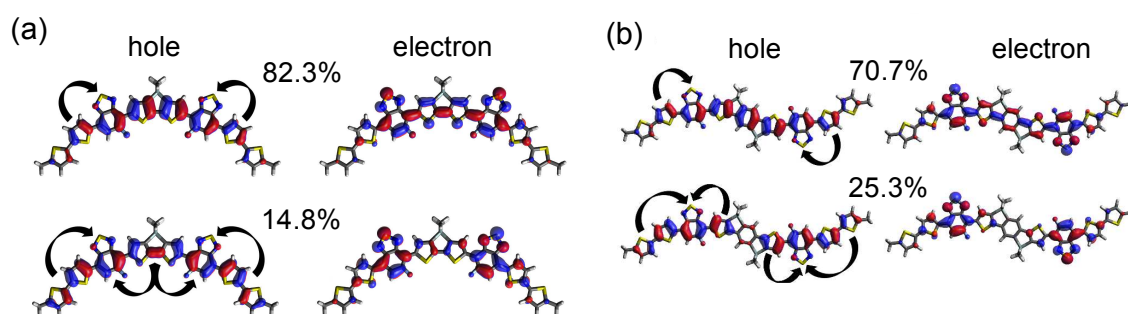
Figure S9: Natural transition orbitals (NTOs) for the first singlet excited state of (a) T1 and (b) H1. Hole orbitals are depicted on the left, with corresponding electron orbitals on the right, where values denote the contribution of a given pair of NTOs to the excitation and the arrows serve to highlight the changes in electron density. Parts of picture a are taken from ref. [3].

An analysis of the natural transition orbitals of T1 and H1 shows that the electron density is transferred from the central and outer donor units, DTS or SIDT and dithiophene, to the fluorobenzothiadiazole acceptor (Figure S9), hence this state has a charge-transfer character. Accompanied with this charge transfer is an increase in dipole moment: for T1 in THF from 0.64 D in the ground state to 1.77 D upon vertical excitation, reducing a bit to 1.33 D in the relaxed excited state geometry in THF, as calculated in ref. [3]. For H1 in THF the dipole moment in the optimized ground state is negligible (0.00 D), and it does not change upon vertical excitation, however in the relaxed geometry of the excited state the dipole moment grows to 7.52 D.

References

1. van der Poll, T. S.; Love, J. A.; Nguyen, T.-Q.; Bazan, G. C. Non-Basic High-Performance Molecules for Solution-Processed Organic Solar Cells. *Adv. Mater.* **2012,** *24*, 3646-3649.

2. Love, J. A.; Nagao, I.; Huang, Y.; Kuik, M.; Gupta, V.; Takacs, C. J.; Coughlin, J. E.; Qi, L.; van der Poll, T. S.; Kramer, E. J., et al. Silaindacenodithiophene-Based Molecular Donor: Morphological Features and Use in the Fabrication of Compositionally Tolerant, High-Efficiency Bulk Heterojunction Solar Cells. *J. Am. Chem. Soc.* **2014,** *136*, 3597-3606.

3. Reichenberger, M.; Love, J. A.; Rudnick, A.; Bagnich, S.; Panzer, F.; Stradomska, A.; Bazan, G. C.; Nguyen, T.-Q.; Köhler, A. The Effect of Intermolecular Interaction on Excited States in p-DTS(FBTTH₂)₂. *J. Chem. Phys.* **2016,** *144*, 074904.

4. Abraham, M.; Hess, B.; van der Spoel, D.; Lindahl, E. GROMACS Reference Manual. Version 2016.3. **2016**.

5. ATB Database: $C_{10}H_{16}S$ Structure and Topology Files. https://atb.uq.edu.au/molecule.py?molid=29953 (accessed March 31, 2016).

6. ATB Database: $C_{20}H_{38}Si$ Structure and Toplogy Files. https://atb.uq.edu.au/molecule.py?molid=29955 (accessed March 31, 2016).

7. ATB Database : p-SIDT(FBTTh₂)₂ Structure and Toplogy Files. https://atb.uq.edu.au/molecule.py?molid=34613 (accessed October 25, 2016).

8. ATB Database: $C_{20}H_{22}S_4$ Structure and Topology Files. https://atb.uq.edu.au/molecule.py?molid=33494 (accessed on June 28, 2016).

9. Martin, R. L. Natural Transition Orbitals. *J. Chem. Phys.* **2003**, *118*, 4775-4777.

5.2 What is the role of planarity and torsional freedom for aggregation in a π-conjugated donor-acceptor model oligomer?
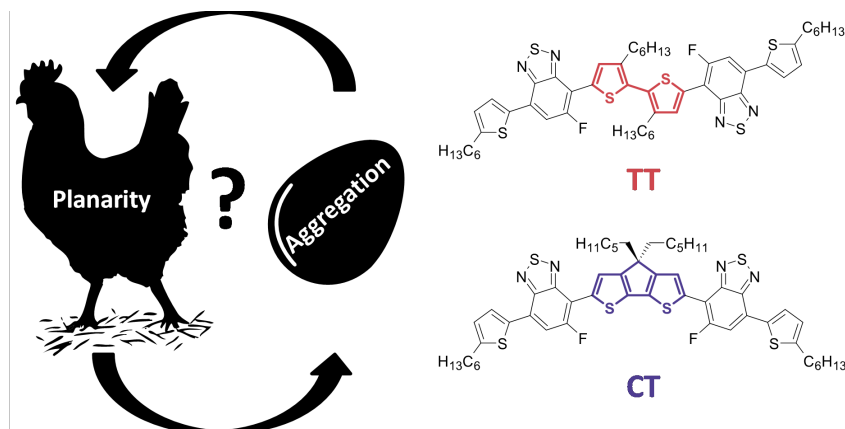
Stefan Wedler, Axel Bourdick, Stavros Athanasopoulos, Stephan Gekle, Fabian Panzer, Caitlin McDowell, Thuc-Quyen Nguyen, Guillermo C. Bazan, Anna Köhler

85

What is the role of planarity and torsional freedom for aggregation in a π-conjugated donor-acceptor model oligomer? †

Stefan Wedler[1], Axel Bourdick[2], Stavros Athanasopoulos[3], Stephan Gekle[2], Fabian Panzer[1], Caitlin McDowell,[4] Thuc-Quyen Nguyen,[4] Guillermo C. Bazan[4], Anna Köhler[1,5*]

[1] Soft Matter Optoelectronics, Experimentalphysik II, University of Bayreuth, Bayreuth 95440, Germany.

[2] Biofluid Simulation and Modeling, Theoretische Physik VI, Universität Bayreuth, Bayreuth 95440, Germany

[3] Departamento de Física, Universidad Carlos III de Madrid, Avenida Universidad 30, 28911 Leganés, Madrid, Spain.

[4] Center for Polymers and Organic Solids, Departments of Chemistry & Biochemistry and Materials, University of California, Santa Barbara

[5] Bayreuth Institute of Macromolecular Research (BIMF) and Bavarian Polymer Institute (BPI), University of Bayreuth, 95447 Bayreuth, Germany.

*e-mail: Anna.Koehler@uni-bayreuth.de

†Electronic supplementary information (ESI) available.

1

Abstract

Ordered structures play a central role in the performance of organic semiconductor devices. We investigate the influence of backbone planarity on the propensity to form ordered structures using a pair of model oligomers with benzothiadiazole acceptor moieties and thiophene donor units. The two oligomers differ by their central unit, where a bithiophene unit either allows for flexible twists ("TT"), or where it is bridged as a cyclopentadithiophene to provide a rigid planar connection ("CT"). Temperature dependent absorption and luminescence spectroscopy in solution along with atomistic simulations show that the more flexible TT readily forms aggregates upon cooling, while CT instead first forms non-emissive excimers and only forms aggregates below 200K. Molecular dynamics simulations reveal that the aggregation in TT can only be accounted for if TT takes on a planar conformation in the course of the aggregation process. The stronger intermolecular interaction in TT can then be related to the larger number of donor-acceptor type interactions that can occur as compared to a dimer in the banana-shaped CT.

1. Introduction

The performance of organic semiconductor devices such as organic solar cells (OSCs), transistors (OFETs) and light emitting diodes (OLEDs) depends not just on the chemical structure of the π-conjugated oligomers used. Rather, over the last decade we learned that the molecular self-assembly, and the resulting intermolecular interactions, as well as disorder can be decisive in controlling device performance.[1-7] An attractive feature of organic semiconductors is that they can be processed from solution, so that fabrication avenues such as printing or roll-to-roll processing are possible.[8-13]

In order to understand the complex film formation processes that are involved in the fabrication of devices from solution, we need to first understand the interactions that prevail between chromophores in solution. A suitable means to study the formation of structures with short-range or even long-range order, is to cool down a solution.[14] This approach keeps the concentration constant while the solvent quality gradually deteriorates. When such studies are carried out on π-conjugated polymers or oligomers it was found that the appearance of an emission or absorption that can be attributed to aggregates is preceded by a planarization process of the polymer or oligomer.[15-19] Also, synthetic approaches to enhance the planarization of a polymer backbone by inserting heteroatoms with interactions that lead to conformational locks have been demonstrated to successfully increase the propensity of a polymer to form ordered structures.[20-23] For oligomers such as acenes or coronenes, it is well known that an extended planar π-system is conducive to aggregation.[24-27] In fact, the challenge is frequently to suppress excessive aggregation by insertion of suitable sidechains or sterically demanding groups.[28-32] From these studies one may infer that a rigidified planar backbone is central to obtaining compounds that can self-assemble into ordered structures.

However, there are also reports that indicate that the aggregation process itself is inducing the planar conformation of the chromophore. For example, De Leneer et al. studied how aggregates form for the polymer MEH-PPV.[33] In their quantum chemical studies, they found that the timescale for conformational fluctuations, notably rotations of the vinyl and phenyl units, are slowed down when two chain segments are brought close. This allows for the build-up of attractive interactions and the eventual formation of a planar, aggregated segment. Further, Kärnbratt et al. investigated

2

the self-assembly process in linear porphyrin oligomers. From the very sudden onset of aggregation they conclude that a planar backbone structure has been induced by the assembly process, rather than vice versa.[25]
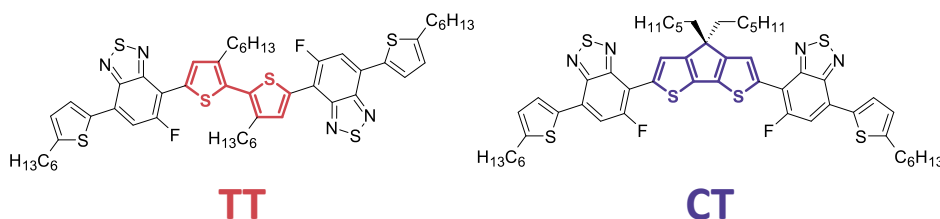
Figure 1:   Chemical structures of TT and CT.

Here we address the question whether pre-existing backbone planarity is of advantage for the self-assembly process, or whether the required planarity may instead also be induced during the assembly process by considering two model oligomers referred to as "TT" and "CT". Figure 1 shows the chemical structures of these molecules. They differ only in their central unit. For TT, the central unit is a flexible bithiophene, marked in red. The hexyl sidechains induce a dihedral angle of 68°, as obtained from DFT calculations, while the flexibility is preserved. In particular, TT is able to planarize. The stiff molecule CT comprises a cyclopentadithiophene, marked in blue, forcing it to be planar. These model oligomers are very similar to compounds used in efficient solar cells, such as T1,[34-37] which are frequently made in a D-A-D-A-D type structure with electron-rich (D) and electron-poor (A) subunits.[27, 38, 39]

This paper is structured as follows. After introducing the methods in section 2, we describe in section 3 our observations and interpretation of the spectroscopic measurements taken in solution. In section 4, these results are compared to and discussed against the predictions made by molecular dynamics simulations. Time dependent density functional theory (TD-DFT) calculations on the excited state structure in dimers are discussed in section 5. Section 6 finally reports and discusses the observation of emission from cis- and trans-conformations of TT. A concluding summary is provided in section 7.

2. Methods

Sample preparation

The molecules 7,7'-(3,3'-dihexyl-[2,2'-bithiophene]-5,5'-diyl)bis(6-fluoro-4-(5-hexylthiophen-2-yl)benzo[c][1,2,5]thiadiazole) (**TT**) and 7,7'-(4,4-dihexyl-4H-cyclopenta[2,1-b:3,4-b']dithiophene-2,6-diyl)bis(6-fluoro-4-(5-hexylthiophen-2-yl)benzo[c][1,2,5]thiadiazole) (**CT**) were synthesized as reported previously,[40] their structures are shown in Figure 1. Solutions with different concentrations were prepared inside a glovebox using O_2-free anhydrous hexane from Acros. To ensure complete dissolution, the solutions were heated to 50 °C and stirred up to one hour. We used quarzglass cuvettes with a thickness of 1.00 mm (10.00 mm) for solutions with concentrations of $5.0 \cdot 10^{-5}$ M and higher ($5.0 \cdot 10^{-6}$ M and lower) for optical characterization.

3

Photoluminescence and absorption measurements

Temperature dependent absorption and emission spectra were measured with a home-built setup.[19] Detection was performed utilizing a CCD camera (Andor iDus 420) coupled to an Andor Shamrock 303 spectrograph. For excitation we used a 405nm diode laser from Coherent for all CT measurements and a 485 nm diode laser from PicoQuant for all TT measurements, both operating in continuous wave mode. Emission spectra were corrected for the efficiencies of all optical components as well as for changes of the absorbance at the laser wavelength. All samples were put into a temperature controlled continuous-flow cryostat (Oxford Instruments) using liquid helium as the coolant. A waiting time of 15 minutes before measurement was sufficient after reaching each temperature to ensure thermal equilibration of the sample.

Time-correlated single photon counting measurements were performed using a FluoTime 200 spectrometer from PicoQuant and a 485 nm diode laser operating in pulsed mode for excitation. Signal acquisition was performed utilizing the counting module PicoHarp 300E (PicoQuant).

Quantum-Chemical Calculations

Ground state optimizations of the individual molecules with the side chains were performed at the density functional theory (DFT) level using the ωB97XD long-range corrected exchange-correlation functional[41] and a split valence 6-31G** polarized double zeta basis set. We have used a range separation parameter of ω=0.13 au^{-1} that has been previously obtained by tuning the fundamental gap of the TT molecule.[40] Excited state geometry optimizations and vertical transition energies of the individual molecules and the dimers were obtained with linear response time dependent density functional theory (TD-DFT). All DFT and TD-DFT calculations were carried out with Gaussian 09 software.[42]

To quantify the extent of intermolecular exciton delocalization on the CT and TT dimers we have computed the participation ratio of the dominant hole and electron natural transition orbitals (NTOs),[7] defined as:

$$PR = (\rho_{mol1}^2 + \rho_{mol2}^2)^{-1}$$

with

$$\rho_{moli} = \sum_{j \,\in\, moli}^{N} C_j^2$$

C_j are the corresponding coefficients of the normalised NTOs. PR takes values between 1 and 2: when PR = 1 the natural transition orbital is fully localized on a single molecule while when PR = 2 it is equally delocalized between the two molecules. To obtain information on the intermolecular charge transfer character we define a CTC parameter as:

$$CTC = \left|\frac{\Delta h - \Delta e}{2}\right|$$

where

$$\Delta h = \sum_{j \,\in\, mol1}^{N} C_{j,HOMO}^2 - \sum_{j \,\in\, mol2}^{N} C_{j,HOMO}^2$$

4

$$\Delta e = \sum_{j \, \in \, mol1}^{N} C_{j,LUMO}^{2} - \sum_{j \, \in \, mol2}^{N} C_{j,LUMO}^{2}$$

The CTC parameter takes values between 0 and 1: CTC = 0 indicates an excitation without intermolecular charge transfer character and CTC = 1 indicates an excitation with complete charge transfer character, meaning the hole (HOMO) NTO is complete localized over the first molecule and the electron (LUMO) NTO is complete localized over the opposite molecule.

MD-Simulations

We performed molecular dynamics simulation with Gromacs[43-46] using the Gromos 54a7 force field.[47] The structure files were generated with JME.[48] The force field files for CT[49] and TT[50] were generated with the automated force field topology builder and repository.[51-53]

In order to make our simulations more accurate we calculated the charge distribution and the potential energy surface (PES) of the dihedral angle between the various donor and acceptor parts of the molecules and between the two thiophene rings in the central donor unit of TT with DFT and adjusted our MD models to reproduce the behaviour calculated with DFT. Structure and topology files for the solvent hexane were taken from the ATB database.[54] More details about how the models were built are specified in the ESI, Section 1. For the simulations all-atom force field topologies were used. We used a cubic box of two solute molecules and between 500 and 1100 solvent molecules. We defined the reaction coordinate as the distance between the center of mass of the central donor unit of TT and the center of mass of the middle ring of the central donor unit of CT. Starting configurations for the umbrella windows were generated from a random configuration from which we squeezed the solute molecules together and pulled them apart along the reaction coordinate. Configuration snapshots were saved in steps of 0.04 nm. Each simulation was equilibrated and conducted as NPT ensemble. To cover the whole configurational phase space, we sampled the reaction pathways independently eight times for TT and eleven times for CT with hexyl sidechains. For the free energy graphs with CH_3 sidechains we sampled the reaction pathway of TT and CT four times each. The free energy graphs are averaged over all these runs. The simulation time varied from 60 ns to 800 ns per window. The free energy graphs were calculated with umbrella sampling[55] and the *Weighted Histogram Analysis Method*,[56] which is implemented in Gromacs as *gmx wham*. Two-dimensional free energy surfaces were calculated with well-tempered metadynamics,[57-60] which was carried out using the open-source community-developed PLUMED library version 2.2 integrated as a plugin to the Gromacs software.[61, 62] Visualisation was done with VMD.[63] All Simulations were performed at T = 300 K. Further details about the simulation parameters and the used force constants can also be found in the ESI, Section 1.

3. Optical spectroscopy

Results

We study the influence of torsional rigidity on the aggregation behaviour using the two molecules shown in Figure 1. They consist of typical building blocks for donor-acceptor-type molecules used in organic solar cells and differ only in their central unit, which consists of connected thiophenes ("CT") or twisted thiophenes ("TT"). The stiff molecule, thereafter referred to as CT, comprises a cyclopentadithiophene marked in blue. For the molecule called TT, the central unit is a flexible bithiophene, marked in red. Its alkyl sidechains result in a twisted geometry with a dihedral angle of

5

68° as determined by quantum chemical calculations (see section 6) and in agreement with literature.[40]
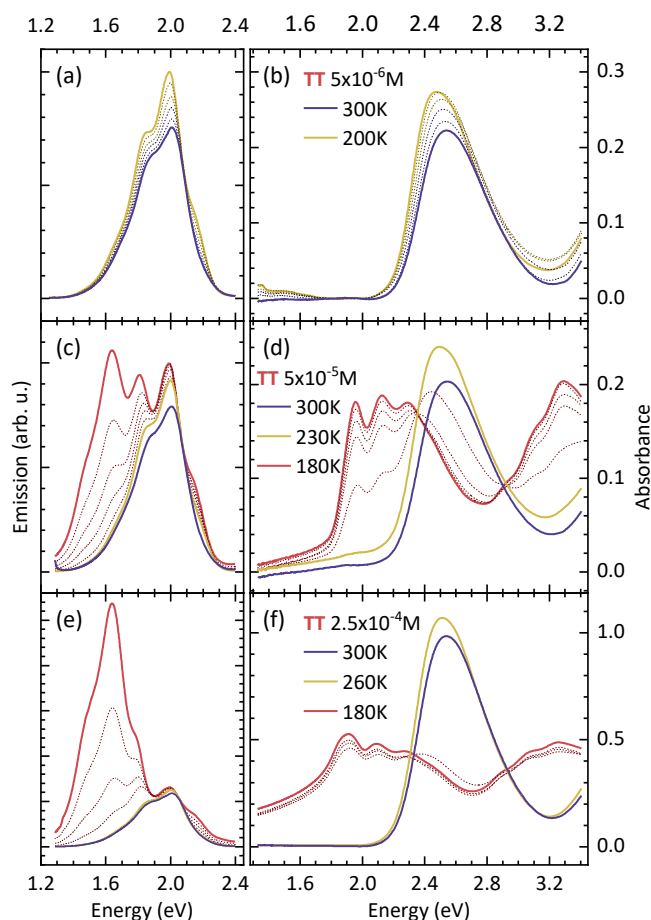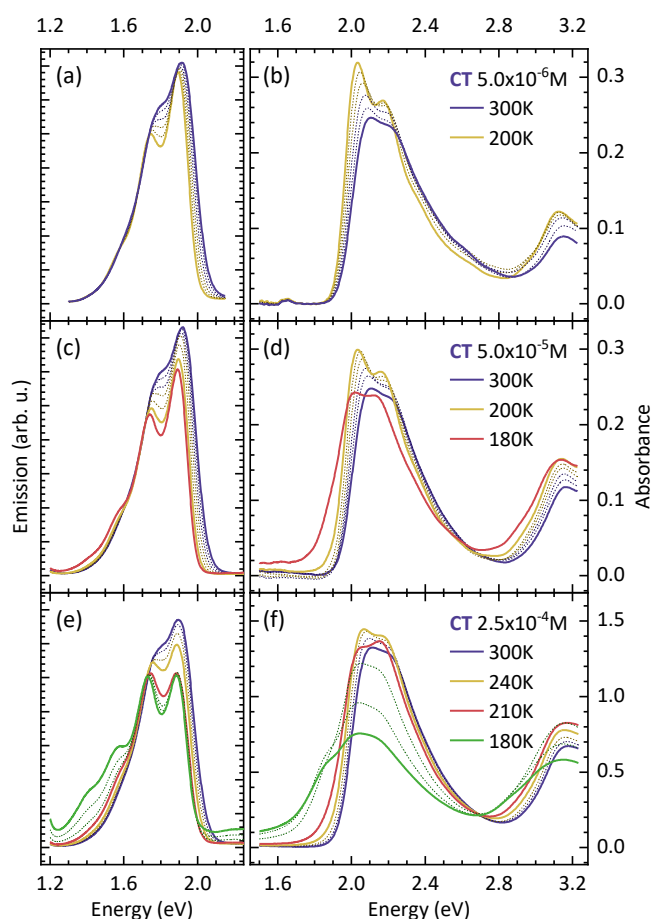

Figure 2: Absorption (b,d,f) and emission (a,c,e) spectra of TT in hexane for different temperatures at a concentration of (a,b) $5.0 \cdot 10^{-6}$ M, (c,d) $5.0 \cdot 10^{-5}$ M and (e,f) $2.5 \cdot 10^{-4}$ M. Emission spectra are normalized to about 2.08 eV. Spectra taken at characteristic temperatures are drawn with solid lines and given in the legend. Temperatures in between are shown in steps of 20 K for a), b) and between 180 K and 260 K in e) and f), and in steps of 10 K between 180 K and 230 K for c) and d).

We conducted temperature dependent absorption and emission measurements in hexane between 300 K and 180 K to investigate their aggregation properties in solution and compare three different concentrations. Figure 2 shows the absorption and emission of TT in hexane at $5.0 \cdot 10^{-6}$ M, $5.0 \cdot 10^{-5}$ M and $2.5 \cdot 10^{-4}$ M. All emission spectra are normalized to coincide at the high energy side at about 2.1 eV. For the lowest concentration of $5.0 \cdot 10^{-6}$ M, both absorption and emission only change little upon cooling. The unstructured absorption (Figure 2b) increases in intensity and the peak position shifts from 2.53 eV at 300 K to 2.47 eV at 200 K. In emission (Figure 2a) we also observe a redshift of the peak around 2.0 eV by 20 meV and a reduction of the linewidth upon cooling. Furthermore, an additional high-energy shoulder at 2.15 eV emerges upon cooling. We discuss the origin of this shoulder further below in section 6.

6

For the medium concentration of 5.0·10⁻⁵ M (Figure 2c,d) we again observe a redshift and increase in absorption until 230 K (solid yellow line) upon cooling. At 220 K and below, new spectral features emerge at lower energies both in absorption and emission. A structured absorption feature with the first peak at 1.95 eV and further vibronic replicas at 2.12 eV and 2.30 eV appear. Concomitantly, the unstructured absorption band centered at 2.5 eV disappears, resulting in an isosbestic point at 2.35 eV. The additional luminescence feature shows peaks at 1.81 eV and 1.64 eV, and a shoulder at 1.46 eV. Again, the high-energy shoulder at 2.15 eV emerges upon cooling.

Figure 3: Absorption (b,d,f) and emission (a,c,e) spectra of CT in hexane for different temperatures at a concentration of (a,b) 5.0·10⁻⁶ M, (c,d) 5.0·10⁻⁵ M and (e,f) 2.5·10⁻⁴ M. Emission spectra are normalized to about 1.7 eV. Spectra taken at characteristic temperatures are drawn with solid lines and given in the legend. Temperatures in between are shown in steps of 20 K for a), b), c), d) and between 240 K and 300 K in e) and f), and in steps of 10 K between 180 K and 210 K for e) and f).

The spectral changes upon cooling become more drastic when we increase the concentration further to 2.5·10⁻⁴ M (Figure 2e,f). The absorption band reduces in intensity below 260 K. The emerging absorption feature shows a strong raising baseline and the structure is smeared out. This is characteristic for light scattering from small particles. Similarly, in emission, the peaks at 1.81 eV and 1.64 eV grow in from 260 K onwards and keep increasing. This is accompanied by a change in relative weight of the vibrational peaks, so that the peak at 1.64 eV eventually dominates and the overall

shape is reminiscent of a classical excimer-type emission.[26] In addition to this evolution at the red side of the spectrum, the already mentioned shoulder at 2.15 eV emerges at low temperatures, independent of concentration.

The changes of the more rigid CT with temperature and concentration are displayed in Figure 3. The emission spectra are normalized to coincide at the low energy side around 1.7 eV. For the lowest concentration (Figure 3a,b), both absorption and emission change little upon cooling. Overall, the intensity of the absorption increases slightly, the spectra shift to the red by 40 meV and the linewidth (full width at half maximum) narrows by 29 meV. A Franck-Condon analysis reveals that the apparent change of the peak ratios is due to the decreasing linewidth, as detailed in the ESI, Section 2.

When increasing the concentration to $5.0 \cdot 10^{-5}$ M (Figure 3c,d), we notice a decrease in absorption intensity for the spectra taken at 200 K, 190 K and 180 K. This is accompanied by a reduction in the ratio between the 0-0 peak at about 2.03 eV and the 0-1 peak at about 2.18 eV as well as a broadening of the low energy tail. The emission spectra have a similar shape at lower concentration. However, the relative contribution of the 0-0 peak at 1.9 eV is less pronounced and at the lowest temperature (180 K) we observe an additional weak feature below 1.6 eV.

In absorption, at the highest concentration (Figure 3f), there is a reduction of the 0-0 peak at about 2.05 eV from 280 K onwards compared to the 0-0 peak intensity observed for the lower concentrations (for better comparison among different concentrations see ESI, Section 3). The overall absorption intensity reduces from 240 K onwards, and the spectra exhibit a low energy shoulder at 1.85 eV for 200 K and below, as well as a scattering offset. In emission (Figure 3e) the trends already observed for the intermediate concentration are more pronounced. In particular, we observe a clear low energy feature with peaks at 1.55 eV and 1.40 eV for 200 K and below.
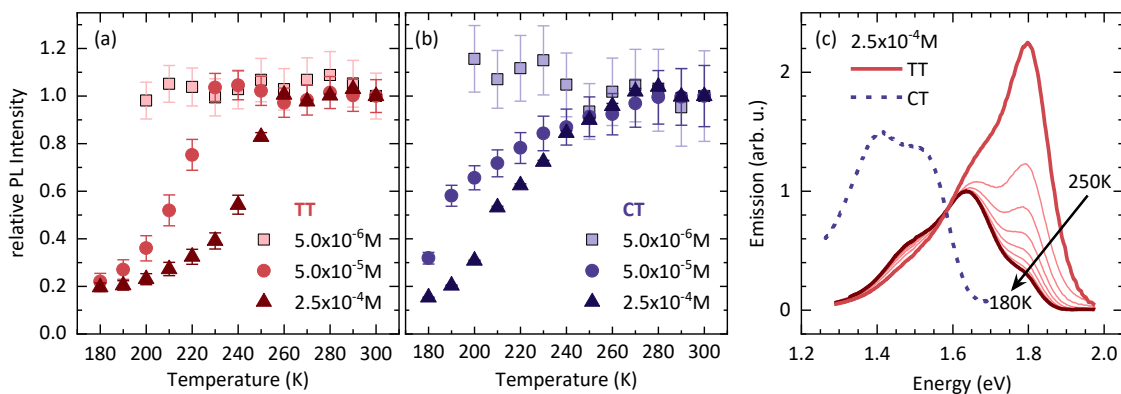
Figure 4: Relative emission intensity as function of temperature for different concentrations for (a) TT and (b) CT. (c) Separated aggregate emission spectra at the concentration of $2.5 \cdot 10^{-4}$ M. The spectra for TT are normalized to 1.6 eV and are taken in steps of 10 K as indicated by the arrow. For CT only the spectrum at 180 K is shown.

We displayed the photoluminescence spectra in Figures 2 and 3 in a normalized manner to allow for a good comparison of the spectral shapes. The relative photoluminescence intensities, integrated over the entire spectrum and normalized to unity at room temperature, are displayed in Figure 4a and b. For TT, the overall intensity remains constant until the lower energy band appears (at 230 K and 260 K for the medium and higher concentration, respectively), and then reduces steeply. For CT,

8

the emission intensity reduces for the medium and higher concentration from about 250 K onwards, which does not correlate in an obvious way with spectral changes.

More information on the low energy bands can be obtained from their spectral shapes. For the concentration of 2.5×10^{-4} M, we separated the low energy band in TT (CT) spectrally from the high energy band. For this, we took the emission spectrum at 260 K (210 K) that displays only the high energy feature, normalized it to the high energy side of the spectra taken at lower temperatures, and subtracted it. The resulting difference spectrum consists only of the low energy band and is shown in Figure 4c. With decreasing temperature, there is a reduction of the 0-0 peak at 1.8 eV for the low energy band in TT. The energy of the 0-0 peak stays constant during the transition, in contrast to an ongoing bathochromic shift observed for aggregate emission in several polymers like P3HT or PCPDTBT.[15, 16] For CT, the separated spectra of the low energy band below 210 K are identical within experimental uncertainty and we only present the result for 180 K, which also shows a reduced intensity of the 0-0 peak.

Discussion

Cooling down a solution is a well-known means to reduce the quality of a solvent to promote aggregation phenomena while keeping the overall concentration unchanged. The different spectral evolutions we observe for CT and TT seem to suggest that the nature of the connecting unit has a strong impact on their propensity to aggregate.

The evolution of the spectra for TT is comparatively straightforward to interpret, as it follows the pattern observed for other conjugated polymers or molecules such as P3HT.[14, 15, 64] Consider for example the absorption at the medium concentration, 5×10^{-5} M. The bathochromic shift and increase in oscillator strength in absorption implies that the conjugation length in the molecule increases upon cooling, suggesting a freezing out of torsional motion between the various heterocyclic units and stronger planarization of the backbone. The appearance of the isosbestic point below a critical temperature T_c of 230 K indicates the transition from individually solvated molecules into aggregates, and this is accompanied by the appearance of associated emission features. At higher concentrations, this transition sets in at higher temperatures. We attribute the appearance of an apparent long low energy tail in the absorption at the highest concentration to light-scattering due to a larger size of the aggregated conglomerates. The reduction in photoluminescence intensity upon aggregate formation, and the reduction of the 0-0 peak upon cooling (Figure 4a and c) are typical for a predominantly H-type interaction. Thus, we can conclude that TT forms weakly interacting H-type aggregates when reducing the solvent quality by cooling.

In contrast, the evolution of the CT spectra is more complex. The small redshift upon cooling in the absorption of the dilute solution indicates a freezing out of torsional modes in the vicinity of the benzothiadiazole that increases the overall conjugation length, which is less pronounced in emission, consistent with a typically already more planar geometry of the excited state. Despite the more planar, rigid character, signs of aggregate formation are less pronounced than for TT. Clear signatures in absorption and emission for the formation of a weakly interaction aggregate prevail in the higher concentrated solution, i.e. at 2.5×10^{-4} M, only below 210 K, and for the medium concentration below 200 K. There are, however, more subtle spectral changes already below 240 K, notably in the ratios of the 0-0 to 0-1 absorption peaks. It is striking that there is a clear decrease in overall

9

photoluminescence intensity below 250 K for the medium and higher concentration, even though this is not accompanied by any emissive features. This suggests that, below 250 K, CT first forms some non-emissive species, and emissive aggregates are only formed at higher concentrations and lower temperatures. A similar observation has been made earlier for the aggregation process in pyrene-derivatives.[65]

This is an unexpected result. For the polymers and oligomers we investigated so far, including the TT reported here, we always observed that a planarization of the backbone preceded the formation of aggregates that had some degree of oscillator strength so that they could be identified in absorption and emission. Moreover, the comparison of more rigid polymers, such as MEH-PPE, with more flexible ones like MEH-PPV showed that the more rigid nature of an ethynylene bond in the chemical structure facilitates aggregate formation compared to a vinyl bond. In contrast, here, it seems that the rigid nature of the connection does not assist the formation of aggregates with some oscillator strength, but rather induces the formation of non-emissive species.

4. Molecular Dynamics simulations

Results

In previous work we found that reduced torsional motion promotes aggregation,[14] and an initial planarization prior to aggregation is also what we observed here for CT and TT, as discussed in section 3. It is thus not immediately clear why CT shows less signs of aggregation than TT. A possible explanation could be that the sidechains of the central CT unit might prevent approximation of adjacent molecules as these chains are pointing out of the molecular plane, whereas the sidechains lie in the molecular plane for TT. To test this hypothesis, we conducted molecular dynamics (MD) simulations for the molecules with the full hexyl sidechains, as well as for the molecules where the central sidechains are replaced by CH_3. The key observable of the simulations is the free energy of the system, which consists of two single molecules surrounded by 500 to 1100 solvent molecules. Free energy curves are computed using Umbrella Sampling as detailed in the Method Section and the ESI, section 1.

Figure 5 compares the resulting average free energies as a function of intermolecular distance, defined as the center of mass distance for the central units, alongside with corresponding dimer geometries. These schematics serve to illustrate the mean configurations of snapshots in the MD simulation at the different minima along the free energy curves. We find that upon approximation the free energy of two molecules reduces. For both, TT and CT, this pathway involves several minima. For TT, we find that the two molecules approach predominantly by successively sliding over each other along the long axis of the molecule. Due to the central twist, the two wings do not lie parallel on top of each other, but rather twist around each other (Figure 5b, position 4, and film clip deposited as ESI). When the sidechains are replaced by CH_3 groups, it seems that this process becomes facilitated, resulting in a significantly deeper minimum at closest approximation.

For CT, we also observe predominantly a sliding process along the long axis. Due to the rigid central cyclopentadithiophene, CT has a banana shape. Correspondingly, there are two possible conformations, depending on the relative orientation of the central cyclopentadithiophene group. The two molecules may arrange with their curvature in opposite direction (type A) or in the same

10

direction (type B). For type A, the sidechains on the two central units are also orientated opposite, thus not causing any steric effects. For type B, the final geometry contains an offset by one ring unit along the molecular long axis, thus avoiding direct interaction of the sidechains. The prevalence of *two* possible energetically favourable arrangements in CT as opposed to only one in TT is further supported by metadynamics calculations, as evident from Figure 5e as well as Figures S1.6 and S1.7 in the ESI.
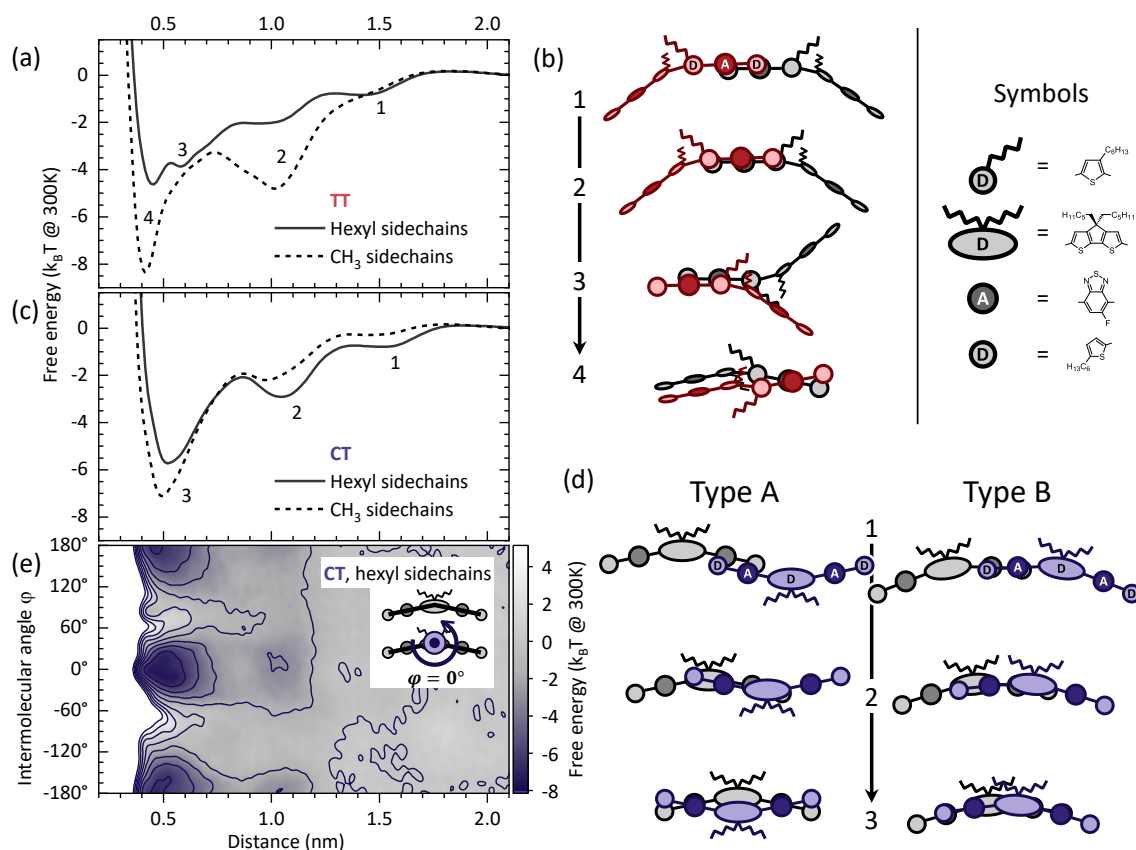
Figure 5: (a) Free energy curves for the TT dimer with hexyl and CH_3 sidechains as function of the distance of the central bithiophenes. (b) Dimer geometries for the closest distance and along the free energy curve as indicated in (a). (c) Free energy curves for the CT dimer with hexyl and CH_3 sidechains as function of the distance of the central cyclopentadithiophenes. (d) Dimer geometries for the closest distance and along the free energy curve as indicated in (c). For CT there are two final conformations possible. (e) Two-dimensional free energy surface calculated by metadynamics for the CT dimer with hexyl side chains as function of intermolecular distance and intermolecular angle φ. The inset visualizes φ and shows the conformation for φ = 0.

Replacing the hexyl side chains by CH_3 hardly affects this arrangement. As a result, there is very little increase in free energy gain when the long alkyl sidechains are replaced by CH_3. Importantly, we do not observe a significantly lower minimum of the free energy for CT without sidechains as compared to TT without sidechains. Thus, the sidechains do not seem to be the decisive factor that renders TT more prone to aggregation than CT.

From the free energy curves obtained for the molecules with sidechains, we would, in fact, expect a stronger propensity to aggregation from CT, at variance with experiment. However, in the MD calculation of Figure 5a we considered a twisted dihedral potential in TT, which was derived from DFT calculations of a single molecule. In other words, the calculations did not take into account any possible planarization effects that may result from a change of the electronic structure caused by intermolecular interactions upon approximation. In fact, TT was found to planarize in the solid state.[40, 66] Therefore, it is conceivable that the molecule also planarizes when two of them approach in order to form an aggregate in solution, and this may need to be considered in the MD calculation. Thus we calculated the free energy between two TT molecules when the rotational potential of central bithiophene has a minimum for both sulphurs of the molecule pointing into the same direction ("cis") or opposite direction ("trans"). The result is shown in Figure 6. Allowing for a planarization of TT indeed results in significant energy gain upon aggregation. Compared to the conformation with a twisted central bithiophene, the cis conformation is favoured by 3.5 $k_B T$, and the trans-conformation is stabilized by 5.0 $k_B T$. Importantly, for both planar conformations the free energy is lower for TT as compared to CT. The same conclusion still applies when the sidechains are replaced by CH_3, as discussed in the ESI (Section 4).
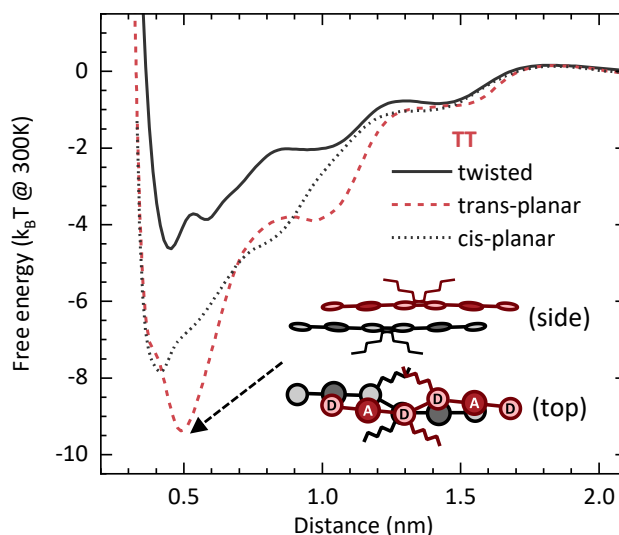
Figure 6: Free energy simulations of TT for the twisted conformation and both planar conformations. The sketch shows the intermolecular geometry for the trans-planar dimer with highest energetic stabilisation.

Allowing for a planarized central bithiophene unit thus results in a free energy curve that is consistent with the experimental observations. We also found that lack of steric hindrance by sidechains is not the reason for the strong tendency to aggregate that we see experimentally for TT. To understand in more detail what promotes the aggregation, we thus proceed to consider interactions between adjacent units in our model dimers. For TT, the final average configuration obtained by MD is illustrated as inset in Figure 6. In the trans-configuration, the molecules adopt a slight zig-zag shape and they arrange offset by one unit along the long molecular axis. As a result, five rings lie directly opposite each other. This comprises four pairs where an electron-rich thiophene is opposite an electron-poor benzothiadiazole, and one thiophene-thiophene pair. In contrast, for CT, there are less points of contact. For type A (Figure 5), only two benzothiadiazole rings lie opposite

each other. For type B, there is slightly more interaction, that is, two thiophene-benzothiadiazole pairs form and the central bithiophene-benzothiadiazole units lie adjacent such as to be able to interact. The interactions between these subunits is attractive, in particular for donor-acceptor type pairs, as already shown earlier[37] and detailed further in the ESI (Section 5). Thus, it appears that the stronger interaction in the TT dimer can be rationalized by its zig-zag like geometry that allows for more contact points where attractive interactions can take place.

Discussion

To summarize the insight gained from the MD simulations, we found that planarization of the TT molecule is essential to reproduce the experimental results. We can therefore say that a more planar structure, preferably trans-planar, is needed to promote aggregation. A temporarily more planar structure can itself be induced by the proximity of two molecules. For example, De Leener et al. performed a combination of molecular dynamics and quantum chemistry calculations for the polymer MEH-PPV.[33] They could show that conformational fluctuations are large for isolated molecules on short timescales. However, these fluctuations happen on longer timescales in the bulk, making polymer chains more planar on average once they are surrounded by other chains. It is conceivable that a similar mechanism contributes here to render the TT molecule more planar when a second molecule comes close, in addition to the electronic-structure-induced planarization discussed above. This would result in the planarity required to allow for persistent aggregation.

The amount of interaction between two adjacent molecules depends on the number of units that come close, and thus it depends on its shape. The MD calculations indicate that the slight zig-zag geometry of TT leads to more contact points than the banana shape of CT, and this seems to advance the propensity for aggregation. At first sight, this seems to be at variance with the results by Welch et al. [67] for related banana-shaped oligomers. They reported that a stronger bend angle is favourable for crystallization, while according to our results, a weaker bend angle inducing more contact points should seem advantageous. The resolution to this apparent contradiction lies in the overall symmetry of the arrangement. The banana-shaped oligomers addressed by Welch et al. arrange in a type A conformation. Here, attractive interactions can result from the contacts between acceptor units. However, the central unit does not contribute to this at a close distance. Rather, there is an unfavourable need to repel solvent molecules between the central units, and the interaction between the central units is itself repulsive (see ESI, Section 5).[37] A stronger bend angle here indeed alleviates this constraint while still preserving the acceptor interactions. The situation is different for the zig-zag geometry of TT, where the attractive interactions between the four donor-acceptor pairs dominate, or for type B of CT where the central units are also attractive.

5. Quantum chemical calculations

Having established what causes the stronger propensity of TT to aggregate, we reconsider the spectral signatures of both molecules. For TT, additional features appear simultaneously upon cooling in the absorption and the emission spectra, consistent with our interpretation of an H-type aggregate. The continuous reduction of the 0-0 peak with cooling in the aggregate emission (compare Figure 4c) can be understood as a sign of increasing strength of electronic interaction, as

13

observed earlier for instance in P3HT or PCPDTBT.[15, 16] In contrast, for CT, signs of aggregation emerged in the absorption spectra only below 200 K (Figure 3). The emission from the aggregate has a broad shape with a 0-0 peak that is slightly lower than the 0-1 peak, indicative of some H-like electronic interaction (Figure 4). However, the emission intensity in CT reduces already from 250 K onwards, even though no additional features appear in absorption or emission. The reduction of emission intensity suggests that an additional non-radiative decay channel opens up. We already mentioned that the most likely candidate for this is the formation of a non-emissive excimer. Such species that form as a precursor to aggregates have been reported before by Haedler et al. for pyrene-derivatives.[65] The formation of more weakly bound precursor species such as excimers would be consistent with the lower number of attractive contact points formed for CT. We have conducted time dependent density functional theory (TD-DFT) calculations to consider the electronic nature of possible dimers formed for TT and CT.

For this, we averaged the dimer structures from the MD simulations, focusing on the relevant conformations with minimal intermolecular distance. For TT we used only the trans-planar aggregate, while for CT we considered both, type A and type B conformers separately. Based on these, we have prepared dimers with one of the molecules on the ground state geometry and the other molecule on the first excited state geometry. These conformations served as starting points for TD-DFT geometry optimizations of the first excited state of the dimer without imposing any symmetry constraints. We thus monitor the structural relaxation of the dimer upon photoexcitation and internal conversion of one of the molecules and therefore the propensity of the aggregate to form excimer states.

Table 1: TD-DFT results for the optimized S1 state of each dimer for TT in the trans-planar conformation and CT type A and type B. We display visualizations of the dominant electron-hole pair natural transition orbitals, the corresponding transition energy, the oscillator strength (f), the charge transfer character (CTC), and the plane-to-plane distances for ground state and excited state.

	TT (trans)	CT (Type A)	CT (Type B)
Electron			
Hole			
Energy (eV)	1.69	1.56	1.68
f	0.0014	0.0000	0.21
CTC	0.23	0.00	0.39
Plane-to-plane distance (Å)			
Ground state	3.63	3.68	3.64
Excited state	3.66	3.48	3.52
Difference	+0.02	-0.20	-0.12

14

Table 1 shows the optimized geometries for all three dimers and the corresponding electron-hole pair natural transition orbitals. The relaxed excited state geometry for the TT dimer has a plane-to-plane distance of 3.66 Å, which is close to the ground state plane-to-plane distance of 3.63 Å. The natural transition orbitals delocalize over the whole dimer, yielding a small charge transfer character of 0.23, and the oscillator strength is low. This is consistent with experiment, as the emission intensity decreases significantly upon aggregation.

The picture is different for CT. Upon excitation, the dimer geometry relaxes such that the plane-to-plane distance decreases significantly. This is most pronounced for the type A conformation where the plane-to-plane distance reduces by 0.20 Å. The excitation is delocalized equally over both molecules of the dimer. Emission from this excited state has no charge transfer character, yet also no oscillator strength. The significant geometry change upon excitation, lack of charge transfer character and lack of oscillator strength imply that this is quasi a textbook example for a non-emissive excimer.[68] Moreover, it is also at lower energy than the type B conformation. For the type B dimer, we find a reduction in plane-to-plane distance still by 0.12 Å. The transition has a large charge transfer character, where the electron is localized mainly on one molecule and the hole is equally delocalized over both molecules of the dimer. The transition to the ground state has a finite oscillator strength. Between 250 K and 200 K we have not observed any emission feature that could be assigned to emission from type B dimers. Evidently, energy is funnelled to a type A excimer-like precursor, which accounts for the reduction in emission intensity, until emissive aggregates can form below 200 K.

6. High energy peak in TT

As a final point we consider briefly the emission feature observed in TT at 2.15 eV for all temperatures and all concentrations, even when diluting further to $5.0 \cdot 10^{-7}$ M (see ESI, Section 6). The fact that this shoulder is independent of concentration excludes intermolecular origins for this spectral feature. We note that this feature does not allow for a description of the overall emission spectra in terms of a single Franck-Condon-transition (see ESI, Section 7). However, assuming two very similar progressions at different energies gives a satisfactory description of the spectral shape. This is shown in Figure 7a exemplary for the 200 K emission spectrum. For both progression, we used a Gaussian linewidth of $\sigma=59$ meV and the same 3 vibrational energies at 55 meV, 135 meV and 180 meV as observed in the Raman spectra, that we tentatively associated with librations or rotations, C-H in plane bending modes on the rings and C=C stretching modes, respectively.[68] A detailed description of the fitting procedure and parameters is given in the ESI (Section 7). To identify the origin of the two features, we performed time-correlated single photon counting measurements at two energies at 200 K. Figure 7b shows the decay curves at 2.23 eV and at 1.89 eV as well as the instrument response function. Both features show about the same exponential decay of $\tau=2.2\pm0.2$ ns from about 1 ns onward. At shorter times, the signal at 2.23 eV is dominated by different contributions from the instrument response function. More precisely, Raman scattering of the 2850 cm^{-1} mode from the solvent takes place and contributes at very short times.[69] The same decay time at both energies excludes a transition from a possible higher energy state into a lower energy state. Rather, both features seem to pertain to very similar excited states. Dual emission from two states on the same chromophore such as S_1 and S_2 can be safely excluded as origin since the two

15

features differ by only 150 meV. After excitation into a S_2 state, internal conversion into S_1 would be very fast and outcompete radiative decay due to the energy gap law (Kasha's rule).
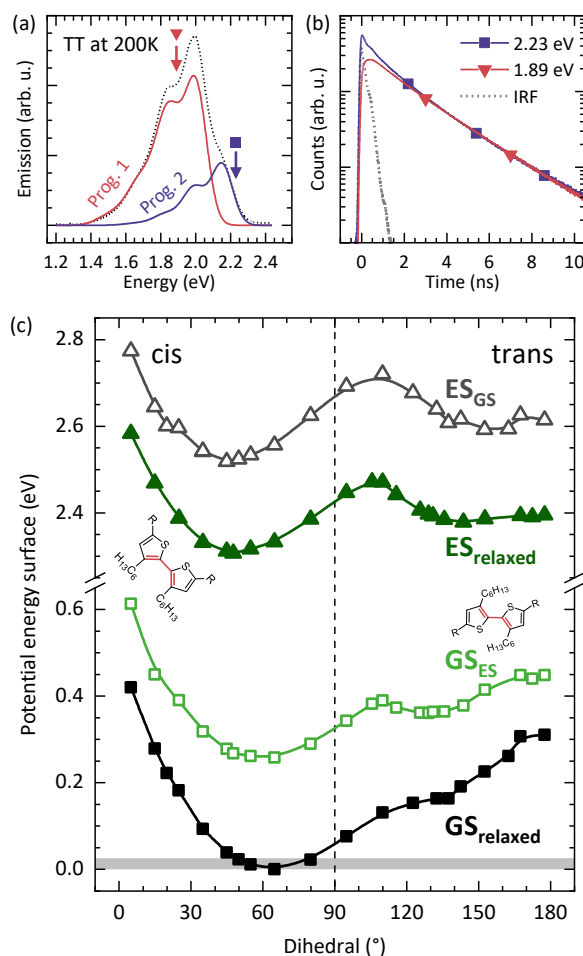
Figure 7: (a) Decomposition of the TT emission spectrum at 200 K into a low energy progression (progression 1) and a high energy progression (progression 2). The symbols mark the spectral positions of the decay curves. (b) Decay curves at 200 K monitored at the energies marked in (a). The grey broken line shows the instrumental response measured at the excitation energy. (c) Potential energy surface of the central thiophene-thiophene dihedral angle in TT for ground state (GS) and excited state (ES) obtained by DFT and TD-DFT. The calculations are performed in the relaxed geometries (filled symbols) and in the non-relaxed geometries after electronic transition (open symbols). The grey area indicates $k_B T$ at room temperature. The dashed line serves to separate the cis-like conformations visually from the trans-like configurations.

A further possibility is to consider that both conformations can be accessed after excitation. Figure 7c shows the potential energy surface for TT as a function of the dihedral angle between the two central thiophenes for the ground state (GS) and lowest excited state (ES) before and after relaxation subsequent to a transition. The S_0 to S_1 transition (absorption) occurs vertically from the $GS_{relaxed}$ curve to the ES_{GS} curve. In the relaxed GS, the conformation has a cis-like character. After the vertical transition, the molecule relaxes into the $ES_{relaxed}$ curve. In this process, it can relax to the cis-like mimium in the $ES_{relaxed}$ curve at 50° or to the trans-like minimum above 140°, from where they can

16

decay to the GS_{ES} curve with a slightly larger (cis-like) or smaller (trans-like) transition energy. Keeping in mind the limitations of DFT calculations for quantitative values for donor-acceptor type compounds, and recalling the case of polyacetylene,[70] we can still safely associate the cis-like configuration with the higher energy transition and the trans-like configuration with the lower energy transition. Thus, the high-energy shoulder we observe in TT is attributed to emission from oligomers where a cis-like configuration of the central bithiophene still prevails.

When wondering why there is no energy transfer to molecules in the trans-like configuration it is worth recalling that the minimum in the GS geometry is for the cis-like configuration, and the trans-like configuration is mostly accessed through the excited state. This explains why emission from both configurations can be observed.

7. Conclusions

In this study we address the role of backbone torsion and planarity in the formation of ordered structures using a pair of model oligomers with a twisted central bithiophene unit (TT) or a rigid central cyclopentadithiophene (CT). Unexpectedly, the more flexible TT is found more disposed to form weakly emissive H-type aggregates than planar CT. It turns out that the propensity of these oligomers to form ordered structures is not controlled by steric demands of their sidechains. Rather, it can be rationalized by considering the number of attractive interactions that can take place between the various subunits along the oligomer. In the MD calculations we find that the experimentally observed aggregation in TT can only be explained when TT is allowed to adopt planar conformation. In this case, the more zig-zag like backbone conformation of TT leads to a larger number of attractive interactions than the banana-shape of CT. This larger interaction accounts not only for the stronger tendency of TT to aggregate, but also can elucidate why TT directly forms emissive aggregates while CT, upon cooling, first forms non-emissive excimer-type precursors until aggregate formation sets in below 200 K.

Acknowledgements

Literature

1. D. Moseguí González, C. J. Schaffer, S. Pröller, J. Schlipf, L. Song, S. Bernstorff, E. M. Herzig and P. Müller-Buschbaum, *ACS Appl. Mater. Interfaces*, 2017, **9**, 3282-3287.
2. F.-J. Kahle, C. Saller, S. Olthof, C. Li, J. Lebert, S. Weiß, E. M. Herzig, S. Hüttner, K. Meerholz, P. Strohriegl and A. Köhler, *J. Phys. Chem. C*, 2018, **122**, 21792-21802.
3. G. Feng, J. Li, Y. He, W. Zheng, J. Wang, C. Li, Z. Tang, A. Osvet, N. Li, C. J. Brabec, Y. Yi, H. Yan and W. Li, *Joule*, 2019, **3**, 1765-1781.
4. N. Gasparini, S. Kahmann, M. Salvador, J. D. Perea, A. Sperlich, A. Baumann, N. Li, S. Rechberger, E. Spiecker, V. Dyakonov, G. Portale, M. A. Loi, C. J. Brabec and T. Ameri, *Adv. Energy Mater.*, 2019, **9**, 1803394.
5. Y.-s. Huang, S. Westenhoff, I. Avilov, P. Sreearunothai, J. M. Hodgkiss, C. Deleener, R. H. Friend and D. Beljonne, *Nat. Mater.*, 2008, **7**, 483-489.
6. T. A. Papadopoulos, L. Muccioli, S. Athanasopoulos, A. B. Walker, C. Zannoni and D. Beljonne, *Chem. Sci.*, 2011, **2**, 1025-1032.
7. A. Sharma, S. Athanasopoulos, P. C. Tapping, R. P. Sabatini, O. F. McRae, M. Müllner, T. W. Kee and G. Lakhwani, *J. Phys. Chem. C*, 2018, **122**, 23910-23916.
8. F. C. Krebs, S. A. Gevorgyan and J. Alstrup, *J. Mater. Chem.*, 2009, **19**, 5442-5451.
9. F. C. Krebs, T. Tromholt and M. Jørgensen, *Nanoscale*, 2010, **2**, 873-886.
10. R. Søndergaard, M. Hösel, D. Angmo, T. T. Larsen-Olsen and F. C. Krebs, *Mater. Today*, 2012, **15**, 36-49.
11. B. Qu and S. R. Forrest, *Appl. Phys. Lett.*, 2018, **113**, 053302.
12. J. Yang, Y. Lin, W. Zheng, A. Liu, W. Cai, X. Yu, F. Zhang, Q. Liang, H. Wu, D. Qin and L. Hou, *ACS Appl. Mater. Interfaces*, 2018, **10**, 22485-22494.
13. K. S. Wienhold, V. Körstgens, S. Grott, X. Jiang, M. Schwartzkopf, S. V. Roth and P. Müller-Buschbaum, *ACS Appl. Mater. Interfaces*, 2019, **11**, 42313-42321.
14. F. Panzer, H. Bässler and A. Köhler, *J. Phys. Chem. Lett.*, 2017, **8**, 114-125.
15. F. Panzer, M. Sommer, H. Bässler, M. Thelakkat and A. Köhler, *Macromolecules*, 2015, **48**, 1543-1553.
16. C. Scharsich, F. S. U. Fischer, K. Wilma, R. Hildner, S. Ludwigs and A. Köhler, *J. Polym. Sci., Part B: Polym. Phys.*, 2015, **53**, 1416-1430.
17. D. Raithel, S. Baderschneider, T. B. de Queiroz, R. Lohwasser, J. Köhler, M. Thelakkat, S. Kümmel and R. Hildner, *Macromolecules*, 2016, **49**, 9553-9560.
18. M. Reichenberger, J. A. Love, A. Rudnick, S. Bagnich, F. Panzer, A. Stradomska, G. C. Bazan, T.-Q. Nguyen and A. Köhler, *J. Chem. Phys.*, 2016, **144**, 074904.
19. M. Reichenberger, D. Kroh, G. M. M. Matrone, K. Schötz, S. Pröller, O. Filonik, M. E. Thordardottir, E. M. Herzig, H. Bässler, N. Stingelin and A. Köhler, *J. Polym. Sci., Part B: Polym. Phys.*, 2018, **56**, 532-542.
20. H. Huang, L. Yang, A. Facchetti and T. J. Marks, *Chem. Rev.*, 2017, **117**, 10291-10318.
21. N. E. Jackson, B. M. Savoie, K. L. Kohlstedt, M. Olvera de la Cruz, G. C. Schatz, L. X. Chen and M. A. Ratner, *J. Am. Chem. Soc.*, 2013, **135**, 10475-10483.
22. K. J. Thorley and I. McCulloch, *J. Mater. Chem. C*, 2018, **6**, 12413-12421.
23. W. Zhang, Z. Mao, N. Zheng, J. Zou, L. Wang, C. Wei, J. Huang, D. Gao and G. Yu, *J. Mater. Chem. C*, 2016, **4**, 9266-9275.
24. M. Levitus, K. Schmieder, H. Ricks, K. D. Shimizu, U. H. F. Bunz and M. A. Garcia-Garibay, *J. Am. Chem. Soc.*, 2001, **123**, 4259-4265.
25. J. Kärnbratt, M. Gilbert, J. K. Sprafke, H. L. Anderson and B. Albinsson, *J. Phys. Chem. C*, 2012, **116**, 19630-19635.
26. J. Gierschner and S. Y. Park, *J. Mater. Chem. C*, 2013, **1**, 5818.
27. A. Mishra and P. Bäuerle, *Angew. Chem. Int. Ed.*, 2012, **51**, 2020-2067.
28. Q. Yan, Y. Zhou, Y.-Q. Zheng, J. Pei and D. Zhao, *Chem. Sci.*, 2013, **4**, 4389.

18

29. Y. Liu, C. Mu, K. Jiang, J. Zhao, Y. Li, L. Zhang, Z. Li, J. Y. L. Lai, H. Hu, T. Ma, R. Hu, D. Yu, X. Huang, B. Z. Tang and H. Yan, *Adv. Mater.*, 2015, **27**, 1015-1020.

30. W. Chen, X. Yang, G. Long, X. Wan, Y. Chen and Q. Zhang, *J. Mater. Chem. C*, 2015, **3**, 4698-4705.

31. W. Chen and Q. Zhang, *J. Mater. Chem. C*, 2017, **5**, 1275-1302.

32. C. B. Nielsen, S. Holliday, H.-Y. Chen, S. J. Cryer and I. McCulloch, *Acc. Chem. Res.*, 2015, **48**, 2803-2812.

33. C. De Leener, E. Hennebicq, J.-C. Sancho-Garcia and D. Beljonne, *J. Phys. Chem. B*, 2009, **113**, 1311-1322.

34. Y. Sun, G. C. Welch, W. L. Leong, C. J. Takacs, G. C. Bazan and A. J. Heeger, *Nat. Mater.*, 2012, **11**, 44-48.

35. J. A. Love, C. M. Proctor, J. Liu, C. J. Takacs, A. Sharenko, T. S. v. d. Poll, A. J. Heeger, G. C. Bazan and T.-Q. Nguyen, *Adv. Funct. Mater.*, 2013, **23**, 5019-5026.

36. J. A. Love, I. Nagao, Y. Huang, M. Kuik, V. Gupta, C. J. Takacs, J. E. Coughlin, L. Qi, T. S. van der Poll, E. J. Kramer, A. J. Heeger, T.-Q. Nguyen and G. C. Bazan, *J. Am. Chem. Soc.*, 2014, **136**, 3597-3606.

37. A. Bourdick, M. Reichenberger, A. Stradomska, G. C. Bazan, T.-Q. Nguyen, A. Köhler and S. Gekle, *J. Phys. Chem. B*, 2018, **122**, 9191-9201.

38. J. E. Coughlin, A. Zhugayevych, I. Bakus, Ronald C., T. S. van der Poll, G. C. Welch, S. J. Teat, G. C. Bazan and S. Tretiak, *J. Phys. Chem. C*, 2014, **118**, 15610-15623.

39. G. C. Welch, L. A. Perez, C. V. Hoven, Y. Zhang, X.-D. Dang, A. Sharenko, M. F. Toney, E. J. Kramer, T.-Q. Nguyen and G. C. Bazan, *J. Mater. Chem.*, 2011, **21**, 12700.

40. C. Zhou, Q. Cui, C. McDowell, M. Seifrid, X. Chen, J.-L. Brédas, M. Wang, F. Huang and G. C. Bazan, *Angew. Chem.*, 2017, **129**, 9446-9449.

41. J.-D. Chai and M. Head-Gordon, *J. Chem. Phys.*, 2008, **128**, 084106.

42. M. J. Frisch, G. W. Trucks, H. B. Schlegel, G. E. Scuseria, M. A. Robb, J. R. Cheeseman, G. Scalmani, V. Barone, G. A. Petersson, H. Nakatsuji, X. Li, M. Caricato, A. V. Marenich, J. Bloino, B. G. Janesko, R. Gomperts, B. Mennucci, H. P. Hratchian, J. V. Ortiz, A. F. Izmaylov, J. L. Sonnenberg, Williams, F. Ding, F. Lipparini, F. Egidi, J. Goings, B. Peng, A. Petrone, T. Henderson, D. Ranasinghe, V. G. Zakrzewski, J. Gao, N. Rega, G. Zheng, W. Liang, M. Hada, M. Ehara, K. Toyota, R. Fukuda, J. Hasegawa, M. Ishida, T. Nakajima, Y. Honda, O. Kitao, H. Nakai, T. Vreven, K. Throssell, J. A. Montgomery Jr., J. E. Peralta, F. Ogliaro, M. J. Bearpark, J. J. Heyd, E. N. Brothers, K. N. Kudin, V. N. Staroverov, T. A. Keith, R. Kobayashi, J. Normand, K. Raghavachari, A. P. Rendell, J. C. Burant, S. S. Iyengar, J. Tomasi, M. Cossi, J. M. Millam, M. Klene, C. Adamo, R. Cammi, J. W. Ochterski, R. L. Martin, K. Morokuma, O. Farkas, J. B. Foresman and D. J. Fox, Gaussian 09 Rev. E.01, Gaussian, Inc., Wallingford, CT, 2013

43. S. Pronk, S. Páll, R. Schulz, P. Larsson, P. Bjelkmar, R. Apostolov, M. R. Shirts, J. C. Smith, P. M. Kasson, D. van der Spoel, B. Hess and E. Lindahl, *Bioinformatics*, 2013, **29**, 845-854.

44. M. J. Abraham, T. Murtola, R. Schulz, S. Páll, J. C. Smith, B. Hess and E. Lindahl, *SoftwareX*, 2015, **1-2**, 19-25.

45. S. Páll, M. J. Abraham, C. Kutzner, B. Hess and E. Lindahl, in *Solving Software Challenges for Exascale*, eds. S. Markidis and E. Laure, Springer International Publishing, 2015, pp. 3-27.

46. B. Hess, C. Kutzner, D. van der Spoel and E. Lindahl, *J. Chem. Theory Comput.*, 2008, **4**, 435-447.

47. N. Schmid, A. P. Eichenberger, A. Choutko, S. Riniker, M. Winger, A. E. Mark and W. F. van Gunsteren, *Eur. Biophys. J.*, 2011, **40**, 843.

48. P. Ertl, *J. Cheminformatics*, 2010, **2**, 1.

49. ATB Database: CT Structure and Toplogy Files, https://atb.uq.edu.au/molecule.py?molid=285451, (accessed June 2019).

50. ATB Database: TT Structure and Toplogy Files, https://atb.uq.edu.au/molecule.py?molid=285450, (accessed June 2019).

51. A. K. Malde, L. Zuo, M. Breeze, M. Stroet, D. Poger, P. C. Nair, C. Oostenbrink and A. E. Mark, *J. Chem. Theory Comput.*, 2011, **7**, 4026-4037.

19

52. S. Canzar, M. El-Kebir, R. Pool, K. Elbassioni, A. K. Malde, A. E. Mark, D. P. Geerke, L. Stougie and G. W. Klau, *J. Comput. Biol.*, 2013, **20**, 188-198.
53. K. B. Koziara, M. Stroet, A. K. Malde and A. E. Mark, *J. Comput. Aided Mol. Des.*, 2014, **28**, 221-233.
54. ATB Database: Hexane Structure and Toplogy Files, https://atb.uq.edu.au/molecule.py?molid=467, (accessed June 2019).
55. J. Kästner, *WIREs Comput. Mol. Sci.*, 2011, **1**, 932-942.
56. J. S. Hub, B. L. de Groot and D. van der Spoel, *J. Chem. Theory Comput.*, 2010, **6**, 3713-3720.
57. A. Barducci, G. Bussi and M. Parrinello, *Phys. Rev. Lett.*, 2008, **100**, 020603.
58. B. M. Dickson, *Phys. Rev. E*, 2011, **84**, 037701.
59. A. Laio and M. Parrinello, *Proc. Natl. Acad. Sci.*, 2002, **99**, 12562-12566.
60. A. Barducci, M. Bonomi and M. Parrinello, *WIREs Comput. Mol. Sci.*, 2011, **1**, 826-843.
61. G. A. Tribello, M. Bonomi, D. Branduardi, C. Camilloni and G. Bussi, *Comput. Phys. Commun.*, 2014, **185**, 604-613.
62. The PLUMED Consortium, *Nat. Methods*, 2019, **16**, 670-673.
63. W. Humphrey, A. Dalke and K. Schulten, *J. Mol. Grapics*, 1996, **14**, 33-38.
64. A. Köhler, S. T. Hoffmann and H. Bässler, *J. Am. Chem. Soc.*, 2012, **134**, 11594-11601.
65. A. T. Haedler, H. Misslitz, C. Buehlmeyer, R. Q. Albuquerque, A. Köhler and H.-W. Schmidt, *ChemPhysChem*, 2013, **14**, 1818-1829.
66. M. T. Seifrid, G. N. M. Reddy, C. Zhou, B. F. Chmelka and G. C. Bazan, *J. Am. Chem. Soc.*, 2019, **141**, 5078-5082.
67. G. C. Welch, I. Bakus, Ronald C., S. J. Teat and G. C. Bazan, *J. Am. Chem. Soc.*, 2013, **135**, 2298-2305.
68. A. Köhler and H. Bässler, *Electronic Processes in Organic Semiconductors: An Introduction*, Wiley-VCH Verlag GmbH & Co. KGaA, Weinheim, Germany, 2015.
69. F. F. Cleveland and P. Porcelli, *J. Chem. Phys.*, 1950, **18**, 1459-1461.
70. H. Eckhardt, *J. Chem. Phys.*, 1983, **79**, 2085-2086.

Electronic Supporting Information

What is the role of planarity and torsional freedom for aggregation in a π-conjugated donor-acceptor model oligomer?

Stefan Wedler[1], Axel Bourdick[2], Stavros Athanasopoulos[3], Stephan Gekle[2], Fabian Panzer[1],...Caitlin McDowell,[4] Thuc-Quyen Nguyen,[4] Guillermo C. Bazan[4], Anna Köhler[1,5]*

[1] Soft Matter Optoelectronics, Experimentalphysik II, University of Bayreuth, Bayreuth 95440, Germany.

[2] Biofluid Simulation and Modeling, Theoretische Physik VI, Universität Bayreuth, Bayreuth 95440, Germany

[3] Departamento de Física, Universidad Carlos III de Madrid, Avenida Universidad 30, 28911 Leganés, Madrid, Spain.

[4] Center for Polymers and Organic Solids, Departments of Chemistry & Biochemistry and Materials, University of California, Santa Barbara

[5] Bayreuth Institute of Macromolecular Research (BIMF) and Bavarian Polymer Institute (BPI), University of Bayreuth, 95447 Bayreuth, Germany.

*e-mail: Anna.Koehler@uni-bayreuth.de

1

1   Methodical details of Simulations

As described in the main text, we used the *automated force field topology builder and repository* [1-3] to get starting force field models for CT[4] and TT[5] which we refined with our own calculations to better reflect the physical properties of the molecules. The model for the solvent Hexane[4] was taken from ATB directly.

Determination of partial charges

To make the models more accurate we calculated the charge distribution for CT and TT with Gaussian09, Revision E.01.[6] We requested tight convergence in geometry optimization and used an ultrafine integration grid. We refined the charge distribution by incorporating charges which were calculated via ground state structure optimization with the Mullikan fitting scheme with the help of Gaussian.

Determination of dihedral potential energy surfaces

The donor and acceptor units of the molecules CT and TT consist of aromatic rings, which are connected via single C-C bonds. To accurately reproduce the aggregation properties, we calculated the potential energy surfaces (PES) of the dihedral angles between the donor and acceptor units for the relevant fragments with quantum chemical calculations. Relaxed potential energy scans were used. We scanned from 0° to 180° in intervals of 5°. We reused the PES data from our previous work,[7] because the fragments in question are the same as for previously investigated systems, for which we used the CAM-B3LYP long-range corrected functional with the 6-31G** basis set. We adjusted our MD models to reproduce the calculated PES by implementing Ryckaert-Bellemans Potentials.

The defining characteristic of TT lies in its twisted geometry. The central donor unit consists of two thiophene units with a hexane side-chain attached to both which determines the resulting structure. To accurately describe the central dihedral, we used the long-range corrected functional *wB97xD*. We determined the long-range correction parameter to be 0.13 bohr^{-1} via the condition

$$IP = -\varepsilon_{HOMO}$$

where IP denotes the ionization energy for the ground state geometry and ε_{HOMO} is the energy of the highest occupied molecular orbital and used that value for the PES scan. The calculated PES is displayed in Figure 7 in the main text (GS$_{relaxed}$). We also calculated the PES for the first excited state (GS$_{ES}$). For each configuration we also calculated the vertical transition energies in order to obtain the graphs for ES$_{relaxed}$ and ES$_{GS}$ in Figure 7.

The models without side chains were made based on the models of the full systems. The side chains were cut off and replaced by CH$_3$ groups. The charge distribution was adjusted near the points of intersection to ensure a vanishing net charge.

2

The planarized TT models were constructed by replacing the twisted central potential in order to force the molecule in the desired orientation with the potential:

$$V(\varphi) = k(1 + \cos(n\varphi - \varphi_s))$$

The intramolecular dihedral angle is denoted as φ. The multiplicity n was set to 1, the force constant k was chosen to be 100 kJ/mol and φ_s was chosen to get a cis- or trans-planar configuration accordingly.

We extracted average configurations from our MD simulations. Because the molecules rotate and move during the simulation, for each time frame we constructed a coordinate system inside the reference frame of the molecule, then transformed the whole simulation box to this coordinate system in which we averaged the position of the solute molecule. This approach works, as long as no aromatic rings flip, because then one would average two different configurations which would skew the final structure. We therefore chose a suitable window for the averaging process in which no flips occur.

To better visualize the dimer conformations, we created rotating video clips of these average configurations of the most stable dimers. For this, the structures are averaged over 10 ns. For clarity of presentation, the sidechains have been replaced with CH_3 groups. For orientation, sulfur atoms are marked in yellow, nitrogen in blue.

Parameters for MD simulations and free energy calculations

The parameters used for all MD simulations are displayed in Table S1.1.

Table S1.1: The Gromacs parameters used for the MD simulations.

Option	Value
Integrator	Md
dt	0.002
Nstxout	200
constraint_algorithm	lincs
constraints	h-bonds
lincs_iter	1
lincs_order	4
ns_type	Grid
nstlist	15
rlist	1.0
rcoulomb	1.0
rvdw	1.0
coulombtype	PME
tcoupl	v-rescale
tau_t	0.1
pcoupl	Berendsen
pcoupltype	isotropic
tau_p	2.0
ref_p	1.0
compressibility	4.5e-5
pbc	xyz

DispCorr	EnerPres
gen_seed	-1

For all free energy graphs shown in the main text, which were made with umbrella sampling, we swept the reaction pathway multiple times independently to ensure a sufficient sampling of the whole configurational phase space. All free energy graphs shown in the main text were made with umbrella sampling by sampling the reaction pathway multiple times independently to ensure a sufficient sampling of the whole configurational phase space. The details for the individual simulations are presented in the following. To give the system time to equilibrate, we cut off the first 200 ps of each window for each simulation.

To calculate the distance between two molecules during an aggregation process, we used the distance between the two molecules as the reaction coordinate. For TT, we defined this as the distance of the center of mass of the central donor units, for CT we used the center of mass of the central ring of the central donor units.

4
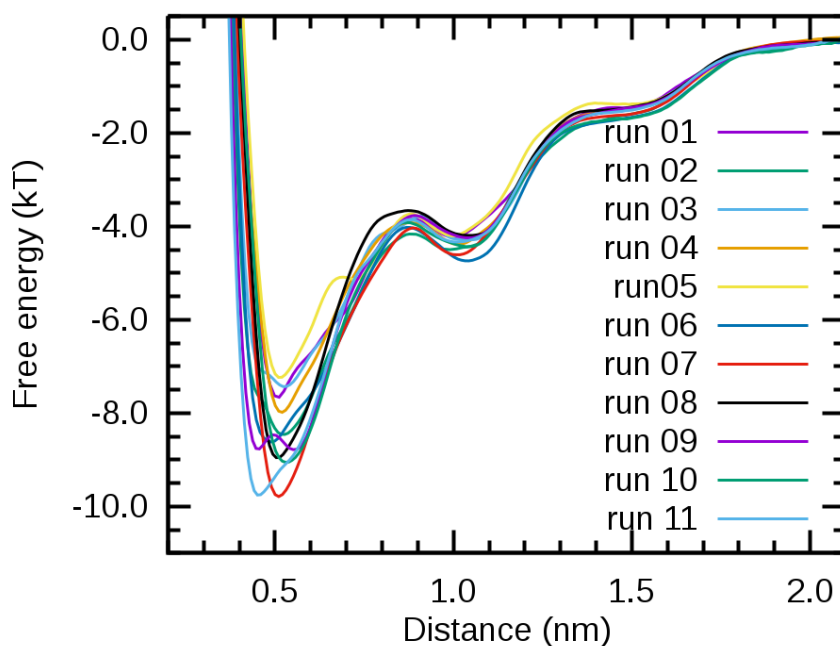
Figure S1.1: All individual free energy graphs for CT. The number of the run corresponds to the parameters defined in Table S1.2.

The free energy of CT with sidechains as displayed in Figure 5c in the main text was made from eleven individual simulations, in all of which the reaction coordinate was sampled independently. The parameters for the individual simulations are shown in Table S1.2. The individual free energy graphs are displayed in Figure S1.1.

Table S1.2: Parameters used in the individual free energy simulations for CT, which are combined to the free energy in Figure 5c in the main text.

Number	Time per window (ns)	Number of windows	Force constant (kJ/mol)	Number hexane molecules
1	60 – 80	44	1200	1100
2	60 – 120	33	1100 - 1200	500
3	60 - 120	33	1100 – 1200	500
4	450	33	1000 – 1200	500
5	100 - 140	33	1000 – 1200	500
6	200	35	800	600
7	200	35	800	600
8	200	34	1000	500
9	380	35	1000	500
10	200	32	1000	450
11	200	33	1000	450

5
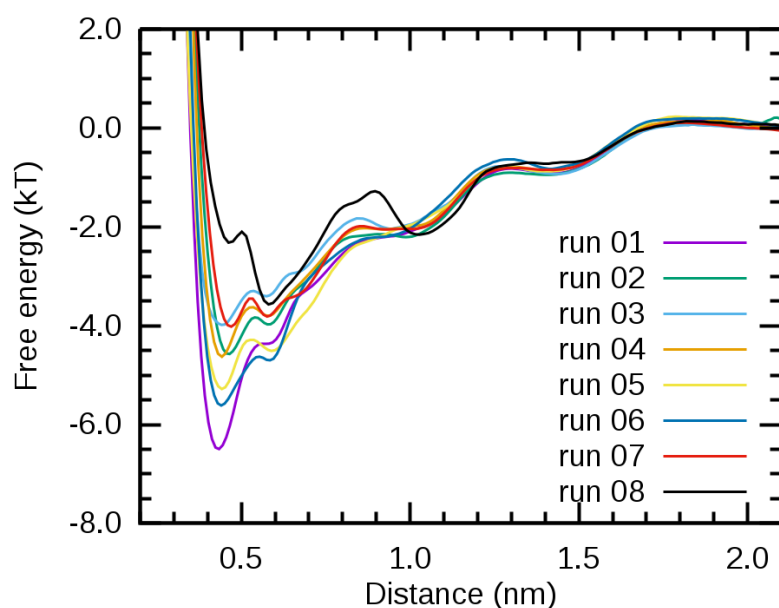
Figure S1.2: The curves used in the individual free energy calculations for TT are displayed here. They are combined to get the full free energy profile displayed in Figure 5a in the main text.

For TT, we combined eight individual free energy calculations. The parameters for each run are shown in Table S1.3 and the corresponding graphs in Figure S1.2. All these simulations were combined to yield the full free energy graph shown in Figure 5a in the main text.

Table S1.3: The parameters used in the individual free energy calculations for TT. They are combined to get the full free energy profile displayed in Figure 5a in the main text.

Number	Time per window (ns)	Number of windows	Force constant (kJ/mol)	Number hexane molecules
1	300	41	1000	600
2	300	34	1000	500
3	200	35	1000	500
4	800	42	1000	800
5	100 – 200	30	1000 – 1200	600
6	80 – 100	34	1000 – 1200	600
7	200 – 760	32	1000 – 1200	600
8	80	47	1200	1100

6
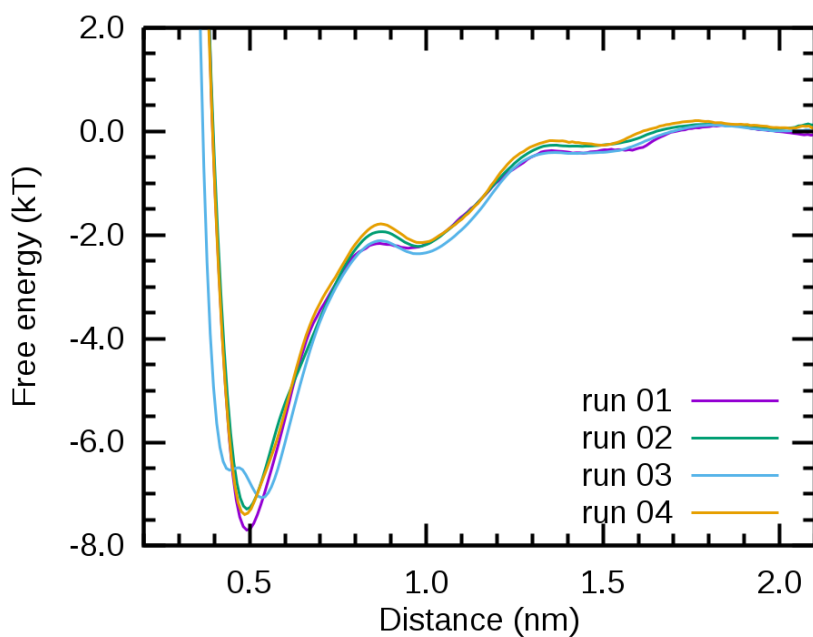
Figure S1.3: Individual free energy calculations used for CT with CH_3 sidechains.

The models without side-chains required less intense sampling, because the absence of them significantly reduces the possible configurational phase space of the system resulting in faster convergence. For CT without side-chains (shown in Figure 5c in the main text) we combined four independent free energy samplings, the parameters of which are displayed in Table S1.4 with their graphs shown in Figure S1.3.

Table S1.4: For CT with CH_3 sidechains we combined four individual free energy calculations, the parameters of which are shown here.

Number	Time per window (ns)	Number of windows	Force constant (kJ/mol)	Number hexane molecules
1	400	33	1000	600
2	180	32	1000	450
3	200	32	1000	450
4	200	30	1000	450

7
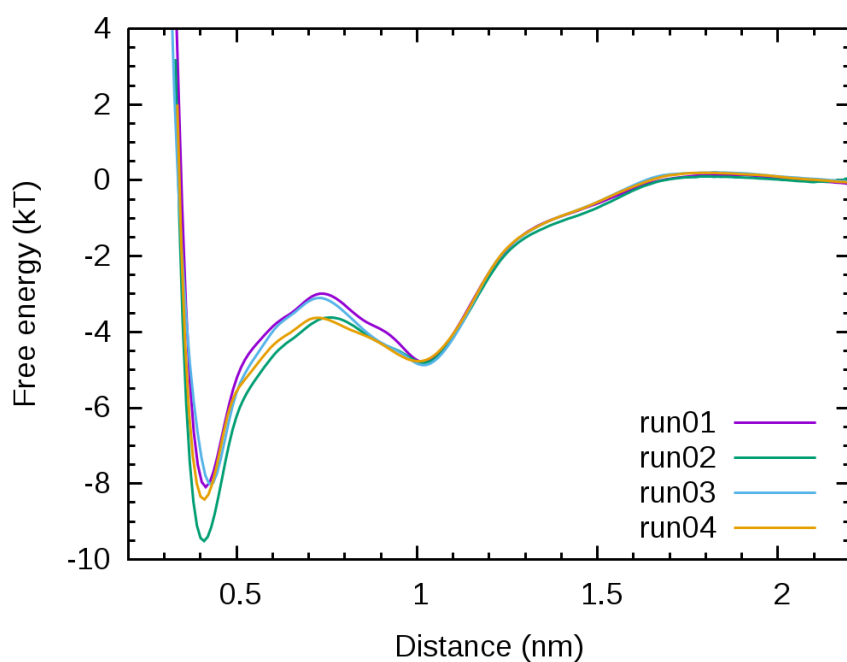
Figure S1.4: Individual free energy calculations used for TT with CH$_3$ sidechains.

For TT without side-chains we also combined four individual samplings of the reaction coordinate to yield the whole free energy graph shown in Figure 5a of the main text. The parameters are shown in Table S1.5 with their corresponding graphs displayed in Figure S1.4.

Table S1.5: Parameters used in the individual free energy calculations for TT with CH$_3$ sidechains. They are combined to get the full free energy profile displayed in Figure 5a in the main text.

Number	Time per window (ns)	Number of windows	Force constant (kJ/mol)	Number hexane molecules
1	400	34	800	650
2	220	35	800	600
3	400	35	900	650
4	250	37	800	650

8

Free energy error analysis

With the *Weighted Histogram Analysis Method* (WHAM), the free energy is calculated for small windows individually, after which they are combined to span the whole parameter space of the reaction coordinate. The statistical error of this recombination process can be estimated with a bootstrap analysis.[8] The results from the error analysis are shown in Figure S1.5
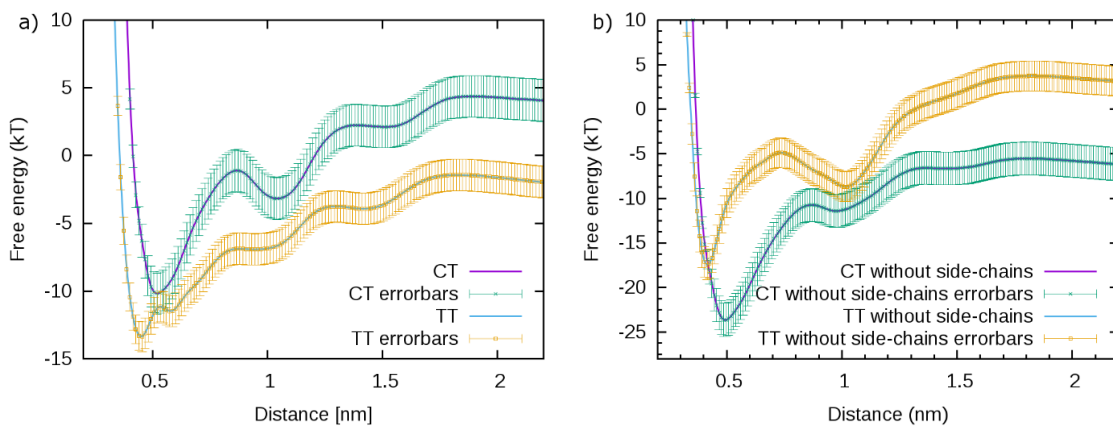
Figure S1.5: a) Free energy of CT and TT with hexyl sidechains with error bars from bootstrap analysis. b) Free energy of CT and TT with CH_3 sidechains with error bars from bootstrap analysis.

9

Metadynamics results

To distinguish the free energy of type A and type B aggregation in CT we employed well-tempered metadynamics to calculate the free energy in dependence of the distance between the molecule and their relative intermolecular orientation simultaneously. The result is presented in Figure S1.6. The offset can be chosen arbitrarily as only free energy differences determine which process can happen spontaneously. For the metadynamics plots we set the zero point to the global minimum. To describe the relative orientation of the two molecules, we defined a dihedral angle consisting of the outer most C atoms of the central donor units for both molecules.
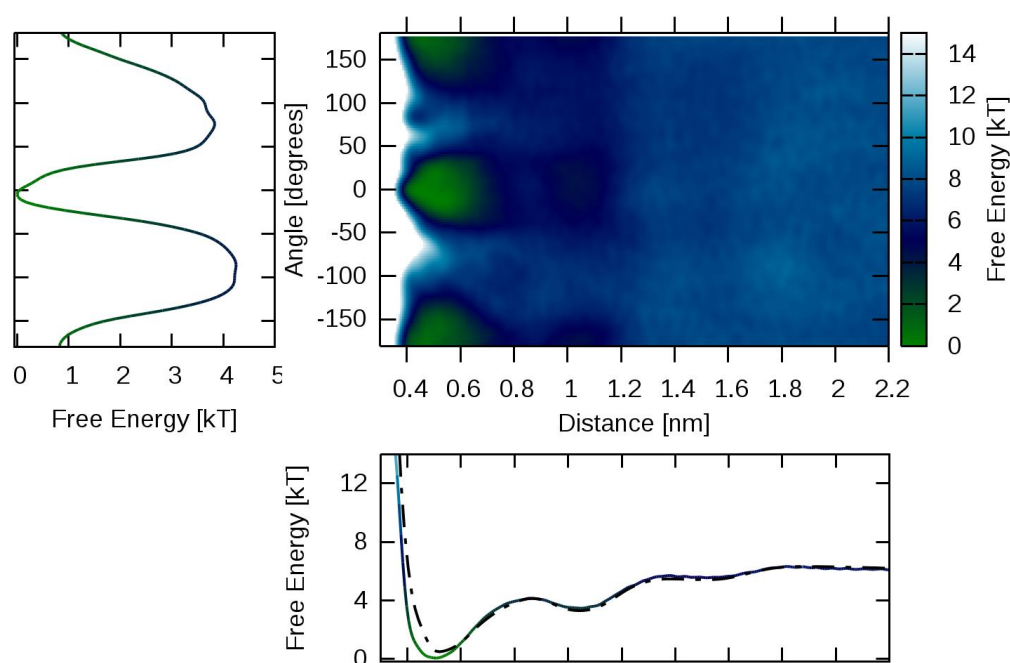
Figure S1.6: Two-dimensional free energy surface of two CT molecules in Hexane in dependence of distance and intermolecular angle calculated with metadynamics. The projections on the one-dimensional reaction coordinates are shown. The dashed line in the distance plot corresponds to the free energy calculated by umbrella sampling (Figure 5c in the main text). Here we placed zero energy to the potential minimum rather than at infinity.

The minima for type A and type B aggregates are at the same energy in the two-dimensional plot. When integrating out over all distances to get the global angular dependence, there is a small energetic difference between type A and type A aggregates of about 0.7 kT.

For the sake of completeness, we also calculated the free energy with metadynamics for TT in Hexane, shown in Figure S1.7. The angular dependence between the molecules is more complicated, probably due to the intramolecular rotational degree of freedom. There is a clear global minimum at about 180°, which corresponds to the configuration we identified in the main text. The comparison

with the free energy in dependence of distance calculated with umbrella sampling shows excellent agreement.
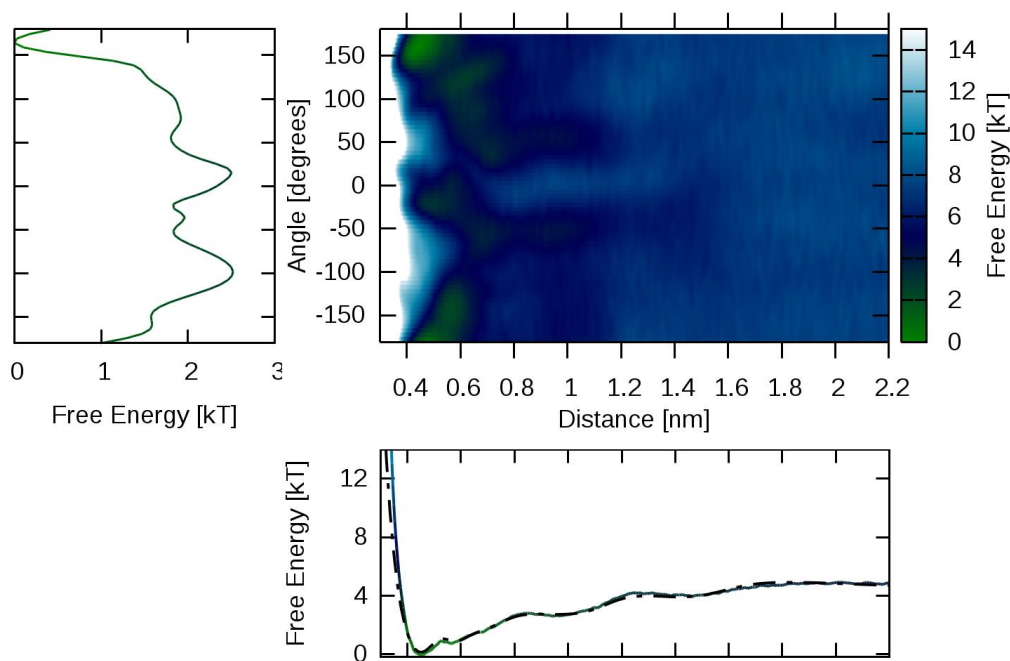
Figure S1.7: Two-dimensional free energy surface of two TT molecules in Hexane in dependence of distance and intermolecular angle calculated with metadynamics. The projections on the one-dimensional reaction coordinates are shown. The dashed line in the distance plot corresponds to the free energy calculated by umbrella sampling (Figure 5a in the main text). Here we placed zero energy to the potential minimum rather than at infinity.

2 Franck-Condon analysis of CT absorption spectra

Fitting procedure

Absorption and emission spectra can be modelled using a simple Franck-Condon description. This allows determining the energetic position of the 0-0 transition, the linewidth and the coupling of the transition to intramolecular vibrations. The intensity of emission I_{PL} and absorption I_{Abs} for several contributing vibrational modes is the sum of all transitions from the vibrational level $(0,0,\dots) \rightarrow (m_1, m_2, \dots)$ and given by[9]

$$\frac{I_{PL}(E)}{(n \cdot E)^3} \propto \sum_{m_i} \prod_i \frac{S_i^{m_i} \exp(-S_i)}{m_i!} \Gamma\left[\left(E - \left(E_0 - \sum_i m_i E_i^{\text{vib}}\right)\right)\right]$$

$$\frac{I_{Abs}(E)}{n \cdot E} \propto \cdot \sum_{m_i} \prod_i \frac{S_i^{m_i} \exp(-S_i)}{m_i!} \Gamma\left[\left(E - \left(E_0 + \sum_i m_i E_i^{\text{vib}}\right)\right)\right]$$

with photon energy E, refractive index n of the surrounding medium (assumed to be constant for dilute solutions), energy of the 0-0 transition E_0, vibrational energy E_i^{vib} and Huang-Rhys factor S_i of the i-th contributing vibrational mode. The factors $(n \cdot E)^3$ in emission and $n \cdot E$ in absorption take the photon density of states into account. $\Gamma(E)$ is the line shape function and assumed as purely Gaussian:

$$\Gamma(E) = \exp\left(-\frac{(E)^2}{2\sigma^2}\right)$$

We get the energies of the vibrational modes from the Raman spectra of both molecules, which are shown in Figure S2.1.
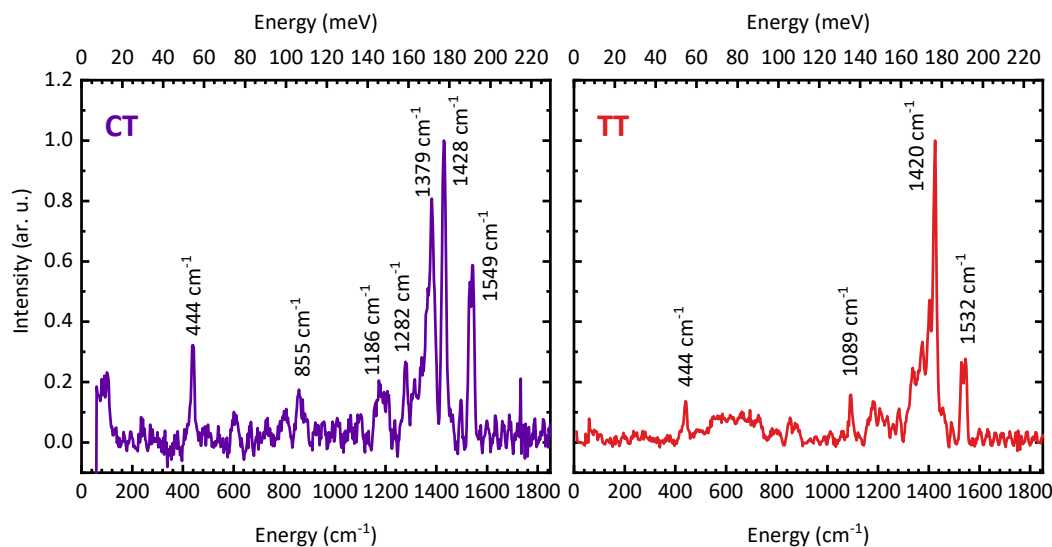
Figure S2.1: Raman spectra of CT and TT. The most prominent modes are labelled with their energies.

For CT we use the modes at 444 cm^{-1} (55 meV), 855 cm^{-1} (106 meV), 1412 cm^{-1} (175 meV) and 1549 cm^{-1} (192 meV), for TT in section 7 we use the modes at 444 cm^{-1} (55 meV), 1089 cm^{-1} (135 meV) and 1452 cm^{-1} (180 meV). Close-by vibrational modes are treated as effective modes in both cases.

Fitting results of the absorption of CT in hexane (5.0·10⁻⁶ M)

We start modelling the spectrum at 200 K. The resulting parameters are then used as starting point for the next temperature, where we mainly varied the energy of the 0-0 transition and the width of the Gaussian line shape. This procedure is then sequentially repeated for all remaining temperatures, varying the Huang-Rhys parameters as little as possible. The final parameters are shown in Table S2, the spectra with the modelled curves are displayed in Figure S2.2 along with the 0-0 transition and the first vibronic transitions. The results clearly show that the linewidth varies strongly with temperature, in contrast to the Huang-Rhys parameters, which mostly remain constant. Therefore, the changes in σ can account for the apparent change in peak ratios.

Table S2: Fitting parameters and resulting reorganization energies of absorption spectra of CT in hexane (5.0·10⁻⁶ M)

Temperature (K)	E_0 (eV)	σ (meV)	S 55 meV	S 106 meV	S 175 meV	S 192 meV	λ (meV)
200	2.014	52.00	0.1141	0.5273	0.1262	0.3420	149.9
210	2.020	53.12	0.1141	0.5273	0.1262	0.3420	149.9
220	2.024	54.31	0.1176	0.5299	0.1269	0.3420	150.5
230	2.029	55.96	0.1314	0.5299	0.1269	0.3419	151.2
240	2.032	57.13	0.1314	0.5382	0.1269	0.3530	154.3
250	2.037	58.38	0.1314	0.5382	0.1269	0.3530	154.3
260	2.040	60.19	0.1314	0.5407	0.1269	0.3670	157.2
270	2.046	61.49	0.1314	0.5407	0.1269	0.3670	157.2
280	2.050	62.22	0.1314	0.5407	0.1269	0.3670	157.2
290	2.054	63.82	0.1314	0.5611	0.1269	0.3714	160.2
300	2.057	64.29	0.1314	0.5643	0.1269	0.3714	160.6
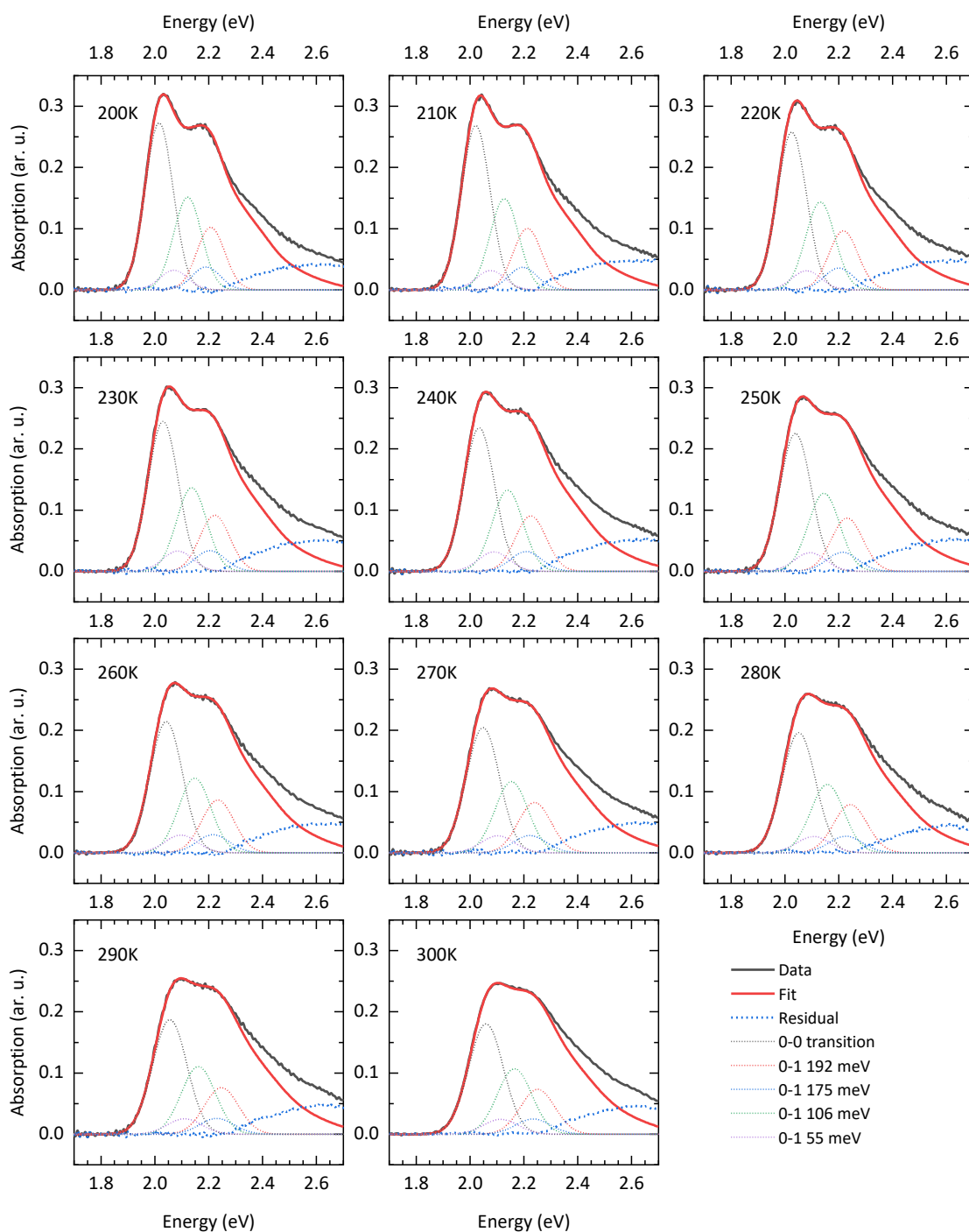
Figure S2.2: Franck-Condon fits of CT absorption spectra in hexane (5.0·10^{-6} M) for different temperatures. The position of the 0-0 transition as well as the first vibronic transitions are shown in dotted lines.

14

3 CT absorption and emission spectra in separate graphs

In the manuscript we compare the spectral shapes at fixed temperatures for different concentrations. We showed them in a tidy and compact format. However, direct comparison may be difficult. Here we show the same data, but plot spectra for different concentrations at the same temperature in a joint graph.
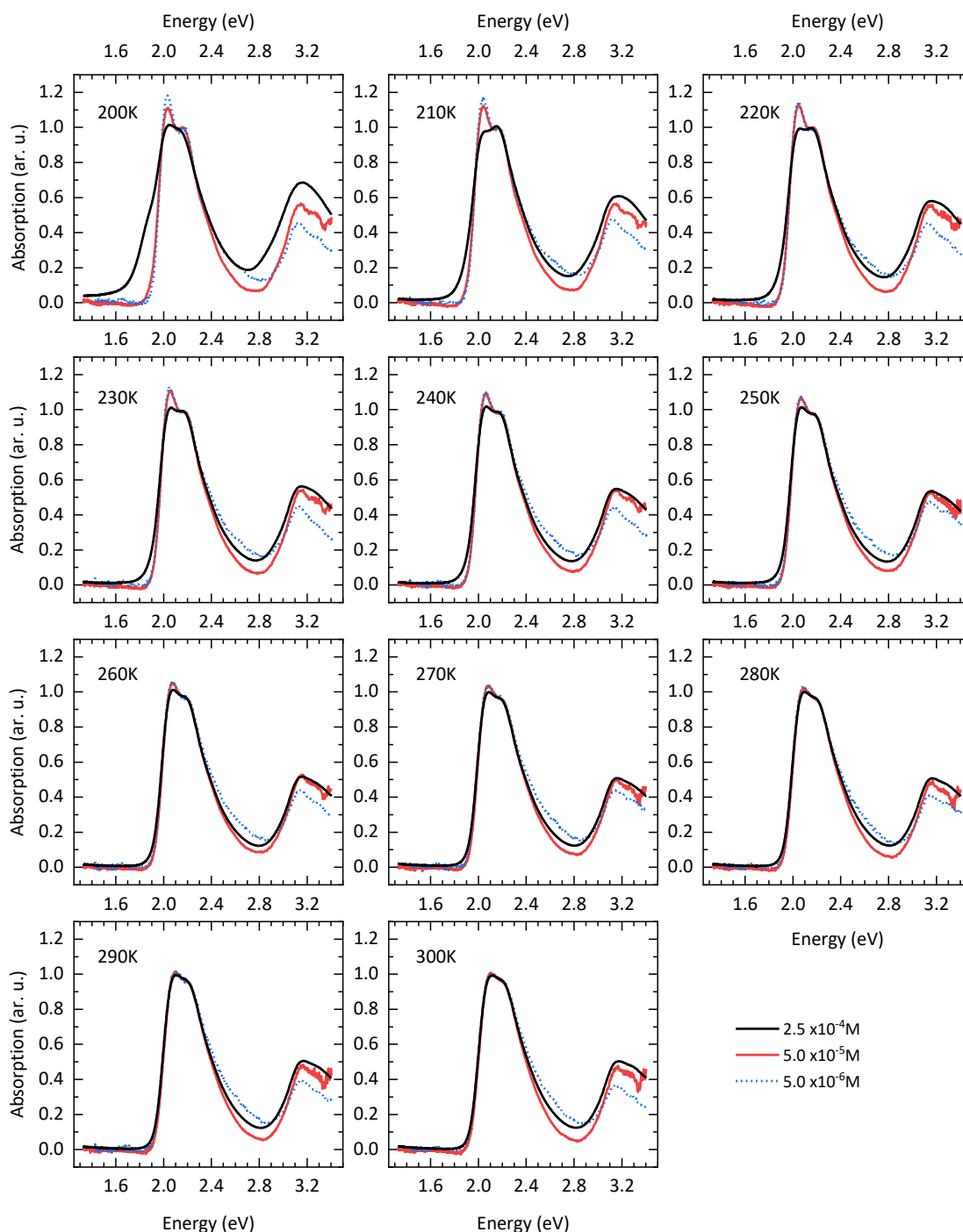
Figure S3.1: Absorption of CT in hexane at different temperatures and concentrations normalized to the vibronic 0-1 transition.
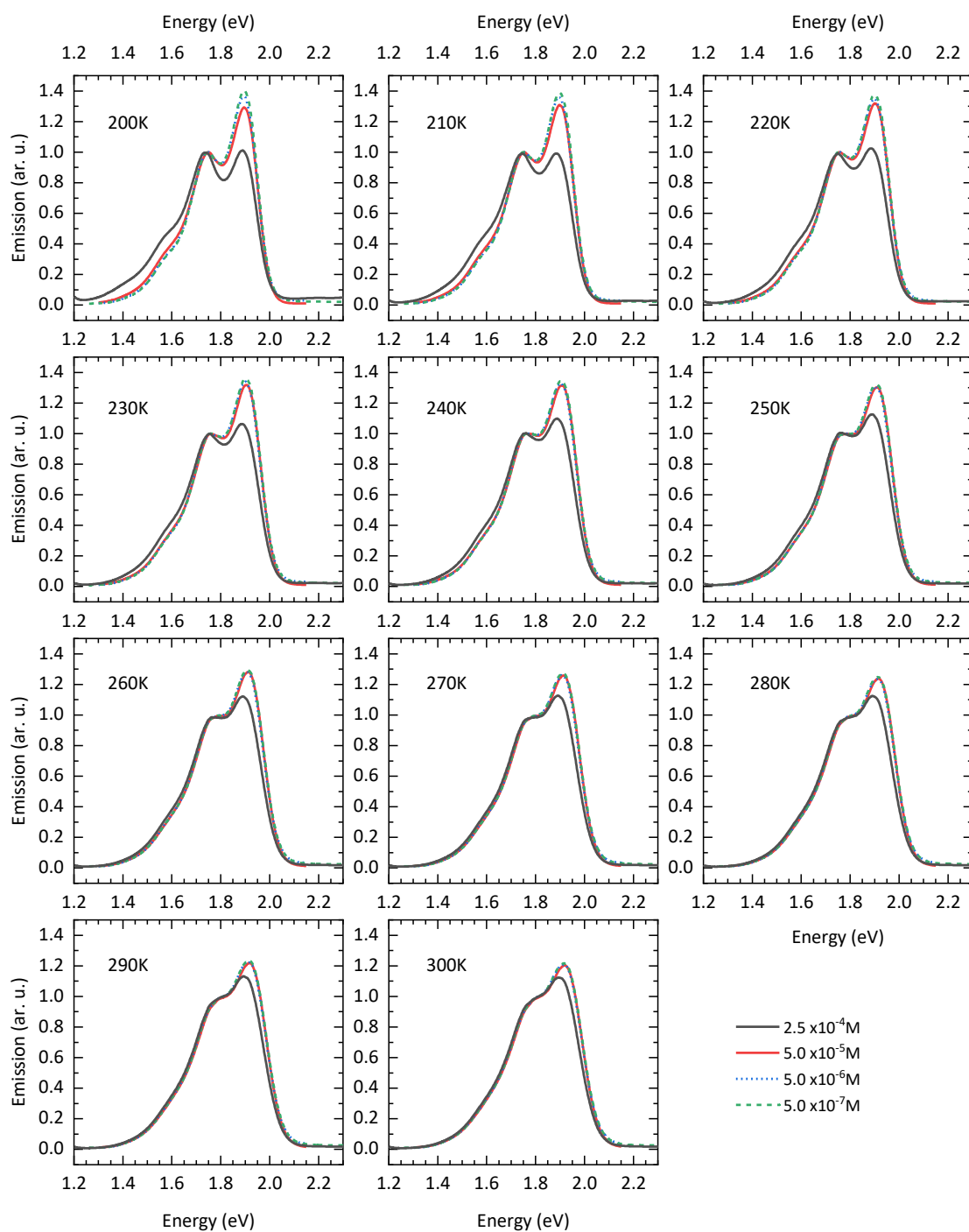
Figure S3.2: Emission of CT in hexane at different temperatures and concentrations normalized to the vibronic 0-1 transition. We additionally measured at a concentration of 5.0×10^{-7} M to safely exclude the possibility of aggregation for all higher concentrations.

16

4 Comparison of planarized TT with CH3 sidechains

In the main text we compared TT with full hexyl sidechains and CT with full hexyl sidechains when TT is allowed to adopt a planar conformation. We concluded that planarization in TT can account for the strong aggregation behaviour as observed experimentally. For CT, a possible steric influence of the central sidechains on the weak preference was excluded in the manuscript as well. To round off the picture, we performed free energy calculations for TT dimers with CH_3 sidechains, allowing the molecules to planarize either into the cis conformation or the trans conformation. Figure S4 shows the result. Again, allowing both molecules to planarize simultaneously results in a strong energetic preference of the planar dimer. Interestingly, now the cis conformation is strongly preferred by 6 k_BT, whereas the trans conformation becomes less favoured by 2 k_BT. The depth of the global minimum of the free energy for the trans conformation is comparable to the corresponding global minimum for CT with CH_3 sidechains. This means that TT still has an enormous energetic advantage to form dimers when allowed to adopt planar conformations, compared to CT.
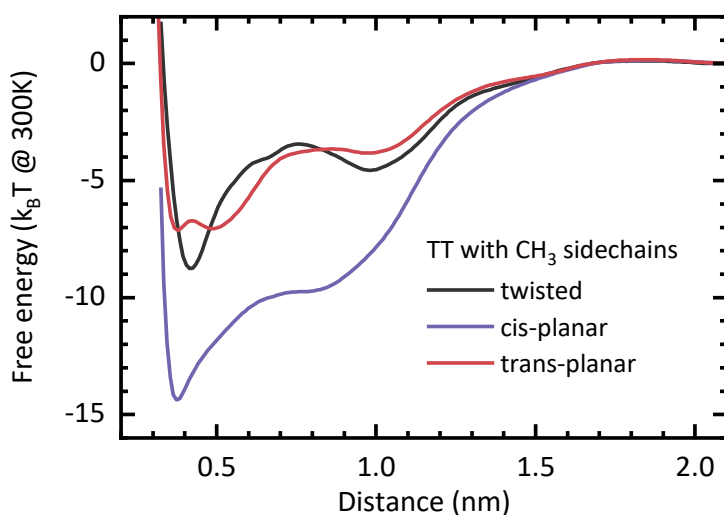
Figure S4: Free energy calculations for the TT dimer with CH_3 sidechains. Both molecules of the dimer adopt either a twisted dihedral angle, a cis-planar conformation or a trans-planar conformation.

5 Interactions between the molecular subunits

Following earlier work[7] we discuss the mutual interactions between the different building blocks of the molecules. Bourdick et al. conducted their calculations in the solvent MTHF. We repeat the calculations in the solvent hexane for the subunits, which are relevant for CT and TT. The results are shown in Figure S5. For clarity of presentation and in order to have a constant reference point at infinity, we removed the ideal contribution of $2k_\mathrm{B}T \cdot \ln r$, which is due to an increase in volume. As the configurational phase space of the individual parts is small, the graphs presented only consist of a single sweeping of the reaction coordinate. We simulated each window between 200 ns and 300 ns.
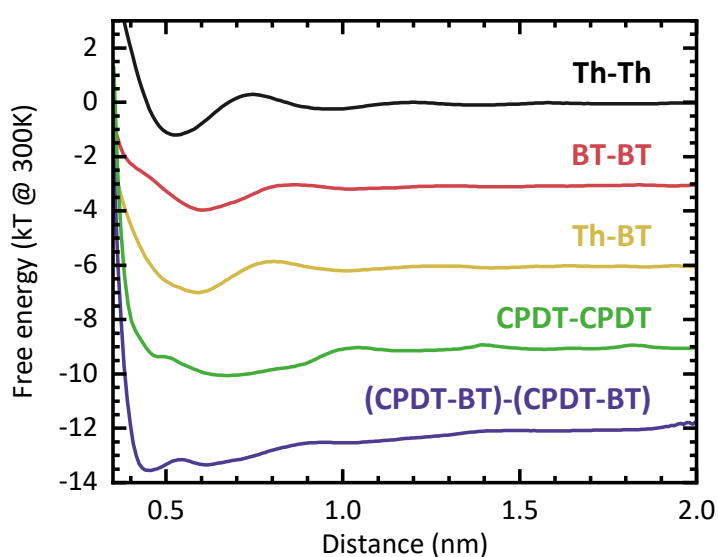
Figure S5: Free energy calculations between the different building blocks in hexane. The units are thiophenes (Th), fluorinated benzothiadiazole (BT), cyclopentadithiophene (CPDT) and a combination of the latter two (CPDT-BT).

18

6 TT Emission spectra in separate graphs
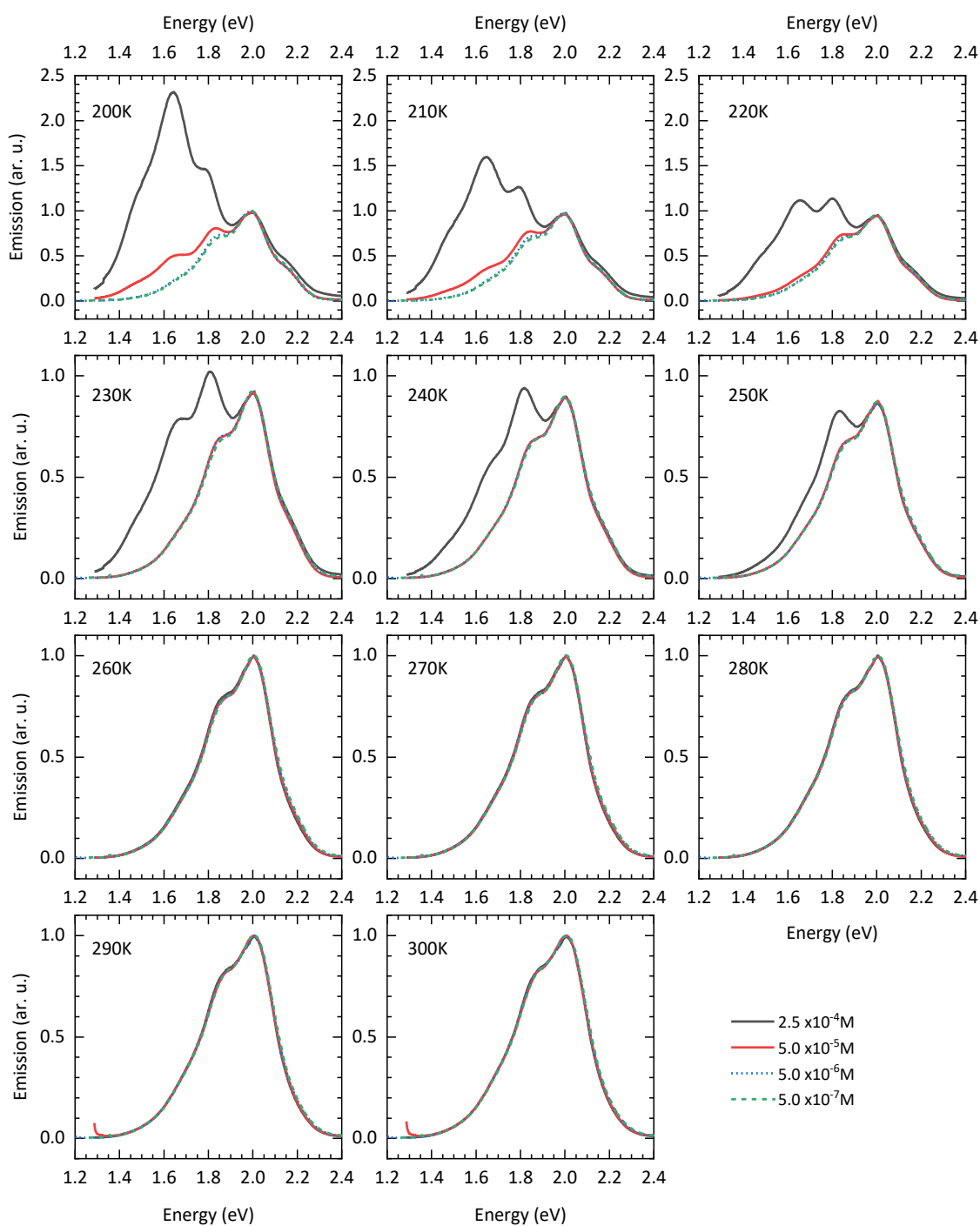
Figure S6: Emission of TT in hexane at different temperatures and concentrations normalized to the peak at 2.0 eV. We additionally measured at a concentration of 5.0×10^{-7} M to safely exclude the possibility of aggregation for all higher concentrations.

7   Franck-Condon analysis for emission spectra of TT

The emission of TT in hexane features a shoulder on the blue side of the spectra, even for the lowest concentration as shown in the previous section. A description of the spectra utilizing a single vibronic progression is incompatible with this spectral feature, as shown in Figure S7.1 for different cases exemplarily at 200 K.
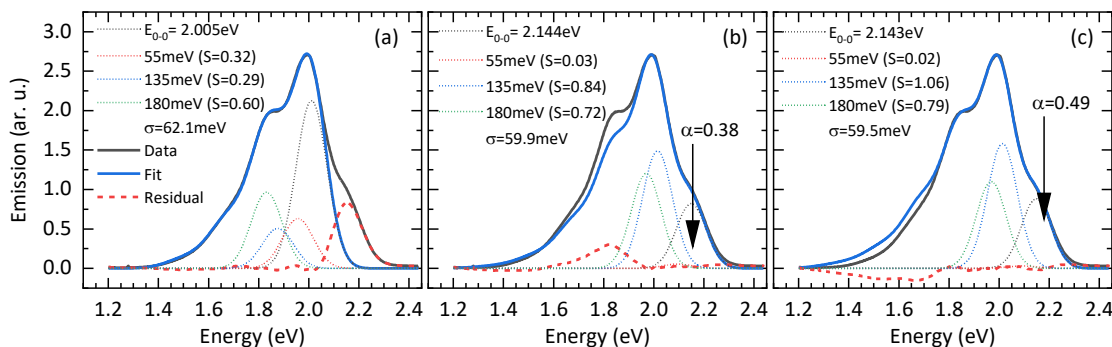
Figure S7.1: Emission of TT in hexane (5.0·10⁻⁶ M) at 200 K with best fits using a single Franck-Condon progression with (a) the 0-0 transition at the dominant peak, (b) with suppressed 0-0 transition and best fit of the red side, and (c) with suppressed 0-0 transition and best fit up to the second vibronic peak at 1.8 eV. The caption contains the fitting parameters. For (b) and (c) the 0-0 suppression factor α is indicated. For details see text.

In case (a) we chose the 0-0 transition energy that it matches the dominant peak at 2.0 eV. This approach entirely fails to describe the blue shoulder. In the other cases we chose a modified Franck-Condon progression, where the amplitude of the 0-0 transition is multiplied with the factor α to account for suppression effects due to H-type interactions:[10]

$$\frac{I_{PL}(E)}{(n \cdot E)^3} \propto e^{-S} \cdot \left(\alpha \Gamma(E - E_0) + \sum_{m_i \neq 0} \prod_i \frac{S_i^{m_i}}{m_i!} \Gamma\left[\left(E - \left(E_0 - \sum_i m_i E_i^{\mathrm{vib}}\right)\right)\right] \right)$$

where S is the sum of the Huang-Rhys parameters of all vibrational modes. For fitting, we first adjusted E_0 and σ to reproduce the shoulder at 2.15 eV. Then we iteratively varied α and all S_i to reproduce the dominant peak at 2.0 eV.

It is not possible to get a parameter set where good description for the complete spectrum is achieved. We can either reproduce the red side at energies lower than 1.65 eV as shown in Figure S6 b, which results in an underestimation of the peak at 1.8 eV. On the other hand, if this peak is reproduced satisfactorily (Figure S6 c), the fit overestimates the spectrum at 1.7 eV and below. Furthermore, the 0-0 transition is suppressed artificially to get an apparently good description of the spectra. This procedure is physically unreasonable, as the shape of the emission spectra remains the same even when decreasing the concentration by an order of magnitude to 5.0·10⁻⁷ M, excluding any intermolecular interactions between the chromophores.

However, modelling is possible using two separate progressions. We again started with the spectrum at 200 K. First we used the vibrational modes of TT to perform a Franck-Condon fit onto the emission of CT at 200 K, as the emitting states should in principle be similar. We then used this approximation as a starting point for both the high energy progression (HEP) as well as the low energy progression

20

(LEP) of the TT emission and iteratively changed the fitting parameters to achieve good agreement between model and data. The other temperatures were then fitted consecutively, varying mainly the Gaussian line widths, the amplitudes and the energetic positions of both contributions. Table S7.1 contains the final parameters and figure S7.2 shows the spectra and the calculated progressions for each temperature.
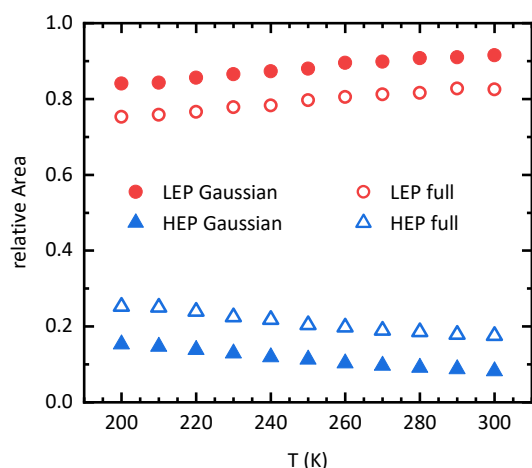
Table S7.1: Fitting parameters and resulting reorganization energies for low energy progression (LEP) and high energy progression (HEP) of TT in hexane ($5.0 \cdot 10^{-6}$ M) at different temperatures.

Temperature (K)		E_0 (eV)	σ (meV)	S 55 meV	S 135 meV	S 180 meV	λ (meV)
200	LEP	2.006	59.3	0.42	0.406	0.614	188.4
	HEP	2.148	59.3	0.09	0.341	0.478	137.0
210	LEP	2.009	59.6	0.417	0.406	0.614	188.3
	HEP	2.151	61.1	0.09	0.341	0.478	137.0
220	LEP	2.013	59.9	0.411	0.415	0.611	188.6
	HEP	2.153	61.7	0.09	0.341	0.478	137.0
230	LEP	2.016	60.2	0.408	0.439	0.602	190.1
	HEP	2.155	62.3	0.09	0.341	0.478	137.0
240	LEP	2.017	60.8	0.387	0.472	0.581	189.6
	HEP	2.155	63.5	0.09	0.341	0.478	137.0
250	LEP	2.019	61.1	0.378	0.472	0.581	189.1
	HEP	2.157	64.1	0.09	0.341	0.478	137.0
260	LEP	2.021	62.3	0.354	0.49	0.575	189.1
	HEP	2.157	67.7	0.09	0.341	0.478	137.0
270	LEP	2.022	62.9	0.354	0.49	0.575	189.1
	HEP	2.157	68.3	0.09	0.341	0.478	137.0
280	LEP	2.025	62.9	0.354	0.523	0.563	191.4
	HEP	2.158	68.3	0.09	0.386	0.478	143.1
290	LEP	2.028	64.1	0.345	0.523	0.578	193.6
	HEP	2.159	69.8	0.09	0.386	0.478	143.1
300	LEP	2.027	64.7	0.321	0.523	0.572	191.2
	HEP	2.159	71.9	0.09	0.386	0.478	143.1

21
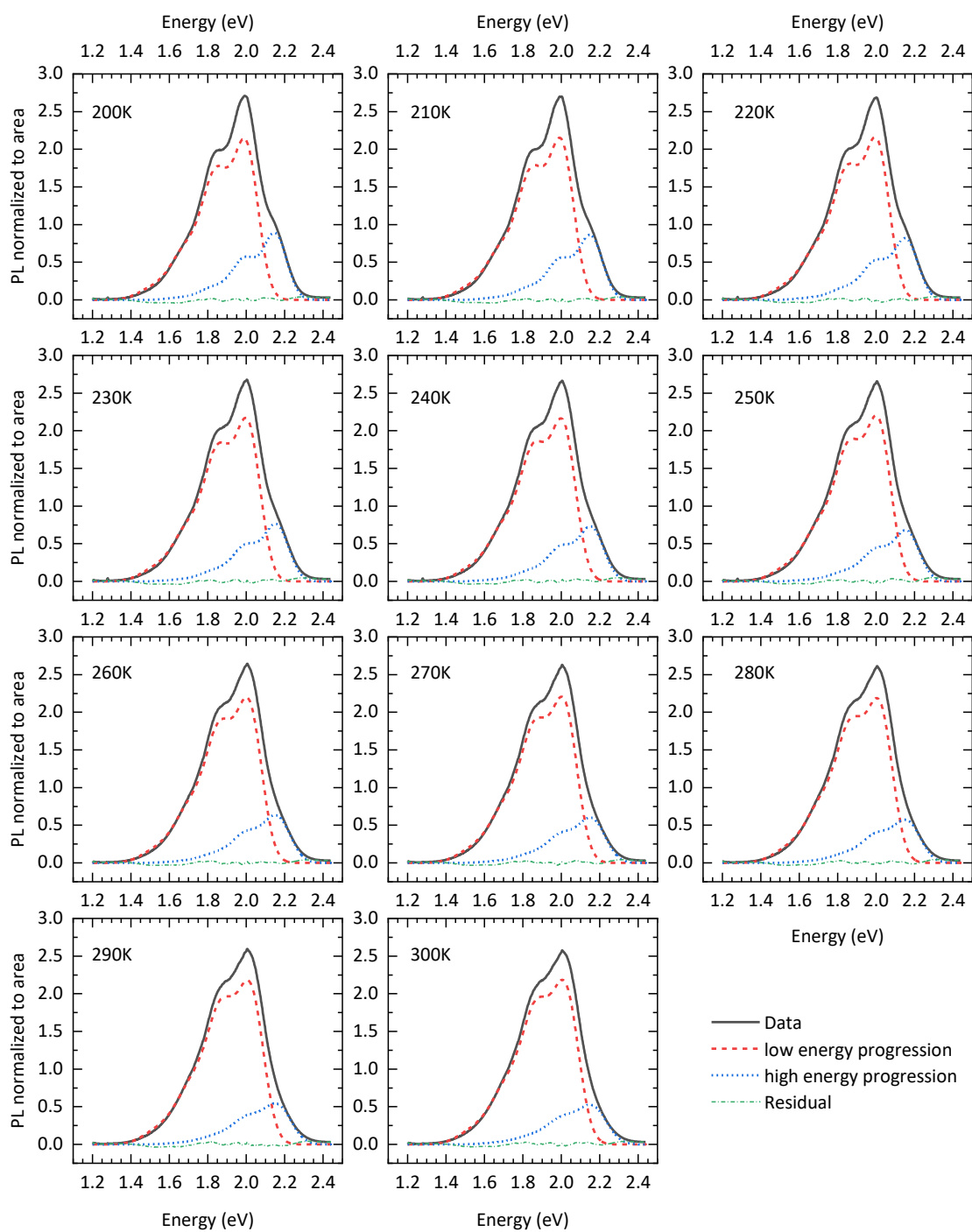
Figure S7.2: Emission of TT in hexane (5.0·10⁻⁶ M) with decomposition into low energy progression and high energy progression at different temperatures.

22

Figure S7.3: Distribution of the total area of high energy and low energy contribution for different decomposition methods

We note that the decomposition is ambiguous, as the high energy progression can also be modelled by a single Gaussian. However, this only affects the intensity ratio between both contributions and not the physical meaning. Figure S7.3 shows the difference for the relative area of both contributions between a high energy Gaussian and a full high energy progression. Table S7.2 contains the corresponding fitting parameters and the related decompositions of the spectra are show in Figure S7.4.

Table S7.2: Fitting parameters and resulting reorganization energies for low energy progression and high energy Gaussian of TT in hexane ($5.0 \cdot 10^{-6}$ M) at different temperatures.

| Temperature (K)		E_0 (eV)	σ (meV)	S 55 meV	S 135 meV	S 180 meV	λ (meV)
200	progression	1.995	59.9	0.26	0.453	0.478	161.5
	Gaussian	2.133	66.7				
210	progression	1.998	60.5	0.26	0.453	0.478	161.5
	Gaussian	2.138	67.5				
220	progression	2.003	62.5	0.26	0.453	0.481	162.0
	Gaussian	2.142	67.8				
230	progression	2.004	64.0	0.204	0.471	0.487	162.5
	Gaussian	2.146	69.0				
240	progression	2.007	65.0	0.204	0.471	0.493	163.5
	Gaussian	2.148	70.2				
250	progression	2.009	65.4	0.204	0.483	0.493	165.2
	Gaussian	2.147	71.0				
260	progression	2.013	66.7	0.204	0.483	0.511	168.4
	Gaussian	2.153	72.2				
270	progression	2.015	67.5	0.204	0.483	0.517	169.5
	Gaussian	2.153	74.1				
280	progression	2.018	68.0	0.204	0.489	0.517	170.3
	Gaussian	2.157	74.3				
290	progression	2.019	68.3	0.198	0.495	0.52	171.3
	Gaussian	2.156	74.3				
300	progression	2.022	69.9	0.198	0.495	0.529	172.9
	Gaussian	2.156	74.0				

23
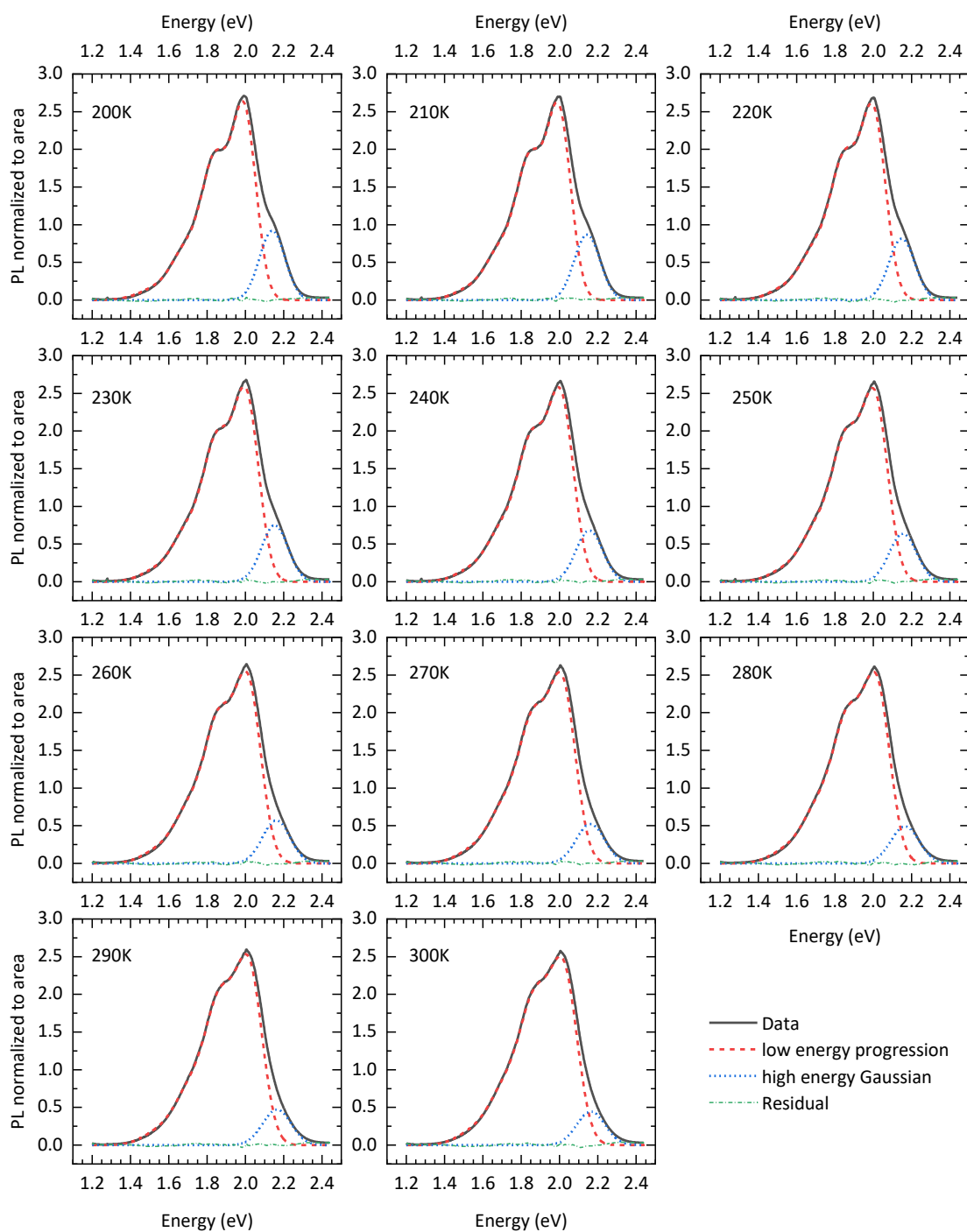
Figure S7.4: Emission of TT in hexane ($5.0 \cdot 10^{-6}$ M) with alternative decomposition into low energy progression and high energy Gaussian at different temperatures.

24

8 Literature

1. A. K. Malde, L. Zuo, M. Breeze, M. Stroet, D. Poger, P. C. Nair, C. Oostenbrink and A. E. Mark, *J. Chem. Theory Comput.*, 2011, **7**, 4026-4037.
2. S. Canzar, M. El-Kebir, R. Pool, K. Elbassioni, A. K. Malde, A. E. Mark, D. P. Geerke, L. Stougie and G. W. Klau, *J. Comput. Biol.*, 2013, **20**, 188-198.
3. K. B. Koziara, M. Stroet, A. K. Malde and A. E. Mark, *J. Comput. Aided Mol. Des.*, 2014, **28**, 221-233.
4. ATB Database: CT Structure and Toplogy Files, https://atb.uq.edu.au/molecule.py?molid=285451, (accessed June 2019).
5. ATB Database: TT Structure and Toplogy Files, https://atb.uq.edu.au/molecule.py?molid=285450, (accessed June 2019).
6. M. J. Frisch, G. W. Trucks, H. B. Schlegel, G. E. Scuseria, M. A. Robb, J. R. Cheeseman, G. Scalmani, V. Barone, G. A. Petersson, H. Nakatsuji, X. Li, M. Caricato, A. V. Marenich, J. Bloino, B. G. Janesko, R. Gomperts, B. Mennucci, H. P. Hratchian, J. V. Ortiz, A. F. Izmaylov, J. L. Sonnenberg, Williams, F. Ding, F. Lipparini, F. Egidi, J. Goings, B. Peng, A. Petrone, T. Henderson, D. Ranasinghe, V. G. Zakrzewski, J. Gao, N. Rega, G. Zheng, W. Liang, M. Hada, M. Ehara, K. Toyota, R. Fukuda, J. Hasegawa, M. Ishida, T. Nakajima, Y. Honda, O. Kitao, H. Nakai, T. Vreven, K. Throssell, J. A. Montgomery Jr., J. E. Peralta, F. Ogliaro, M. J. Bearpark, J. J. Heyd, E. N. Brothers, K. N. Kudin, V. N. Staroverov, T. A. Keith, R. Kobayashi, J. Normand, K. Raghavachari, A. P. Rendell, J. C. Burant, S. S. Iyengar, J. Tomasi, M. Cossi, J. M. Millam, M. Klene, C. Adamo, R. Cammi, J. W. Ochterski, R. L. Martin, K. Morokuma, O. Farkas, J. B. Foresman and D. J. Fox, Gaussian 09 Rev. E.01, Gaussian, Inc., Wallingford, CT, 2013
7. A. Bourdick, M. Reichenberger, A. Stradomska, G. C. Bazan, T.-Q. Nguyen, A. Köhler and S. Gekle, *J. Phys. Chem. B*, 2018, **122**, 9191-9201.
8. J. S. Hub, B. L. de Groot and D. van der Spoel, *J. Chem. Theory Comput.*, 2010, **6**, 3713-3720.
9. P. K. H. Ho, J.-S. Kim, N. Tessler and R. H. Friend, *J. Chem. Phys.*, 2001, **115**, 2709-2720.
10. J. Clark, C. Silva, R. H. Friend and F. C. Spano, *Phys. Rev. Lett.*, 2007, **98**, 206406.

5.3 Directing the Aggregation of Native Polythiophene during in Situ Polymerization
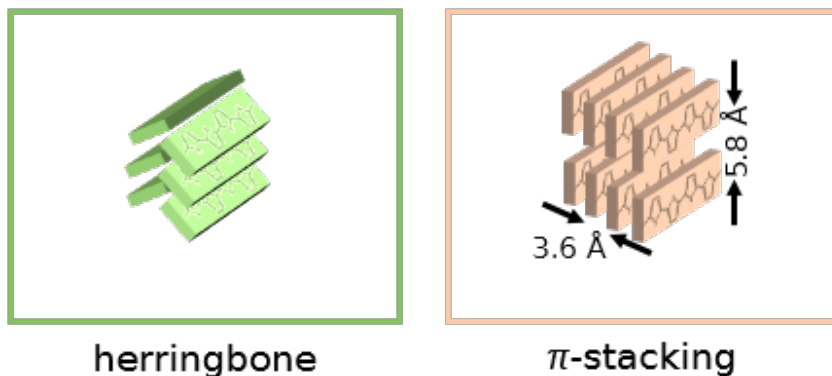
Jenny Lebert, Eva M. Kratzer, Axel Bourdick, Mihael Coric, Stephan Gekle and Eva M. Herzig

ACS OMEGA

Cite This: *ACS Omega* 2018, 3, 6388−6394

Article

Directing the Aggregation of Native Polythiophene during in Situ Polymerization

Jenny Lebert,[†] Eva M. Kratzer,[†] Axel Bourdick,[‡] Mihael Coric,[†] Stephan Gekle,[‡] and Eva M. Herzig*[,†,§]

[†]Herzig Group, Munich School of Engineering, Technische Universität München, Lichtenbergtstraße 4a, 85748 Garching, Germany

[‡]Biofluid Simulation and Modeling, Theoretische Physik, Universität Bayreuth, Universitätsstraße 30, 95440 Bayreuth, Germany

[§]Dynamics and Structure Formation - Herzig Group, Experimentalphysik, Universität Bayreuth, Universitätsstraße 30, 95447 Bayreuth, Germany

S *Supporting Information*

ABSTRACT: The performance of semiconducting polymers strongly depends on their intra- and intermolecular electronic interactions. Therefore, the morphology and particularly crystallinity and crystal structure play a crucial role in enabling a sufficient overlap between the orbitals of neighboring polymers. A new solution-based in situ polymerization for the fabrication of native polythiophene thin films is presented, which exploits the film formation process to influence the polymer crystal structure in the resulting thin films. The synthesis of the insoluble polythiophene is based on an oxidative reaction in which the oxidizing agent, iron(III) *p*-toluenesulfonate (FeTos), initially oxidizes the monomers to enable the polymer chain growth and secondly the final polymers, thereby chemically doping the polythiophene. To exploit the fact that the doped polythiophene has a different crystal packing structure compared to the undoped polythiophene, we investigate the structural effect of this inherent doping process by varying the amounts of FeTos in the reaction mixture, creating polythiophene thin films with different degrees of doping. The structural investigation performed by means of grazing incidence wide-angle X-ray scattering (GIWAXS) suggests that the strongly doped polymer chains aggregate in a π-stacked manner in the film formation process. Moreover, this π-stacking can be maintained after the removal of the dopant molecules. GIWAXS measurements, molecular dynamics simulations, and spectroscopic analysis suggest the presence of polythiophene in a novel and stable crystal structure with an enhanced intermolecular interaction.
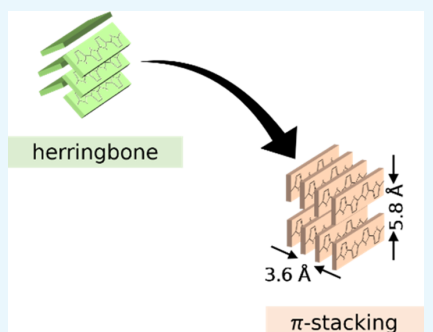
INTRODUCTION

Semiconducting polymers are the subject of intense research because of their highly attractive applications in organic electronic devices.[1−3] The charge carrier transport in the conjugated polymers takes place either along the conjugated backbone of a single polymer chain (intramolecular) or through the overlapping orbitals of neighboring molecules (intermolecular). While the intramolecular transport requires an elongated and planarized backbone for an outstretched conjugated system, the intermolecular transport depends on the overlap of the orbitals and therefore on the geometry of the backbone aggregation, i.e., the crystal structure. Hence, electronic properties of semiconducting polymers are strongly dictated by their morphology and crystallinity.[4,5] Thin films of semiconducting polymers, however, are often amorphous or semicrystalline, creating a need for methods to enhance their crystallinity. Changing the molecular structure of the polymers is the most common approach to induce crystallinity. The addition of, for example, electronically insulating alkyl side chains to the backbone strongly increases the tendency of semiconducting polymers to crystallize, leading to a significant improvement of their electronic properties. Moreover, the side chains enhance the polymer solubility, enabling an easier

processing from solution. One of the most investigated semiconducting polymers that was designed accordingly is the polythiophene (PT) derivative poly-3-hexylthiophene (P3HT).

In this letter, we present how crystallization and intermolecular interaction of polythiophene (PT) can be steered by the choice of processing route instead. We introduce a solution-based in situ polymerization which employs iron(III) *p*-toluenesulfonate hexahydrate (FeTos) as an oxidizing agent and a chemical dopant in the same fabrication step. The included doping process additionally has a strong effect on polymer aggregation, inducing a new and stable PT crystal structure that leads to an enhanced chromophore interaction within the semiconducting thin films. Since the dopant is rinsed out after the synthesis, no electronically inactive material remains incorporated in the insoluble thin films.

Article

■ RESULTS AND DISCUSSION

We choose to perform the oxidative polymerization reaction with FeTos, as it is well-established in the in situ synthesis of high-performing poly-3,4-ethylenedioxythiophene (PEDOT) thin films.[6] In our study, bithiophene (BT) serves as a monomer molecule for the polymerization of polythiophene. We perform the in situ polymerization from a metastable reaction mixture of both BT and FeTos. While within the dilute solution the reaction is prevented by the close redox potentials of the two reactants, the polymerization only starts during the processing, when the concentration of the reactants is significantly increased by the drying of the solvent.[7,8] The reaction mechanism can be divided into two subsequent steps.[9] Initially, iron(III) ions oxidize the monomer molecules to radical cations which subsequently polymerize. Depending on the employed amount of oxidizing agent, the already synthesized polymer chains are further oxidized by excess iron(III) ions in a second step. Effectively, this further oxidation is a chemical doping of the chains, introducing free charge carriers into the conjugated molecules.[9] The positive charges on the chain are stabilized by the anions of FeTos, the tosylates, which are electrostatically attached to it. Simulations show that the tosylates align perpendicular to the polythiophene backbones.[10] We are interested in fabricating an insoluble semiconducting material with improved performance, exploiting the doping procedure during the processing. We therefore spin coat the metastable mixture and subsequently rinse out all residual monomers and oxidant molecules. It is known that the choice of washing solvent has a strong effect on the electronic properties of the obtained PT.[11] While rinsing in acetonitrile leaves the polymer chains in their doped and therefore in conducting state, ethanol additionally de-dopes the PT and removes the previously electrostatically attached tosylate counter ions, leaving PT in its semiconducting, unsubstituted state. Hence, we are able to obtain doped and undoped PT in the final thin films, depending on the last rinsing step, but using the same reaction mixtures. For an improved intermolecular interaction, the thin films of semiconducting PT are thermally annealed at 200 °C for 10 min right after the washing procedure.

To investigate the effect of the doping process occurring during the film formation step on the nanostructure of the final PT films, we vary the molar fraction of FeTos

$$X_{FeTos} = \frac{n_{FeTos}}{n_{FeTos} + n_{BT}} \qquad (1)$$

with n_{FeTos} and n_{BT} as the amounts of FeTos and BT in the reaction mixture, respectively. We employ fractions ranging from 0.25 to 0.75. Afterwards, we investigate the properties of both processing routes with conducting (acetonitrile-rinsed) and semiconducting (ethanol-rinsed and annealed) PT films separately. First, we analyze the electronic and structural properties of the conducting PT films by means of four-point probe measurements, UV/vis spectroscopy, and grazing incidence wide-angle X-ray scattering (GIWAXS). Thereafter, we show the effect of the process on the structure (GIWAXS) and the electronic interaction (UV/vis absorbance and emission spectroscopy) of the semiconducting PT chains.

We performed four-point probe measurements on the conducting PT films to show that the final doping level is controlled by the amount of FeTos in the reaction mixture. Figure 1a displays the in-plane electrical conductivities which
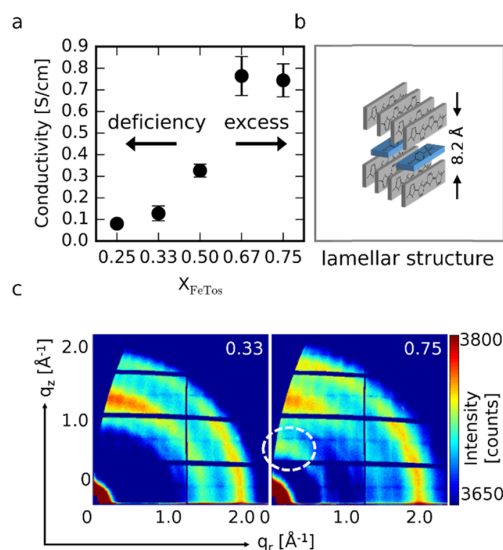
Figure 1. Properties of in situ polymerized conducting polythiophene thin films. (a) In-plane conductivities of films synthesized from the reaction mixtures with varied molar fractions of FeTos obtained by four-point probe measurements. (b) Schematic depiction of the proposed lamellar structure of doped PT and tosylate ions, and the given crystal lattice distance corresponds to lamellar backbone spacing, orientation of tosylate according to simulations found in the literature.[10] (c) The two-dimensional (2D) GIWAXS pattern of films synthesized with FeTos molar fractions of 0.33 (FeTos deficiency) and 0.75 (FeTos excess), Bragg diffraction of lamellar ordering is encircled in white.

we employ as a measure for the doping levels of the films. All conductivities are in the range of 0.1–0.8 S cm^{-1} and thereby several orders of magnitude above the conductivity of semiconducting, undoped PT (10^{-8}–10^{-4} S cm^{-1}).[12,13] Hence, rinsing in acetonitrile definitely leaves the PT thin films in their doped, conducting state. The achieved conductivities are of the same dimension as for the doped PT thin films synthesized in situ with other oxidizing agents.[7] Furthermore, the conductivity shows a drastic increase with increasing molar fraction X_{FeTos} in the reaction mixture.

While it is around 0.1 S cm^{-1} for low X_{FeTos} (0.25 and 0.33), it rises up to 0.8 S cm^{-1} beyond a fraction of 0.5. Thus, we divide the investigated films into two different regimes. The films prepared from the reaction mixtures with X_{FeTos} below 0.5 are from now on referred to as synthesized under iron deficiency, as they show a strongly decreased doping level in comparison to those synthesized under iron excess (X_{FeTos} larger than 0.5). This is additionally supported by the UV/vis absorbance spectra of the conducting thin films (see Figure S1), which show a strong rise in the absorbance band of the doped thiophene chromophores with respect to the π–π^* absorbance band of the undoped molecules with increasing X_{FeTos}, supporting that the increased conductivity is indeed caused by a higher fraction of oxidized thiophenes and not, for example, by a change in film quality or polymer chain length.

We investigate the structural effect of the doping level on the thin film morphology by performing GIWAXS measurements. Figure 1c shows the obtained 2D images of the conducting films obtained from the reaction mixtures with X_{FeTos} of 0.33 and 0.75, respectively. Both scattering patterns exhibit two broad signals centered at q = 1.4 and 1.8 Å^{-1} (real space

distances $d = 4.5$ and 3.5 Å). These peaks are in agreement with what has been observed for doped, conducting PT synthesized via an oxidative polymerization e.g., as nanoparticles or in bulk.[14−16] At a high doping level ($X_{FeTos} = 0.75$), however, an additional Bragg signal arises at $q = 0.77$ Å^{-1} ($d = 8.2$ Å), implying the development of an additional new crystal plane. Yamamoto et al. first found that the bulk PT changes its packing motif beyond a critical level of doping with iodine.[16] According to their findings, a high dopant concentration results in a structural rearrangement of the molecules. The polythiophene backbones arrange in a π-stacked fashion, with the planar molecules parallel to each other. A lamellar structure evolves, in which the dopant molecules are located in between these PT π-stacks. Later, this effect has been explained by the tendency of oligothiophene cations to form π-stacked dimers.[17,18] These dimers develop a chemical bond between the two parallel-arranged backbones, resulting in an additional stabilization of the positive charges. If a large number of positively charged oligothiophenes is present in a system, they even form π-stacked crystal structures.[17,18] Chaalane et al. performed density functional theory calculations of tosylate-doped oligothiophenes to predict the orientation of the tosylate anions with respect to the polymer backbones. They found the sidewise arrangement to be most stable, with an intermolecular distance of 3.56 Å between the sulfur atoms of polythiophene and tosylate, respectively.[10] Therefore, we propose the formation of a similar crystal structure for the PT thin films synthesized under iron excess in our study. The highly doped PT chains arrange in a lamellar structure, giving rise to the new Bragg peak arising in the GIWAXS pattern for $X_{FeTos} = 0.75$. It is therefore assigned to a lamellar distance of 8.2 Å between the polythiophene layers, with tosylate anions sandwiched in between as depicted in Figure 1b.

In the following, we discuss the structure and properties of the semiconducting PT films obtained from the same synthesis by subsequent rinsing with ethanol. Usually, semiconducting native PT is known to exhibit only a short-range order, with the backbones aggregating in a herringbone (HB) fashion as displayed in Figure 2d. The HB packing motif, induced by the electrostatic repulsion of the π-orbitals, leads to a poor overlap of the π-orbitals. Therefore, the intermolecular electronic interaction in unsubstituted PT is weak when compared to its substituted, π-stacked derivatives such as P3HT.

Figure 2a shows the 2D GIWAXS images we measured for semiconducting PT films synthesized under iron deficiency ($X_{FeTos} = 0.33$, left image) and strong iron excess ($X_{FeTos} = 0.75$, right image), respectively. Both patterns show three sharp rings at scattering vectors $q = 1.40$, 1.63, and 1.98 Å^{-1}. While these rings are isotropic for $X_{FeTos} = 0.33$, meaning the crystallites have no favored orientation with respect to the sample surface, they show a strong anisotropy in the case of $X_{FeTos} = 0.75$. Here, the peak intensity is increased in a vertical direction. On the basis of the positions of the rings, we assign them to the main Bragg peaks of polythiophene HB crystals.[16,19,20] Since these peaks are assigned to lattice distances perpendicular to the backbone axis, the anisotropy in the excess film is interpreted as HB crystallites with polymer backbones oriented preferably parallel to the substrate plane.[12,21]

For further analysis of the crystal structures, we radially integrate the intensities of the GIWAXS pattern in vertical (Figure 2b) and horizontal directions (Figure 2c). The vertical cuts of both samples show the three distinct peaks, which match the HB crystal structure. Additionally, a small peak arises
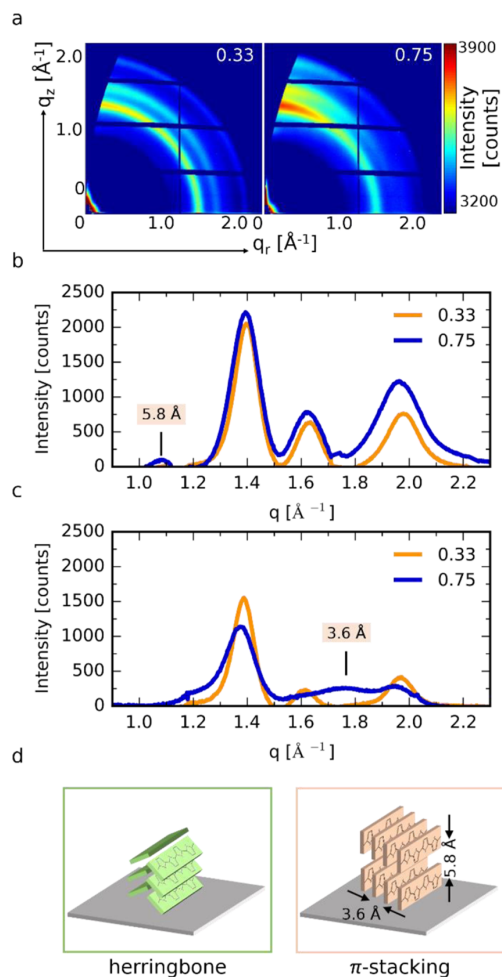

Figure 2. Properties of in situ polymerized semiconducting polythiophene thin films. (a) Two-dimensional GIWAXS scattering pattern of films obtained with FeTos molar fractions of 0.33 (FeTos deficiency) and 0.75 (FeTos excess). (b) Radially integrated scattering intensity in the vertical and (c) horizontal directions. The marked peaks correspond to the π-stacked crystal structure. (d) Schematic depiction of the two crystal structures of the semiconducting PT: herringbone (green box) and π-stacking (beige box).

at $q = 1.08$ Å^{-1} ($d = 5.8$ Å) when iron excess is employed in the synthesis. In the horizontal cuts there is an even larger difference between the two samples. In the horizontal direction, the PT synthesized with $X_{FeTos} = 0.75$ exhibits a new peak at approximately $q = 1.76$ Å^{-1} ($d = 3.6$ Å). From these two new peaks, we conclude that an additional crystal structure is present in the PT thin films for iron excess. On the one hand, the three most prominent peaks of both samples fit to the natural herringbone structure that is known for unsubstituted polythiophene. For PT synthesized under iron deficiency, this seems to be the only crystal structure present within the final semiconducting film. The second sample, prepared under iron excess, on the other hand, shows two additional peaks, one in each of the respective cuts, which is present after washing out the tosylate ions and annealing the film. From the examination of the conducting films, we know that the samples with iron excess contain π-stacked PT structures forming a lamellar

structure with the tosylate ions. Since the processing prior to the washing is identical, we analogously propose a π-stacked structure for the semiconducting PT. The detected new lattice distance of 3.6 Å is close to the calculated intermolecular distance for tosylate-doped oligothiophenes (3.7 Å)[10] and also in the same range as the π-stacking distances of both P3HT (3.8 Å)[22] and PEDOT (3.4 Å).[23] The small peak arising in the vertical direction is consequently interpreted as the side-by-side distance between the backbones. Hence, the difference between the lamellar spacing in the conducting PT processed with iron excess (8.2 Å) and the backbone distance in the semiconducting PT processed with iron excess (5.8 Å) must arise from the removal of the tosylate ion in the ethanol-washing process and a resulting shrinkage of the intermolecular distance. The proposed crystal structure is schematically displayed in Figure 2d.

To our knowledge, this is the first reported π-stacked crystal structure of undoped, semiconducting, unsubstituted polythiophene. The GIWAXS data clearly show that in the presented processing route the doping of the polymer backbones during the film formation has a strong effect on the resulting PT thin film structure. Beyond a critical level of doping, the polymer chains rearrange into a lamellar structure of alternating cationic PT π-stacks and layers of tosylate counter ions in between. However, contrary to the findings of Yamamoto et al. for bulk PT, the induced π-stacking stays intact after the tosylate is removed by rinsing with ethanol. The π-stacked crystal structure is maintained even after thermal annealing at 200 °C, indicating a certain stability. Using molecular dynamics (MD) simulations, we can confirm the feasibility of the discussed structures of PT without the presence of tosylate. We simulate a crystal of 100 PT 10-mers. The calculations show that if the PT chains are constrained to the crystal plane separations observed in the experiment (5.8 and 3.6 Å), but are nevertheless free in rotation around the backbone, all the PT chains tilt in the same direction and form π-stacks. When removing the constraints, the vertical PT stacks slide in position and tilt in an alternating fashion, resulting in a typical herringbone structure with the calculated separations (unit cell parameters $a = 7.10$ Å and $b = 5.71$ Å) agreeing well with the experimental values here and in the literature ($a = 7.81$ Å and $b = 5.56$ Å).[19,20] This indicates that the herringbone structure exhibits a strong global minimum, while a π-stacked structure is possible if the movement of the polymer chains is prevented due to the polymer chains being embedded in the densely packed films (see Figure S2).

Finally, we perform absorbance and emission spectroscopy measurements on the semiconducting thin films to investigate the effect of the altered crystal structure on the intermolecular interaction of the PT chains. Figure 3 shows the spectra of the semiconducting PT films. The UV/vis absorbance of all investigated thin films expands from the ultraviolet region to beyond 600 nm. As the plot shows, the maximum of the absorbance shifts from 465 to 500 nm for PT synthesized under iron excess. Moreover, the intensity decreases in the low wavelength region, while the intensity of the shoulders increases at higher wavelengths. We assume that the absorption properties of PT are very similar to those of the well-investigated P3HT, since their backbones are composed of the same thiophene chromophores. Therefore, we can interpret the spectra as a superposition of the amorphous contributions of the disordered PT chains in the higher energy section and the vibronic transitions of the aggregated thiophene chromophores
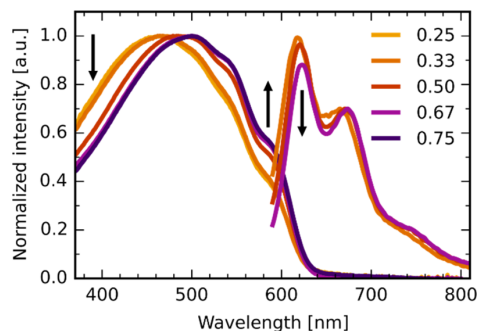

Figure 3. Normalized absorbance and emission spectra of semiconducting PT films polymerized in situ with varied molar fractions of FeTos (see legend). Each absorbance spectrum is normalized to its respective maximum, emission spectra are normalized to the intensity of the 0−1 transition. Arrows indicate a decrease in amorphous contributions and an increase of vibronic transitions in the absorbance spectra and a decrease of the 0−1 transition in the emission spectra. Excitation wavelength for all emission measurements is 500 nm.

of elongated, ordered polymer chains at higher wavelengths.[24] Hence, the fraction of ordered PT backbones in the films increased when synthesized under iron excess.

Moreover, the relative increase of the vibronic shoulders compared to the amorphous contribution induces the shift of the absorbance maximum, although the positions of the single absorbance bands seem to remain unchanged. Thus, the chemical constitution of the semiconducting polymers is not altered by the different synthetic parameters.

The emission spectra give further insight into the character of the chromophore interaction. All spectra exhibit the most intense emission band at around 620 nm and a second strong emission at 670 nm. With increasing fraction of FeTos, the relative intensity of the first band decreases. Moreover, the spectra are slightly redshifted at higher fractions. The energy of the different emissions as well as the ratio between the single emission bands is comparable to those of aggregated but not fully crystallized P3HT, with the thiophene chromophores surrounded by the π-system of the other backbones.[24] This is plausible, as PT is the backbone of P3HT and therefore features very similar electronic properties. The decreasing ratio of the 0−0 to 0−1 emission is a clear indication of an increased order within the films. The redshift on the other hand suggests an increased interaction between the chromophores of neighboring polymer chains. Therefore, the synthesis under iron excess appears to have two effects: firstly, the overall order within the thin film increased, while secondly, the new π-stacked crystal structure results in an increased intermolecular interaction between the backbones compared to the purely HB packed PT.[25,26]

Combining the results of the four-point probe measurements, the GIWAXS data and spectroscopic analysis, we draw a model of how the doping process influences the crystal structure of the in situ polymerized PT. Figure 4 schematically depicts the processes of the BT polymerization and the following doping as well as the resulting crystal structures of the differently doped chains. In the first part of the film forming process, the monomers are oxidized by the iron ions and subsequently polymerize. Although the oligothiophenes become insoluble beyond a certain chain length, they still possess enough mobility to undergo additional oxidation by
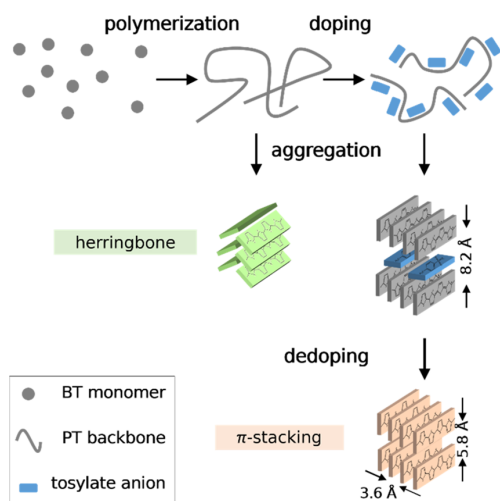
Figure 4. Schematic representation of the in situ polymerization and crystal structures present in PT films synthesized with FeTos. The two-step process of BT polymerization and subsequent doping with excess FeTos, which results in semiconducting PT chains aggregating in the herringbone motif, while highly doped PT arranges into π-stacked lamellae. Finally, dedoping of the lamellae results in a stable π-stacked, semiconducting PT crystal structure.

excess iron. Therefore, it is possible to control the resulting doping level by variation of the molar fraction of FeTos in the reaction mixture. Beyond a critical doping level, the doped polythiophene chains form cationic π-stacks. In the final doped films obtained after acetonitrile rinsing, these are arranged in a layered structure with layers of the tosylate counter ions in between. Opposite to that, the undoped chains aggregate in their natural HB motif. After dedoping and removal of the tosylate ions from the highly doped chains, the PT chains originally in the lamellar configuration retain their π-stacking motif, despite it usually not being their equilibrium crystal structure.

In summary, we presented a solution-based in situ polymerization process for unsubstituted semiconducting polymers that offers the possibility to exploit the involved doping process for influencing the type of crystal structure and aggregation of the polymer chains. We show that upon variation of the amount of oxidizing agent in the reaction mixture, the level of doping of the resulting films can be tuned. Aside from an increase in conductivity of the resulting conducting PT films, we are also able to show that an increased doping level has a sustainable impact on the structure. The GIWAXS measurements confirm the formation of a π-stacked lamellar structure beyond a critical level of doping. This π-stacking of the PT backbones is preserved in the crystallites even after dedoping and removal of the tosylate counter ions. This results in a new crystal structure of unsubstituted semiconducting polythiophene and, as shown by the spectroscopic analysis, in an increased intermolecular interaction. Here, native polythiophene (PT) serves as a model polymer for this process, which should be transferable to other conjugated polymers of similar chemical architecture.

■ METHODS

Thin Film Preparation. The in situ polymerization was performed by spin coating the metastable reaction mixture of 2,2′-bithiophene (Alfa Aesar) and iron(III) p-toluenesulfonate

hexahydrate (Aldrich) in 1-propanol (synthesis grade, Roth). The precleaned glass substrates were coated with thin layers of polypropylene (Aldrich) by spin coating from 1-chlorobenzene (synthesis grade, Roth) to increase the adhesion of the polythiophene films during the posttreatment steps. All chemicals involved were used without further purification. The metastable reaction mixture was spin coated with 2000 rpm for 60 s at a substrate temperature of 90 °C. Afterwards, the films were rinsed in either acetonitrile (doped polythiophene films) or ethanol (undoped polythiophene) for 30 min. Finally, the undoped PT films were annealed at 200 °C for 10 min in ambient atmosphere. For each experiment, the sum of the molar concentrations of PT and FeTos in the reaction mixture was kept constant upon variation of the ratio between them. Nevertheless, the overall concentration was set to match the resulting thickness required for each experimental method.

Four-Point Probe Measurements. The voltage was detected for a current sweep between 1.0 and −1.0 μA, the sheet resistance was obtained by linear regression. The film thickness necessary for the conductivity calculation was determined by profilometry. The concentration of the reaction mixtures was 0.2 mol L^{-1}.

Grazing Incidence Wide-Angle X-ray Scattering. The GIWAXS measurements were performed at the beamline 7.3.3 at the Advanced Light Source with an X-ray wavelength of λ = 0.124 nm (energy of 10 keV).[27] The scattered intensity was detected with a Pilatus 2D detector at a sample-to-detector distance of 299 mm. The incident angle between the beam and the sample was 0.16°. The solid angle corrected 2D pattern as well as the radially integrated intensities were obtained with the GIXSGUI 1.6 software of Argonne National Laboratory, taking into account the necessary corrections.[28] The concentration of the reaction mixtures was set to 0.7 mol L^{-1}.

UV/vis Spectroscopy. The absorbance was obtained by performing transmission and reflection measurements with an integrating sphere. The luminescence spectra were obtained by spin coating onto polypropylene coated silicon substrates and measured in reflection. All emission spectra were measured with an excitation wavelength of 500 nm. The concentration for both experiments was 0.2 mol L^{-1}.

MD Simulations. Molecular dynamics simulations were performed with Gromacs using the Gromos 53a6 force field.[29,30] For the simulations, united-atom force field topologies were used, and the visual analysis of the molecular structure and trajectories was carried out with VMD.[31] The structure file for the model of a PT 10-mer was generated with JME,[32] based on which a force field file was created using the Automated Force Field Topology Builder and Repository.[33] We enhanced the model by calculating partial charge distribution and the potential energy surface (PES) of the dihedrals between individual thiophene rings ourselves with Gaussian 09, rev. E.01.[34] We used the B3LYP/6-31g(d,p) level for theory in all quantum chemical calculations. Tight convergence criteria were requested in geometry optimization. We utilized the symmetry of the molecule, so that the PES for the first dihedral was also used for the last and so on. We adjusted the model used for MD simulations to replicate the PES calculated by the quantum chemical calculations by rotating the molecule around the angle in question with enforced rotation. The potential energy of this process was determined with the Gromacs tool gmx energy. We implemented the new dihedrals with Ryckaert–Bellemans potentials.[35] Simulations were performed locally and on the

Jureca Supercomputer.[36] Further information on the model system is given in the Supporting Information.

■ ASSOCIATED CONTENT

⑤ Supporting Information

The Supporting Information is available free of charge on the ACS Publications website at DOI: 10.1021/acsomega.8b00684.

> Absorbance spectra of doped polythiophene films; description and results of MD simulations (PDF)

■ AUTHOR INFORMATION

Corresponding Author

*E-mail: eva.herzig@uni-bayreuth.de.

ORCID ⓘ

Stephan Gekle: 0000-0001-5597-1160

Eva M. Herzig: 0000-0002-0151-5562

Notes

The authors declare no competing financial interest.

■ ACKNOWLEDGMENTS

■ REFERENCES

(1) Thompson, B. C.; Fréchet, J. M. J. Polymer-Fullerene Composite Solar Cells. *Angew. Chem., Int. Ed.* **2008**, *47*, 58−77.

(2) Arias, A. C.; MacKenzie, J. D.; McCulloch, I.; Rivnay, J.; Salleo, A. Materials and Applications for Large Area Electronics: Solution-Based Approaches. *Chem. Rev.* **2010**, *110*, 3−24.

(3) Rogers, J. A.; Someya, T.; Huang, Y. Materials and Mechanics for Stretchable Electronics. *Science* **2010**, *327*, 1603−1607.

(4) Sirringhaus, H.; Brown, P. J.; Friend, R. H.; Nielsen, M. M.; Bechgaard, K.; Langeveld-Voss, B. M. W.; Spiering, A. J. H.; Janssen, R. A. J.; Meijer, E. W.; Herwig, P.; de Leeuw, D. M.; et al. Two-Dimensional Charge Transport in Self-Organized, High-Mobility Conjugated Polymers. *Nature* **1999**, *401*, 685−688.

(5) Singh, C. R.; Gupta, G.; Lohwasser, R.; Engmann, S.; Balko, J.; Thelakkat, M.; Thurn-Albrecht, T.; Hoppe, H. Correlation of Charge Transport with Structural Order in Highly Ordered Melt-Crystallized poly(3-Hexylthiophene) Thin Films. *J. Polym. Sci., Part B: Polym. Phys.* **2013**, *51*, 943−951.

(6) Bubnova, O.; Khan, Z. U.; Malti, A.; Braun, S.; Fahlman, M.; Berggren, M.; Crispin, X. Optimization of the Thermoelectric Figure of Merit in the Conducting Polymer Poly (3, 4-Ethylenedioxythiophene). *Nat. Mater.* **2011**, *10*, 429−433.

(7) Bravo-Grimaldo, E.; Hachey, S.; Cameron, C. G.; Freund, M. S. Metastable Reaction Mixtures for the in Situ Polymerization of Conducting Polymers. *Macromolecules* **2007**, 7166−7170.

(8) McFarlane, S. L.; Deore, B. A.; Svenda, N.; Freund, M. S. A One-Step, Organic-Solvent Processable Synthesis of PEDOT Thin Films via in Situ Metastable Chemical Polymerization. *Macromolecules* **2010**, *43*, 10241−10245.

(9) Elschner, A. From EDOT to PEDOT Oxidative Polymerization and Other Routes. In *PEDOT - Principles and Applications of an Intrinsically Conductive Polymer*; Taylor and Francis Group, 2011; pp 67−82.

(10) Chaalane, A.; Mahi, D.; Dkhissi, A. Structural and Electronic Properties of Doped Oligothiophenes in the Presence of P-Toluensulfonate Acids. *Theor. Chem. Acc.* **2015**, *134*, No. 66.

(11) Borrelli, D. C.; Barr, M. C.; Bulović, V.; Gleason, K. K. Bilayer Heterojunction Polymer Solar Cells Using Unsubstituted Polythiophene via Oxidative Chemical Vapor Deposition. *Sol. Energy Mater. Sol. Cells* **2012**, *99*, 190−196.

(12) Borrelli, D. C.; Lee, S.; Gleason, K. K. Optoelectronic Properties of Polythiophene Thin Films and Organic TFTs Fabricated by Oxidative Chemical Vapor Deposition. *J. Mater. Chem. C* **2014**, *2*, 7223.

(13) Kaneto, K.; Yoshino, K.; Inuishi, Y. Electrical and Optical Properties of Polythiophene Prepared by Electrochemical Polymerization. *Solid State Commun.* **1983**, *46*, 389−391.

(14) Jeon, S. S.; Yang, S. J.; Lee, K. J.; Im, S. S. A Facile and Rapid Synthesis of Unsubstituted Polythiophene with High Electrical Conductivity Using Binary Organic Solvents. *Polymer* **2010**, *51*, 4069−4076.

(15) Li, X. G.; Li, J.; Meng, Q. K.; Huang, M. R. Interfacial Synthesis and Widely Controllable Conductivity of Polythiophene Micro-particles. *J. Phys. Chem. B* **2009**, *113*, 9718−9727.

(16) Yamamoto, T.; Morita, A.; Miyazaki, Y.; Maruyama, T.; Wakayama, H.; Zhou, Z.-H.; Nakamura, Y.; Kanbara, T.; Sasaki, S.; Kubota, K. Preparation of .Ir-Conjugated Poly(thiophene-2,5-Diyl), Poly@-Phenylene), and Related Polymers Using Zerovalent Nickel Complexes. Linear Structure and Properties of the 7-Conjugated Polymers. *Macromolecules* **1992**, *25*, 1214−1223.

(17) Miller, L. L.; Mann, K. R. π -Dimers and π -Stacks in Solution and in Conducting Polymers. *Acc. Chem. Res.* **1996**, *29*, 417−423.

(18) Brocks, G. Π-Dimers of Oligothiophene Cations. *J. Chem. Phys.* **2000**, *112*, 5353−5363.

(19) Brückner, S.; Porzio, W. The Structure of Neutral Polythiophene. An Application of the Rietveld Method. *Makromol. Chem.* **1988**, *189*, 961−967.

(20) Mo, Z.; Lee, K. B.; Moon, Y. B.; Kobayashi, M.; Heeger, A. J; Wudl, F. X-Ray Scattering from Polythiophene: Crystallinity and Crystallographic Structure. *Macromolecules* **1985**, *18*, 1972−1977.

(21) Youm, S. G.; Hwang, E.; Chavez, C. A.; Li, X.; Chatterjee, S.; Lusker, K. L.; Lu, L.; Strzalka, J.; Ankner, J. F.; Losovyj, Y.; et al. Polythiophene Thin Films by Surface-Initiated Polymerization: Mechanistic and Structural Studies. *Chem. Mater.* **2016**, *28*, 4787−4804.

(22) Prosa, T. J.; Winokur, M. J.; Moulton, J.; Smith, P.; Heeger, A. J X-Ray Structural Studies of Poly(3-Alkylthiophenes): An Example of An Inverse Comb. *Macromolecules* **1992**, *25*, 4364−4372.

(23) Aasmundtveit, K. E.; Samuelsent, E. J.; Pettersson, L. A. A.; Inganäs, O.; Johansson, T.; Feidenhans, R. Structure of Thin Films of Poly (3, 4-Ethylenedioxythiophene). *Synth. Met.* **1999**, *101*, 561−564.

(24) Panzer, F.; Bässler, H.; Köhler, A. Temperature Induced Order-Disorder Transition in Solutions of Conjugated Polymers Probed by Optical Spectroscopy. *J. Phys. Chem. Lett.* **2017**, *8*, 114−125.

(25) Spano, F. C. Modeling Disorder in Polymer Aggregates: The Optical Spectroscopy of Regioregular poly(3-Hexylthiophene) Thin Films. *J. Chem. Phys.* **2005**, *122*, No. 234701.

(26) Spano, F. C.; Silva, C. H- and J-Aggregate Behavior in Polymeric Semiconductors. *Annu. Rev. Phys. Chem.* **2014**, *65*, 477−500.

(27) Hexemer, A.; Bras, W.; Glossinger, J.; Schaible, E.; Gann, E.; Kirian, R.; MacDowell, A.; Church, M.; Rude, B.; Padmore, H. A

SAXS/WAXS/GISAXS Beamline with Multilayer Monochromator. *J. Phys.: Conf. Ser.* **2010**, *247*, No. 012007.

(28) Jiang, Z. GIXSGUI: A MATLAB Toolbox for Grazing-Incidence X-Ray Scattering Data Visualization and Reduction, and Indexing of Buried Three-Dimensional Periodic Nanostructured Films. *J. Appl. Crystallogr.* **2015**, *48*, 917−926.

(29) Hess, B.; Kutzner, C.; van der Spoel, D.; Lindahl, E. GROMACS 4: Algorithms for Highly Efficient, Load-Balanced, and Scalable Molecular Simulation. *J. Chem. Theory Comput.* **2008**, *4*, 435−447.

(30) Oostenbrink, C.; Villa, A.; Mark, A. E.; Van Gunsteren, W. F. A Biomolecular Force Field Based on the Free Enthalpy of Hydration and Solvation: The GROMOS Force-Field Parameter Sets 53A5 and 53A6. *J. Comput. Chem.* **2004**, *25*, 1656−1676.

(31) Humphrey, W.; Dalke, A.; Schulten, K. VMW: Visual Molecular Dynamics. *J. Mol. Graphics* **1996**, *14*, 33−38.

(32) Ertl, P. Molecular Structure Input on the Web. *J. Cheminf.* **2010**, *2*, 1.

(33) Malde, A. K.; Zuo, L.; Breeze, M.; Stroet, M.; Poger, D.; Nair, P. C.; Oostenbrink, C.; Mark, A. E. An Automated Force Field Topology Builder (ATB) and Repository: Version 1.0. *J. Chem. Theory Comput.* **2011**, *7*, 4026−4037.

(34) Frisch, M. J.; Trucks, G. W.; Schlegel, H. B.; Scuseria, G. E.; Robb, M. A.; Cheeseman, J. R.; Scalmani, G.; Barone, V.; Mennucci, B.; Petersson, G. A.; Nakatsuji, H.; Caricato, M.; Li, X.; Hratchian, H. P.; Izmaylov, A. F.; Bloino, J.; Zheng, G.; Sonnenberg, J. L.; Hada, M.; Ehara, M.; Toyota, K.; Fukuda, R.; Hasegawa, J.; Ishida, M.; Nakajima, T.; Honda, Y.; Kitao, O.; Nakai, H.; Vreven, T.; Montgomery, J. A., Jr.; Peralta, J. E.; Ogliaro, F.; Bearpark, M.; Heyd, J. J.; Brothers, E.; Kudin, K. N.; Staroverov, V. N.; Keith, T.; Kobayashi, R.; Normand, J.; Raghavachari, K.; Rendell, A.; Burant, J. C.; Iyengar, S. S.; Tomasi, J.; Cossi, M.; Rega, N.; Millam, J. M.; Klene, M.; Knox, J. E.; Cross, J. B.; Bakken, V.; Adamo, C.; Jaramillo, J.; Gomperts, R.; Stratmann, R. E.; Yazyev, O.; Austin, A. J.; Cammi, R.; Pomelli, C.; Ochterski, J. W.; Martin, R. L.; Morokuma, K.; Zakrzewski, V. G.; Voth, G. A.; Salvador, P.; Dannenberg, J. J.; Dapprich, S.; Daniels, A. D.; Farkas, O.; Foresman, J. B.; Ortiz, J. V.; Cioslowski, J.; Fox, D. J. *Gaussian 09*, revision E.01; Gaussian, Inc.: Wallingford, CT, 2013.

(35) Abraham, M.; Hess, B.; van der Spoel, D.; Lindahl, E. *GROMACS Reference Manual*, version 2016.3, 2016.

(36) Jülich Supercomputing Centre. JURECA: General-Purpose Supercomputer at Jülich Supercomputing Centre. *JLSRF* **2016**, *2*, A62.

Supporting information

Directing the aggregation of native polythiophene during *in situ* polymerization

Jenny Lebert[1], Eva M. Kratzer[1], Axel Bourdick[2], Mihael Coric[1], Stephan Gekle[2], Eva M. Herzig[1,3]*

[1]Herzig Group, Munich School of Engineering, Technische Universität München, Lichtenbergtstraße 4a, 85748 Garching, Germany

[2]Biofluid Simulation and Modeling, Theoretische Physik, Universitätsstraße 30, 95440 Bayreuth, Germany

[3]Dynamics and Structure Formation – Herzig Group, Experimentalphysik, Universität Bayreuth, Universitätsstraße 30, 95447 Bayreuth, Germany

E-mail: eva.herzig@uni-bayreuth.de

Contents.

1. Absorbance spectra of doped polythiophene films

2. Description and results of MD simulations
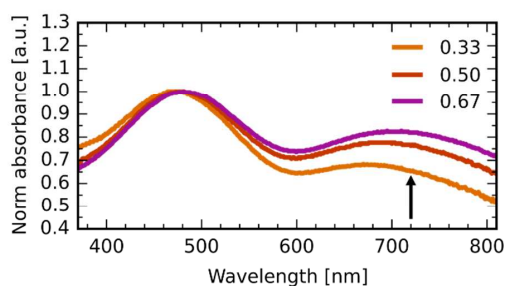
Figure S1. Absorbance spectra of doped polythiophene thin films synthesized with different molar fractions of FeTos. Spectra normalized to maximum of π-π* absorbance of undoped chromophores. Absorbance of oxidized species increases with increasing fraction, as indicated by arrow.
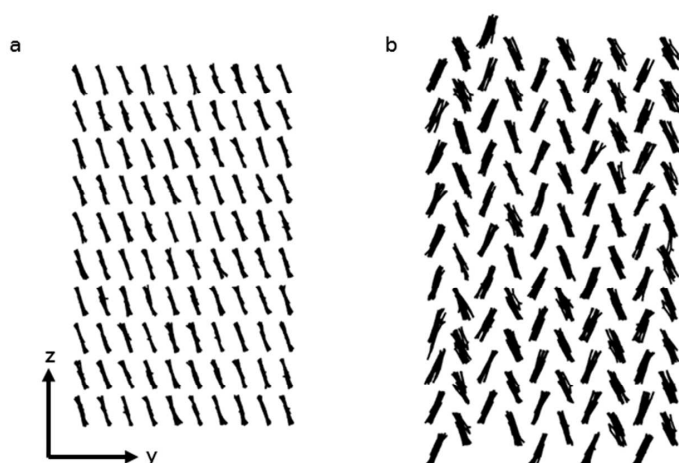
Figure S2. Side view (along the backbone) of a PT 10-mer crystal calculated with the help of MD simulations. In a) the distances are constraint to 5.8 Å in lamellar (vertical) direction and 3.6 Å perpendicular to it (horizontal). As a result, the PT chains align parallel to each other. The translational chain movement is restricted into y and z direction. b) When the constraints are removed, the system aligns in a typical herringbone structure.

MD-calculations:

We generated crystals with the desired lattice spacing with 10 rows and 10 columns. The box size was chosen, such that the crystal continues through its own mirror image via the periodic boundary conditions. The positions of atoms along the backbone of the chain were restricted by spring potentials with a strong spring constant of $10000 \, kJ/(mol \, nm^2)$ in yz direction. All atoms were free to move along the backbone (x direction). We then performed a short NVT simulation of 400 ps locally without a thermostat until the molecules aligned in a stable configuration. The molecules align perpendicular to one another (Figure S2a). Performing the same simulations without the position restraints resulted in a Herringbone structure (Figure S2b).

S3

6 Additional results

6.1 Metadynamics free energy

The analysis of the possible aggregates of the molecules has shown that in dependence of the molecular symmetry, the relative orientation between them plays a crucial role during the aggregation process and the possible resulting structures. The free energy graphs discussed in the publications were calculated mostly with WHAM and umbrella sampling. They display the free energy of two solute molecules in dependence of their distance, while not taking their relative orientation into account. To investigate the difference between varying orientations (type A and type B), we artificially subdivided the configurational phase space by preparing the starting configurations in a certain alignment and compare different starting orientations with one another. This approach is suboptimal, because by design we do not want to sample the whole phase space of the system but still want to simulate long enough for the free energy to converge. Due to the bulky side-chains on the molecules, it is difficult for them to reorientate when they are restraint to small distances, which makes this division plausible. A better approach is to project the system on a two-dimensional free energy surface, so that the dependency of relative distance and angle can be investigated at the same time. Because this is difficult to implement with the umbrella sampling method, we employed metadynamics simulation to investigate the configurational phase space in two dimensions.

The two dimensional free energy surface of CT in hexane solution is shown in figure 8. At low distances two minima are emerging, one at 0° and one at 180°, corresponding to type B and type A aggregation respectively, which are very similar energetically. Umbrella sampling and metadynamics show very good agreement, confirming the validity of this new approach. The results from metadynamics for TT in hexane is displayed in figure 9. The angular dependence of the free energy is more complicated in comparison to CT which is due to the intramolecular twisted nature of the molecules. One distinct global minima exists at an intermolecular angle of about 180° which is in agreement to the one possible aggregate conformation discussed in the publication presented in section 3.3.2.There is an excellent agreement between umbrella sampling and metadynamics.The intramolecular angles were defined as torsional dihedral angles between the molecules.
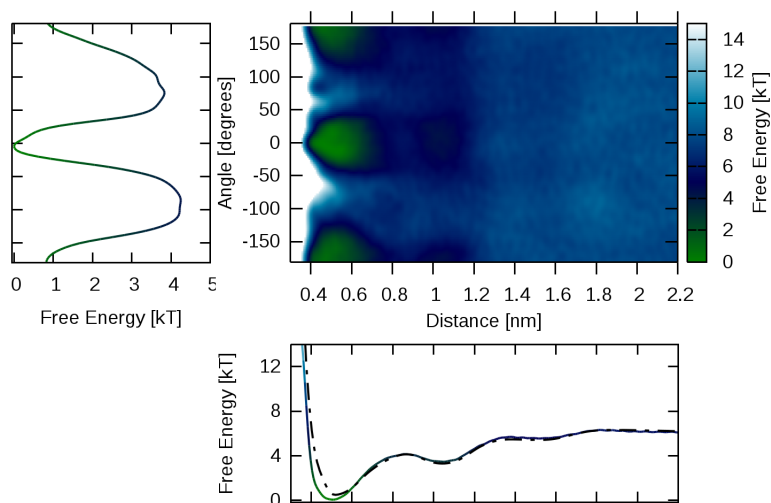
Figure 8: Two dimensional free energy surface of the aggregation process of two CT molecules in hexane solution in dependence of distance and the angle between the molecules. Additionally, projections on the one dimensional reaction coordinates are displayed. The free energy in dependence of intermolecular distance calculated by umbrella simulations in hexane is shown as a dashed line. The data was obtained with metadynamics.
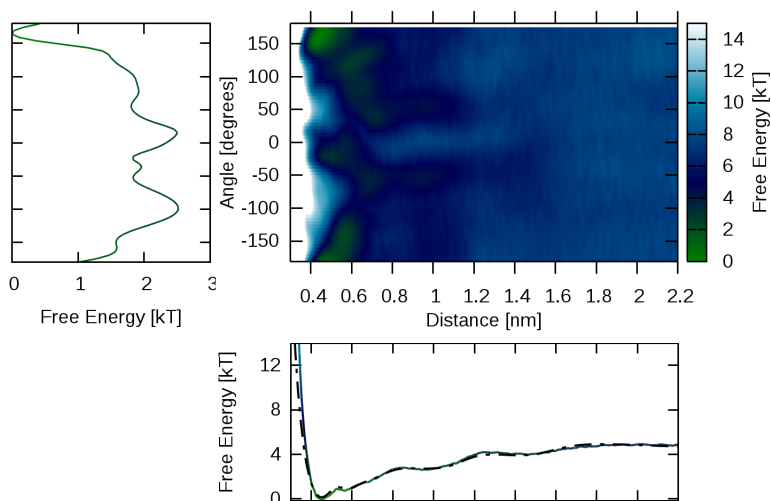
Figure 9: Free energy surface, calculated by 2-d metadynamics for two TT molecules in hexane solution in dependence of distance and the angle between the molecules. Projections on the one-dimensional reaction coordinates are shown alongside the 2d plot. Free Energy calculated with umbrella sampling in mexane is shown as a dashed line.
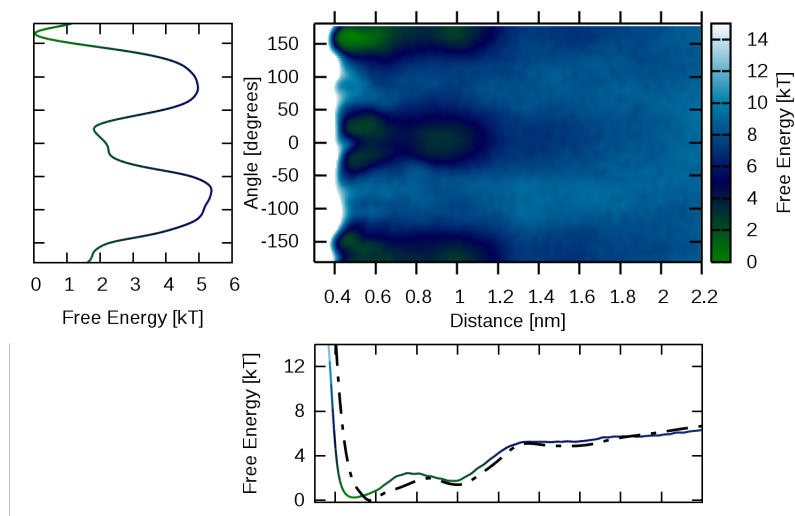
Figure 10: Results from metadynamics for T1 in hexane solution are displayed in dependence of intermolecular distance and the angle between the molecules alongside projections on the one dimensional reaction coordinates. The result from umbrella simulations in hexane for the same system is shown as a dashed line.
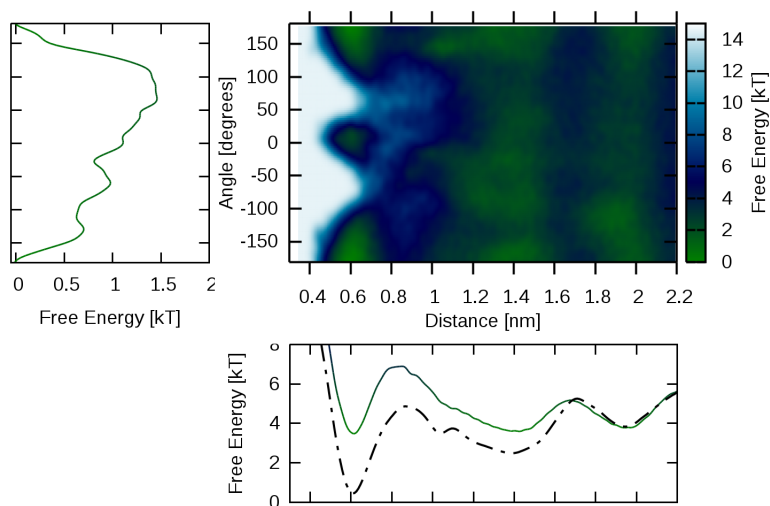
Figure 11: Free energy for H1 in hexane solution calculated with metadynamics in dependence of intermolecular distance and the angle between them together with one dimensional projections on the individual reaction coordinates. We also calculated the free energy with umbrella sampling which is shown as a dashed line.

Like CT, T1 also can aggregate via a type A or a type B pathway. This is also

reflected in the free energy obtained from metadynamics (fig. 10) in hexane solution. Here, type A aggregation is energetically significantly more favored than type B. This is also the case in the other solvent MTHF, which was used in the publication presented in section 3.3.1. The agreement between metadynamics and umbrella sampling is good, but the position of the global minimum is slightly shifted.

The results for H1 in hexane calculated with metadynamics are shown in figure 11. There is one clear global minimum with an intermolecular angle of about 180° which corresponds to the aggregate conformation discussed in the publication which is shown in section 3.3.1. Interestingly, there is a very tight local minimum at 0° surrounded by an energetic barrier. Free energy from metadynamics and from umbrella sampling show good agreement qualitatively but differ in the ratio of the minima. Given that aggregation in H1 is kinetically hindered, umbrella sampling requires averaging over multiple independently sampled reaction pathways in order to sweep the whole configurational phase space. Because the free energy from umbrella sampling in hexane was calculated specifically for this plot, and due to the fact that very good agreement could be achieved for the other systems, we renounced here from excessive sampling.

In summary, metadynamics provides a powerful computational tool in order to characterize complicated free energy surfaces in dependence of two or more reaction coordinates.

Acknowledgments

First and foremost I would like to express my gratitude to my supervisor Prof. Stephan Gekle, who supported me the best he could. With the help of the work environment provided and his calm and patient manner, he provided the framework for me to develop myself freely in this time. Through this, I was able to evolve, develop skills and learn a lot. Nobody can take away the treasures I have found the last few years and that is in part due to his support. I always had the feeling that I can be like I am. I valued frequent discussions with him and his innovative, clever and lateral thinking never stopped to surprise me.

I want to thank Markus Reichenberger and Stefan Wedler, who were the main experimenters I worked with. Through our cooperation, we were able to gain interesting results. Through the combination of computational and experimental approaches insights can be gained which would not be achievable with either one alone.

I want to thank Prof. Anna Köhler, who was frequently part in discussions and supervised the experimental parts. I was able to learn a lot from her, due to her excellent skill set, open mind and light-hearted approach to complicated questions. I also want to thank Prof. Anna Köhler and Prof. Stefan Kümmel for being my mentors. There were never any serious problems, which would have led me to search advise from them within the scope of their mentorship. However, the pure existence of this possibility was always there, which made me feel safe, because I would always have someone to talk to if need be. This is very valuable.

I want to thank the former and current members of the Gekle group. I really liked ever single one of them and they all contributed to a comfortable work environment. Special thanks go to Sebastian Müller for frequent interesting discussions and coffee. I thank Markus Hilt for his work as an IT administrator. If there was a problem, he tackled and solved it right away.

I thank the graduate school 1640 for the financial support, which made this thesis possible. I also thank the Volkswagenstiftung, which made the Juniorprofessur of Stephan Gekle possible, which enabled me to start my PhD in this group.

Finally, I want to thank all my friends and the wild foxes, which are the most valuable things in my life. I also thank the whole universe for existing.

Eidesstattliche Versicherung

Hiermit versichere ich an Eides statt, dass ich die vorliegende Arbeit selbständig verfasst und keine anderen als die von mir angegebenen Quellen und Hilfsmittel verwendet habe.

Weiterhin erkläre ich, dass ich die Hilfe von gewerblichen Promotionsberatern bzw. -vermittlern oder ähnlichen Dienstleistern weder bisher in Anspruch genommen habe, noch künftig in Anspruch nehmen werde.

Zusätzlich erkläre ich hiermit, dass ich keinerlei frühere Promotionsversuche unternommen habe.

Bayreuth, den 20.12.2019

—————————————

Axel Bourdick